Università degli studi di Camerino

School of Advanced Studies

Doctoral course in

CHEMICAL AND PHARMACEUTICAL SCIENCES AND

BIOTECHNOLOGY CHMICAL SCIENCES

XXXVII cycle

Investigation of Metal Porphyrin-Based Porous Organic Polymers for Catalytic Peroxymonosulfate Activation in the Degradation of Organic Pollutants

PhD candidate

Cong Li

Supervisors

Prof. Mario Berrettoni

Prof. Hongzhong Zhang

Co-supervisor

Prof. Silvia Zamponi

Prof. Xia Cao

Coordinator of the PhD Programme
Prof. Claudio Pettinari

Abstract

In this study, metal-porphyrin porous organic polymers (M-P/POP, where M = Fe, Co, or Cu) were synthesized and successfully applied as catalysts for PMS activation to degrade organic pollutants. The catalytic activity was attributed to the selective generation of high-valence metal oxo species (HVMOs: Fe(IV)=O, Co(IV)=O, and Cu(III)=O), which served as the primary reactive species in a non-radical electron transfer pathway. Mechanistic investigations, including quenching experiments, electron paramagnetic resonance (EPR) spectroscopy, and isotope labeling, confirmed that conventional radicals (•OH, $SO_4^{\bullet-}$, and $O_2^{\bullet-}$) contributed negligibly to pollutant degradation, further validating the predominance of the HVMO oxidation mechanism.

The Fe-P/POP and Co-P/POP catalysts demonstrated superior catalytic performance compared to Cu-P/POP, achieving higher degradation efficiencies across a range of organic pollutants. Theoretical calculations revealed a strong correlation between pollutant ionization potential (IP) and degradation rate constants (K_obs), supporting the hypothesis that oxidation proceeded via electron transfer from the pollutant's HOMO to the catalyst's LUMO. Additionally, the M-P/POP/PMS system exhibited excellent stability, recyclability, and negligible metal leaching, confirming its feasibility for long-term applications.

Overall, this study advances the understanding of PMS activation mechanisms and highlights the potential of M-P/POP catalysts for practical wastewater treatment. The combination of high efficiency, selective degradation pathways, and environmental sustainability makes M-P/POP a promising candidate for the removal of persistent organic pollutants in contaminated water sources.

Key words

porous organic polymer; high-valent metal oxo; M-N_4 sites; peroxymonosulfate;

Scientific field of the dissertation (SSD):

CHEM-01/A Analytical Chemistry

School the Ph.D. Student belongs to at UNICAM:

School of Science and Technology, Chemistry Division

Table of Contents

1. Introduction

1.1 General introduction

Water is fundamental to life and human livelihoods, making the protection of water ecosystems critical for societal well-being. Despite the vast global water reserves of approximately 13,860 billion m^3, 96.5% consists of seawater that is unsuitable for direct human use. Of the remaining freshwater, much is locked away in deep aquifers, glaciers, or polar permafrost, leaving only 2.53% of the total water resources accessible for human needs (Fig. 1-1a)[1]. This limited availability is further strained by the rapid expansion of human activities, industrialization, and agricultural development, which have significantly increased water consumption (Fig. 1-1b). At the same time, the discharge of toxic and hazardous pollutants has severely contaminated these already scarce water resources, profoundly affecting their quality and usability. Environmental pollution has consequently emerged as one of the three major global crises, alongside resource scarcity and ecological degradation. Effectively managing polluted water bodies has thus become an urgent challenge for countries worldwide.

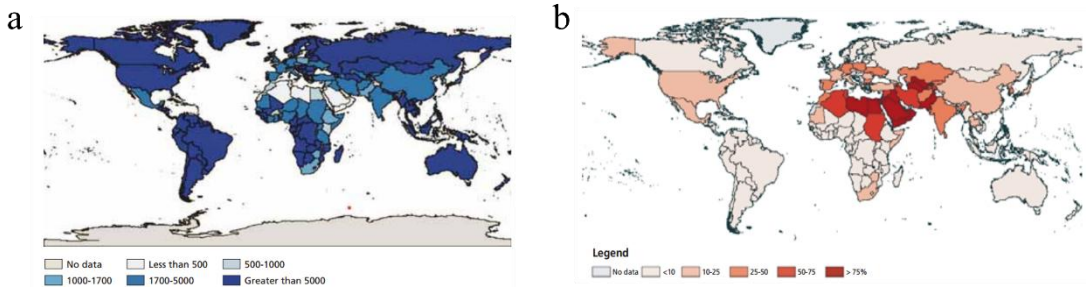

Fig. 1-1 (a) Per Capita Actual Renewable Water and Groundwater Resources, (b) Water Use Intensity Utilization Index by Country.

1.2 Hazards and Management of Organic Pollutants in Water

1.2.1 Overview of Typical Organic Pollutants in Water

Organic pollutants in water encompass a wide variety of substances, including antibiotics, dyes, pesticides, industrial chemicals, and active ingredients from personal care products. These pollutants originate from various sources, such as agricultural runoff, industrial discharges, domestic wastewater, and the transformation of natural organic compounds in the environment. Due to their complex chemical structures and stability, they are resistant to natural degradation, leading to persistence, bioaccumulation, and potential ecological toxicity.[2] As a result, organic pollutants are considered a major challenge in modern water management. Antibiotics, as a class of drugs designed to inhibit and eliminate microorganisms, have experienced steadily increasing global usage, particularly in livestock farming and human healthcare. This widespread use has led to the accumulation of antibiotic residues in surface water, groundwater, and drinking water sources. Although the concentrations of antibiotics in environmental water bodies are typically low (ranging from ng/L to μg/L), their highly effective mechanisms of action against microorganisms mean even low levels can significantly impact aquatic organisms and ecosystems.[3] Furthermore, the pervasive presence of antibiotics increases the environmental load of antibiotic resistance genes, which can spread through water systems and food chains, posing a considerable threat to human health.[4] In the environment, the molecular structures of antibiotics, including aromatic rings and aminoglycoside groups, confer high chemical stability and low degradability under standard natural conditions. Additionally, some antibiotics undergo photochemical reactions when exposed to light, producing more toxic intermediate metabolites. Studies have shown that certain antibiotics, such as sulfonamides and tetracyclines, exhibit significant persistence and pose high potential toxicity to organisms. Antibiotic pollution not only disrupts the balance of aquatic ecosystems but also threatens public health and food safety through the dissemination of antibiotic resistance genes.[5]

Dyes represent another significant class of pollutants, primarily originating from industrial activities such as textile production, dyeing, leather processing, papermaking, and plastic manufacturing. Known for their vivid colors and remarkable chemical

stability, dyes often possess complex structures, including benzene rings, azo groups, nitro groups, and amine groups, which are highly resistant to microbial degradation. During industrial operations, it is estimated that 10% to 20% of dyes are released into water bodies as wastewater. This wastewater not only exhibits intense coloration but also reduces water clarity and light penetration, inhibiting the photosynthesis of aquatic plants and disrupting ecological balance. Additionally, dye wastewater frequently contains heavy metal ions and auxiliary chemicals, further compounding its toxicity. Notably, azo dyes can degrade under anaerobic conditions into aromatic amines, compounds that are often carcinogenic, mutagenic, and potential endocrine disruptors. The unique characteristics of dye pollution, such as its high intensity and complex toxicological effects, pose significant environmental challenges. For example, certain dyes in industrial wastewater exhibit exceptional chemical stability, persisting in the environment and resisting natural degradation, thereby causing long-term cumulative harm to ecosystems.

The behavior of organic pollutants in aquatic environments is influenced by their chemical structure, solubility, volatility, and environmental conditions. For instance, volatile organic compounds (VOCs) can evaporate and diffuse into the atmosphere, while high-molecular-weight organic pollutants tend to accumulate in sediments. The environmental persistence of these pollutants is closely linked to the stability of their molecular structure, with certain aromatic compounds persisting in the environment due to their high chemical stability. The migration and transformation of organic pollutants in water are further affected by factors such as pH, redox potential, light exposure, and aquatic biological activity. For example, photochemical and biodegradation processes may produce more complex or toxic intermediates, which further impact water quality and ecological safety.

Organic pollutants in water, particularly antibiotics and dyes, have profound effects on ecosystems and human health due to their complex chemical structures and environmental behaviors. The spread of antibiotic resistance and the high toxicity of dyes pose significant global challenges for water management. Therefore, developing

effective pollution control strategies and ensuring water quality are of critical importance for environmental sustainability and public health.

1.2.2 Treatment Technologies for Typical Organic Pollutants in Water

Given the widespread distribution of organic pollutants in aquatic environments and their ecological toxicity, the development of efficient wastewater treatment technologies for organic pollutants is essential. Currently, there are various treatment technologies for typical organic pollutants in water, which can be broadly categorized into physical, biological, and chemical methods. In recent years, several advanced oxidation technologies have also been developed. These methods have been optimized for different types of organic pollutants (such as antibiotics, dyes, pesticides, etc.) and water conditions (such as pH, temperature, and organic load) to enhance treatment efficiency and environmental sustainability

1.2.2.1 Physical Methods

(1) Adsorption Technology: Adsorption is a classical method for removing organic pollutants, where porous materials (such as activated carbon, modified biochar, and metal-organic frameworks, MOFs) are used to adsorb organic molecules. Activated carbon, known for its large surface area and strong adsorption capacity, is one of the most widely used adsorbents. Tang et al. [6] reported a novel high-performance magnetic nitrogen-doped nanoporous carbon (MNPC) material. The optimized MNPC-700-0.4 exhibited an adsorption capacity of 1563.7 $mg \cdot g^{-1}$ for target pollutants and was effective across a wide pH range. The MNPC-700-0.4 high surface area, large pore volume, and structural features provide abundant adsorption sites, enhancing its ability to adsorb target pollutants. However, one limitation of adsorption is the issue of saturation, requiring periodic replacement or regeneration of the adsorbent.

(2) Membrane Separation Technology: Membrane technology operates on the principle of selective permeability, using nanofiltration (NF) and reverse osmosis (RO) membranes to retain organic pollutants. S. Banerjee et al. [7] investigated the removal

efficiency of hydrophobically modified ceramic ultrafiltration membranes for target pollutants at different feed concentrations (0.1–1 $mg \cdot L^{-1}$). The study revealed that hydrophobic interactions played a key role in the removal process. Dogan et al. [8] evaluated six commercially available elastic nanofiltration membranes for the removal of target pollutants from aqueous solutions, finding that elastic nanofiltration membranes had relatively low removal efficiency. In contrast, the dense NF90 membrane achieved a 98.9% total organic carbon (TOC) removal rate under appropriate operating conditions. Although membrane technology is highly effective for removing organic pollutants at low concentrations, its widespread application is limited by issues such as membrane fouling, high energy consumption, and high costs.

(3) Extraction Method: The extraction method relies on the differences in solubility between the target pollutants and the extracting solvent, enabling the transfer of the target pollutants into the solvent for enrichment and recovery. However, this method carries the risk of secondary pollution, is costly, and requires specific properties from the extracting solvent, which limits its practicality.

(4) Plasma Technology: This method utilizes high-energy electrons and reactive species in low-temperature plasma to oxidatively degrade organic pollutants. While it offers fast processing speeds, it is still in the experimental stage, though it holds great potential for future applications.

1.2.2.2 Biological Methods

(1) Activated Sludge Method: This method utilizes the metabolic activity of microorganisms to degrade organic pollutants and is one of the core processes in wastewater treatment. While effective for many organic pollutants, the biological treatment efficiency for more persistent pollutants, such as antibiotics and dyes, is relatively low. Typically, pre-treatment or process enhancement is required to improve the degradation efficiency of these refractory compounds.

(2) Anaerobic Digestion: This process uses anaerobic bacteria to break down organic pollutants into harmless gases such as methane and carbon dioxide, making it

suitable for treating high-concentration wastewater. However, anaerobic digestion requires strict control of water temperature and pH conditions for optimal performance.

(3) Constructed Wetlands: Constructed wetlands degrade organic pollutants through the synergistic action of plants, microorganisms, and substrates. This method is cost-effective and environmentally friendly, but its treatment capacity is limited, making it suitable for small-scale wastewater treatment systems.

1.2.2.3 Chemical Methods

(1) Chemical Oxidation: Chemical oxidation methods use traditional oxidants, such as ozone or hydrogen peroxide, to decompose organic pollutants. Ozone oxidation is particularly effective for degrading dyes and pesticides. However, the process must be conducted under highly alkaline conditions with low soluble organic carbon content, as these factors can impair the oxidation capacity of the reaction system. Additionally, the by-products of the reaction may be toxic, requiring careful evaluation.

(2) Electrochemical Methods: Electrochemical methods, which include both electrooxidation and electroreduction, involve the degradation of target pollutants through various chemical reactions induced by an electric field. These methods offer several advantages, such as versatility, high efficiency, and low cost, making them promising for the treatment of emerging pollutants. However, in practical applications, the effectiveness of the process is highly influenced by the electrodes used, and the operational costs are relatively high. Additionally, these methods require skilled operators, limiting their widespread adoption in wastewater treatment plants.

(3) Advanced Oxidation Processes (AOPs): AOPs focus on generating highly reactive oxidants, such as hydroxyl radicals, sulfate radicals, and non-radical species like singlet oxygen and high-valent metals, to degrade organic pollutants. These processes are known for their broad-spectrum and high efficiency, effectively degrading most organic pollutants in water while avoiding secondary pollution. Due to their excellent performance in treating organic contaminants in water, AOPs have garnered widespread attention from both the academic and industrial sectors.[9]

1.3 Application of Advanced Oxidation Processes in Water Treatment

1.3.1 Overview of Advanced Oxidation Processes

Advanced Oxidation Processes (AOPs), also referred to as deep oxidation technology, originated in the 1950s as a method for degrading emerging pollutants. The core principle of AOPs is the activation of free radicals or non-radicals through mechanisms such as high temperature, high pressure, light, or catalytic transition metals. These reactive species—such as hydroxyl radicals (·OH), sulfate radicals ($SO_4^{\cdot-}$), singlet oxygen ($^1O_2$), and high-valent metal oxides (HVMO)—oxidize large organic pollutants, breaking them down into smaller, less toxic or non-toxic molecules. Unlike traditional methods, such as physical or biological treatments, AOPs offer the distinct advantage of fully mineralizing pollutants into harmless substances like CO_2, H_2O, and other inorganic compounds.[10-12] This technology is known for its rapid reaction times and the absence of secondary pollution, making it a powerful tool for ensuring safe drinking water and protecting aquatic ecosystems.

Depending on the oxidizing agents and catalytic conditions used, common Advanced Oxidation Processes (AOPs) include ozonation, Fenton oxidation, Fenton-like oxidation, photochemical oxidation, and electrochemical oxidation. These processes involve the in-situ activation of ozone (O_3) or unstable oxidants such as hydrogen peroxide (H_2O_2), generating highly reactive oxidizing species like hydroxyl radicals (•OH) to degrade various organic pollutants in wastewater.[13] However, these methods have limitations, including high energy consumption and stringent pH requirements. Moreover, the oxidants (O_3 or H_2O_2) are expensive, unstable, and pose challenges in transportation and storage. In the late 1990s, to overcome the technical limitations of H_2O_2 in soil and groundwater remediation, persulfate (PS) oxidants began to receive widespread attention and application.[14] Over the past few decades, advanced oxidation technologies based on PS (PS-AOPs) have increasingly attracted the interest of researchers.

1.3.2 Research Progress on Persulfate Activation Technology

1.3.2.1 Overview of Persulfate Activation Technology

Persulfate (PS) includes two forms: peroxydisulfate (PDS, $S_2O_8^{2-}$) and persulfate (PMS, HSO_5^-), each with distinct molecular structures and properties. Both PDS and PMS have relatively low redox potentials, 2.01 V and 1.82 V, respectively, and thus show limited degradation efficiency for pollutants in their inactivated forms. However, both can be activated to generate reactive species such as sulfate radicals ($SO_4^{\bullet-}$), hydroxyl radicals (•OH), singlet oxygen ($^1O_2$), high-valent metals, and surface-complexed PS, which facilitate pollutant degradation via both free radical and non-radical pathways. PDS is a colorless or white crystalline solid with high stability and excellent water solubility, with a solubility of 730 g/L in water. Its structure is symmetrical, with an O-O bond length of 1.497 Å and a bond energy of 140 kJ/mol. Common forms of PDS include potassium peroxydisulfate, sodium peroxydisulfate, and ammonium peroxydisulfate. In contrast, PMS is a white powder that is highly soluble in water, with a solubility greater than 250 g/L. The molecular size of PMS is smaller, and its structure is asymmetrical, leading to smaller steric hindrance. The O-O bond length is 1.453 Å, with an estimated bond energy range of 140–213.3 kJ/mol, making it more easily activated. In experiments, PMS is often used as a mixed oxidant containing persulfate.

Compared to other advanced oxidation technologies that activate different oxidants, PS-AOPs have distinct technical advantages: (1) They offer a wide range of highly efficient activation methods; (2) They can generate various types of free radicals and non-radicals, which have longer half-lives and thus allow for longer contact times with organic pollutants; (3) The activation process is simple, easy to operate, and more tolerant to variations in pH and background solution components, making it more versatile; (4) Since persulfate is a solid, it has lower transportation and storage costs.[15] As a strong oxidant, persulfate plays a key role in the treatment of various environmental pollutants. To efficiently activate persulfate and enhance its degradation

performance, researchers have employed different activation methods to generate a range of highly reactive oxidative species.

1.3.2.2 Key Reactive Species in the Persulfate Advanced Oxidation System

As research on persulfate catalytic oxidation systems advances, an increasing number of catalysts are being developed. Given that persulfate is inherently more complex than oxidants such as hydrogen peroxide and ozone, the complexity of persulfate catalytic oxidation systems has grown significantly. Initially focused on the strong oxidative capacity of $SO_4^{\bullet-}$, this system has since evolved to include a wider range of reactive species, such as free radicals (•OH, $O_2^{\bullet-}$), as well as non-radical oxidation pathways involving $^1O_2$ and high-valent metals.

(1) sulfate radical

As a strong oxidant, the sulfate radical ($SO_4^{\bullet-}$) has a redox potential ranging from 2.5 to 3.1 V and a relatively long lifetime (30–40 μs). This allows it to effectively facilitate mass transfer and contact with target pollutants in heterogeneous catalytic systems, where it can react with organic compounds containing unsaturated bonds and aromatic π electrons through electron transfer.[16] During the oxidation process, sulfate radicals ($SO_4^{\bullet-}$) can directly attack specific functional groups on organic molecules, breaking down large organic compounds into smaller molecules or even mineralizing them into water and carbon dioxide. Due to its electrophilic nature, $SO_4^{\bullet-}$ preferentially reacts with organic compounds that contain electron-donating groups such as hydroxyl (−OH), amino ($-NH_2$), and alkoxy (−OR) groups. In contrast, its oxidation efficiency is lower for organic compounds with electron-withdrawing groups, such as nitro ($-NO_2$) or carbonyl (C=O) groups.[16] Therefore, $SO_4^{\bullet-}$ shows a certain degree of selectivity in the degradation of organic pollutants.

(2) Hydroxyl Radicals and Superoxide Radicals

When PMS molecules are activated, hydroxyl radicals (•OH) are generated in addition to sulfate radicals ($SO_4^{\bullet-}$). Furthermore, the free $SO_4^{\bullet-}$ produced during the activation of either PMS or PDS can further react with water molecules or OH^- ions in

the solution to produce •OH, as demonstrated in equations 1-1 and 1-2.

$$SO_4^{\cdot-} + H_2O \rightarrow SO_4^{2-} + {\cdot}OH + H^+ \quad 1\text{-}1$$

$$SO_4^{\cdot-} + OH^- \rightarrow SO_4^{2-} + {\cdot}OH \quad 1\text{-}2$$

The oxidation-reduction potential of hydroxyl radicals (•OH) is approximately 2.8 V, enabling them to degrade most organic compounds, potentially breaking them down into carbon dioxide and water. Additionally, •OH has an electron affinity of 569.3 kJ, giving it a strong electrophilic ability that allows it to effectively attack sites with high electron density.[17] The reaction mechanism of •OH with organic compounds is similar to that of sulfate radicals ($SO_4^{\cdot-}$), but differences arise when comparing their interactions with aliphatic carboxylic acids. The first step in •OH-induced oxidation typically involves the extraction of hydrogen from the carbon atom in the fatty chain connected to the carboxyl group, forming a carbon-centered radical. This radical further reacts through oxygen addition and generates various products according to Russel or Bennett-type reactions.[18] In contrast, $SO_4^{\cdot-}$ tends to preferentially extract electrons from the oxygen in the carboxyl group, making $SO_4^{\cdot-}$ more selective than •OH.[19, 20] Overall, the oxidative ability of both •OH and superoxide ($O_2^{\cdot-}$) is weaker than that of $SO_4^{\cdot-}$.[21]

(3) Singlet oxygen

Singlet oxygen ($^1O_2$) is the excited state of molecular oxygen, exhibiting a stronger oxidative capacity than ground-state oxygen, and plays a crucial role in natural environments.[22] In recent years, $^1O_2$ has gained significant attention from researchers due to its frequent identification in persulfate catalytic oxidation systems, making it a prominent non-radical oxidation pathway. On one hand, PMS molecules can generate $^1O_2$ through self-decomposition, although this process is relatively slow (Equation 1-27). Therefore, catalytic methods are typically employed to enhance the production of $^1O_2$, enabling the efficient removal of organic pollutants.

$$HSO_5^- + SO_5^{2-} \rightarrow HSO_4^- + SO_4^{2-} + {}^1O_2 \quad 1\text{-}3$$

$^1O_2$ exhibits stronger selectivity compared to radical-based systems, reacting

almost exclusively with unsaturated organic compounds through electrophilic addition and electron extraction. The 1,2-cycloaddition occurs with electron-rich or sterically hindered alkenes, producing dioxetanes, while 1,3-addition involves allylic hydrogens, resulting in allyl hydroperoxides. These unstable intermediates readily undergo bond cleavage or rearrangement to form alcohols or carbonyl-containing fragments. Additionally, 1,4-addition and subsequent endoperoxide formation are often observed with conjugated dienes. Phenolic compounds containing electron-donating substituents (e.g., alkyl or hydroxyl groups) can transfer electrons to $^1O_2$, forming superoxide ($O_2^{\bullet-}$), radical cations (with an intact aromatic ring), or phenoxy radicals. These radicals may be further oxidized or rearranged by ground-state oxygen into dioxetanes, yielding quinone-like open-ring products.[23, 24] In fine chemical synthesis, the high selectivity of $^1O_2$ is leveraged for controlled oxygen incorporation into organic substrates.[25] While many studies on persulfate catalytic oxidation highlight $^1O_2$ as a key reactive species for efficient organic pollutant degradation, its actual effectiveness remains debated.[26] For instance, phenolic compounds have shown efficient removal under neutral or acidic conditions but reduced removal efficiency under alkaline conditions.[27, 28] Such findings contradict the pH dependency typically associated with $^1O_2$ reactivity with target compounds.[29]

(4) High-Valent Metal Oxides

During the activation of PMS, high-valent metals such as Fe^{4+}, Co^{4+}, and Cu^{3+} are commonly generated through redox reactions with metal ions like Fe^{2+}, Co^{2+}, and Cu^{2+}. These high-valent metals act as potent oxidants, directly participating in the degradation of organic pollutants. The primary mechanism involves electron transfer, which breaks the chemical bonds in organic molecules, enabling rapid pollutant degradation. The specific mechanisms are described below:

Activation of PMS by Ferrous (Fe^{2+}):

$$Fe^{2+}+HSO_5^- \rightarrow Fe^{4+}+SO_4^{2-}+OH^- \qquad 1\text{-}4$$

In this process, Fe^{2+} is oxidized by PMS to form high-valent Fe^{4+}, which exhibits exceptionally strong oxidative potential.

Activation of PMS by Cobalt (Co^{2+}):

$$Co^{2+}+HSO_5^- \rightarrow Co^{3+}+SO_4^{\cdot-}+OH^- \quad 1\text{-}5$$

$$Co^{3+}+HSO_5^- \rightarrow Co^{4+}+SO_4^{2-}+OH^- \quad 1\text{-}6$$

Co^{4+} as a highly reactive species, can directly interact with organic compounds to facilitate their degradation.

Activation of PMS by Copper (Cu^{2+}):

$$Cu^{2+}+HSO_5^- \rightarrow Cu^{3+}+SO_4^{2-}+OH^- \quad \text{v} \quad 1\text{-}7$$

Cu^{3+} as a highly reactive species, can directly interact with organic compounds to facilitate their degradation.

High-valent metals react with organic pollutant molecules through electron transfer, disrupting their molecular structure. This direct oxidation process typically involves the following steps:

Electron Transfer

High-valent metals utilize their strong oxidative potential to extract electrons from organic molecules, resulting in the formation of oxidation products. For example:

$$R\text{—}H + Fe^{4+} \rightarrow R^{\cdot} + Fe^{3} + H^+ \quad 1\text{-}8$$

Where R—H represents the organic compound and $R^{\cdot}$ denotes the intermediate radical.

Bond Cleavage Reaction

Under the influence of high-valent metals, chemical bonds in organic molecules (e.g., C-H, C=C, C-Cl bonds) are cleaved, leading to the formation of smaller molecules or intermediate products. For example:

$$C\text{-}Cl + Co^{4+} \rightarrow C^{\cdot} + Cl^- + Co^{3+} \quad 1\text{-}9$$

Further Mineralization

The intermediate products (e.g., radicals or small molecules) may undergo further oxidation by high-valent metals, resulting in the formation of inorganic molecules such as CO_2 and H_2O. For example:

$$R^{\cdot} + Fe^{4+} \rightarrow CO_2 + H_2O + Fe^{3+} \quad 1\text{-}10$$

Compared to traditional radical-based systems, high-valent metals offer significant advantages. Their strong oxidative potential enables the direct degradation of organic pollutants, efficiently disrupting molecular structures via electron transfer, with reaction rates faster than those of diffusing radicals. Additionally, the direct oxidation pathway of high-valent metals exhibits greater selectivity, preferentially targeting specific pollutants while minimizing ineffective consumption of background organic matter, thereby reducing the risk of byproduct formation. High-valent metals also demonstrate superior stability and resistance to interference under complex water conditions, with minimal impact from anions such as Cl^- and HCO_3^-, showcasing excellent environmental compatibility. The flexible oxidation mechanism, combining synergistic radical and non-radical pathways, enables high-valent metals to achieve greater efficiency and broader applicability in treating various recalcitrant organic pollutants.

The generation of these reactive species provides powerful oxidative capabilities for the catalytic reactions of persulfate. Next, we will explore two common activation methods for persulfate—homogeneous activation and heterogeneous activation—and compare their different performances in pollutant degradation.

1.3.2.2 Homogeneous Activation of Persulfate

Persulfate (PS) is structurally stable and does not readily decompose under ambient conditions. As a result, homogeneous activation methods are typically employed to catalyze PS, generating oxidative radicals that degrade organic pollutants. Current research highlights several major homogeneous activation approaches, including thermal activation, photochemical activation, and activation by transition metal ions.[30-32]

Thermal activation

At the current stage of technological research, thermal activation of PS is relatively well-developed. In this process, PS molecules absorb thermal energy from the environment, initiating activation to generate SO_4^- radicals (as shown in Equations 1-

16 and 1-17), which degrade organic pollutants. This method has stringent requirements for reaction conditions, as it necessitates a relatively high temperature source. Therefore, it is most effective for treating industrial wastewater with elevated temperatures. However, its performance is less efficient for other types of wastewater due to the additional energy consumption from external heat sources, which increases the overall cost of degradation.

Photolytic activation

Similar to the photo-Fenton system, photolytic activation of PS utilizes the energy from ultraviolet (UV) light to break molecular bonds in PS, generating $SO_4^{\bullet-}$ radicals. Introducing UV light into the PS activation process avoids the use of additional chemical reagents, thereby reducing the risk of secondary pollution. However, since UV light accounts for only about 5% of natural sunlight, the activation efficiency of PS is limited, and the degradation performance for organic pollutants cannot be fully ensured.

Transition metal activation

Studies have shown that transition metal ions (e.g., Co^{2+}, Ag^{+}, Fe^{2+}, Cu^{2+}, Mn^{2+}, Ce^{2+}) can decompose PS molecules by strongly attracting their electrons, generating SO_4^{-} radicals. These radicals effectively degrade organic pollutants in aquatic environments. Compared to thermal and photolytic activation, transition metal ion activation operates under milder conditions and offers relatively stable performance, providing certain advantages. However, many transition metal ions are toxic and hazardous, and the metal hydroxides formed during the reaction can have adverse effects on water quality.

In traditional homogeneous PS activation processes, thermal and photolytic activation require external heat sources, making the equipment complex and the activation effects unstable, leading to significant fluctuations in water treatment efficiency. Transition metal ion activation, on the other hand, often causes secondary pollution and involves highly intense reactions that are difficult to control. To address these challenges, researchers have increasingly focused on heterogeneous systems,

exploring the assembly of various catalysts to activate PS and generate either radical or non-radical species.

1.3.2.2 Heterogeneous Activation of Persulfate

The limitations of homogeneous PS activation systems hinder their large-scale application, whereas heterogeneous catalytic systems effectively overcome these drawbacks.[33] First, as solid materials, catalysts in heterogeneous systems are easy to recover, separate, and reuse after use. Second, heterogeneous systems have a broader pH tolerance, making them suitable for diverse water treatment scenarios. Additionally, heterogeneous metal-based catalysts minimize the risk of secondary pollution caused by the addition of metal ions. Owing to these advantages, advanced oxidation technologies based on heterogeneous PS activation systems have garnered significant attention. Developing suitable heterogeneous catalysts is now a key focus in PS activation research. The main types of heterogeneous catalysts used for PS activation include metal-organic polymer (M-POPs) materials and their derivatives, carbon materials (e.g., activated carbon (AC), graphene, carbon nanotubes (CNTs)), metal oxides, and various composite materials (e.g., metal/metal oxide-supported carbon materials).

In recent years, extensive research has been conducted on the radical pathways of PMS activation, while studies on non-radical mechanisms remain limited. Further exploration of the mechanisms underlying non-radical pathways for degrading organic pollutants through PMS activation is of significant theoretical value for future practical applications. Despite the promising application prospects of PMS activation, challenges persist in real-world and industrial applications. These include the need to enhance catalyst performance (e.g., catalytic activity, cycling stability, and reusability), improve selective oxidation of organic pollutants, and increase resistance to interference from background water quality.

1.4 Advances in the Application of Metal-Organic Polymer Materials for Organic

Wastewater Treatment

1.4.1 Overview of Metal-Organic Polymer Materials

Porous organic polymers (POPs) are a class of highly cross-linked network materials formed by covalently bonding organic monomers.[34, 35] Their tunable porous structures, low density, high specific surface area, and chemical stability have made them widely studied in fields such as gas storage, separation, catalysis, and environmental remediation. POPs can be synthesized using various chemical reactions, including cross-linking polymerization, condensation reactions, and click chemistry, enabling precise design of their composition and pore size to meet specific requirements. Due to their purely organic framework, POPs exhibit excellent chemical and thermal stability, maintaining structural integrity under extreme conditions.[36, 37] Functional modifications or the incorporation of active sites into their framework further enhance their performance in catalytic reactions (e.g., persulfate activation), adsorption-separation processes, and molecular sieving.[38, 39] Additionally, composites of POPs with other materials, such as metal nanoparticles or metal-organic frameworks, extend their functionality and application scope. Current research focuses on green synthesis methods, functional regulation, and practical applications in complex systems, showcasing their potential in energy, environmental, and material sciences.[40, 41] Notably, POPs play a prominent role as catalysts or activators in advanced oxidation technologies.

1.4.2 Applications of Metal-Organic Polymers in Advanced Oxidation Processes

POPs can efficiently activate persulfates PMS through surface active sites or supported metal active centers, generating highly oxidative radicals or non-radicals for degrading organic pollutants. For instance, functional groups like pyridine nitrogen and indole nitrogen in nitrogen-doped POPs can synergistically interact with PMS, significantly enhancing activation efficiency. Additionally, the combination of POPs with metals such as Fe, Co, or Mn forms metal-organic composites that further boost

catalytic activity. POPs also serve as highly efficient carriers for metal nanoparticles or single-atom catalysts. Their highly cross-linked porous structure not only provides abundant dispersion sites but also prevents metal agglomeration, improving catalytic stability. For example, single-atom iron or cobalt catalysts supported on POPs exhibit outstanding performance in PMS activation or photocatalytic processes. Porous organic polymers offer several advantages in advanced oxidation applications:

(1) Customizable Structure: The pore size, functional groups, and active sites of POPs can be precisely tailored through chemical synthesis to meet specific reaction requirements.

(2) High Chemical Stability: POPs maintain structural integrity even under extreme acidic, alkaline, and high-temperature conditions.

(3) Environmental Friendliness: POPs are synthesized from low-toxicity and renewable organic monomers, aligning with the principles of sustainable development.

(4) Multifunctionality: POPs integrate adsorption, catalysis, and separation functions, enabling efficient removal of complex pollutants from water systems.

Porous organic polymers (POPs) show great potential in advanced oxidation processes. Through rational design and functionalization, POPs can serve as highly efficient heterogeneous catalysts, activating peroxides to generate reactive oxygen species for the effective degradation of organic pollutants in water. Among these, metal-based porphyrin organic polymers, with their unique molecular structures and catalytic properties, have become a research focus, offering innovative solutions for water pollution treatment.

1.4.3 Research on Metalloporphyrin-Based Organic Polymers in Advanced Oxidation Technologies

Metalloporphyrin-based organic polymers (M-POPs) are porous materials assembled from metalloporphyrin units through covalent or coordination bonds. Their unique molecular structures, abundant active sites, and excellent chemical stability make them highly valuable in advanced oxidation processes (AOPs). M-POPs combine

the molecular catalytic properties of metalloporphyrins with the structural advantages of porous polymers, making them ideal catalysts for efficient oxidative degradation. However, to the best of our knowledge, no studies have been reported on the activation of PMS by metalloporphyrin-based porous organic polymers, and the activation mechanisms remain unclear. This research aims to develop an environmentally friendly, highly efficient, and stable activator for PS-based AOPs by studying metalloporphyrin-based porous polymers, thereby enabling effective removal of organic pollutants from water. The study provides an in-depth analysis of the mechanisms by which different metalloporphyrins (Co, Fe, Cu) activate PS, offering theoretical guidance for the future design and development of superior PS catalysts.

1.5 Research Objectives, Scope, and Technical Roadmap

1.5.1 Research Objectives

The rapid growth of the global economy has led to significant environmental pollution, with water pollution becoming increasingly prominent. Organic pollutants in wastewater, characterized by their stable structures, resistance to degradation, high toxicity, and costly treatment, have drawn considerable attention. Consequently, there is an urgent need for a cost-effective, efficient, and secondary pollution-free method for removing organic pollutants from water. Advanced oxidation processes (AOPs) are widely applied for water pollutant treatment, with persulfates emerging as a research focus due to their broad pH applicability and strong oxidation potential of generated reactive species. Compared to PDS, the asymmetric molecular structure of PMS makes it more readily activated to produce oxidative reactive species. A wide range of heterogeneous materials has been developed to activate PMS, yet the efficiency and mechanisms of similar catalysts remain debated. Porous organic polymers, with their highly customizable structure, excellent chemical and thermal stability, and adaptability to extreme water conditions, hold great potential for diverse applications. However, studies on their use for PMS activation in organic pollutant degradation are relatively

limited, with only a few reports available. Metalloporphyrin-based porous organic polymers combine the molecular catalytic properties of metalloporphyrins with the structural advantages of porous polymers, making them ideal catalysts for efficient oxidative degradation. Moreover, reactive species vary in their effectiveness against different organic pollutants, making the selective generation of highly oxidative species a key strategy in AOP research. Based on this, this study focuses on metalloporphyrin-based porous organic polymers, aiming to develop catalysts that efficiently activate persulfates while selectively generating non-radicals (e.g., high-valent metals). The activation mechanisms are explored to create a green, environmentally friendly persulfate-based AOP system for organic pollutant degradation.

1.5.2 Research Scope

This study is structured into four main chapters, each addressing key aspects of the development and application of metal-porphyrin-based porous organic polymers (M-P/POP) as catalysts for peroxymonosulfate (PMS) activation in wastewater treatment.

1. Synthesis and Characterization of M-P/POP Catalysts

This chapter focuses on the design and synthesis of cobalt (Co), iron (Fe), and copper (Cu) porphyrin-based porous organic polymers. The well-defined M-N_4 coordination structures were confirmed using various characterization techniques, including Fourier-transform infrared (FTIR) spectroscopy, X-ray diffraction (XRD), scanning electron microscopy (SEM), and X-ray photoelectron spectroscopy (XPS). These structural analyses provide insight into the electronic properties and surface morphology of the catalysts, which are crucial for their catalytic performance.

2. Catalytic Performance in PMS Activation

The second chapter evaluates the catalytic efficiency of M-P/POP in PMS activation for the degradation of different organic pollutants, including ranitidine (RAN), tetracycline (TC), and sulfamethoxazole (SMX). Degradation kinetics, pollutant removal efficiency, and the impact of operational parameters (such as pH,

PMS dosage, and pollutant concentration) were systematically investigated. Comparative studies among Fe-P/POP, Co-P/POP, and Cu-P/POP highlight the differences in catalytic activity and pollutant selectivity.

3. Mechanistic Insights into PMS Activation

This chapter delves into the fundamental reaction mechanisms underlying PMS activation. Radical quenching experiments, electron paramagnetic resonance (EPR) spectroscopy, and isotope labeling techniques were employed to confirm that high-valent metal-oxo species (HVMOs: Fe(IV)=O, Co(IV)=O, and Cu(III)=O) are the dominant reactive species, following a non-radical oxidation pathway. Density functional theory (DFT) calculations further elucidate the correlation between pollutant ionization potential (IP) and degradation kinetics, reinforcing the electron transfer-driven oxidation mechanism.

4. Stability, Recyclability, and Environmental Applications

The final chapter assesses the long-term stability, recyclability, and environmental feasibility of M-P/POP catalysts. Metal leaching tests, reusability experiments, and performance evaluations in different water matrices (e.g., tap water, river water) demonstrate the catalysts' robustness and resistance to background interferences. Additionally, an economic and sustainability analysis highlights the potential of M-P/POP as a cost-effective and scalable solution for practical wastewater treatment.

This research provides a comprehensive understanding of PMS activation mechanisms and presents a promising strategy for designing advanced catalysts for the efficient and selective degradation of organic pollutants in aqueous environments.

1.5.3 Technical Roadmap

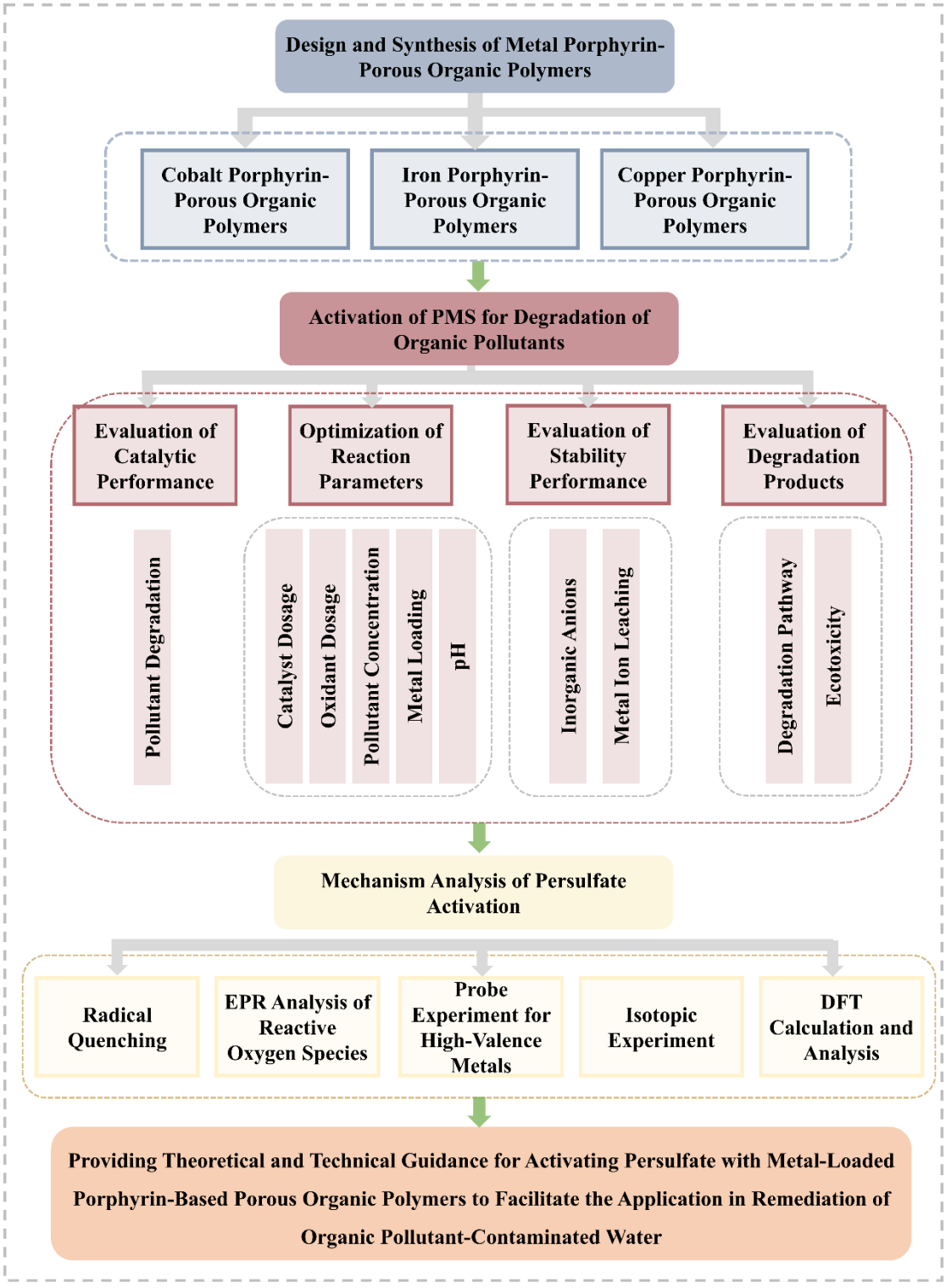

Fig. 1-2 Technical roadmap of this study.

2. Experimental Materials and Methods

2.1 Materials and Equipment

2.1.1 Reagents

All chemicals and reagents were at least analytical grade and used as received without any treatment. meso-Tetraphenylporphyrin (TPP) and Ranitidine hydrochloride (RAN) were sourced from Aladdin Biochemical Technology Co., Ltd. (Shanghai, China). Aluminum chloride ($AlCl_3$), Cobalt(II) acetate tetrahydrate ($Co(AC)_2 \cdot 4H_2O$), Iron(II) Acetate tetrahydrate ($Fe(AC)_2 \cdot 4H_2O$), Copper acetate monohydrate ($Cu(AC)_2 \cdot H_2O$), Acetonitrile (ACN), Methanol (MeOH), P-benzoquinone (PBQ), L-histidine (L-his), Dimethyl sulfoxide (DMSO), Deuterium oxide (D_2O), Methyl phenyl sulfoxide (PMSO), methyl phenyl sulfone ($PMSO_2$), Heavy-oxygen water (H_2O^{18}), 2,2'-azinodi(3-ethylbenzothiazoline-6-sulfonic) (ABTS), Cobalt(II)oxide (CoO) and Tricobalt tetroxide (Co_3O_4) were bought from Shanghai Maclin Biochemical Technology Co., Ltd. (Shanghai, China). Ethyl alcohol (EtOH), Methanol (MeOH), hydrochloric acid (HCl), Sodium hydroxide (NaOH) and hydrogen peroxide (H_2O_2) were purchased from Tianjin Komio Chemical Reagent Co., Ltd. (Tianjin, China). Tert-butanol (TBA) was sourced from Tianjin Tianli Chemical Reagent Co., Ltd. (Tianjin, China). NaCl and NaBr were acquired from Tianjin Dingsheng Xin Chemical Co., Ltd. (Tianjin, China). $NaHCO_3$ was purchased from Tianjin Fengchuan Chemical Reagent Technology Co., Ltd. (Tianjin, China). $Na_2HPO_4 \cdot 12H_2O$ was sourced from Tianjin Yongda Chemical Reagent Co., Ltd. (Tianjin, China).

2.1.2 Instruments and Equipment

The microstructure of catalysts was investigated via transmission electron microscopy (TEM, JEL 2100, Japan) and high-resolution transmission electron microscope (HRTEM, JEL 2100, Japan). The atomic distribution images were obtained in the Aberration-Corrected Transmission Electron Microscope operated at 200 kV

(HAADF-STEM, JEM-2100Plus, Japan). The crystalline structure of the catalysts were explored by an X-ray diffraction instrument (XRD, D8 ADVANCE, Germany) with a radiation from 10° to 40° with a scan speed of 5 °C/min. The Raman spectra of the samples were detected by using a confocal Raman microscope (In Via Reflex, Renishaw, England). The element states of the catalyst surface were analyzed by an X-ray photoelectron spectrometer (XPS, Axis Ultra DLD, Britain). Solid-state 13C NMR spectroscopy was acquired by the Agilent 600 MHz DD2 spectrometer. FT-IR spectroscopy of Por-POPs was determined by the Nicolet™ iS™5 (Thermo Scientific™) instrument. The concentration of persistent organic contaminants was determined with high-performance liquid chromatography (HPLC, Ultimate3000DGLC, America). The intermediates in RAN degradation were analyzed by High-Performance Liquid Chromatography Mass Spectrometer (HPLC-MS, Ultimate3000DGLC/TSQ Endura, America). The S vacancy and reactive species generated by the reaction were determined by using an electron paramagnetic resonance spectrometer (EPR, JES FA200, Japan). The ion leaching concentration of the catalysts were detected by Inductively coupled plasma atomic emission spectroscopy/mass spectrometry (ICP-AES/MS, Agilent 5800 ICP-OES, China). The total organic carbon (TOC) of reaction solutions was determined by a TOC analyzer (TOC, Multi N/C 3100, Germany). Raman spectra of the samples were detected by using a confocal Raman microscope (In Via Reflex, Renishaw, England) at an excitation wavelength of 532 nm.

2.2 Experimental Methods

2.2.1 Preparation of Catalyst Materials

The specific methods and procedures for catalyst preparation are detailed in subsequent chapters.

2.2.2 Characterization of Catalyst Materials

2.2.2.1 High-Resolution Field Emission Scanning Electron Microscopy (SEM)

The surface morphology of the catalyst was observed using high-resolution field emission scanning electron microscopy (SEM). First, the powdered material was applied onto a copper SEM sample holder. To enhance conductivity, the sample surface was gold-coated for 30 minutes before imaging under the SEM.

2.2.2.2 X-ray Photoelectron Spectroscopy (XPS)

The chemical composition of the material's surface was analyzed using X-ray photoelectron spectroscopy (XPS). Testing conditions: The sample was first pressed into a single crystal pellet and stored under a nitrogen atmosphere. The analysis was conducted using a Mono Al Kα source with a binding energy scan range of 0–1100 eV. All elemental peak positions were calibrated using the C1s peak at 284.6 eV as a reference.

2.2.2.3 X-ray Diffraction (XRD)

The crystal structure of the material surface was determined using X-ray diffraction (XRD). The prepared sample was loaded onto a detection substrate and placed in the XRD detector for analysis. The radiation source used was CuKα with a wavelength of 0.15418 nm, and the scanning range was 10–90°. The detector was calibrated using a standard Si crystal. The resulting XRD patterns were compared with literature or standard reference cards to identify the crystal structure of the sample.

2.2.2.4 Fourier Transform Infrared Spectroscopy (FTIR)

The functional groups on the material's surface were determined using Fourier Transform Infrared Spectroscopy (FTIR). First, the sample was pelletized by mixing an appropriate amount of dried sample with potassium bromide (KBr) in a fixed ratio. The mixture was ground into a fine powder using a mortar and then pressed into a transparent pellet. The pellet was placed in the sample chamber of the FTIR instrument for analysis. The scanning range was 400–4000 cm^{-1} with a step size of 1 cm^{-1}, and each sample was scanned 5 times. For in situ FTIR, an attenuated total reflection (ATR)

accessory was used to observe surface changes of the catalyst in liquid conditions with and without PMS. Pure water was first scanned as the background. Then, 50 mg of the sample was dispersed in 10 ml of deionized water or a 20 mM PMS solution. After reacting for 10 minutes, the sediment was dropped onto a zinc selenide (ZnSe) window for scanning. The scanning range was 650–4000 cm^{-1}, with a step size of 4 cm^{-1} and 10 scans performed.

2.2.2.5 Solid-State Nuclear Magnetic Resonance (NMR)

Solid-state nuclear magnetic resonance (NMR) was used to characterize the chemical environment and functional groups of the catalyst materials. The prepared samples were first dried and placed in an NMR sample tube. High-resolution solid-state NMR using ^{13}C or ^{1}H nuclei was performed, with the spinning frequency adjusted to eliminate magnetic anisotropy. The testing conditions included a spinning rate of 5–10 kHz, a pulse duration of 3–5 μs, a repetition interval of 1–3 seconds, and 128 scans. The resulting spectra were analyzed to identify chemical shift peaks, allowing determination of the chemical environment and functional group distribution within the material.

2.2.2.6 Synchrotron Radiation

Synchrotron radiation was employed to characterize the microstructure and chemical composition of the catalyst materials. Samples were prepared as thin films or powders, mounted on a sample holder, and placed in the synchrotron beamline detection channel. An appropriate energy range (e.g., 5–25 keV) was selected for X-ray Absorption Fine Structure (XAFS) analysis, including X-ray Absorption Near Edge Structure (XANES) and Extended X-ray Absorption Fine Structure (EXAFS). XANES spectra were used to determine the oxidation states of metals through absorption edge energy shifts, while EXAFS data fitting provided insights into bond lengths and coordination numbers between metals and their coordinating atoms. This technique offered critical structural information to better understand the catalytic mechanisms.

2.2.3 Performance Analysis of Catalyst Materials

2.2.3.1 Organic Pollutant Degradation Experiments and Analysis Methods

Organic Pollutant Degradation Experiment: All degradation experiments were conducted in 100 mL flasks at a reaction temperature of 25°C. A specific amount of catalyst was first dispersed into an organic pollutant solution of a predetermined concentration and allowed to react for a period to reach adsorption-desorption equilibrium. PMS was then added to initiate the catalytic degradation reaction. Throughout the adsorption and catalytic reaction process, a magnetic stirrer set at 200 rpm ensured thorough mixing of PMS, organic pollutants, and the catalyst. Samples were collected at regular intervals, with 1.0 mL of reaction solution taken each time and immediately mixed with 1.0 mL of ethanol to quench free radicals. The samples were filtered using a 0.22-μm filter membrane, and the concentration of organic pollutants was subsequently analyzed.

Organic Pollutant Detection Method: Organic pollutants were analyzed using high-performance liquid chromatography (HPLC). A C18 column was used, with the flow rate of the mobile phase set to 1 mL/min and the injection volume set to 20 μL.

All experiments, including control tests, were conducted in triplicate to ensure the reliability of the results.

2.2.3.2 Effects of Water Quality Factors

This section investigates the effects of various water quality factors on the pollutant degradation efficiency of the constructed oxidation system. These factors include the initial pollutant concentration, catalyst dosage, persulfate concentration, initial pH of the solution, and the concentration of inorganic anions in the solution. This study provides preliminary guidance for practical applications. The initial pH of the solution was adjusted using dilute sulfuric acid or NaOH solutions. To examine the impact of inorganic anions on the pollutant removal performance, specific amounts of inorganic anion sodium salts were added when preparing the initial pollutant solution.

2.2.3.3 Recycling Experiments

Recycling experiments were conducted on a thermostatic stirrer at 25°C. A specific amount of catalyst was dispersed into an organic pollutant solution of a predetermined concentration, followed by the addition of a fixed concentration of PMS. The reaction was allowed to proceed for a set time, completing the first cycle. After the reaction, the catalyst material was recovered by filtration and reused in subsequent cycles.

2.2.3.4 Determination of Metal Ion Concentration in the Reaction System

The leaching concentrations of transition metals (Co, Fe, Cu) from the catalyst in the oxidation system were determined using an inductively coupled plasma mass spectrometer (ICP-MS, NexION 2000). This analysis was performed to evaluate the stability of the catalyst and its potential for causing secondary environmental pollution.

2.2.4 Analysis of the Mechanism for Catalyst Degradation of Target Organic Pollutants

2.2.4.1 Radical Quenching Experiments

Radical Quenching Experiments: Radical quenching experiments were conducted on a thermostatic stirrer at 25°C. A specific amount of catalyst was dispersed into an organic pollutant solution of a predetermined concentration, followed by the addition of a fixed amount of quenching agent and PMS. Samples were collected at regular intervals, with 1.0 mL of the reaction solution taken each time and immediately mixed with 1.0 mL of ethanol to quench radicals. The samples were then filtered through a 0.22-μm filter membrane, and the concentration of the organic pollutants was analyzed.

In persulfate-based oxidation systems, common radicals include •OH, $SO_4^{\bullet-}$, $^1O_2$, and $O_2^{-\bullet}$. The selection of quenching agents is based on their reaction rate constants with specific radicals. For example, methanol (MeOH) reacts with •OH and $SO_4^{\bullet-}$ at rate constants of $K_{MeOH/OH}$=9.7×108 $M^{-1}s^{-1}$ and $K_{MeOH/SO4^{\bullet-}}$=2.5×10^7 $M^{-1}s^{-1}$, respectively. Since the reaction rate of tert-butanol (TBA) with •OH ($K_{TBA/\cdot OH}$=3.8–7.6×10^9 $M^{-1}s^{-1}$ is 1500 times higher than that with $SO_4^{\bullet-}$ ($K_{TBA/SO_4\bullet-}$=4×10^5 $M^{-1}s^{-1}$), TBA is selected as

the •OH scavenger, while MeOH is used as the $SO_4^{\bullet-}$ scavenger. For $O_2^{\bullet-}$, $K_{p-BQ/O_2^{\bullet-}}$=0.9–1.0×10^9 $M^{-1}s^{-1}$, which is significantly higher than its reaction rates with •OH, $SO_4^{\bullet-}$, and $^1O_2$, making p-BQ the scavenger for $O_2^{\bullet-}$. L-histidine (L-his) serves as the scavenger for $^1O_2$, and dimethyl sulfoxide (DMSO) is used to eliminate high-valent metal oxides.

2.2.4.2 Reactive Oxygen Species (ROS) Trapping Experiments

Identification of ROS: The identification of reactive oxygen species (ROS) in this study was based on quenching experiment results, further confirmed using an electron paramagnetic resonance (EPR) spectrometer (Bruker, Germany). The EPR parameters were set as follows: microwave frequency = 9.50 GHz, microwave power = 3 MW, central magnetic field strength = 3550 G, and scan width = 100 G. Radical trapping agents 5,5-dimethyl-1-pyrroline-N-oxide (DMPO) and 2,2,6,6-tetramethylpiperidine-N-oxide (TEMP) were used to quickly capture ROS in the oxidation system. The signals of the complexes formed between ROS and DMPO or TEMP were analyzed to further confirm the ROS present.

- The presence of $^1O_2$ can be inferred when the TEMP-$^1O_2$ complex shows characteristic peak intensity ratios of 1:1:1.
- The presence of •OH and $SO_4^{\bullet-}$ can be inferred when DMPO-•OH and DMPO- $SO_4^{\bullet-}$ complexes exhibit characteristic peak intensity ratios of 1:2:2:1.
- The presence of $O_2^{\bullet-}$ can be inferred when the DMPO-OOH complex exhibits characteristic peak intensity ratios of 1:2:1:2:1:2:1.

2.2.4.3 Total Organic Carbon (TOC) Analysis

The removal of total organic carbon (TOC) was analyzed using a TOC analyzer (Multi N/C 3100, Analytik Jena, Germany). The mineralization degree of organic matter in the water was used to evaluate the catalytic performance differences among the oxidation systems.

2.2.4.4 Detection of Degradation Reaction Intermediates

The degradation intermediates were detected using a liquid chromatography-mass spectrometry (LC-MS) system. Liquid chromatography was performed using an Agilent 1290 UPLC equipped with a C18 column. The mobile phases A and B were appropriate solutions, with a flow rate of 0.3 mL/min and an injection volume of 20 μL. Mass spectrometry analysis was carried out using an Agilent QTOF 6550, with the primary mass spectrometry scan range set to 50–1000 m/z. Secondary mass spectrometry was used to identify potential intermediate products in the system.

2.2.4.5 DFT Theoretical Calculations

Gaussian 09 and Gauss View software were used to analyze the RAN molecule, calculate the Fukui index, and determine the HOMO distribution using the B3LYP/6-311+G (3d, 2p) method. Materials Studio (MS) was employed to calculate the adsorption energy and Fermi level between the catalyst and PMS, as well as the Gibbs free energy changes during the reaction process.

2.2.4.6 Toxicity Analysis of Intermediate Products

The toxicity of intermediate products was assessed using the toxicity evaluation software TEST and ECOSAR. The steps were as follows: First, the structural information of the intermediate products, including molecular weight, molecular formula, and molecular structure, was inputted. Based on this information, TEST and ECOSAR automatically calculated the toxicity index of the intermediates. Finally, the toxicity index generated by the software was used to evaluate the toxicity level of the intermediate products.

3. The Preparation of Cobalt Porphyrin-Based Porous Organic Polymers and the Activation of Peroxymonosulfate for the Degradation of RAN.

Abstract:

Water pollution caused by persistent organic contaminants poses a significant environmental challenge, necessitating the development of efficient and selective catalytic degradation systems. In this study, we synthesized cobalt-porphyrin porous organic polymers (PPC) as a platform for peroxymonosulfate (PMS) activation, aiming to selectively generate high-valence metal-oxo (HVMO) species for organic pollutant degradation. The well-defined M-N_4 coordination structure in the porous polymer framework facilitates effective PMS activation and electron transfer, thereby promoting the formation of reactive HVMO species. Among the investigated catalysts, PPC exhibited outstanding catalytic activity across a broad pH range, achieving nearly 100% conversion of Co(II) to Co(IV)=O as the dominant oxidative species. The system demonstrated high efficiency in degrading ranitidine (RAN), achieving complete removal within 30 minutes. Mechanistic investigations, including radical quenching experiments, electron paramagnetic resonance (EPR) spectroscopy, and density functional theory (DFT) calculations, confirmed that non-radical oxidation pathways predominated in the system. Additionally, the system demonstrated high reusability, negligible metal leaching, and excellent stability in diverse water matrices, making it an environmentally friendly and cost-effective alternative for wastewater treatment. This study provides fundamental insights into the structure–activity relationship of PPC catalysts and highlights their potential for practical applications in advanced oxidation processes.

Keywords: cobalt-porphyrin porous organic polymers; peroxymonosulfate; high-

valence metal-oxo; ranitidine.

3.1 Introduction

Water resources, indispensable to human survival and a vital environmental medium, are increasingly recognized for their significance. To ensure the provision of safe drinking and industrial water, Advanced Oxidation Processes (AOPs) are increasingly adopted as supplements to traditional biological treatments to eliminate pervasive organic pollutants.[42, 43] Persulfate-based heterogeneous Fenton-like reaction is an appealing for water decontamination because of abundance reactive oxygen species (ROS) formation upon the cleavage of per-oxo bond (O-O) in persulfate molecule.[44] Particularly, peroxymonosulfate (PMS, HSO_5^-) with an asymmetrical molecular structure (H-O-O-SO_3^-) can readily decompose into highly reactive sulfate ($SO_4^{\cdot-}$) and hydroxyl radicals (·OH) upon accepting electron from catalysts.[45] Compared to the conventional sulfate radical-based AOPs, the high-valence metal-oxo (HVMO) species offer the advantages such as high steady-state concentrations (approximately 10^{-8} M>10^{-15}-10^{-12} M for radicals), extended lifetimes (7^{-1}-10^{-1} s>10^{-9}-10^{-6} s for radicals), and reduced susceptibility to quenching by nontarget substrates.[46] Therefore, the high-valence cobalt-oxo (Co(IV)=O) species-dominated AOPs has stimulated a widespread interest because of its high selectivity and excellent anti-interference.[47, 48] Despite these advantages, current research on Co(IV)=O species in heterogeneous AOPs remains largely limited by pH conditions.[49, 50] Consequently, developing an efficient oxidation system dominated by Co(IV)=O were expected but challenging.

In recent years, considerable effort has been devoted to exploring metal coordination environments capable of facilitating high rates of electron transfer, as well as understanding the mechanisms underlying the formation of Co(IV)=O during the activation of persulfates.[51] Research indicates that the chemical reactivity and stability of metal-based catalysts are highly dependent on the local coordination of the

metal sites, which is directly linked to the interplay between electronic and geometric structures.[52-55] Studies have also confirmed that the N coordination could significantly enhance the Fenton performance due to the reduced adsorption energy and facilitates electron transfer in the activation of PMS.[56]

Liu et al. developed a cobalt oxide-loaded CN catalyst, which under the Co-N-C structure, enabled the efficient conversion of Co(II) to Co(IV) for the removal of sulfonamide antibiotics.[57] Wang et al. synthesized a water-soluble sulfonated Co(II) phthalocyanine (CoPcS), with cobalt acting as the metal center coordinated with pyrrolic nitrogen.[58] This complex activates PMS to form Co(IV)=O, which serves as the primary oxidative intermediate in the breakdown of organic substances under acidic conditions. However, the production of Co(IV)=O is strictly limited by pH, typically forming under acidic or neutral conditions. The pH sensitivity of Co(IV)=O restricts its application in organic wastewater treatment. Therefore, developing a catalyst that effectively activates PMS to produce high-valent cobalt across a broad pH range is of significant importance. Wang et al. constructed a CoSA-N_3-C/PMS system that exhibited excellent oxidative performance for norfloxacin across a wide pH range (3-11), with nonradical Co(IV)=O and electron transfer playing a primary role in pollutant degradation.[59] However, as the pH increases, leaching of cobalt ions has been detected during the degradation process. Therefore, further development of stable cobalt-based catalysts that activate PMS to predominantly produce Co(IV)=O as the active species holds significant importance.

Porous organic polymers (POPs), composed of organic monomers connected by covalent bonds, with their exceptional design flexibility and structural control, can offer precise structural information for determining the catalytic active site and studying the catalytic reaction mechanism.[60] And POPs have high chemical stability and extended π-conjugated structures to ensure effective charge delocalization, favoring electron transfer.[61-63] Porphyrin-based POPs are one of the POPs materials.[64] Porphyrins, as conjugated N_4 macrocycles, exhibit redox activity and function as chelating agents, possessing rigid planar structures that offer excellent stability for the formation of a

four-coordinate (M-N_4) structure by metal ions.[65] Therefore, porphyrin-base POPs could act as an intriguing platform to tether active metals cobalt with uniform and independent distribution for PMS activation to produce Co(IV)=O. However, to the best of our knowledge, the relative investigations on PMS activation by Co confined in porphyrin-based POPs have not been reported and the associated activation mechanism is still unclear.

To address the aforementioned critical points, we assess the property relationships of Co-N_4 active sites that regulate PMS oxidation. Dispersed cobalt on porphyrin-based POPs was used as a model to precisely regulate the generation of Co(IV)=O in the PMS activation process. The evidence indicates that Co-N4 is the active site; that is, dispersed cobalt in porphyrin-based POPs, achieved near 100% generation of Co(IV)=O. Benefiting from the admirable electronic structure, Co-N4 configuration is advantageous for the generation of electron transfer process and Co(IV)=O species. Excellent degradation activity of Co(IV)=O for several organic pollutants was achieved in a broad pH range.

3.2 Experiments and Methods

3.2.1 Catalyst Preparation

Synthesis of Porphyrin-Porous Organic Polymer (PP)

Tetraphenylporphyrin (0.96 g, 0.2 mmol) and aluminum chloride (4 g, 3.2 mmol) were added to a two-necked flask at room temperature. Under a nitrogen atmosphere, trichloromethane (8 mL) was introduced into the flask. The mixture was refluxed and stirred at 30°C for 8 h, at 40°C for 12 h, and at 58°C for 28 h. After the reaction, the dark precipitate was washed with hydrochloric acid-water (v/v=2:1, 40 mL), distilled water, and ethanol. The solid was then purified by Soxhlet extraction with methanol for 24 h. Finally, it was dried in a vacuum oven at 60°C for 24 h to yield a black polymer powder designated as PP.

Synthesis of Porphyrin-Porous Organic Polymer-Co (PPC)

Por-POP (1 g) and cobalt (II) acetate tetrahydrate ($C_4H_6CoO_4 \cdot 4H_2O$, 0.1 g) were added to an acetonitrile solution (30 mL). The mixture was stirred at 82°C for 24 h. After the reaction, the solid was obtained by centrifugation and washed three times with methanol, followed by Soxhlet extraction with methanol for 24 h. Finally, the product was dried in a vacuum oven at 60°C for 24 h to yield a black solid powder designated as PPC.

3.2.2 Characterization of PPC

3.2.2.1 High-Resolution Field Emission Scanning Electron Microscopy (SEM)

The SEM analysis method for PPC is detailed in Chapter 2 – 2.2.2.1.

3.2.2.2 X-ray Photoelectron Spectroscopy (XPS)

The XPS analysis method for PPC is detailed in Chapter 2 – 2.2.2.2.

3.2.2.3 X-ray Diffraction (XRD)

The XRD analysis method for PPC is detailed in Chapter 2 – 2.2.2.3.

3.2.2.4 Fourier Transform Infrared Spectroscopy (FT-IR)

The FT-IR analysis method for PPC is detailed in Chapter 2 – 2.2.2.4.

3.2.3 Performance Analysis of PPC

3.2.3.1 RAN Degradation Experiments and Analysis Methods

The methods for RAN degradation experiments and detection are detailed in Chapter 2 – 2.2.3.1.

3.2.3.2 Effects of Water Quality on PPC Performance

The experimental method for studying the effects of water quality on PPC performance is detailed in Chapter 2 – 2.2.3.2.

3.2.3.3 Recycling Experiments

The experimental method for RAN recycling experiments is detailed in Chapter 2 – 2.2.3.3.

3.2.3.4 Determination of Metal Ion Concentrations in the Reaction System

The method for detecting metal ion concentrations in the reaction system is detailed in Chapter 2 – 2.2.3.4.

3.2.4 Mechanistic Analysis of RAN Degradation by PPC

3.2.4.1 Radical Quenching Experiments

The method for radical quenching experiments is detailed in Chapter 2 – 2.2.4.1.

3.2.4.2 Detection of Degradation Reaction Intermediates

The method for detecting intermediate products formed during SMX degradation is detailed in Chapter 2 – 2.2.4.4.

3.3 Results and Discussion

3.3.1 Characterization Analysis of PPC

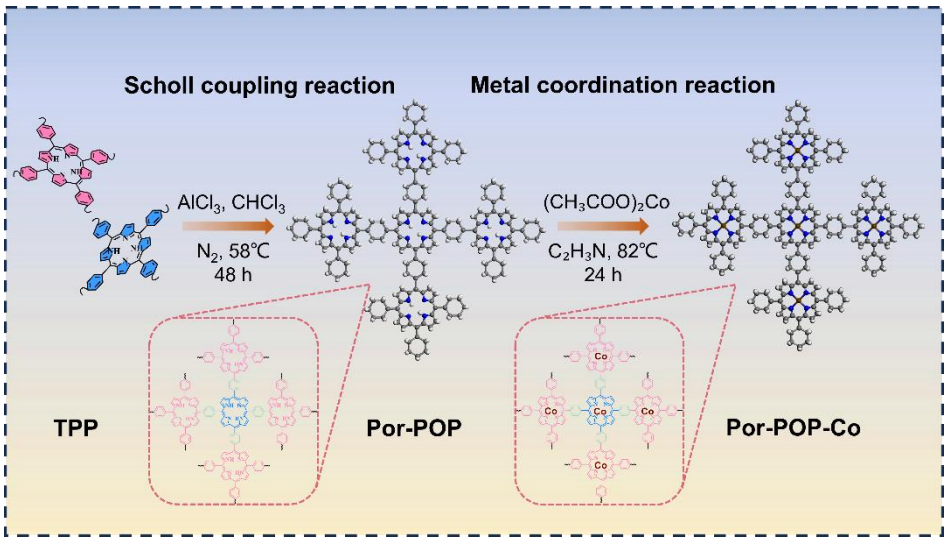

Fig. 3-1. Schematic illustration of the preparation procedures of the $PPC_{0.1}$ samples.

Fig. 3-1 shows the preparation process of Porphyrin-Porous Organic Polymer-Co (PPC). The tetraphenylporphyrin was applied as the building block to construct PP with extensively conjugated microporous networks via Friedel-Crafts alkylation coupling reaction catalyzed by $AlCl_3$ under nitrogen protection. The hydrogen atoms on the aromatic rings of porphyrin were substituted with alkyl groups, the pyrrolic N atoms in porphyrin do not participate in the coupling reaction. Therefore, after the coupling reaction. Pyrrolic N atoms are still theoretically reserved in the frameworks of porphyrin and could be used as coordination sites for metallization. Since Co(II) is an active metal for activating PMS, PP can be metallized with Co(II) in acetonitrile, yielding PPC.

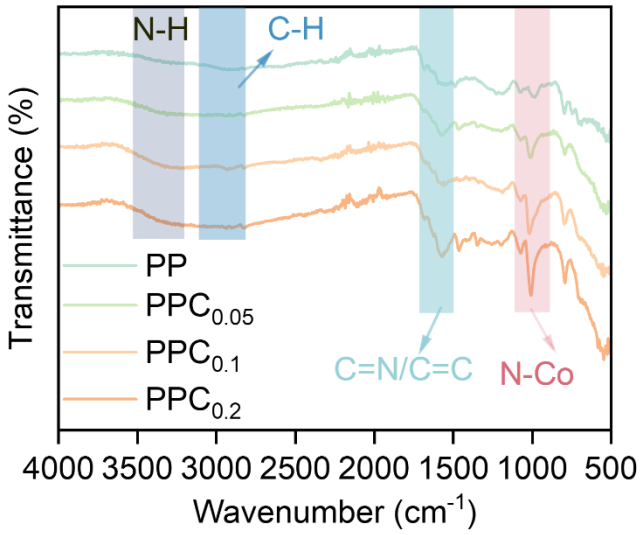

Fig. 3-2. FT-IR spectra of PPC, $PPC_{0.05}$, $PPC_{0.1}$ and $PPC_{0.2}$.

Fig. 3-2 presents the FT-IR spectra of PP and PPC. The obvious adsorption peaks in the region from 1655 to 1570 cm^{-1} for PP and PPC belong to the C=N and C=C stretching vibrations of the porphyrin macrocycle and benzene ring. The C-H stretching vibration peaks of methylene could be easily observed near 2900-3080 cm^{-1}, which indicated the existence of methylene linkers in PP and PPC, confirming the successful coupling of porphyrin units into polymers. The N-H stretching in pyrrole (3308 cm^{-1})

disappears and the characteristic N-Co in-plane bending at 1007 cm^{-1} appears in the FT-IR spectrum of PPC, indicating the coordination of cobalt.[66]

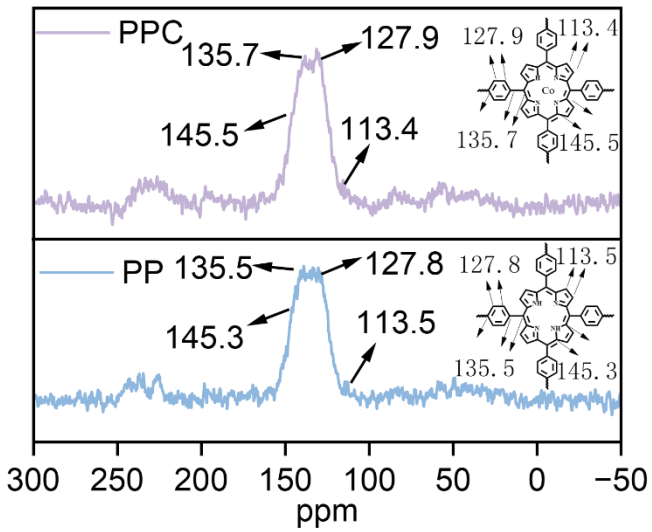

Fig. 3-3. Solid-state ^{13}C NMR spectrum of PP and $PPC_{0.1}$.

The structural details of PP and PPC were determined by solid-state ^{13}C NMR spectroscopy. As show in **Fig. 3-3**, the resonance peaks at approximately 127.8 -137.9 and 135.5–135.7 ppm ascribed to the phenylene linkages and those at approximately 113.5–113.4 and 145.3–145.5 ppm to the porphyrin macrocycles.[67] Hence, the results preliminarily indicate porphyrin units are successfully integrated into polymeric networks.

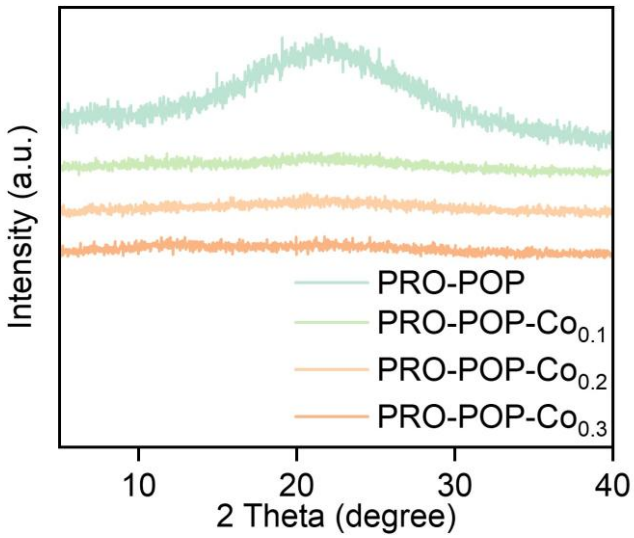

Fig. 3-4. XRD profiles of catalysts.

The XRD pattern of PP and PPC was show in **Fig. 3-4**. No characteristic peaks were observed in the XRD pattern due to the low crystallinity resulting from disordered stacking.[68] The widening of the peak at 22.1° might be attributed to turbulence between the PP and PPC polymers or structural defects within the PP and PPC system, resulting in some degree of disorder in the pore distribution, which revealed its amorphous nature.[69-71] The absence of diffraction peaks from metallic Co nanoparticles or Co oxides excludes the possibility that these impurities were formed and present in the PPC.[72]

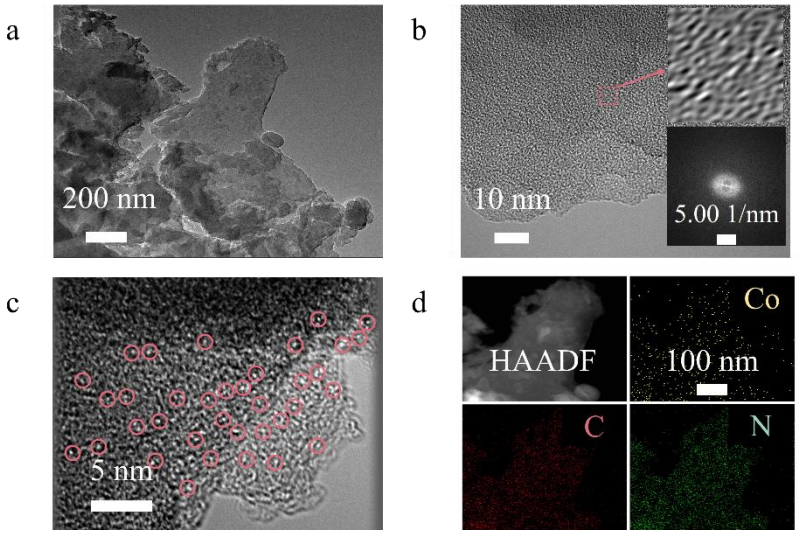

Fig. 3-5. (a) and (b) TEM image of $PPC_{0.1}$ (inset: SAED pattern). (c) AC HAADF-STEM

image of $PPC_{0.1}$, the isolated bright dots marked with red circles are cobalt atoms. (d) HAADF-STEM image with the corresponding EDS elemental mapping.

In **Fig. 3-5 (a** and **b)**, the TEM image confirms that the as-prepared PPC had a homogeneous two-dimensional lamellar structure without nanoparticles, and the SAED confirms the amorphous nature of PPC, consistent with the XRD results. Aberration-corrected HAADF-STEM image **Fig. 3-5c** shows a number of isolated bright spots representing the uniformly dispersed individual Co atoms, and no Co particles were observed on PPC. Moreover, the EDS mapping images **Fig. 3-5d** display the existence and homogeneous distribution of Co, N and C elements. Overall, it can be preliminarily judged that atomically dispersed Co exists on PPC.

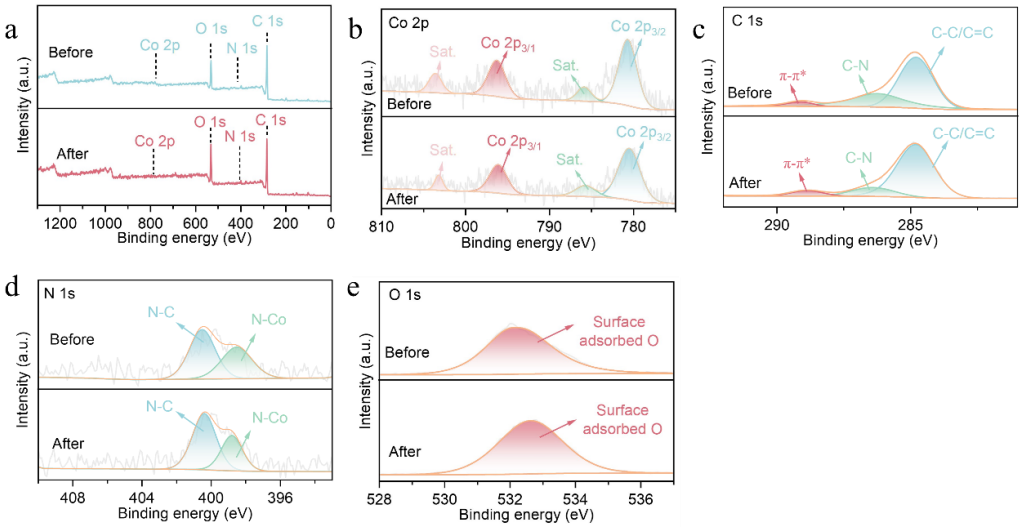

Fig. 3-6. The XPS spectra before and after the reaction of (a) survey, (b) Co 2p, (c) C 1s, (d) N 1s, and (e) O 1s.

The XPS full-scan spectrum **Fig. 3-6a** of PPC shows the existence of Co, N, C and O elements. The Co 2p XPS spectrum **Fig. 3-6b** shows two major peaks at 780.9 eV, 796.2 eV, which were attributed to the Co-N bond of Co $2p_{3/2}$ and Co $2p_{1/2}$ respectively.[73] These binding energies of Co 2p are similar to those of Co $(OAC)_2 \cdot 4H_2O$, recorded at 781.5 eV and 797.7 eV.[74] Additionally, the N 1s spectrum shown in **Fig. 3-6d** features two bands with peaks at 400.3 eV and 398.5 eV, which

correspond to pyrrole-N and Co-N within the porphyrin ring, respectively.[75] The C 1s spectrum **Fig. 3-6c** features peaks at 284.8 eV and 286.2 eV, corresponding to C-C (C=C) and C-N bonds respectively. Furthermore, a minor peak at 288.9 eV indicates π-π* transitions within the conjugated porphyrin system. In the O 1s spectrum **Fig. 3-6e**, the peak at 532.5 eV is associated with water molecules (H-O-H bond) adsorbed onto the surface. XPS analysis conducted before and after the catalytic reaction reveals that the peak positions of these elements are unchanged, demonstrating the catalyst's exceptional stability. Combining the results of FT-IT, NMR, TEM-EDS and XPS spectra, it can be concluded that the PPC has been successfully synthesized.

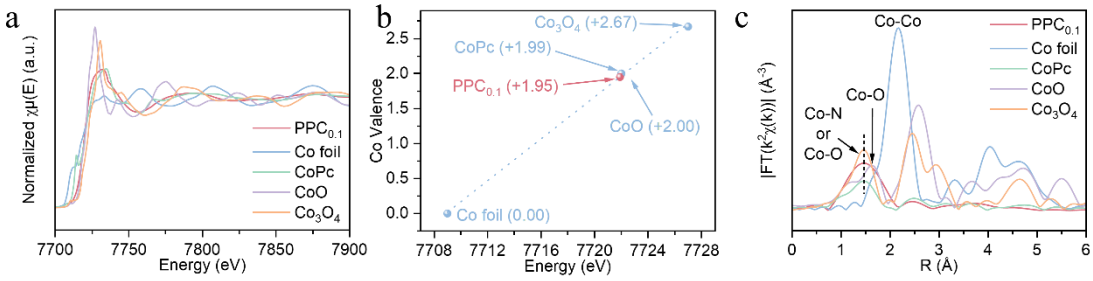

Fig. 3-7. (a) XANES spectra of $PPC_{0.1}$ and reference materials. (b) Relation between the Co K-edge absorption energy and Co valence for $PPC_{0.1}$ and reference materials. (c) FT-EXAFS spectra of $PPC_{0.1}$ and reference materials.

To further confirm the precise structure of $PPC_{0.1}$, X-ray absorption near edge structure (XANES) and extended X-ray absorption fine structure (EXAFS) spectroscopies were conducted. The normalized Co *k*-edge XANES spectra show that the absorption edge of $PPC_{0.1}$ has an obvious shift toward the high energy region compared with Co foil and is close to CoPc and CoO **Fig. 3-7a and b**, indicating that the Co atoms in $PPC_{0.1}$ possess positive charge with valence state close to +2.[76] The FT-EXAFS spectrum and corresponding EXAFS *k* space curve **Fig. 3-7c** of $PPC_{0.1}$ were similar to that of CoPc, which exhibited a solitary peak at approximately 1.48 Å, belonging to the Co-N scattering paths, whereas no Co-Co or Co-O peaks were observed.[77] This result confirms the isolated distribution of Co atoms on the $PPC_{0.1}$

support.

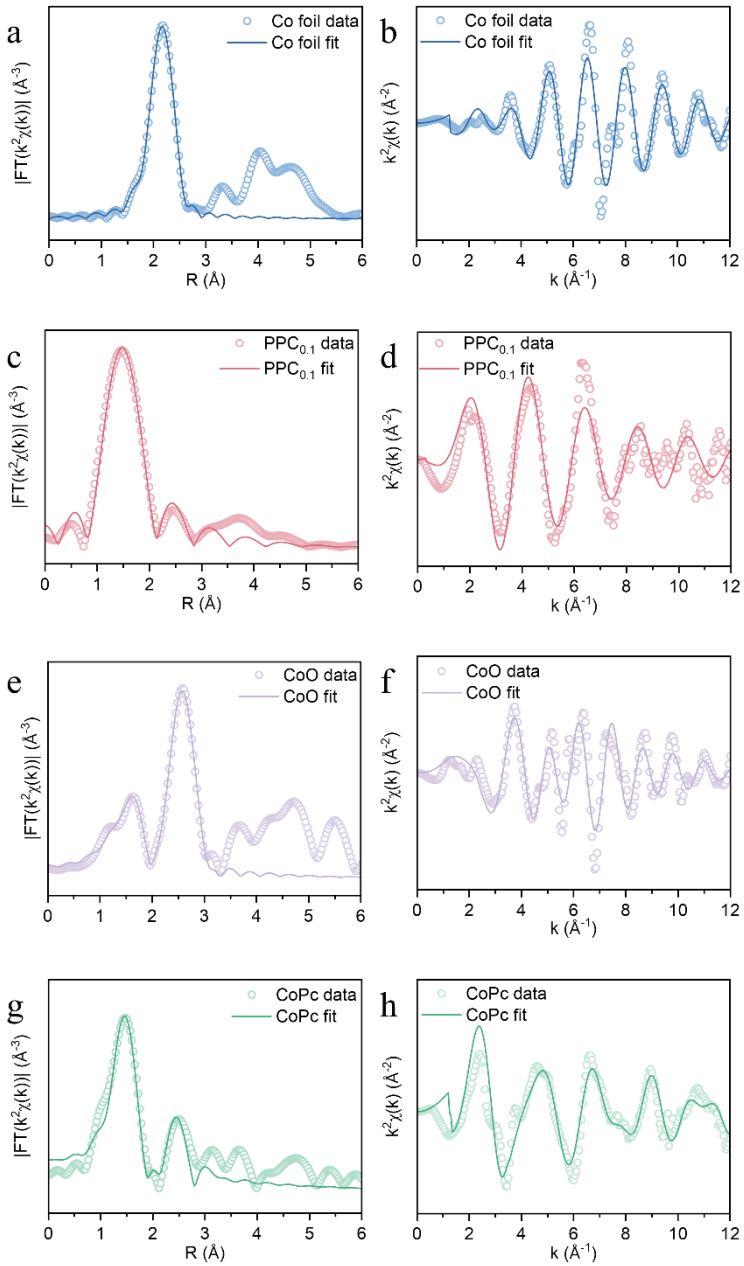

Fig. 3-8. FT-EXAFS spectra of $PPC_{0.1}$ and reference materials. Corresponding EXAFS fitting curves of Co foil (a), $PPC_{0.1}$(c), CoO(e) and CoPc(g) at *R*-space. EXAFS fitting curve of Co foil (b), $PPC_{0.1}$(d), CoO(f) and CoPc(h) at *K*-space.

In addition, EXAFS fitting analyses **Fig. 3-8 (a-h), and Table 3-1** revealed that the Co atom was coordinated by four N atoms (Co-N4) on an average, which was consistent with the model mentioned above.

Table. 3-1. EXAFS fitting parameters at the Co K-edge for various samples.

Sample	Shell	CN	R (Å)	σ^2 (10^{-3} Å^2)	ΔE_0 (eV)	R factor
Co foil	Co-Co	12(fixed)	2.49±0.01	6.3±0.4	6.3±0.5	0.002
CoPc	Co-N	3.9±0.6	1.92±0.01	2.1±3.7	6.3±4.2	0.010
	Co-C	7.2±1.7	2.91±0.01	6.3±7.2		
CoO	Co-O	5.5±0.8	2.10±0.01	2.8±3.6	1.9±3.5	0.012
	Co-Co	12.6±1.5	3.01±0.01	6.1±0.7		
$PPC_{0.1}$	Co-N	4.2±0.3	2.02±0.01	1.7±2.9	3.5±6.0	0.015

CN is the coordination number; R is interatomic distance (the bond length between central atoms and surrounding coordination atoms); σ^2 is Debye-Waller factor to account for both thermal and structural disorders; ΔE_0 is inner potential correction; R factor indicates the goodness of the fit.

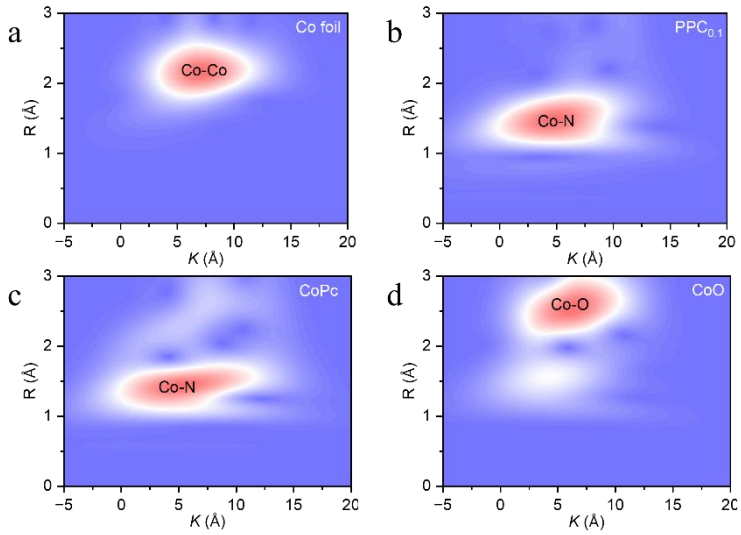

Fig. 3-9. WT-EXAFS plots of Co foil (a), $PPC_{0.1}$(b), CoPc(c) and CoO(d).

Meanwhile, the wavelet transform (WT) plot shows an intensity maximum at 5.26 Å^{-1} for $PPC_{0.1}$, corresponding to the Co-N rather than Co-Co bond and Co-O bond **Fig. 3-9 (a-d)**, indicating the absence of Co clusters or oxides, further indicating atomically dispersed cobalt.[34]

These characterizations show that the $PPC_{0.1}$ catalysts physicochemical properties and coordination structure (CoN4), which provided an ideal platform for revealing the electronic structure-dependent catalytic feature in $PPC_{0.1}$/PMS system.

3.3.2 Catalytic performance

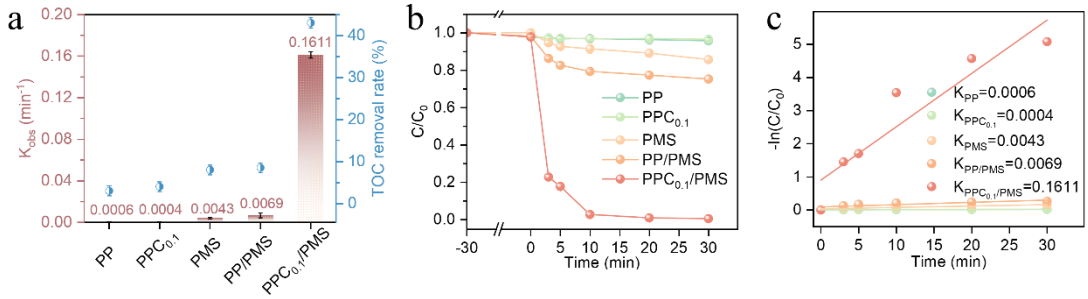

Fig. 3-10. (a) The corresponding pseudo-first-order kinetic constants and TOC removal efficiency of RAN in several systems. (b) and (c) RAN removal efficiency and reaction kinetics in different catalyst/PMS systems.

The degradation of RAN served as a metric to assess catalyst performance. The catalytic performance of PPC and control samples on RAN degradation was investigated **Fig. 3-10 (a-c)**. Remarkably, the degradation efficiency and mineralization rate of RAN achieved 100% and 43.03% within 30 min in the $PPC_{0.1}$/PMS system, respectively. While, the PP achieved RAN degradation efficiency and mineralization rate of 24.69% and 8.52% within 30 min in the present of PMS, respectively. The significantly enhanced degradation rate of PPC compared with PP implied that the introduced atomic Co provided additional active sites.

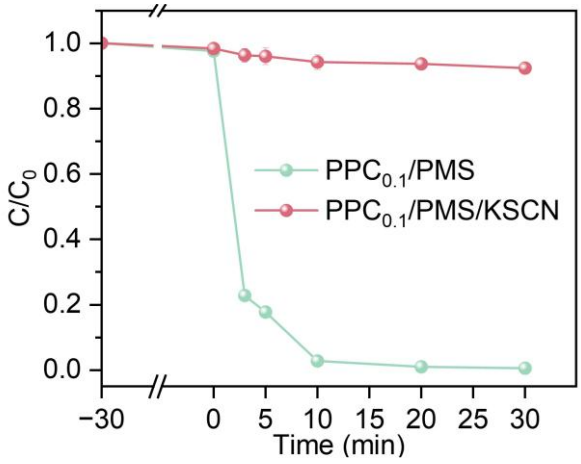

Fig. 3-11. Performance of $PPC_{0.1}$/PMS to degrade RAN with or without KSCN.

When the reaction system contained 10 mM KSCN, the RAN degradation process was almost blocked **Fig. 3-11** . This situation indicates that the active site of $PPC_{0.1}$ catalyzing RAN degradation is Co atom center, and the introduced SCN^- ions can combine with Co in CoN4, thus poisoning the catalytic site point.[78] The KSCN poisoning experiment also reflected that atom Co plays a key role in the activation of PMS by $PPC_{0.1}$. In addition, when only the presence of PMS or PP, the removal efficiency and mineralization rate of RAN were 14.32% or 3.45% and 8.12% or 4.32%, respectively.

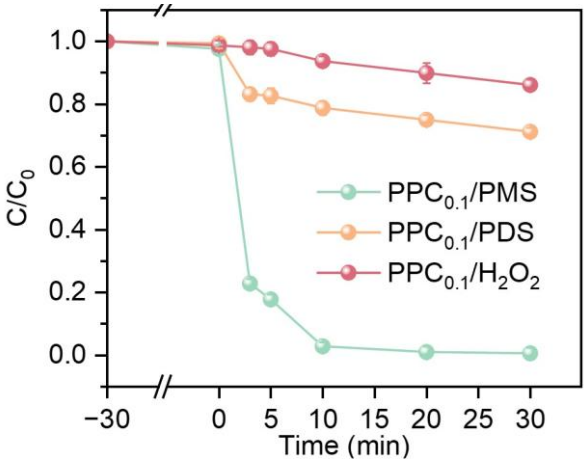

Fig. 3-12. The comparison of RAN degradation efficiency by different oxidants in $PPC_{0.1}$/PMS system.

To further evaluate the activation efficiency of $PPC_{0.1}$ with different oxidants,

$Na_2S_2O_8$ (PDS) and H_2O_2 were added to the RAN solution for comparison. As shown in **Fig. 3-12**, in the presence of PMS, the RAN degradation rate reached 100% within 30 min, which was significantly higher than those achieved with PDS (28.81%) and H_2O_2 (13.91%). The symmetric structure of PDS contributes to its greater stability and steric hindrance compared to PMS, while the high bond energy of the O-O bond in H_2O_2 hinders its cleavage.[79] These factors likely limit the catalytic activation of PDS and H_2O_2. Consequently, PMS was selected as the oxidant for this experiment. Moreover, the influence of cobalt load, PMS dosage, RAN concentration, and catalyst dosage on RAN degradation in PPC/PMS system was investigated, because the active species production and RAN degradation are of high dependent on the above factors.

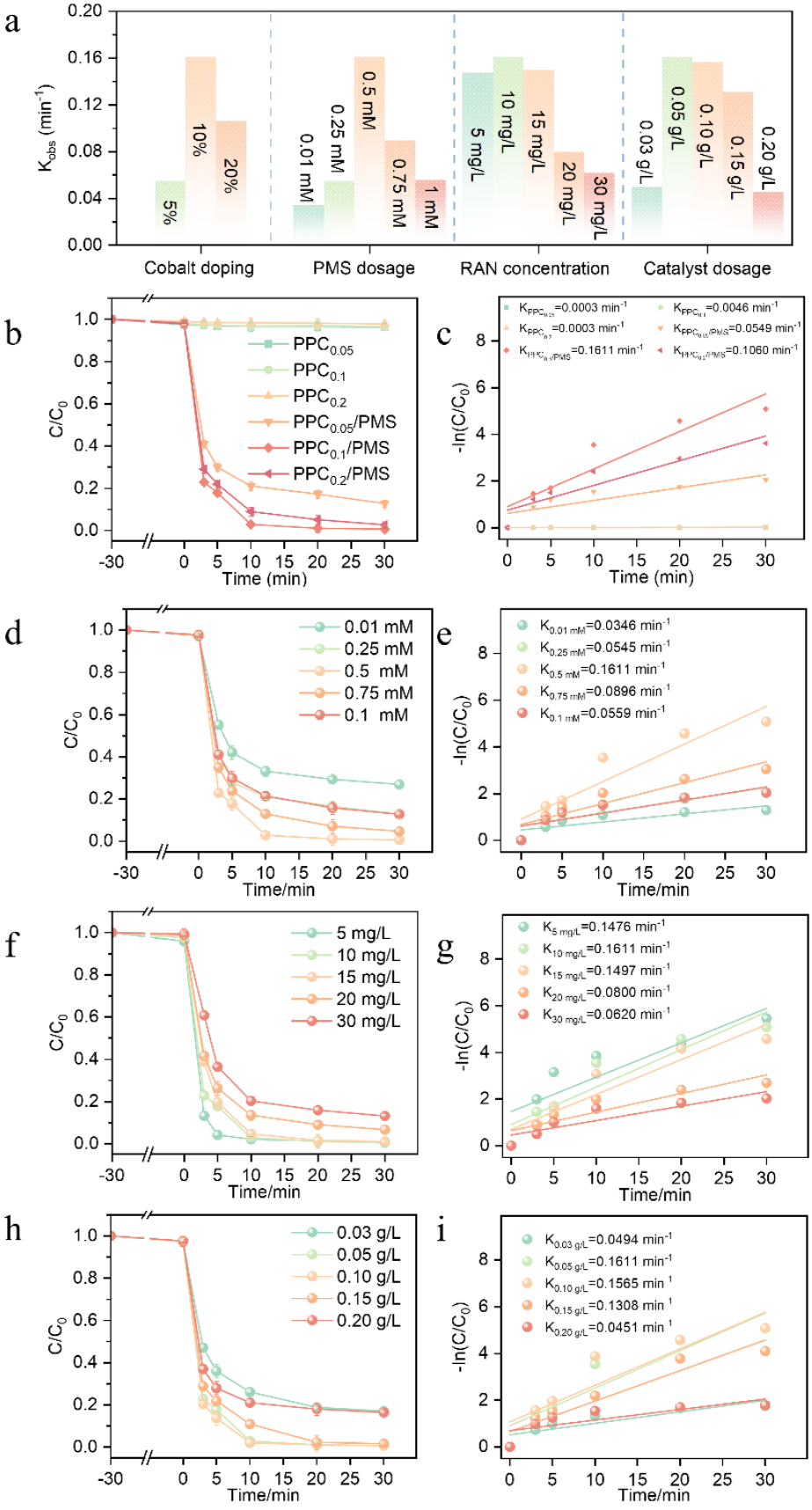

Fig. 3-13. (a) The corresponding rate constants *k* under various conditions. (b) and (c) Effects

of cobalt load, (d) and (e) Effects of PMS concentration, (f) and (g) Effects of RAN concentration, (h) and (i) Effects of catalyst content on the RAN degradation in $PPC_{0.1}$/PMS system.

Moreover, the influence of cobalt doping, PMS dosage, RAN concentration, catalytic dosage and initial pH on RAN degradation in PPC/PMS system was investigated, because the active species production and RAN degradation are of high dependent on the above factors. For better comparison, the apparent rate constant (k) for catalytic degradation is analyzed via first-order kinetic model [$\ln(C/C_0) = -kt$]. As shown in **Fig. 3-13 (a-c)** optimization experiments of Co doping amount indicated that more Co(II) contents are introduced, better catalytic oxidation of RAN can be achieved. The catalyst with 10wt% Co had the best performance for RAN removal, and excessive Co doping led to clustering and a decrease in catalytic performance. The concentration of the oxidant is a major factor in the generation of. The concentration of the oxidant is a major factor in the generation of radicals or non-radicals oxidation species. In this experiment, the dosages of PMS were from 0.01 mM to 1 mM. **Fig. 3-13d and e** displays the effect of different PMS dosage (0.01, 0.25, 0.5, 0.75, 0.1 mM) on RAN degradation in the $PPC_{0.1}$/PMS system. As the source of reactive non-radical, PMS with low concentration (0.01 mM) failed to generate sufficient Co(IV)=O, leading to the incomplete degradation of RAN. Increasing PMS concentration from 0.25 to 0.5 mM obviously speeded up the process of RAN degradation, with the constant k evidently increasing from 0.0545 min^{-1} to 0.1611 min^{-1}. Furthermore, low dosage of PMS might be not conducive to the regeneration reaction of Co(II). However, no enhancement of RAN degradation was observed when PMS concentration was further increased to 0.75 and 0.1 mM, which was likely due to excessive PMS might alter the pH of the solution, reducing the catalytic efficiency. As shown in **Fig. 3-13f and g** that as the concentration of RAN increased from 5 mg/L to 30 mg/L, the degradation rates of RAN displayed a decreasing trend, which may be related to the free radicals generated by the $PPC_{0.1}$/PMS system. When the concentration of RAN gradually increased, many by-products may be produced. By-products may compete with the parent contaminants for free radicals

and non-radicals in the system, resulting in reduced efficiency of catalytic oxidation. **Fig. 3-13h and i** illustrated the variation of degradation efficiency of RAN and the k with the increase of $PPC_{0.1}$ dosage under a certain amount of PMS (0.5 mM) and RAN (10 mg/L). RAN removal rate increased rapidly when the $PPC_{0.1}$ dosage increased from 0.03 to 0.05 g/L. However, further increase of $PPC_{0.1}$ dosage (0.05-0.20 g/L) would inhibit RAN degradation, and the constant k was reduced from 0.1611 to 0.0451 min^{-1}. The improvement of the constant k was due to the increase of surface active sites of $PPC_{0.1}$, which enhanced the number of Co(IV)=O generated during the activation of PMS. However, excessive catalyst would lead to tardiness mass transfer and the unavailability of active sites, thus decreasing the catalytic activity.

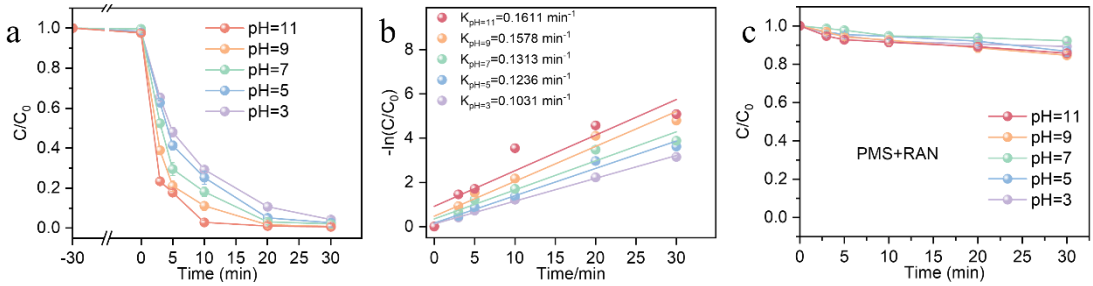

Fig. 3-14. (a) and (b) Effects of initial pH on the RAN degradation in $PPC_{0.1}$/PMS systems. (c) The comparison of RAN degradation efficiency by different pH in PMS system.

The pH value is a critical factor in the efficiency and effectiveness of catalyst-activated persulfate degradation of antibiotics.[80] Different pH levels can affect the type and quantity of radicals produced, the stability and reactivity of the antibiotic, and the performance of the catalyst. Therefore, the effect of different initial pH on the degradation of RAN in the $PPC_{0.1}$/PMS system was primarily evaluated. As shown in **Fig. 3-14a and b**, $PPC_{0.1}$/PMS system exhibited a sound maneuverability system and achieved satisfactory RAN degradation over a wide pH range (3.0–11.0). It seems that, contrary to most previous reports on the degradation of organic pollutants by PMS, the $PPC_{0.1}$/PMS system does not favor acidic environments and is more well-adapted to excel in higher pH conditions. The particular radicals and non-radicals produced and

the base activation of PMS should be important contributors to this discrepant result. The **Fig. 3-14c** demonstrates the degradation efficiency of RAN solely by PMS across varying pH. Under alkaline conditions, there is no acceleration in the degradation of RAN, thus ruling out the possibility that alkaline activation of PMS contributes to the degradation of RAN. Therefore, the results mentioned above could be due to radicals or non-radical species produced upon the activation of PMS by $PPC_{0.1}$, which accelerate the degradation of RAN under alkaline conditions.

To verify the aforementioned hypothesis, we further identified the active species in the $PPC_{0.1}$/PMS system across various pH conditions. Tert-butyl alcohol (TBA), Methanol (MeOH), P-benzoquinone (PBQ), L-histidine (L-His), and dimethyl sulfoxide (DMSO) were used as the scavengers of ·OH, $SO_4^{\cdot-}$, $O_2^{\cdot-}$, $^1O_2$ and HVMO species, respectively.[81] The radical pathways in the $PPC_{0.1}$/PMS system under alkaline conditions were firstly discussed.

3.3.3 Mechanistic Study of RAN Degradation by PPC

3.3.3.1 Identification of Dominant Reactive Species

To verify the aforementioned hypothesis, we further identified the active species in the $PPC_{0.1}$/PMS system across various pH conditions. Tert-butyl alcohol (TBA), Methanol (MeOH), P-benzoquinone (PBQ), L-histidine (L-His), and dimethyl sulfoxide (DMSO) were used as the scavengers of ·OH, $SO_4^{\cdot-}$, $O_2^{\cdot-}$, $^1O_2$ and HVMO species, respectively.[81] The radical pathways in the $PPC_{0.1}$/PMS system under alkaline conditions were firstly discussed.

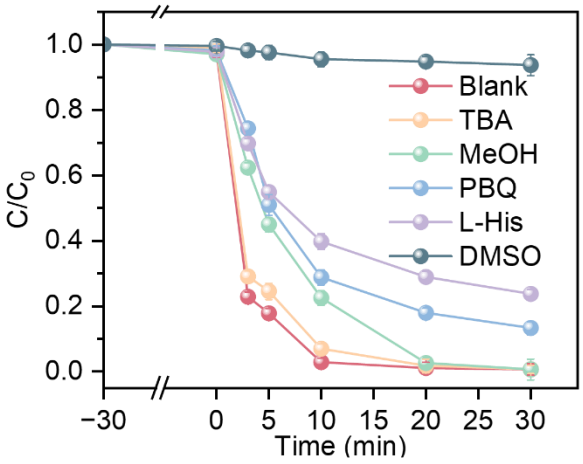

Fig. 3-15. Effect of scavengers on RAN degradation in $PPC_{0.1}$/PMS.

MeOH is frequently utilized as a quencher for both ·OH and $SO_4^{\cdot-}$ radicals due to its comparable reaction rates ($k_{\cdot OH/MeOH}$ =1.6-7.7×10^7 M^{-1} S^{-1}, $k_{SO4\cdot-/MeOH}$ =9.7×10^8 M^{-1} S^{-1}) with these species. TBA shows a greater propensity to react with ·OH radicals, evidenced by a higher reaction constant $k_{\cdot OH/TBA}$ =3.8-7.6×10^8 M^{-1} S^{-1} compared to $k_{SO4\cdot-/TBA}$ =4-9.1×10^5 M^{-1} S^{-1}.[41] When adding TBA and MeOH as the scavenger into $PPC_{0.1}$/PMS system to quench ·OH and $SO_4^{\cdot-}$, the contribution of ·OH and $SO_4^{\cdot-}$ for RAN degradation was negligible (**Fig. 3-15**). PBQ was used as a quencher of $O_2^{\cdot-}$, the constant k declined to 0.0663 min^{-1} after adding PBQ, suggesting the production of $O_2^{\cdot-}$. However, the contribution of $O_2^{\cdot-}$ for RAN degradation was minimal, indicating that not the primary active species. In addition to radical pathways, non-radical pathways may also exist during the removal process of RAN in the system. First, L-His was used as a scavenger to detect $^1O_2$.

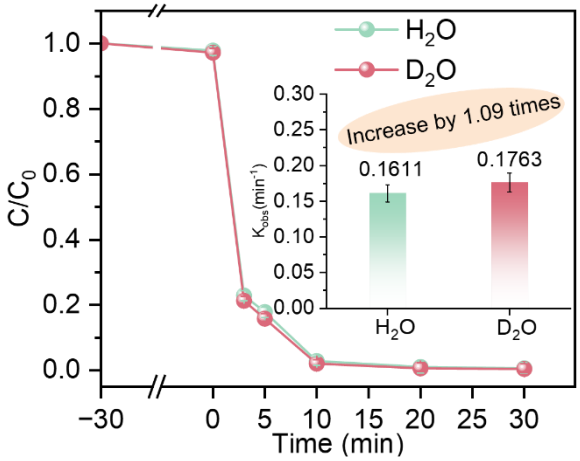

Fig. 3-16. The degradation of RAN by the $PPC_{0.1}$/PMS systems in H_2O and D_2O solvent.

The RAN degradation was minor effect with the addition of L-His. To further determine the role of $^1O_2$, solvent exchange experiment from H_2O to D_2O was performed. The lifetime of $^1O_2$ in D_2O is much longer than that in H_2O, thus, the degradation efficiency could be enhanced if $^1O_2$ was involved in attacking pollutant.[82] However, RAN degradation was not enhanced in D_2O system (**Fig. 3-16**), suggesting that $^1O_2$ was not involved in RAN degradation.

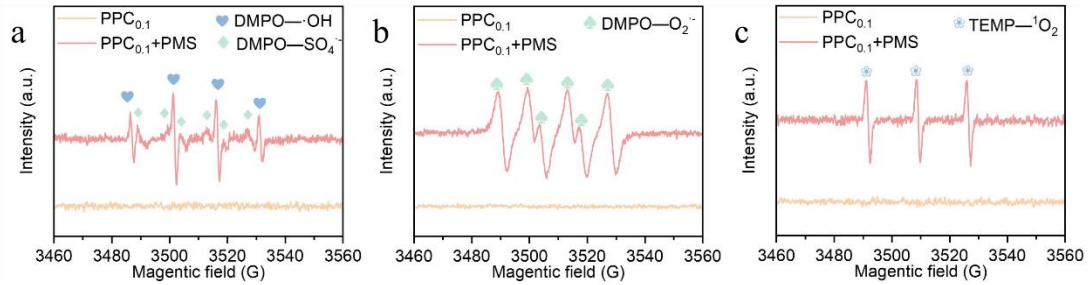

Fig. 3-17. EPR spectra of (a) DMPO-$SO_4^{\cdot-}$ and DMPO-·OH, (b) DMPO-$O_2^{\cdot-}$, and (c) TEMP-$^1O_2$ in $PPC_{0.1}$/PMS systems.

EPR was carried out to further identify the presence of reactive oxygen species in the $PPC_{0.1}$/PMS system. The results demonstrated that the addition of PMS would indeed generate $O_2^{\cdot-}$ and $^1O_2$ (**Fig. 3-17b and c**), but the detected signals of DMPO-$O_2^{\cdot-}$ and TEMP-$^1O_2$ were very weak. As DMPO was used as a trapping agent to detect ·OH and $SO_4^{\cdot-}$, the typical 1:2:2:1 quartet of DMPO-·OH and the 1:1:1:1:1:1 sextet of DMPO- $SO_4^{\cdot-}$ did not appear (**Fig. 3-17a**), but an intense DMPO-X signal was recorded, which can be explained by the rapid and efficient activation of PMS producing large amounts of ·OH and $SO_4^{\cdot-}$ or by some surface oxidation reactions such as high-valent cobalt-oxo species.[83] The latter is preferred to be logical considering the indications of the quenching experiments. Therefore, there must be other reactive species dominating RAN degradation during $PPC_{0.1}$/PMS oxidation, instead of ·OH, $SO_4^{\cdot-}$, $O_2^{\cdot-}$ and $^1O_2$.

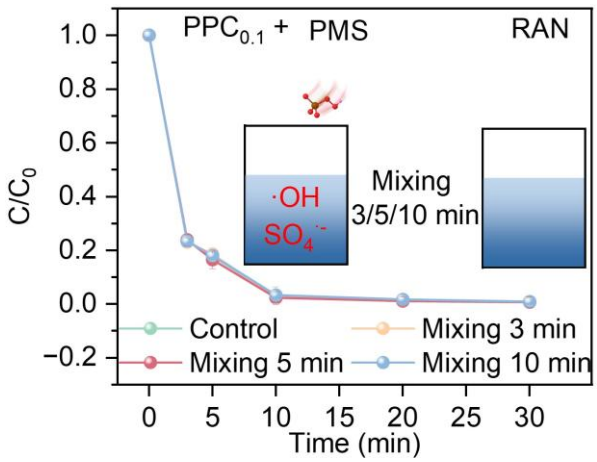

Fig. 3-18. RAN oxidation via a premixture of $PPC_{0.1}$ and PMS at estimated time intervals.

The contribution of radicals for oxidating RAN in the $PPC_{0.1}$/PMS system was further identified by a premixing experiment via premixing the $PPC_{0.1}$ and PMS at estimated time intervals before adding RAN.[84, 85] By premixing PMS and catalyst in the system, radicals were generated instantaneously in the catalytic system, a process that resulted in significant consumption of PMS. Therefore, the degradation of pollutants will be affected after the subsequent addition of pollutants. This helps to accurately assess the role of free radicals in the system. If the oxidation mechanism was not dominated by the radicals, the premixture of $PPC_{0.1}$ and PMS would only cause a minor effect on the RAN oxidation. Results showed that premixing the $PPC_{0.1}$ and PMS for 3, 5 and 10 min only showed a very weak inhibition on the RAN oxidation (**Fig. 3-18**), which indicated that some nonradical (not $^1O_2$) overwhelmed the effect of radicals in oxidating the RAN, although large amounts of radicals were produced in $PPC_{0.1}$/PMS system and contributed to the degradation of RAN.[86]

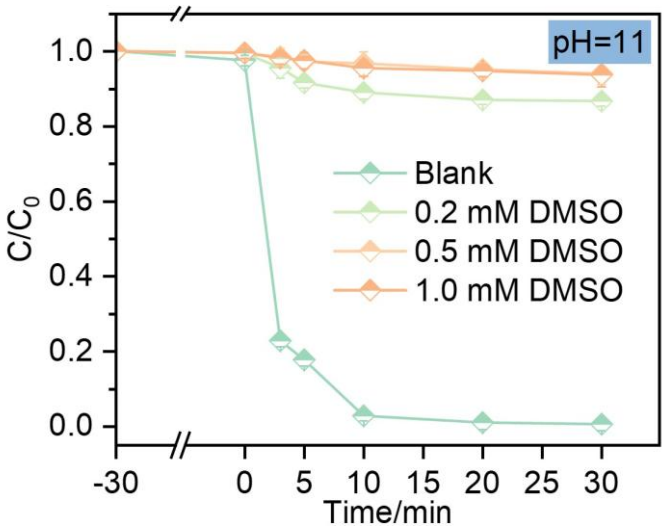

Fig. 3-19. Effects of DMSO scavenger concentrations on RAN degradation in $PPC_{0.1}$/PMS system at pH=11.

As the addition of DMSO into the $PPC_{0.1}$/PMS system resulted in the complete stagnation of RAN degradation (**Fig. 3-19**), we postulate that high valent Co species like CoIV=O are the dominant reactive species.

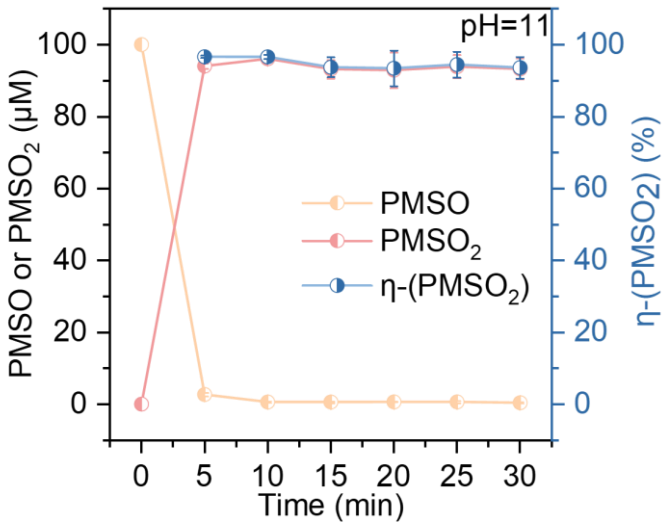

Fig. 3-20. PMSO consumption, $PMSO_2$ production, and η-($PMSO_2$) in the $PPC_{0.1}$/PMS system at pH=11.

This was corroborated by the detection of methyl phenyl sulfone ($PMSO_2$) during methyl phenyl sulfoxide PMSO oxidation (**Fig. 3-20**), which PMSO can be converted

to $PMSO_2$ by CoIV=O ($k_{CoIV=O/PMSO}=2.0\times10^6$ M^{-1} S^{-1}) through a unique oxygen transfer step, while hydroxylated and/or polymeric products will be introduced from PMSO oxidation by free radicals($k_{\cdot OH/PMSO}=3.61\times10^9$ M^{-1} S^{-1} and $k_{SO4\cdot-/PMSO}=3.17\times10^8$ M^{-1} S^{-1}) (Eqs. (3-1)-(3-3)).[83, 87-89]

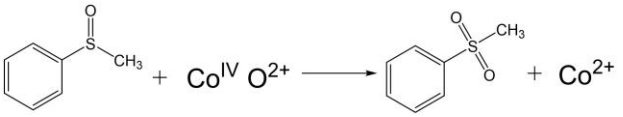

(3-1)

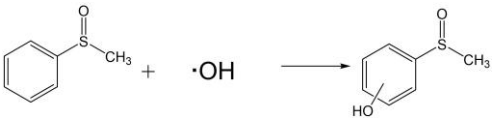

(3-2)

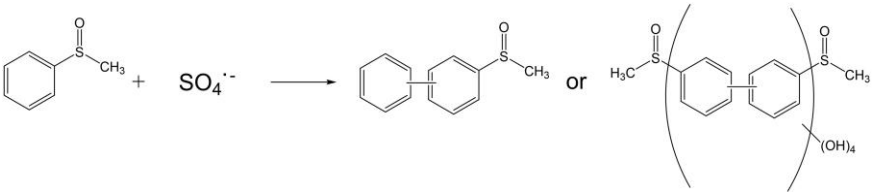

(3-3)

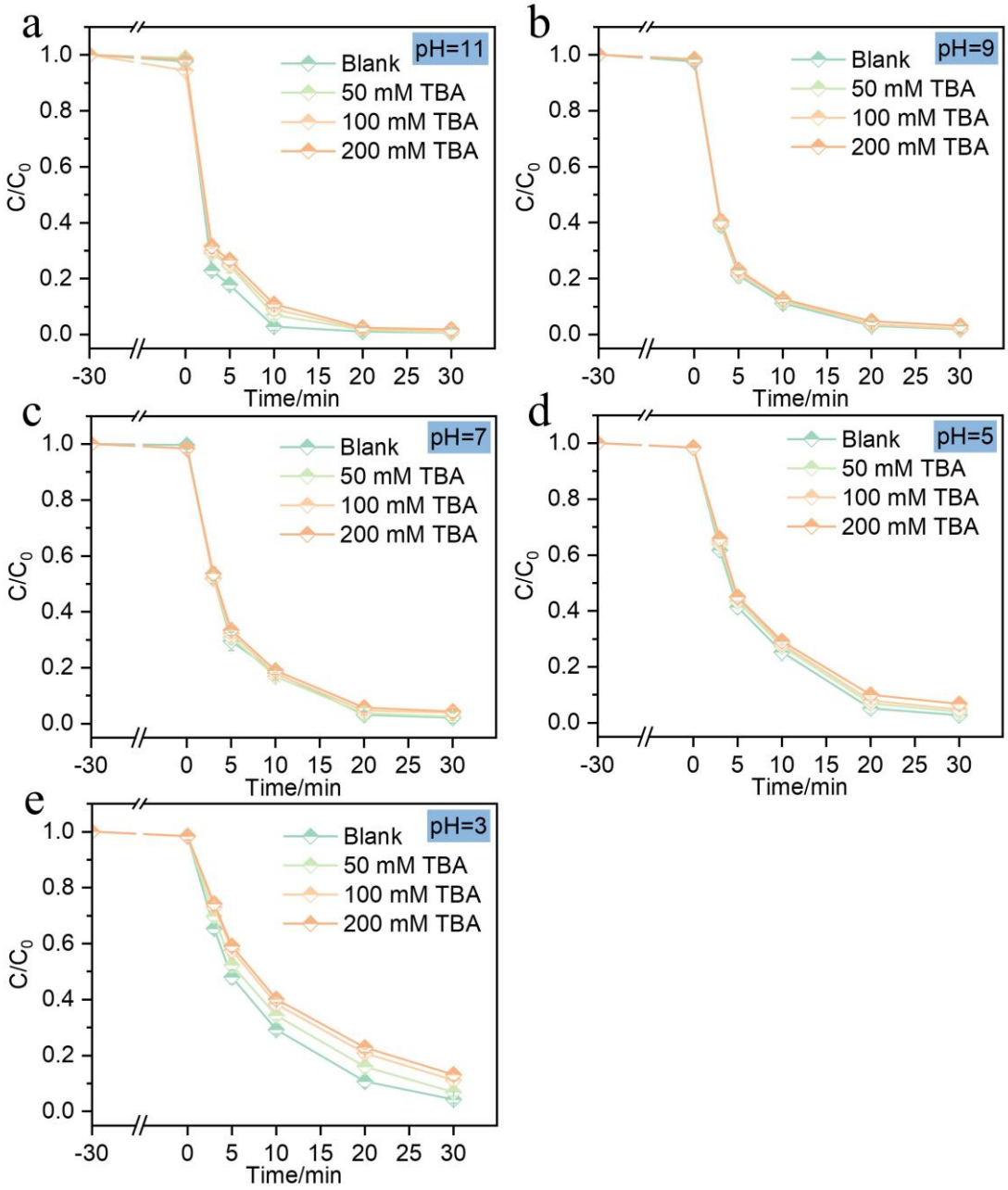

Fig. 3-21. (a)-(e) Effects of TBA scavenger concentrations on RAN degradation by different pH in $PPC_{0.1}$/PMS system.

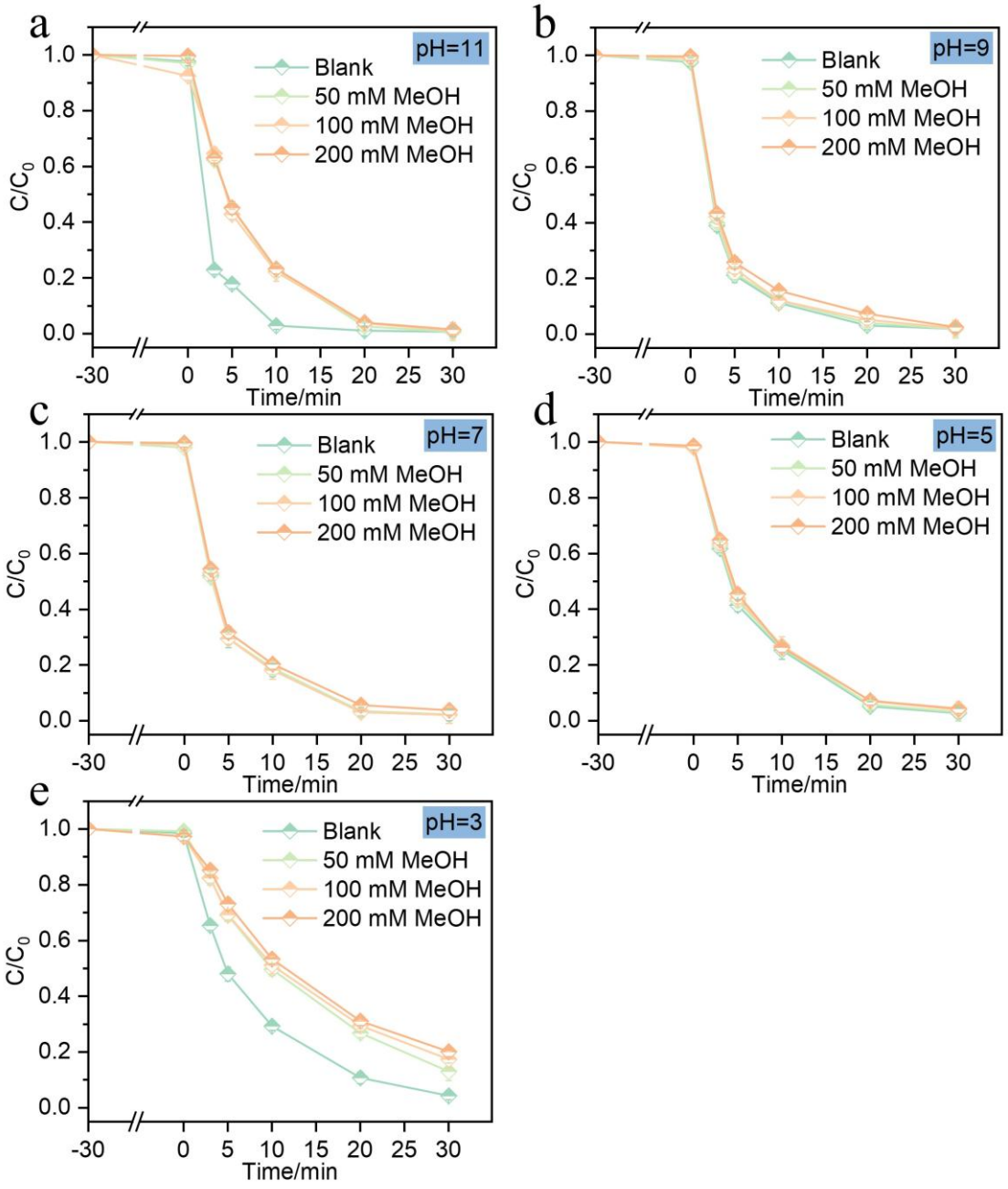

Fig. 3-22. (a)-(e) Effects of MeOH scavenger concentrations on RAN degradation by different pH in $PPC_{0.1}$/PMS system.

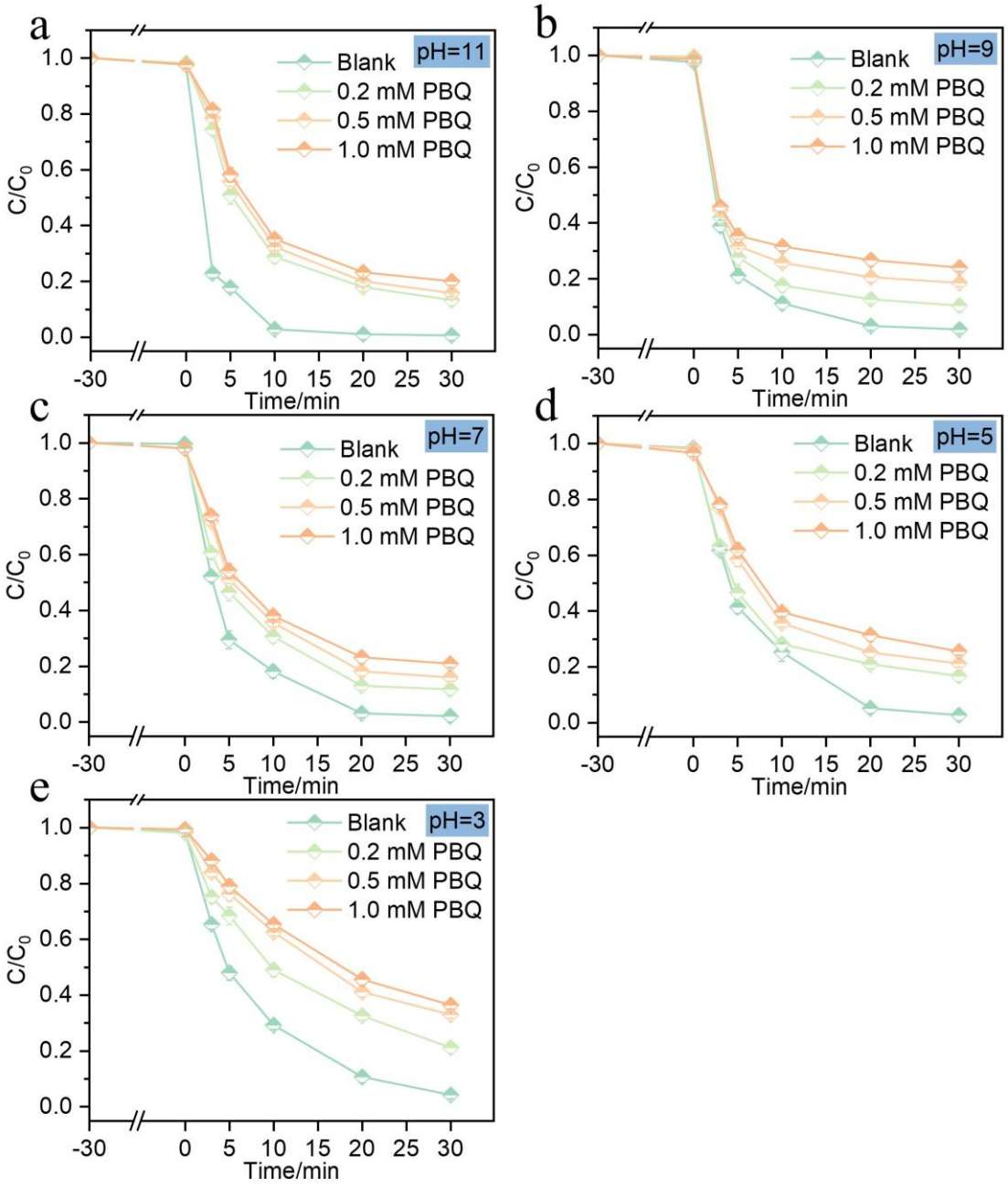

Fig. 3-23. (a)-(e) Effects of PBQ scavenger concentrations on RAN degradation by different pH in $PPC_{0.1}$/PMS system.

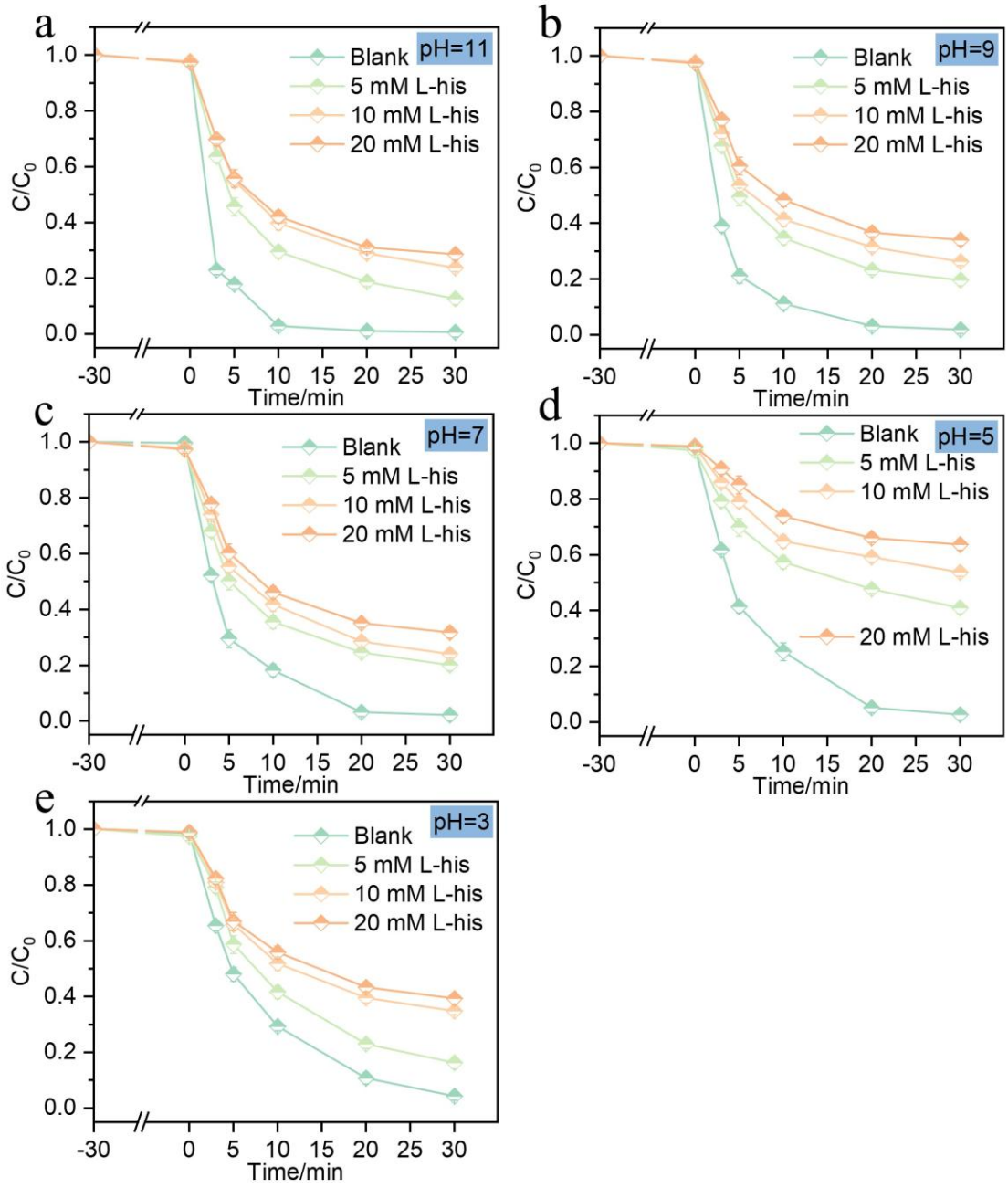

Fig. 3-24. (a)-(e) Effects of L-his scavenger concentrations on RAN degradation by different pH in $PPC_{0.1}$/PMS system.

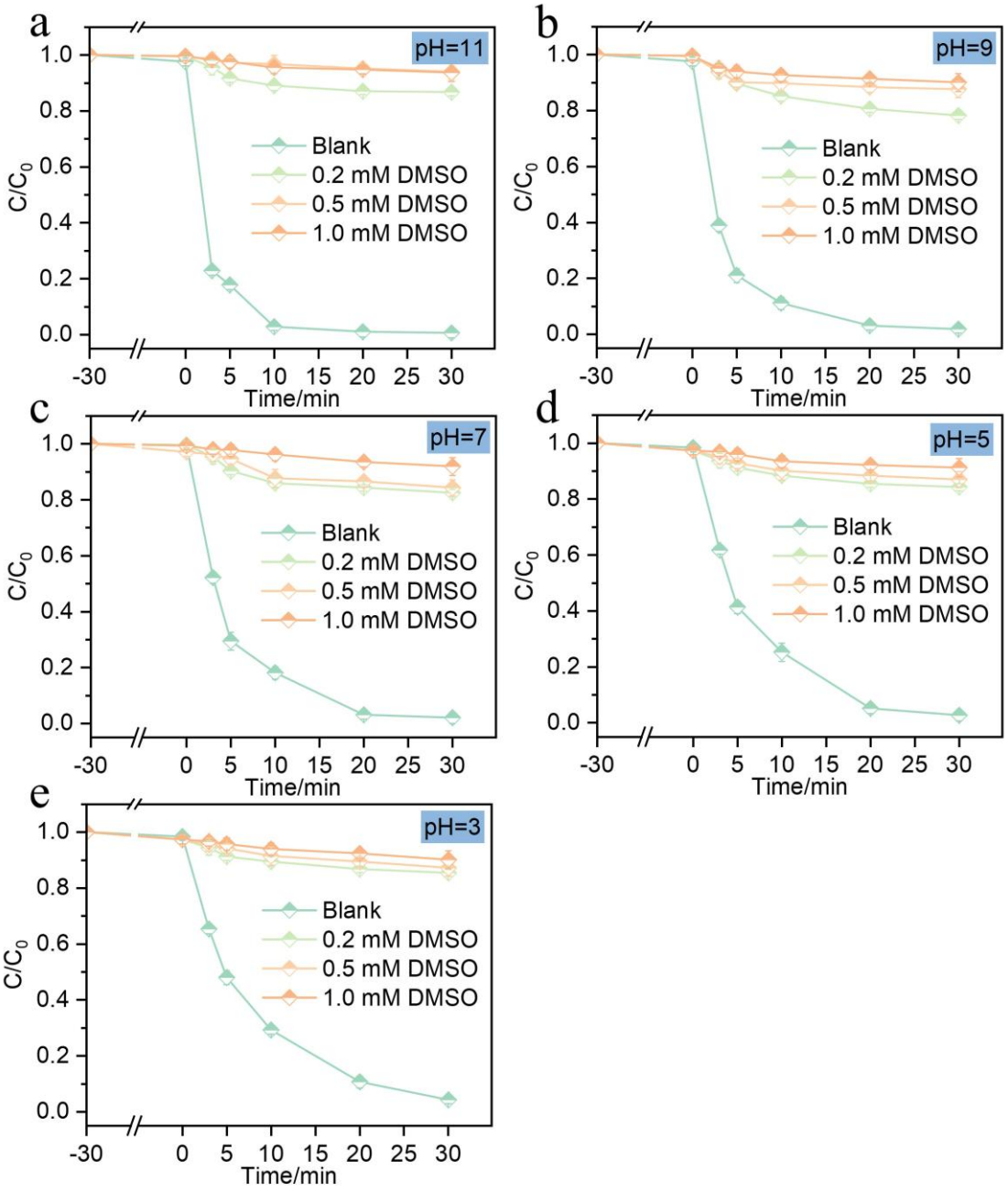

Fig. 3-25. (a)-(e) Effects of DMSO scavenger concentrations on RAN degradation by different pH in $PPC_{0.1}$/PMS system.

As show in **Fig. (3-21)-(3-25)**, the results of quenching experiments are consistent across different pH values, indicating that the $PPC_{0.1}$/PMS system selectively generates CoIV=O active species under a broad range of pH conditions. In this regard, μ-$PMSO_2$ yield (the molar proportion of $PMSO_2$ formation to PMSO abatement) can discern the formation of radicals and quantify the relative contributions of CoIV=O species.[90]

Therefore, in this research, PMSO degradation was investigated with a focus on its characteristic product, $PMSO_2$

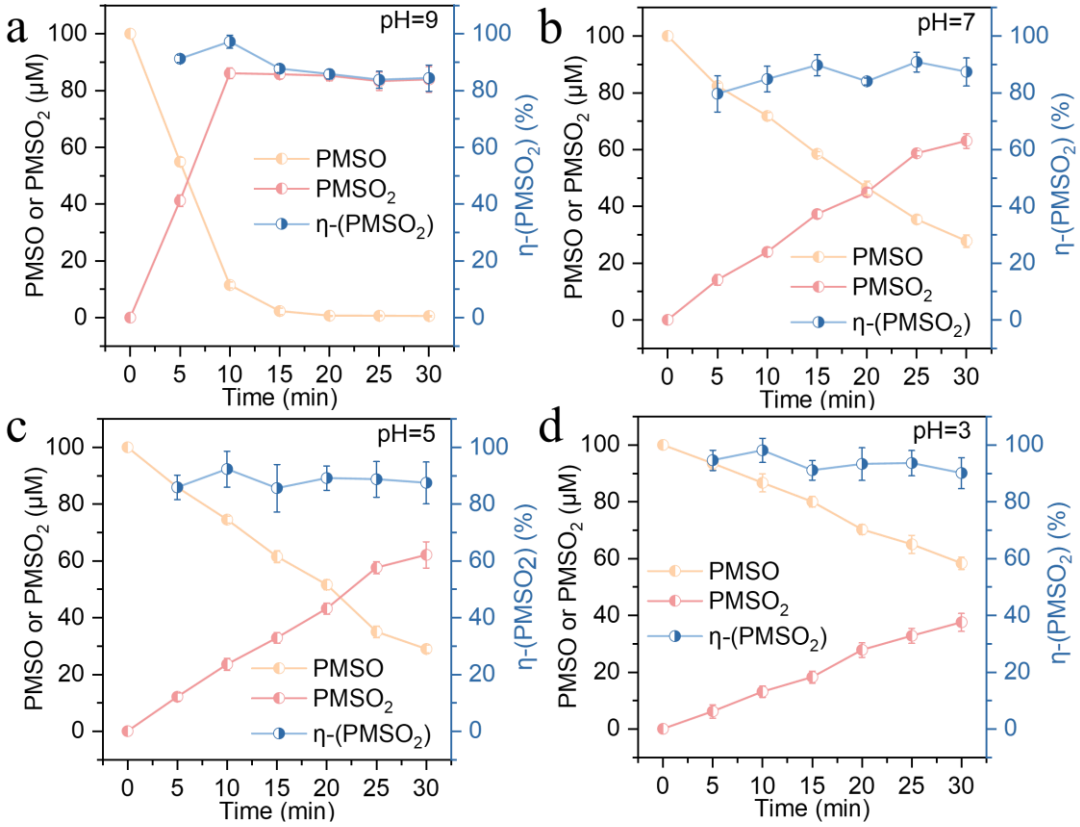

Fig. 3-26. (a)-(d) PMSO consumption, $PMSO_2$ production, and η-($PMSO_2$) in the $PPC_{0.1}$/PMS system at different pH.

Fig. 3-26 shows that CoIV=O can oxidize PMSO at pH 3.0-11.0. The highest removal of PMSO by CoIV=O occurred at pH 11.0. In addition, at pH 3.0-11.0, the consumption of PMSO is equal to the production of $PMSO_2$ (μ-$PMSO_2$ around 100%), indicating the participation of CoIV=O species in the studied system rather than free radicals. Because if free radicals were involved, it would not be possible for $PMSO_2$ to achieve an efficiency close to 100%.

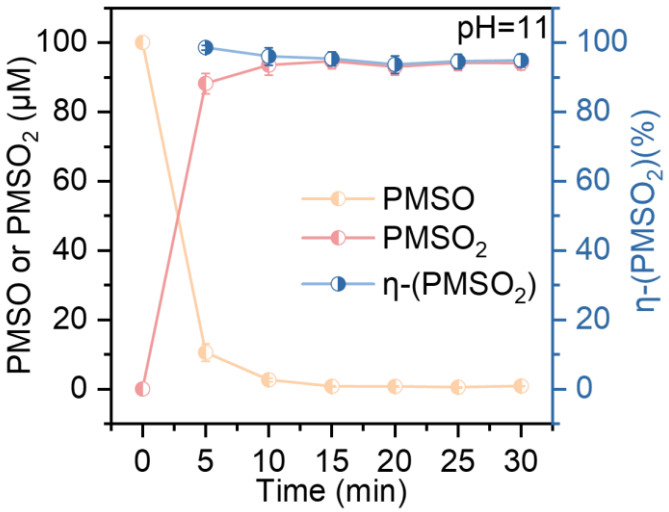

Fig. 3-27. PMSO consumption, $PMSO_2$ production, and η-($PMSO_2$) in the $PPC_{0.1}$/PMS/RAN system at pH=11.

The **Fig. 3-27** demonstrates a slight decrease in both the consumption of PMSO and the production of $PMSO_2$ following the addition of RAN. This reduction is attributed to a portion of Co(IV)=O reacting with RAN during the PMSO transformation process and participating in the degradation process.

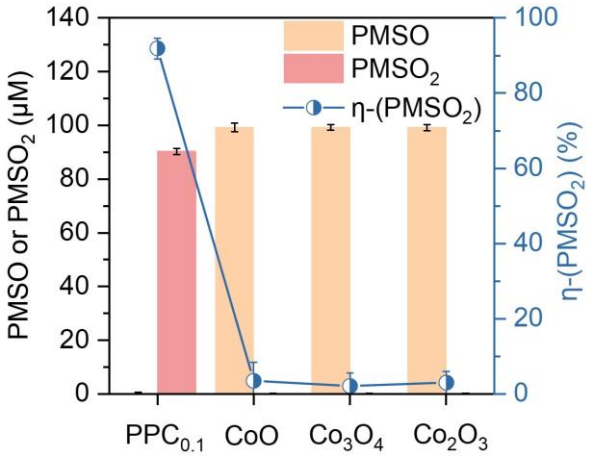

Fig. 3-28. PMSO consumption, $PMSO_2$ production, and η-($PMSO_2$) in the different cobalt oxides/PMS system and $PPC_{0.1}$/PMS system.

Additionally, the **Fig. 3-28** indicates that various cobalt oxides do not produce high-valency cobalt. This lack of high-valency cobalt formation may be attributed to

the absence of necessary electron transfer during the interaction between cobalt oxides and PMS.

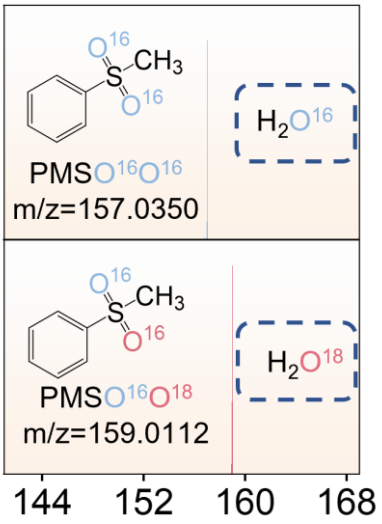

Fig. 3-29. high-resolution mass spectrometry analyses of O^{18}-labeled $PMSO_2$ generated in H_2O^{18} matrix.

Spontaneous exchange of O atoms between the intermetallic Co–O bond and the solvent water can provide supplementary evidence for Co(IV)=O formation and oxidation. Using O^{18}-isotope-labeled H_2O^{18} as the solvent, Co(IV)=O would form Co(IV)= O^{18} through spontaneous O-atom exchange and then oxidize PMSO to form $PMSO^{16}O^{18}$, which was, as expected, detected in this study.[91] When the reaction systemwas carried over into the H_2O^{18} matrix, the oxidation product $PMSO^{16}O^{18}$ was observed, as evidenced by the two peaks in the extracted ion chromatogram at m/z = 157.0350 ($PMSO^{16}O^{16}$) and 159.0112 ($PMSO^{16}O^{18}$) **(Fig. 3-29)**. The results further demonstrate the intermediate role of Co(IV)=O in oxidation of $PPC_{0.1}$/PMS.

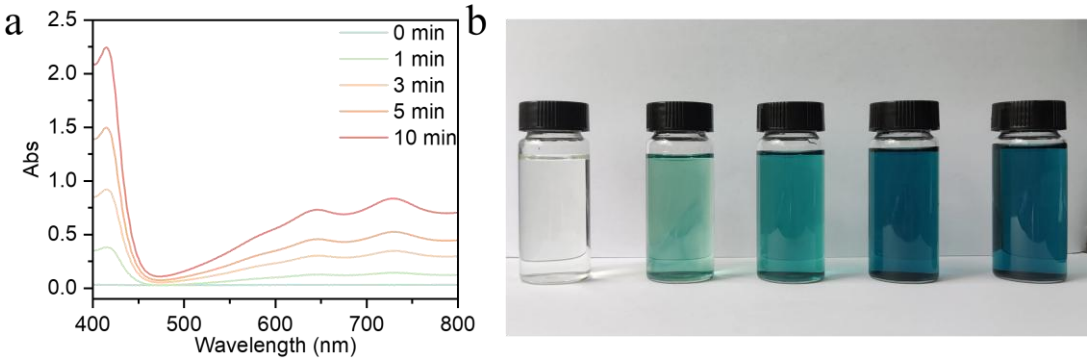

Fig. 3-30. (a) and (b) The UV–Visible absorption spectra of the $PPC_{0.1}$/PMS system were quenched by ABTS.

Additionally, 2,2'-azinodi(3-ethylbenzothiazoline-6-sulfonic) (ABTS) can be oxidized into $ABTS^{\cdot+}$ by high-valent metal oxides through one-electron oxidation with the color turning blue.[92] The formation of $ABTS^{\cdot+}$ is detectable in the UV-visible spectrum, particularly around 415 nm and 660 nm. Observations of spectral changes in ABTS during the $PPC_{0.1}$/PMS catalytic oxidation process suggest the generation of Co(IV)=O species in the reaction(**Fig. 3-30**) (Eqs. (3-4)).

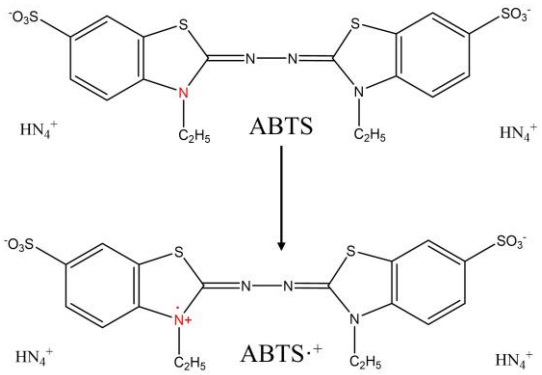

(3-4)

3.3.3.2 DFT Calculations

he catalytic mechanism of $PPC_{0.1}$ was investigated through density functional theory (DFT) calculations and experiments.

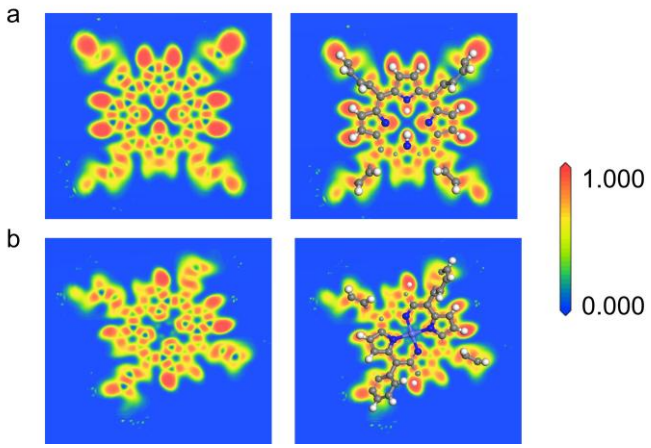

Fig. 3-31. Electron localization functions of (a) PP and (b) $PPC_{0.1}$.

Analysis of the electronic localization functions (ELF, **Fig. 3-30**) revealed significant distorted electronic symmetry in $PPC_{0.1}$ due to the incorporation of Co atoms. Furthermore, the Co sites exhibited a high degree of electron delocalization, implying that the electronic coupling bolsters the efficient transport of electrons in $PPC_{0.1}$, which played a crucial role in the Co(IV)=O formation.

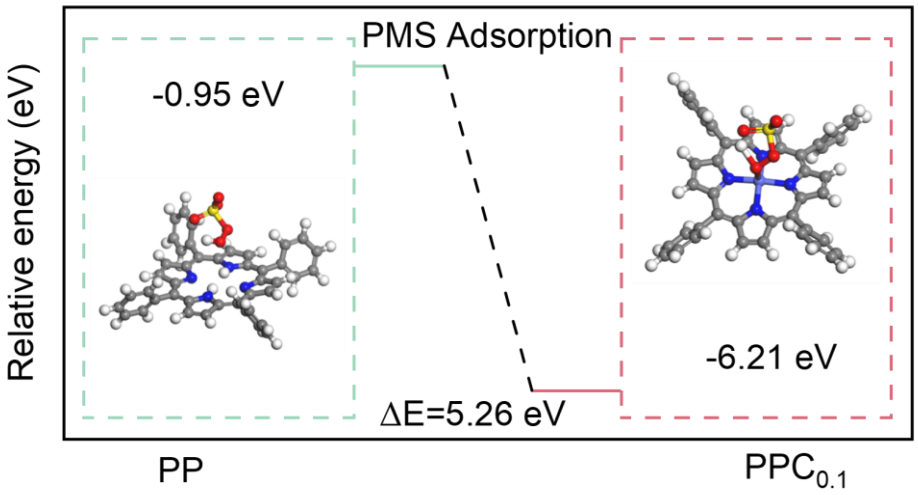

Fig. 3-32. The adsorption energy of PMS (HSO_5^-) on PP and $PPC_{0.1}$ sites.

DFT calculations were used to clarify the effects of Co site on adsorption of PMS. PP and PPC0.1 models were constructed. In contrast to the non-spontaneous adsorption of PMS on PP surface (E_{ads}= -0.95 eV**, Fig. 3-32**), PMS (-$HOOSO_3^-$) was chemically bound to the Co sites on $PPC_{0.1}$ spontaneously by one peroxyl oxygen in a terminal end-

on mode with a large negative adsorption energy (E_{ads}= -6.21 eV). The lower E_{ads} of PMS on $PPC_{0.1}$ is conducive to the adsorption of PMS onto the $PPC_{0.1}$, thus promoting the Co(IV)=O formation and RAN degradation.

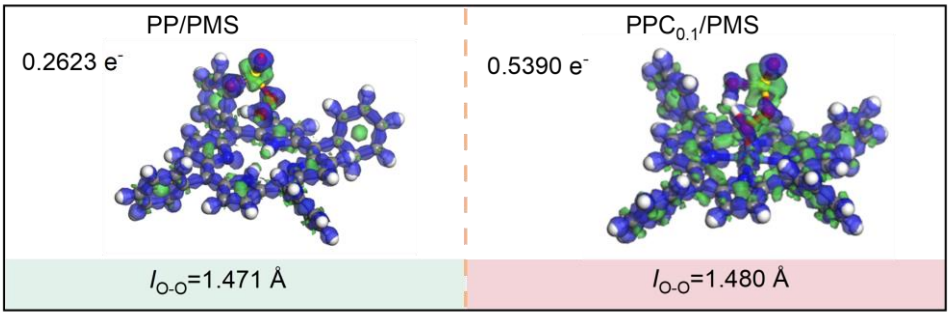

Fig. 3-33. Charge density differences of PMS absorbed on PP and $PPC_{0.1}$.

As show in **Fig. 3-33**, Due to the presence of the Co atom, the peroxide O-O bond of chemically adsorbed PMS was largely stretched (*I*O-O = 1.480 Å) in $PPC_{0.1}$/PMS systems compared to PP surface physically adsorbed PMS (*I*O-O= 1.471 Å), promoting the breakup of the O-O bond to generate the Co(IV)=O. In addition, the CoN4 configuration, a strong charge density could be observed in the adjacent regions between the PMS molecule and CoN4 while a small charge cloud appeared between PMS and the N4 sample. This significant electron transfer between PMS and the CoN4 site indicates that the unique isolated atomic Co sites can serve as conductive bridges to facilitate charge migration, further accelerate the rate of Co(IV)=O formation.

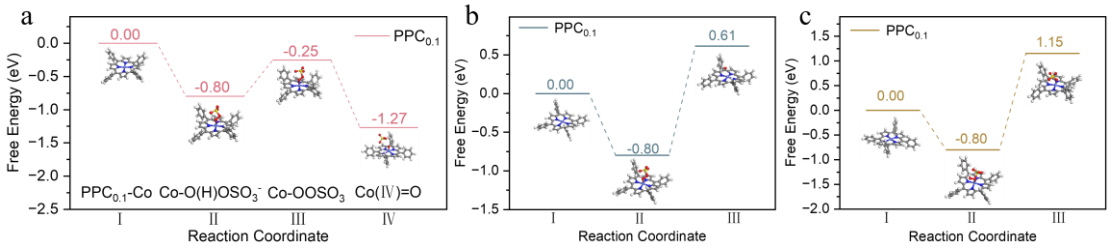

Fig. 3-34. Energy profiles of CoIV=O (c), $SO_4^{\cdot -}$ (d) and ·OH (e) species formation for $PPC_{0.1}$ by PMS activation.

DFT calculations further revealed the mechanism and related pathways of PMS

activation by the decorated atom Co sites centered in the porphyrin rings of $PPC_{0.1}$. **Fig. 3-34** were conducted to reveal the generation mechanism of Co(IV)=O, which involves two crucial stages, i.e., deprotonation and O-O bond cleavage.[46] First, PMS adsorbs Co sites to form Co-O(H)OSO_3^- (II), and then dissociates into Co-$OOSO_3$ (III) by deprotonation. Eventually, the O-O bond is broken to generate Co(IV)=O and $SO_4^{\cdot-}$ anions. The energy potential of $PPC_{0.1}$/PMS system is obviously favorable to produce Co(IV)=O (-1.27 eV), but infeasible to produce ·OH (+0.61 eV) and $SO_4^{\cdot-}$ (+1.15 eV). In this system, the Gibbs free energy for Co(IV)=O formation is negative, while it is positive for ·OH and $SO_4^{\cdot-}$ generation. Thus, PMS activation to produce Co(IV)=O is thermodynamically more favorable. The diminished energy barrier further proves the goodness of CoN4 structures in boosting Co(IV)=O formation during PMS activation. This means that the two-electron transfer pathway to generate Co(IV) is more thermodynamically favorable than that of one-electron transfer pathway to produce radical species during the $PPC_{0.1}$/PMS reaction, which is consistent with the proven non-radical pathway of the $PPC_{0.1}$/PMS system.

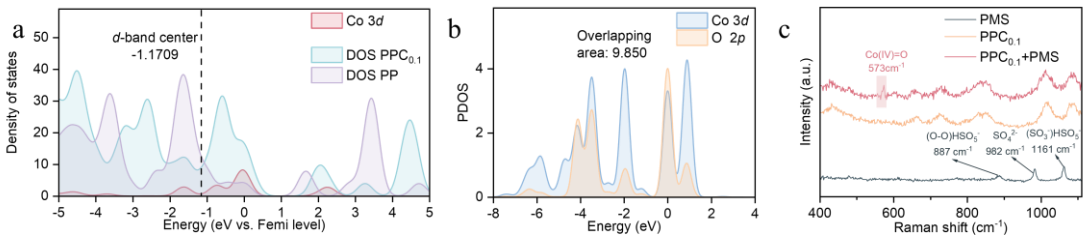

Fig. 3-35. (a) Density of states of pristine Co PP and $PPC_{0.1}$. (b) The PDOS of O 2*p* and Co 3*d* states on Co(IV)=O structure, and the integrated overlapping area is labeled in the top. (c) In situ Raman study (the red shade represents the signal of Co(IV)=O).

In the calculated density of electronic states (DOS), the optimized electron distribution of the Co atom at the CoN4 site yields a d-band center positioned in close proximity to the Fermi level, highlighting its enhanced electronic properties (**Fig. 3-35a**). Following the NewnsAnderson-Grimley theory, the more centralized d orbitals tend to split to create bonding and antibonding orbitals when interacting with the adsorbate under energy level matching to firmer adsorption.[93] Typically, A d-band

center proximity to the Fermi-level (E_F) typically indicates an enhanced propensity of the catalyst to donate charge to the adsorbate. Consequently, $PPC_{0.1}$ demonstrates superior electron transfer capabilities, thereby facilitating the formation of Co(IV)=O upon PMS adsorption. Besides, Co(IV)=O conspicuously exhibits an augmented overlap of the Co 3*d* and O 2*p* orbitals (**Fig. 3-35b**), leading to a more extensive electron delocalization over the Co(IV)=O configuration and a stronger binding ability of the Co for PMS.[94] The presence of Co(IV)=O was further confirmed by in situ Raman studies. The new peak at 571 cm^{-1} after the introduction of PMS could be attributed to the stretching vibration of the Co(IV)=O structure.(**Fig. 3-35c**)

Collectively, theoretical calculations indicate that $PPC_{0.1}$ with CoN4 coordination is exceptionally competitive in activating PMS to selectively generate Co(IV)=O. The extensive electron delocalization resulting from the CoN4 coordination enhances the adsorption and electron transfer between the catalyst and PMS, thereby promoting more efficient PMS activation. Furthermore, the optimized electron transfer structure facilitates deprotonation and O-O bond cleavage via an intramolecular proton transfer pathway, leading to the selective formation of Co(IV)=O.

3.3.3.3 Degradation Pathways and Toxicity Assessment of Intermediates

RAN molecules were analyzed using Gaussian 09 to obtain the frontier orbital characteristics and charge distribution patterns through DFT calculations.

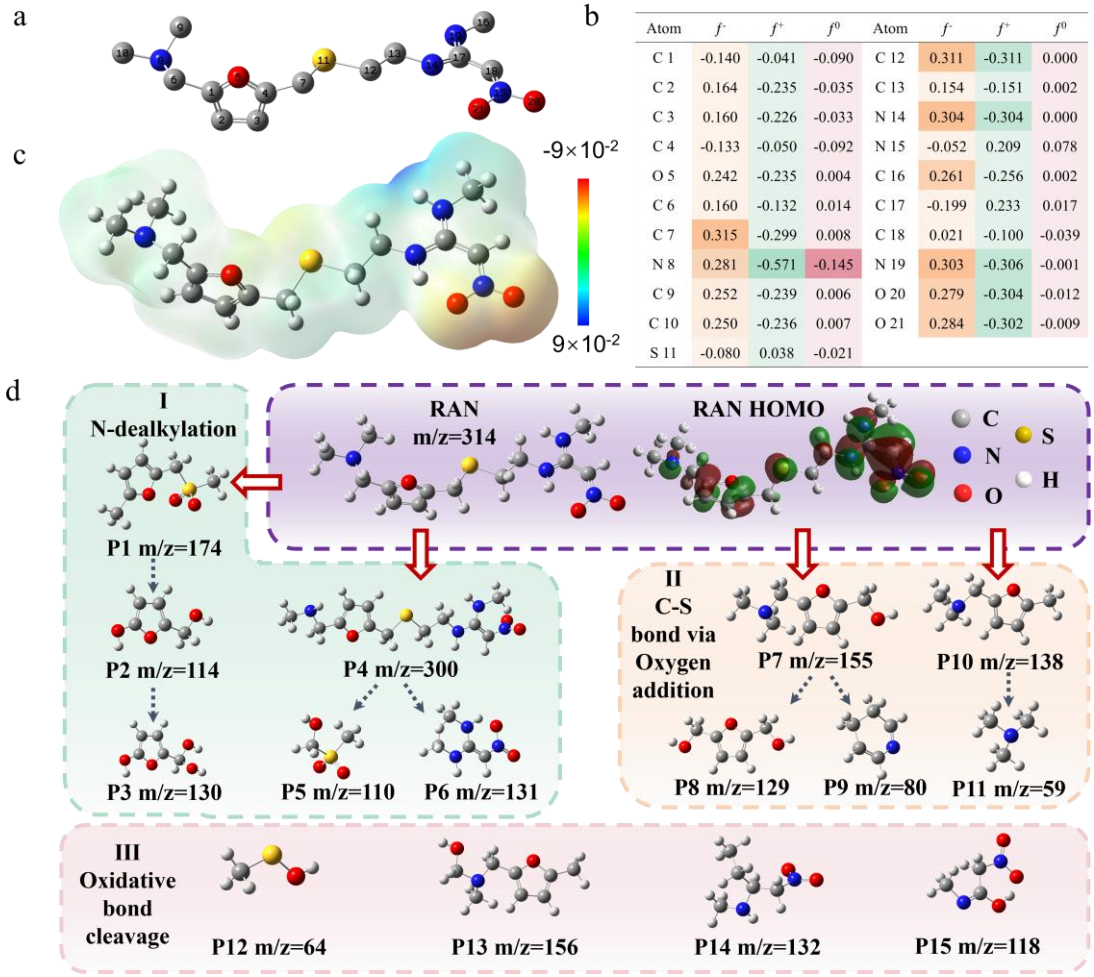

Atom	f^-	f^+	f^0	Atom	f^-	f^+	f^0
C 1	-0.140	-0.041	-0.090	C 12	0.311	-0.311	0.000
C 2	0.164	-0.235	-0.035	C 13	0.154	-0.151	0.002
C 3	0.160	-0.226	-0.033	N 14	0.304	-0.304	0.000
C 4	-0.133	-0.050	-0.092	N 15	-0.052	0.209	0.078
O 5	0.242	-0.235	0.004	C 16	0.261	-0.256	0.002
C 6	0.160	-0.132	0.014	C 17	-0.199	0.233	0.017
C 7	0.315	-0.299	0.008	C 18	0.021	-0.100	-0.039
N 8	0.281	-0.571	-0.145	N 19	0.303	-0.306	-0.001
C 9	0.252	-0.239	0.006	O 20	0.279	-0.304	-0.012
C 10	0.250	-0.236	0.007	O 21	0.284	-0.302	-0.009
S 11	-0.080	0.038	-0.021				

Fig. 3-36. (a) RAN structure; (b) RAN charge distributions and f. (c) Electrostatic potential distribution of RAN. (d) Proposed degradation pathways of RAN.

Data on the highest occupied molecular orbital (HOMO) and lowest unoccupied molecular orbital (LUMO) of ran were obtained. In this study, DFT calculations were conducted to determine the f value of RAN, which represents charge distribution and electrophilic attacks (**Fig. 3-36a**). Among all regions, 7C, 8N, 12C, 14N, 16C, 19N, 20O, and 21O with high f^- were regarded as the most likely regions for electrophilic attacks in RAN (**Fig. 3-36b**). According to the electrostatic potential distribution depicted in **Fig. 3-36c**, regions 12C, 14N, and 19N were vulnerable to electrophilic attacks. Further analyses were conducted to examine the degradation pathways of RAN in the $PPC_{0.1}$/PMS system (**Fig. 3-37d**). Highest occupied molecular orbital (HOMO) and lower unoccupied molecular orbital (LUMO) collectively referred to the frontier

molecular orbital (FMO), and the electrons that exist on the FMO are referred to as FMO-electrons.[62] The FMO was initially involved in the intermolecular chemical reaction, and the FMO-electrons played the most critical role. As a result, the highest electron distributions of the RAN molecule were principally located at its furan ring and nitrate group, and these electron-rich positions were preferentially attacked by the reactive oxygen species.[95] According to the degradation intermediates generated during RAN degradation, RAN degradation occurs via multiple reaction pathways. There are three possible degradation pathways. Pathways I (N-dealkylation): Ranitidine was first attacked to generate P1 and P4, which was then further degraded by N-dealkylation to form P2, P3, P5 and P6. Pathways II (C–S bond lysis): with rupture of the C–S bonds, to form P7 and P10, further react to form P8, P9, and P11. Pathways III (oxidative bond cleavage): oxidative bond cleavage generates various fragment ions (such as P12, P13, P14 and P15,) with smaller molecular weights. And finally, a portion is mineralized to CO_2, H_2O, and other small-molecule substances.

Some toxic products might have been formed in degradation system. The ecotoxicity of RAN and its products was evaluated by TEST and ECOSAR programs through the Quantitative Structure and Activity Relationship (QSAR) method.

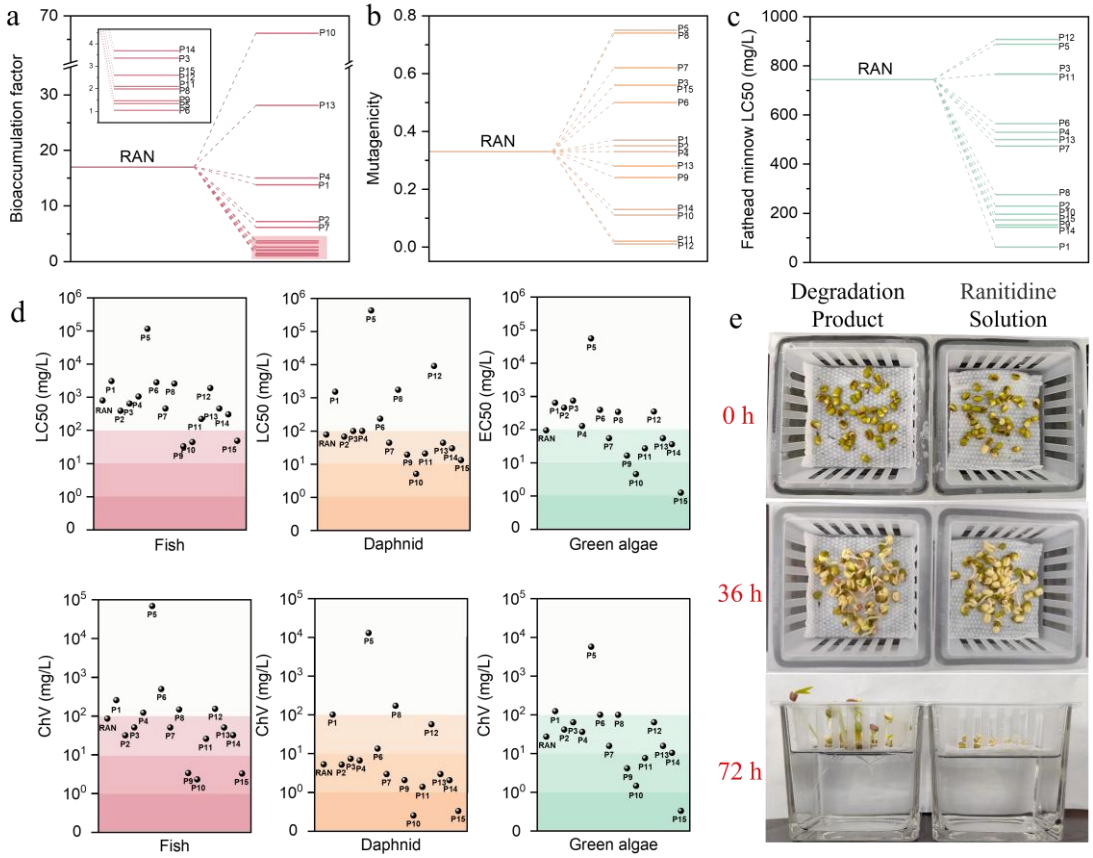

Fig. 3-37. (a)-(c) Toxicity calculated by TEST program. (d) The acute and chronic toxicity calculated by ECOSAR program. (e) Growth of mung bean sprouts cultured in PPC0.1 degraded RAN solution, and 10 mg/L RAN solution.

The bioticaccumulation factor, mutagenicity, and fathead minnow LC50 were evaluated based on the TEST program. As shown in **Fig. 3-37a**, most of these products had lower bioaccumulation factors than RAN. They were less easily enriched in organisms than RAN. **Fig. 3-37b** shows the mutagenicity results, half of these products had lower mutagenicity than RAN. In **Fig. 3-37c**, the LC50 values of some intermediates were higher than RAN, indicating that they were comparatively less toxic than parent RAN for fathead minnow.

Estimation of the bioaccumulation factor, mutagenicity and Fathead minnow LC50 for RAN and its transformation products using the TEST program.

Compound	Bioaccumulation factor	Mutagenicity		Fathead minnow LC50 (mg/L)
		value	result	
RAN	17	0.33	negative	744.41
P1	13.8	0.37	negative	62.55
P2	7.22	0.35	negative	228.94
P3	3.36	0.56	positive	766.79
P4	15	0.33	negative	530
P5	1.34	0.75	positive	887.67
P6	1.04	0.5	negative	565
P7	6.16	0.62	positive	473.73
P8	1.99	0.74	positive	276.35
P9	1.47	0.24	negative	152
P10	66.29	0.11	negative	195.76
P11	2.1	0.02	negative	765.78
P12	2.59	--	negative	907
P13	28.1	0.28	negative	499.22
P14	3.69	0.13	negative	143.48
P15	2.61	0.56	positive	173.62

Fig. 3-37d display the toxicity of intermediates for fish, daphnid, and green algae calculated by the ECOSAR program. The LC50 and EC50 values for most of the byproducts were generally higher than those of RAN. The intermediates showed a similar toxicity order in the aspects of acute and chronic toxicities. However, the intermediates (such as P9, P10, and P15) had stronger toxicities than RAN. Different products had respective toxicity, but they could eventually be adequately mineralized. Therefore, the $PPC_{0.1}$/PMS system is advisable for degrading the organics to decrease the ecotoxicity. It is meaningful for environmental and ecological assessment.

Estimation of acute and chronic toxicity of RAN and its transformation products to fish,

daphnid, and green algae using the ECOSAR program.

Compound	Acute toxicity (mg/L)			Chronic toxicity (Chv) (mg/L)		
	Fish (LC_{50})	Daphnid (LC_{50})	Green Algae (EC_{50})	Fish	Daphnid	Green algae
RAN	798	78	95	85	5.28	27.4
P1	3060	1520	641	254	101	124
P2	390	67.4	456	31.4	5.17	41.6
P3	642	99.9	745	50.5	7.36	64.2
P4	1050	100	128	121	6.62	36.3
P5	115000	429000	55800	68400	12900	5710
P6	2800	233	393	492	13.4	100
P7	4555	44	54.9	50.1	2.95	15.7
P8	2570	1740	342	146	171	99.7
P9	33.1	19.4	16.4	3.35	2.06	4.16
P10	44.5	5.1	4.55	2.29	0.403	1.47
P11	221	20.9	27.1	25.7	1.38	7.64
P12	1880	9099	350	152	56.8	64.2
P13	455	44	54.9	50.1	2.95	15.7
P14	304	30	36.1	31.7	2.05	10.4
P15	48.5	13.2	1.25	3.25	0.52	0.52

Notes: LC_{50}: Median Lethal Concentration. A statistically derived concentration of a substance that can be expected to cause death in 50% of test animals. It is usually expressed as milligrams (mg) of substance per liter (L) water. EC_{50}: Median Effect Concentration. A statistically derived concentration of a substance that can be expected to cause a specific effect (e.g., growth inhibition) in 50% of test animals. It is usually expressed as milligrams (mg) of substance per liter (L) water.

ChV, Chronic Value, represents chronic toxicity. ChV is defined as the geometric mean of the no observed effect concentration and the lowest observed effect concentration.

To evaluate the effectiveness of PPC/PMS in degrading RAN and lessening its biotoxic effects, we conducted a visual inspection of mung bean sprouts grown in various treated solutions over three days.[96] **Fig. 3-37e** depict the thriving and healthy emergence of sprouts in $PPC_{0.1}$/PMS-treated solutions. Conversely, sprouts in a 10 mg/L RAN solution displayed stunted growth and severe undernourishment. These observations indicate that the $PPC_{0.1}$/PMS treatment considerably reduces the toxic effects of RAN, facilitating healthy growth in most sprouts. Furthermore, this confirms $PPC_{0.1}$/PMS potent ability to degrade RAN, effectively lowering its biotoxicity in these environments.

3.3.4 Potential superiority in environmental applications

To evaluate the potential applications of PPC, its reproducibility, stability, and adaptability to real-world water environments, both domestically and internationally, were assessed.

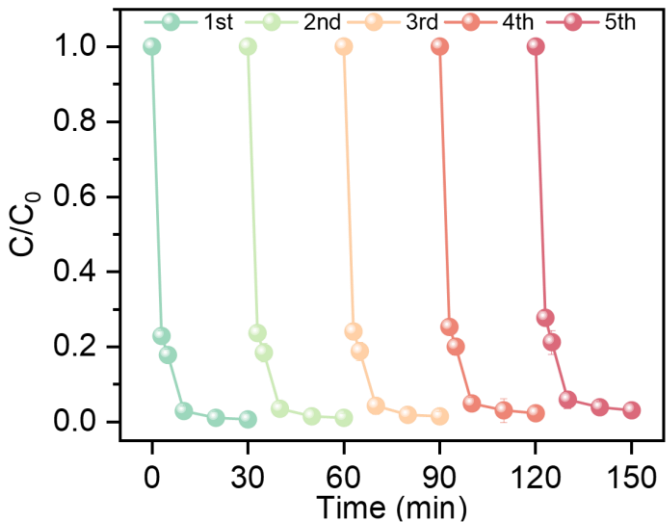

Fig. 3-38. Cycling test of $PPC_{0.1}$ for the RAN degradation in $PPC_{0.1}$/PMS.

Fig. 3-38 shows that the removal efficiency can still remain at 97.97 % after five successive degradation cycles, indicating that $PPC_{0.1}$ has good reusability and stability.

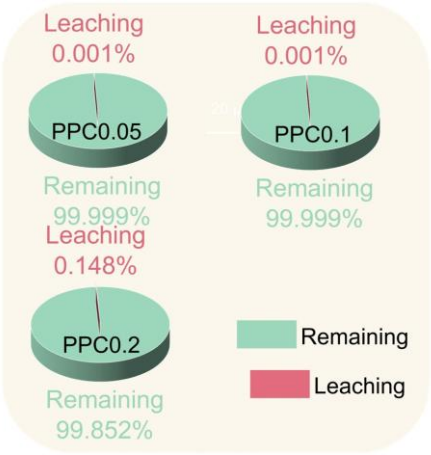

Fig. 3-38. The percentage of leached Co in $PPC_{0.05}$, $PPC_{0.1}$ and $PPC_{0.2}$ determined by ICP after reaction in 30 min.

Furthermore, ICP was used to understand whether the catalyst will cause serious metal pollution during use process. The **Fig. 3-38** shows that the leaching concentration of Co from PPC was 0.0034 mg/L. The results suggest that the $PPC_{0.1}$ possesses the advantages of being more stable and environmentally friendly, which will lead to good performance in practical application.

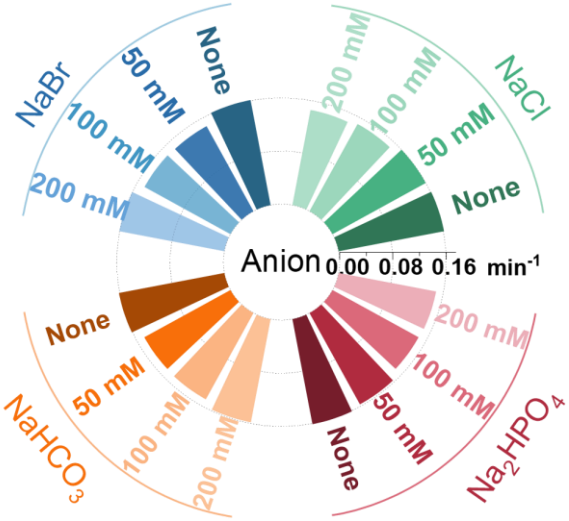

Fig. 3-39. Influences of the degradation of coexisting inorganic ions in $PPC_{0.1}$/PMS system.

Various ions were involved in the actual aqueous matrices. As depicted in **Fig. 3-**

39, Cl^-, Br^-, HCO_3^-, and HPO_4^{2-} exhibited little effects on the RAN removal, indicating that $PPC_{0.1}$ could greatly resist the disturbance of nontarget background substances.

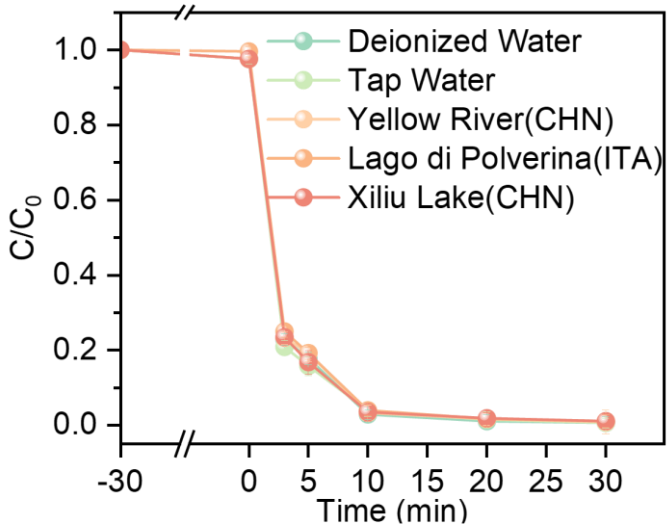

Fig. 3-40. Different water sources in $PPC_{0.1}$/PMS system.

Moreover, the **Fig. 3-40** shows that nearly 100% of RAN was removed within 30 min across different water samples, including deionized water, tap water, water from the Yellow River (China), a natural lake (Italy), and Xiliu Lake (Henan). This demonstrates the system's potential applicability in real-world water environments.

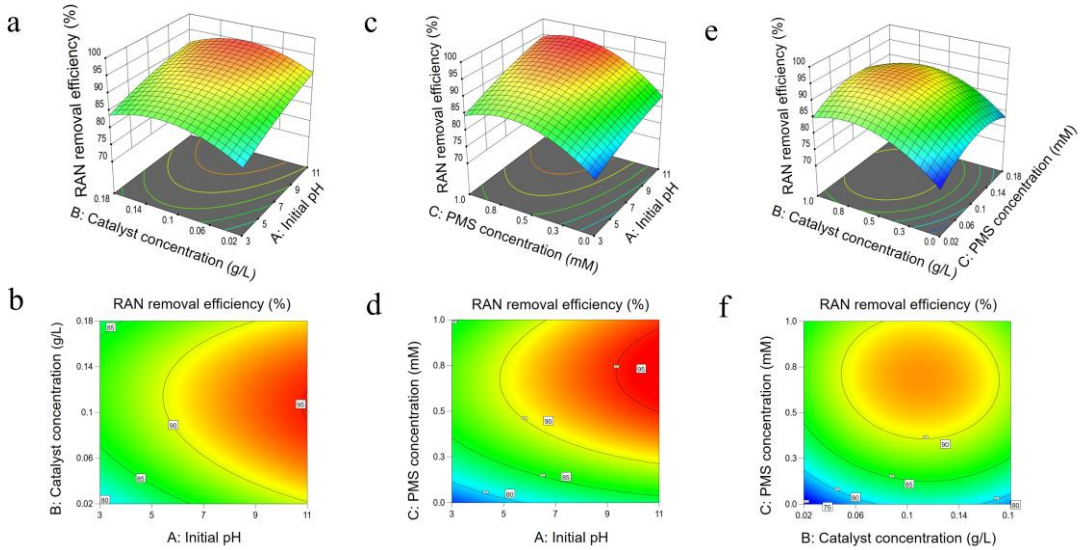

Fig. 3-41. 2D contour and 3D surface to evaluate the effects of (a, b) initial pH and catalyst

concentration; (c, d) initial pH and PMS concentration; (e, f) catalyst concentration and PMS concentration.

A central composite design was used in Design-Expert v.13 software to optimize the reaction parameters for the real-world wastewater scenario (**Fig. 3-41**).[97] The following reaction conditions were simulated: initial pH of 3–11, $PPC_{0.1}$ concentration of 0.06–0.18 g/L and PMS concentration of 0.06–0.14 mM. Consequently, the removal efficiency of RAN exceeded 85 %. Overall, these findings can be used as a reference in the design of $PPC_{0.1}$/PMS processes for sewage remediation.

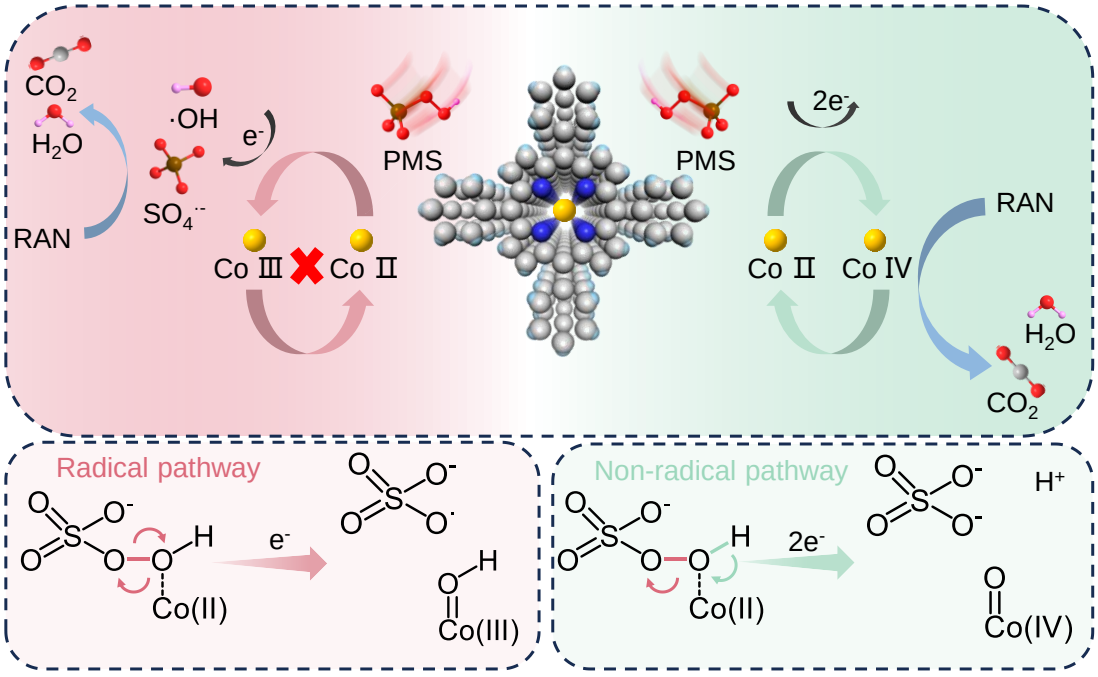

Fig. 3-42. Schematic representation of the pathways for RAN degradation and the proposed PMS activation mechanism.

The presence of a layered porous structure increases active sites on the catalyst, thereby significantly enhancing its catalytic activity for the oxidation of wastewater pollutants. Moreover, the unique electronic transfer effect induced by the CoN4 structure efficiently generates Co(IV)=O, further promoting the oxidation of RAN(**Fig. 3-42**). Compared with traditional free radicals, Co(IV)=O is more resistant and more selective for pollutants. Therefore, in this study, $PPC_{0.1}$ exhibited excellent selectivity

and stability. The turnover frequency (TOF) of RAN degradation catalyzed by $PPC_{0.1}$ was 0.0128 s^{-1},

The equation for the TOF:

$$TOF = \frac{n_{RAN,degradation}}{n_{Co} \times t}, S^{-1} \quad (3\text{-}5)$$

Where $n_{RAN,degradation}$ and n_{Co} represent the amount of substance of degraded RAN and cobalt atom in the catalyst, t is the reaction time (s).

This thus demonstrates that the $PPC_{0.1}$ catalyst could enable the efficient utilization of Co atoms. We conducted an economic analysis to determine the feasibility of the $PPC_{0.1}$/PMS system for actual use in electrical energy per order (EE/O) scenarios.

The electrical energy per order (EE/O) has been used as a popular approach for evaluating the energy and cost of reaction system. It is defined as electrical required to reduce the content of a specific pollutant by one order of magnitude. This method often involves consumed electrical energy and chemicals, where the catalyst is usually assumed to be reusable so it is not considered a consumable in the system. Herein, the economic evaluation of the optimal $PPC_{0.1}$/PMS system was performed based on the EE/O_{total} using the following Equations **(3-6), (3-7)**, and **(3-8)**. Due to the lack of input of external energy such as light and ultrasonic energy in the $PPC_{0.1}$/PMS system, the external energy input was zero. Therefore, the value of EE/O_{total} would be converted from PMS/O. According to the literature, the non-house electrical energy cost and PMS were estimated to be 0.1319 $/kWh and 1.30 $/kg. Thus, the electrical energy cost of PMS was calculated as 9.85 kWh/kg. Then, based on the results of the **Fig. 3-10**, 99% of RAN was removed and 70% of PMS was consumed within 30 min. The calculated EE/O_{total} value of the $PPC_{0.1}$/PMS system was 0.001 kWh/m3, and the corresponding cost was 0.0001 $/$m^3$. The cost was almost lower than that of advanced oxidation processes (AOPs) in previously reported literature. Based on the analysis, our $PPC_{0.1}$/PMS system presented a much more promising application potential in terms of cost and environmental friendliness.

$$EE/O_{Total} = EE/O_{Energy} + EE/O_{Chemicals} = EE/O_{Chemicals} \quad (3\text{-}6)$$

$$EE/O_{Chemicals} = PMS/O = \frac{[PMS]_0 - [PMS]_f}{log\left(\frac{C_i}{C_f}\right)}(mg/L) \quad (3\text{-}7)$$

$$In\left(\frac{C_i}{C_f}\right) = k \times t \quad (3\text{-}8)$$

Where $[PMS]_0$ and $[PMS]_f$ are the concentration (mg/L) of PMS at the reaction time of 0 and t (min), respectively. t is reaction time (min), C_i is the initial concentration of RAN and C_f is the concentration of RAN after reaction time of t mins with the unit of mg/L, respectively.

According to our calculations, the $PPC_{0.1}$/PMS system had an EE/O_{total} value of 0.001 kWh/m^3, with a corresponding cost of \$0.0001/m^3. This cost is lower than that of AOPs reported in other studies. Taken together, our findings can be used as a reference for establishing highly efficient and economical Fenton-like systems by regulating CoN4 coordination.

3.4 Conclusion

In this study, cobalt porphyrin-based porous organic polymers (PPC) were successfully synthesized and employed as an efficient catalyst for peroxymonosulfate (PMS) activation, achieving selective degradation of organic pollutants, particularly ranitidine (RAN). The well-defined Co-N_4 coordination structure facilitated efficient electron transfer, leading to nearly 100% conversion of Co(II) to Co(IV)=O, which was identified as the dominant reactive species. Mechanistic investigations, including radical quenching experiments, electron paramagnetic resonance (EPR) spectroscopy, and density functional theory (DFT) calculations, confirmed that the degradation process primarily followed a non-radical oxidation pathway. Additionally, the system demonstrated excellent stability, recyclability, and negligible metal leaching, making it

a promising catalyst for sustainable water treatment. This study not only enhances the understanding of PMS activation mechanisms but also provides a novel strategy for designing high-performance catalysts for the removal of emerging organic pollutants in wastewater treatment applications.

4. The Preparation of Iron Porphyrin-Based Porous Organic Polymers and the Activation of Peroxymonosulfate for the Degradation of Tetracycline.

Abstract:

The increasing prevalence of antibiotic contamination in aquatic environments poses significant ecological and health risks. Among various antibiotics, tetracycline (TC) is widely used in both human and veterinary medicine, leading to its persistent accumulation in water bodies due to its high stability and resistance to biodegradation. In this study, an iron-porphyrin-based porous organic polymer (Fe-P/POP) was synthesized and employed as an efficient catalyst for peroxymonosulfate (PMS) activation to degrade TC. The Fe-P/POP system exhibited excellent catalytic activity, achieving nearly 100% TC removal within 30 minutes. Comprehensive characterization confirmed the successful incorporation of Fe into the porphyrin framework, providing abundant Fe-N_4 active sites for PMS activation. Mechanistic investigations, including quenching experiments, electron paramagnetic resonance (EPR) spectroscopy, and density functional theory (DFT) calculations, demonstrated that high-valent Fe(IV)=O species were the primary reactive species responsible for TC degradation, following a non-radical oxidation pathway. Further studies revealed that Fe-P/POP maintained high catalytic efficiency across a wide pH range, exhibited excellent stability, and demonstrated strong resistance to interference from coexisting ions in real water samples. This study not only provides fundamental insights into the catalytic mechanism of Fe-P/POP in PMS activation but also highlights its potential as a sustainable and cost-effective approach for antibiotic degradation in wastewater treatment.

Keywords: Fe-P/POP; PMS; HVMO; TC.

4.1 Introduction

With the development of industrialization and urbanization, the widespread use and abuse of antibiotics have increasingly attracted attention due to their potential severe threats to water environments, agriculture, human health, and livestock. Among various antibiotics, tetracycline (TC) is extensively used in both animal and human medicine worldwide, commonly in clinical treatments and livestock farming, resulting in its discharge into natural water bodies through pharmaceutical and aquaculture wastewater.[98-101] The high ecological toxicity of TC and its derivatives poses a significant risk to both the ecological environment and human health.[102-104] It is resistant to biodegradation and tends to accumulate in the environment.[105-107] Therefore, the development of a convenient and efficient method for the removal of antibiotics has become an urgent necessity.

Advanced Oxidation Processes (AOPs) are particularly attractive for the degradation of refractory organic pollutants, as they involve the generation of highly reactive oxygen species (ROS) from various peroxides, such as free radicals or high-valent metals. These ROS can effectively mineralize organic pollutants into carbon dioxide and water. Hydrogen peroxide (H_2O_2), ozone (O_3), peroxydisulfate (PDS), and peroxymonosulfate (PMS) are commonly used oxidants in AOP processes. Compared to H_2O_2 and O_3, PMS and PDS are more stable, easier to transport, and store. In particular, the asymmetric structure of PMS makes it more readily activated by various catalysts. Metal-based catalysts are effective in activating PMS, with transition metal-based materials being widely used as PMS activators due to their variable metal oxidation states. Iron-based activators have gained increasing popularity due to their environmental benefits and excellent activation efficiency. High-valent Fe(IV) is a key ROS commonly found in biological enzymes and has been widely studied in Fenton-like reactions in recent years. Unlike the ROS commonly found in natural water systems, Fe(IV)=O is an interfacial ROS, whose properties are largely dependent on its coordination environment. Therefore, the coordination regulation of Fe(IV)=O holds

promise for enhancing its oxidative capacity and manipulating oxidation pathways.

Based on the above experiments, Fe was loaded onto a porphyrin framework, successfully preparing an iron porphyrin-based porous organic polymer. The properties of the iron porphyrin porous organic polymer were summarized through characterization analysis, and its activation performance was examined by activating PMS for the degradation of tetracycline (TC). The influence of different catalytic conditions on TC degradation was evaluated, providing new insights for the future development of novel, multifunctional, and stable iron-based catalysts.

4.2 Experiments and Methods

4.2.1 Catalyst Preparation

Synthesis of Porphyrin-Porous Organic Polymer (P/POP)

Tetraphenylporphyrin (0.96 g, 0.2 mmol) and aluminum chloride (4 g, 3.2 mmol) were added to a two-necked flask at room temperature. Under a nitrogen atmosphere, trichloromethane (8 mL) was introduced into the flask. The mixture was refluxed and stirred at 30°C for 8 h, at 40°C for 12 h, and at 58°C for 28 h. After the reaction, the dark precipitate was washed with hydrochloric acid-water (v/v=2:1, 40 mL), distilled water, and ethanol. The solid was then purified by Soxhlet extraction with methanol for 24 h. Finally, it was dried in a vacuum oven at 60°C for 24 h to yield a black polymer powder designated as P/POP.

Synthesis of Porphyrin-Porous Organic Polymer-Fe (Fe-P\POP)

Por-POP (1 g) and iron (II) acetate tetrahydrate ($C_4H_6FeO_4 \cdot 4H_2O$, 0.1 g) were added to an acetonitrile solution (30 mL). The mixture was stirred at 82°C for 24 h. After the reaction, the solid was obtained by centrifugation and washed three times with methanol, followed by Soxhlet extraction with methanol for 24 h. Finally, the product was dried in a vacuum oven at 60°C for 24 h to yield a black solid powder designated

as Fe-P\POP.

4.2.2 Characterization of Fe-P\POP

4.2.2.1 High-Resolution Field Emission Scanning Electron Microscopy (SEM)

The SEM analysis method for PPC is detailed in Chapter 2 – 2.2.2.1.

4.2.2.2 X-ray Photoelectron Spectroscopy (XPS)

The XPS analysis method for Fe-P\POP is detailed in Chapter 2 – 2.2.2.2.

4.2.2.3 X-ray Diffraction (XRD)

The XRD analysis method for Fe-P\POP is detailed in Chapter 2 – 2.2.2.3.

4.2.2.4 Fourier Transform Infrared Spectroscopy (FT-IR)

The FT-IR analysis method for Fe-P\POP is detailed in Chapter 2 – 2.2.2.4.

4.2.3 Performance Analysis of Fe-P\POP

4.2.3.1 TC Degradation Experiments and Analysis Methods

The methods for TC degradation experiments and detection are detailed in Chapter 2 – 2.2.3.1.

4.2.3.2 Effects of Water Quality on Fe-P\POP Performance

The experimental method for studying the effects of water quality on Fe-P\POP performance is detailed in Chapter 2 – 2.2.3.2.

4.2.3.3 Recycling Experiments

The experimental method for TC recycling experiments is detailed in Chapter 2 – 2.2.3.3.

4.2.3.4 Determination of Metal Ion Concentrations in the Reaction System

The method for detecting metal ion concentrations in the reaction system is detailed in Chapter 2 – 2.2.3.4.

4.2.4 Mechanistic Analysis of TC Degradation by Fe-P\POP

4.2.4.1 Radical Quenching Experiments

The method for radical quenching experiments is detailed in Chapter 2 – 2.2.4.1.

4.2.4.2 Detection of Degradation Reaction Intermediates

The method for detecting intermediate products formed during TC degradation is detailed in Chapter 2 – 2.2.4.4.

4.3 Results and Discussion

4.3.1 Characterization Analysis of Fe-P\POP

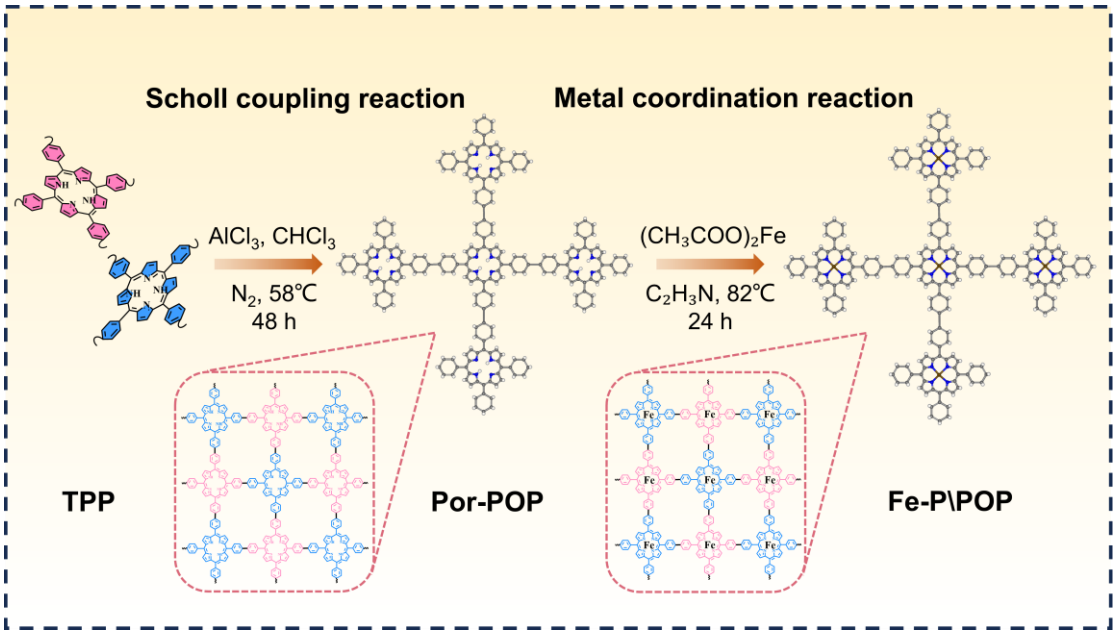

Fig. 4-1. Schematic illustration of the preparation procedures of the Fe-P\PPC samples.

Fig. 4-1 shows the preparation process of Fe-Porphyrin-Porous Organic Polymer

(Fe-P\PPC). The tetraphenylporphyrin was applied as the building block to construct PP with extensively conjugated microporous networks via Friedel-Crafts alkylation coupling reaction catalyzed by $AlCl_3$ under nitrogen protection. The hydrogen atoms on the aromatic rings of porphyrin were substituted with alkyl groups, the pyrrolic N atoms in porphyrin do not participate in the coupling reaction. Therefore, after the coupling reaction. Pyrrolic N atoms are still theoretically reserved in the frameworks of porphyrin and could be used as coordination sites for metallization. Since Fe(II) is an active metal for activating PMS, P\PPC can be metallized with Fe(II) in acetonitrile, yielding Fe-P\PPC.

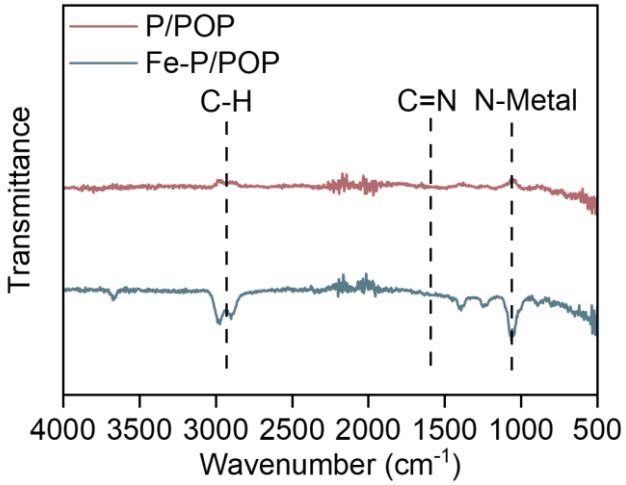

Fig. 4-2. FT-IR spectra of P\PPC and Fe-P\PPC.

Fig. 4-2 presents the FT-IR spectra of P\PPC and Fe-P\PPC. The distinct adsorption peaks in the region from 1655 to 1570 cm^{-1} for both P\PPC and Fe-P\PPC are attributed to the C=N and C=C stretching vibrations of the porphyrin macrocycle and the benzene ring. The C-H stretching vibration peaks of methylene are clearly observed near 2900-3080 cm^{-1}, indicating the presence of methylene linkers in both P\PPC and Fe-P\PPC, thereby confirming the successful incorporation of porphyrin units into the polymer framework. The N-H stretching vibration in pyrrole at 3308 cm^{-1} disappears, while the characteristic N-Fe in-plane bending at 1007 cm^{-1} appears in the FT-IR spectrum of Fe-P\PPC, suggesting the successful coordination of iron.

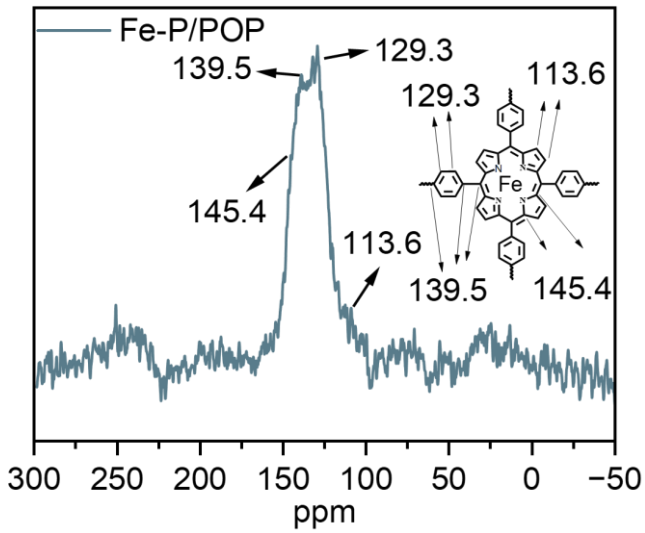

Fig. 4-3. Solid-state ^{13}C NMR spectrum of Fe-P\PPC.

The structural details of Fe-P\PPC were determined by solid-state ^{13}C NMR spectroscopy. As shown in **Fig. 4-3**, the resonance peaks at approximately 129.3 and 139.5 ppm are attributed to the phenylene linkages, while those at approximately 113.6 and 145.4 ppm correspond to the porphyrin macrocycles. These results preliminarily confirm that the porphyrin units have been successfully integrated into the polymeric network.

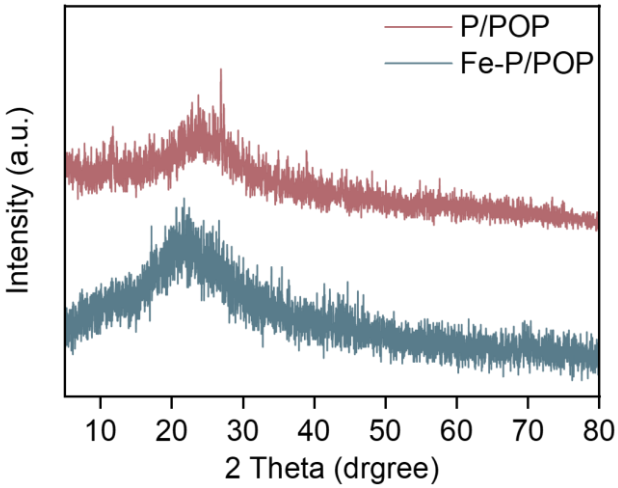

Fig. 4-4. XRD profiles of catalysts.

The XRD patterns of P\PPC and Fe-P\PPC are shown in **Fig. 4-4**. No characteristic

peaks were observed, which can be attributed to the low crystallinity resulting from disordered stacking. The broadening of the peak at 22.1° may be due to turbulence between the P\PPC and Fe-P\PPC polymers or structural defects within the system, leading to some degree of disorder in the pore distribution, thereby indicating its amorphous nature. The absence of diffraction peaks corresponding to metallic Fe nanoparticles or Fe oxides rules out the formation and presence of these impurities in Fe-P\PPC.

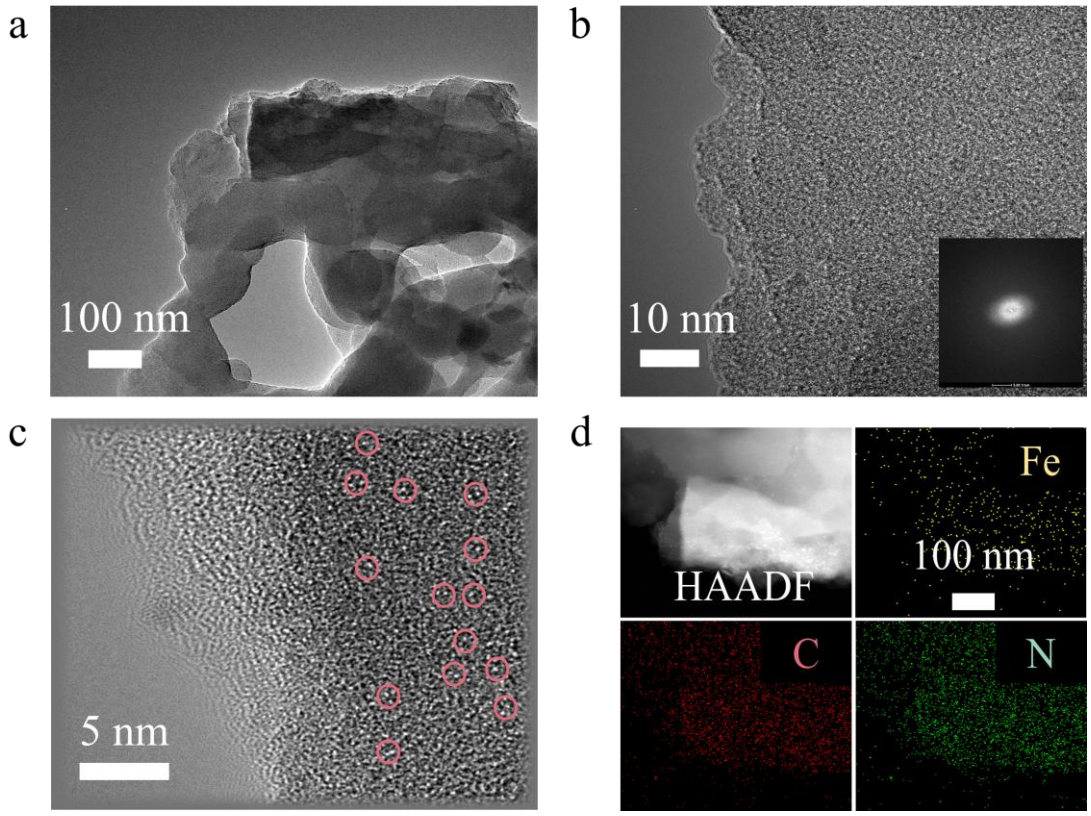

Fig. 4-5. (a) and (b) TEM image of Fe-P/PPC (inset: SAED pattern). (c) AC HAADF-STEM image of Fe-P/PPC, the isolated bright dots marked with red circles are cobalt atoms. (d) HAADF-STEM image with the corresponding EDS elemental mapping.

In **Fig. 4-5 (a** and **b)**, the TEM image confirms that the as-prepared Fe-P/PPC possesses a homogeneous two-dimensional lamellar structure without the presence of nanoparticles, while the SAED pattern verifies its amorphous nature, consistent with the XRD results. The aberration-corrected HAADF-STEM image (**Fig. 4-5c**) reveals a

number of isolated bright spots, which correspond to the uniformly dispersed individual Fe atoms, with no Fe particles observed on Fe-P/PPC. Additionally, the EDS mapping images (**Fig. 4-5d**) demonstrate the existence and uniform distribution of Fe, N, and C elements. Overall, these results suggest that Fe is atomically dispersed on Fe-P/PPC.

4.3.2 Catalytic performance

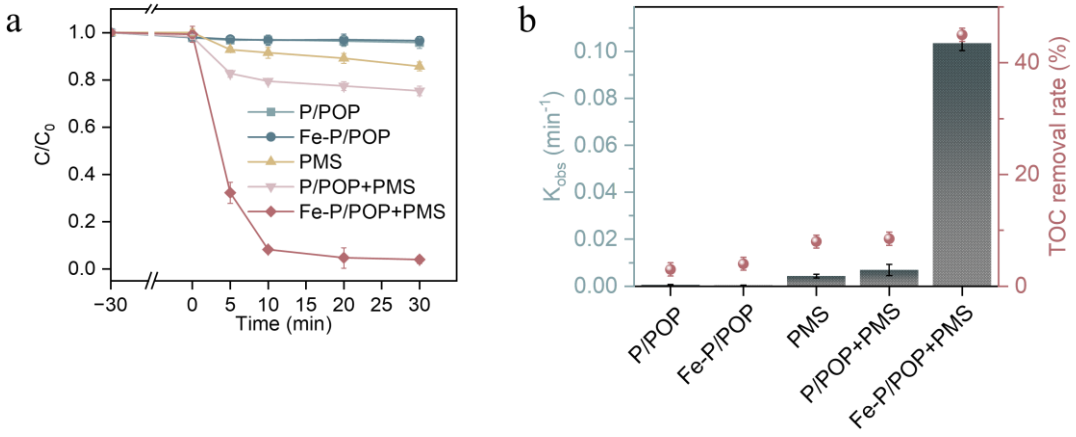

Fig. 4-6. (a) The corresponding pseudo-first-order kinetic constants and TOC removal efficiency of TC in several systems. (b) and (c) TC removal efficiency and reaction kinetics in different catalyst/PMS systems.

The degradation of tetracycline (TC) was used as a metric to assess the catalyst performance. The catalytic performance of Fe-P/POP and control samples in TC degradation was investigated **Fig. 4-6 (a-c)**. Remarkably, the Fe-P/POP/PMS system achieved a 100% degradation efficiency and a 45.07% mineralization rate within 30 minutes. In contrast, the P/POP system attained a TC degradation efficiency of 24.69% and a mineralization rate of 8.52% within the same time frame in the presence of PMS. The significantly enhanced degradation rate of Fe-P/POP compared to P/POP suggests that the introduction of atomic Fe provided additional active sites, thereby improving catalytic performance.

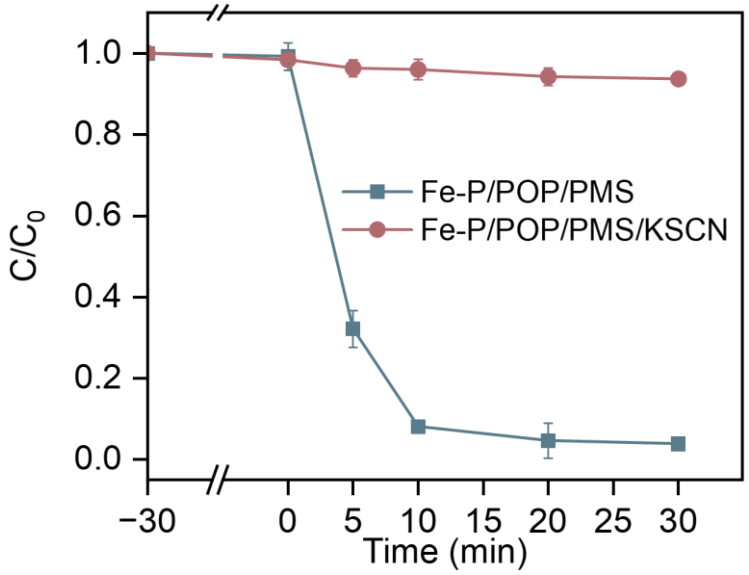

Fig. 4-7. Performance of Fe-P/POP /PMS to degrade TC with or without KSCN.

When the reaction system contained 10 mM KSCN, the TC degradation process was nearly blocked (**Fig. 4-7**). This result suggests that the active site responsible for catalyzing TC degradation in Fe-P/POP is the Fe atom center. The introduced SCN^- ions can bind to the Fe in FeN_4, thereby poisoning the catalytic site. The KSCN poisoning experiment further indicates that atomic Fe plays a crucial role in the activation of PMS by Fe-P/POP.

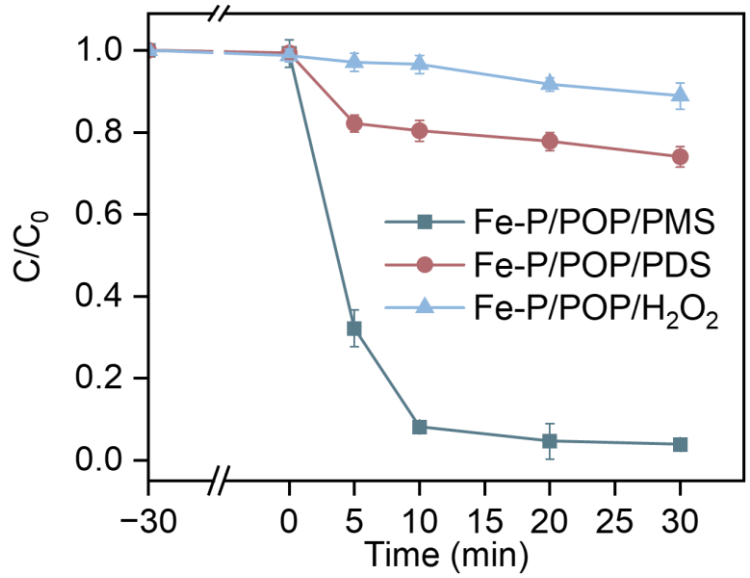

Fig. 4-8. The comparison of TC degradation efficiency by different oxidants in Fe-P/POP /PMS system.

To further evaluate the activation efficiency of Fe-P/POP with different oxidants, $Na_2S_2O_8$ (PDS) and H_2O_2 were introduced into the TC solution for comparison. As shown in **Fig. 4-8**, in the presence of PMS, the TC degradation rate reached 100% within 30 minutes, significantly outperforming those achieved with PDS (26%) and H_2O_2 (11%). The symmetric structure of PDS contributes to its greater stability and steric hindrance compared to PMS, while the high bond energy of the O–O bond in H_2O_2 hinders its cleavage. These factors likely restrict the catalytic activation of PDS and H_2O_2. Therefore, PMS was selected as the oxidant for this experiment. Furthermore, the effects of cobalt loading, PMS dosage, TC concentration, and catalyst dosage on TC degradation in the Fe-P/POP/PMS system were systematically investigated, as the production of active species and TC degradation are highly dependent on these factors.

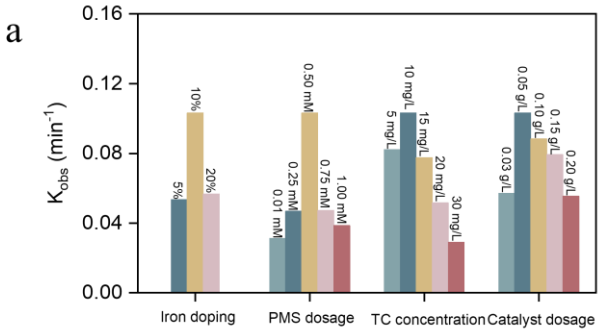
a
0.16
0.12
0.08
0.04
0.00
K_{obs} (min^{-1})
5%
10%
20%
0.01 mM
0.25 mM
0.50 mM
0.75 mM
1.00 mM
5 mg/L
10 mg/L
15 mg/L
20 mg/L
30 mg/L
0.03 g/L
0.05 g/L
0.10 g/L
0.15 g/L
0.20 g/L
Iron doping
PMS dosage
TC concentration
Catalyst dosage

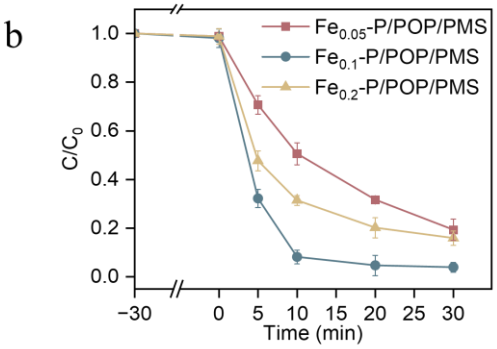
b
$Fe_{0.05}$-P/POP/PMS
$Fe_{0.1}$-P/POP/PMS
$Fe_{0.2}$-P/POP/PMS
C/C_0
Time (min)

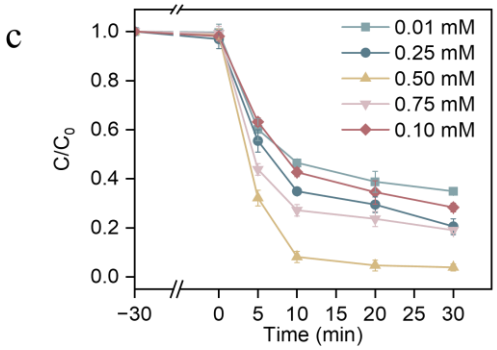
c
0.01 mM
0.25 mM
0.50 mM
0.75 mM
0.10 mM
C/C_0
Time (min)

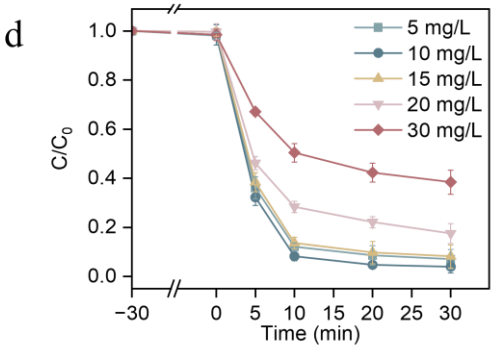
d
5 mg/L
10 mg/L
15 mg/L
20 mg/L
30 mg/L
C/C_0
Time (min)

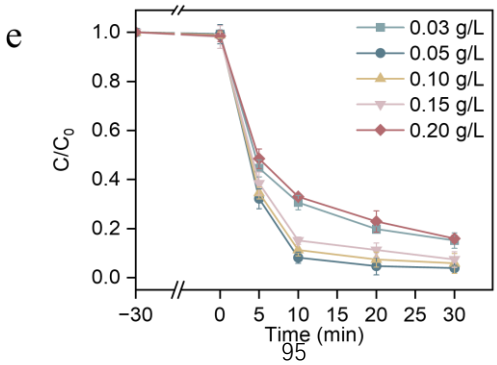
e
0.03 g/L
0.05 g/L
0.10 g/L
0.15 g/L
0.20 g/L
C/C_0
Time (min)

Fig. 4-9. (a) The corresponding rate constants *k* under various conditions. (b) Effects of iron load, (c) Effects of PMS concentration, (d) Effects of TC concentration, (e) Effects of catalyst content on the TC degradation in Fe-P/POP /PMS system.

The influence of iron doping, PMS dosage, TC concentration, catalyst dosage, and initial pH on TC degradation in the Fe-P/POP/PMS system was systematically investigated, as these factors significantly affect the production of active species and the efficiency of TC degradation. For a quantitative comparison, the apparent rate constant (k) for catalytic degradation was determined using a first-order kinetic model [$\ln(C/C_0) = -kt$].

As shown in **Fig. 4-9a and b**, optimization experiments for Fe doping indicated that increased Fe content improved the catalytic oxidation of TC. The catalyst with 10 wt% Fe exhibited the best performance for TC removal, while excessive Fe doping led to clustering, which reduced catalytic performance.

The concentration of PMS, as a critical factor in generating radical and non-radical oxidative species, was varied from 0.01 mM to 1 mM. **Fig. 4-9c** demonstrates the effect of different PMS dosages (0.01, 0.25, 0.5, 0.75, and 1 mM) on TC degradation. At a low concentration of PMS (0.01 mM), insufficient Fe(IV)=O was generated, leading to incomplete TC degradation. Increasing the PMS concentration from 0.25 to 0.5 mM significantly accelerated TC degradation, with the rate constant k rising from 0.0469 min^{-1} to 0.1031 min^{-1}. However, further increases in PMS concentration to 0.75 and 1 mM did not enhance TC degradation, likely because excessive PMS altered the solution pH, reducing catalytic efficiency.

Fig. 4-9d shows that as the TC concentration increased from 5 mg/L to 30 mg/L, the degradation rates of TC decreased. This trend may be attributed to the competition between parent contaminants and by-products for the free radicals and non-radicals generated by the Fe-P/POP/PMS system. The accumulation of by-products likely hindered the efficiency of catalytic oxidation.

Fig. 4-9e illustrates the variation in TC degradation efficiency and the rate constant

k with increasing Fe-P/POP dosage under fixed conditions of PMS (0.5 mM) and TC (10 mg/L). TC removal efficiency improved rapidly as Fe-P/POP dosage increased from 0.03 to 0.05 g/L. However, further increases in Fe-P/POP dosage (0.05–0.20 g/L) inhibited TC degradation, with k decreasing from 0.1031 min^{-1} to 0.0554 min^{-1}. The initial improvement in k was attributed to the increased surface active sites on Fe-P/POP, which enhanced Fe(IV)=O generation during PMS activation. Conversely, excessive catalyst dosage likely caused mass transfer limitations and the unavailability of active sites, thereby diminishing catalytic activity.

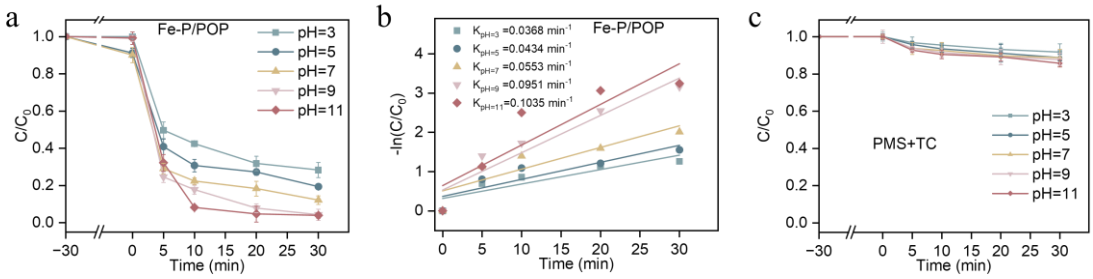

Fig. 4-10. (a) and (b) Effects of initial pH on the TC degradation in Fe-P/POP /PMS systems. (c) The comparison of TC degradation efficiency by different pH in PMS system.

The pH value is a critical factor influencing the efficiency and effectiveness of catalyst-activated persulfate degradation of antibiotics. Different pH levels can significantly affect the type and quantity of radicals produced, the stability and reactivity of the antibiotic, and the overall performance of the catalyst. Therefore, the effect of varying initial pH on the degradation of TC in the Fe-P/POP/PMS system was systematically evaluated.

As shown in **Fig. 4-10a and b**, the Fe-P/POP/PMS system exhibited excellent operational flexibility and achieved effective TC degradation across a broad pH range (3.0–11.0). Interestingly, contrary to most previous studies on PMS-mediated degradation of organic pollutants, the Fe-P/POP/PMS system did not favor acidic conditions but instead performed more efficiently under higher pH conditions. The specific radicals and non-radicals produced, coupled with the base activation of PMS, are likely key contributors to this unusual behavior.

Fig. 4-10c illustrates the degradation efficiency of TC when only PMS was used, across various pH values. Under alkaline conditions, no significant enhancement in TC degradation was observed, ruling out the possibility that alkaline activation of PMS alone contributes to the degradation of TC. Therefore, the observed results suggest that the radicals or non-radical species produced upon PMS activation by Fe-P/POP play a crucial role in accelerating TC degradation under alkaline conditions.

To validate the aforementioned hypothesis, we further identified the active species in the Fe-P/POP/PMS system under varying pH conditions. Tert-butyl alcohol (TBA), methanol (MeOH), p-benzoquinone (PBQ), L-histidine (L-His), and dimethyl sulfoxide (DMSO) were employed as scavengers for ·OH, $SO_4{\cdot}^-$, $O_2{\cdot}^-$, $^1O_2$, and high-valent metal oxide (HVMO) species, respectively. The radical pathways involved in the Fe-P/POP/PMS system under alkaline conditions were then thoroughly investigated.

3.3.3 Mechanism of Fe-P/POP Degradation of TC

3.3.3.1 Identification of Dominant Active Species

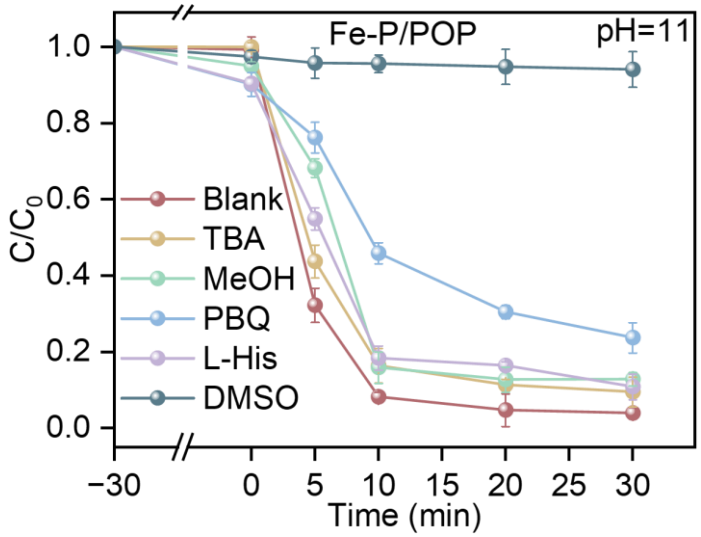

Fig. 4-11 Effect of scavengers on TC degradation in Fe-P/POP/PMS.

MeOH is frequently employed as a quencher for both ·OH and $SO_4{\cdot}^-$ radicals due to its comparable reaction rates ($k_{\cdot OH/MeOH}$ = 1.6–7.7 × 10^7 M^{-1} s^{-1}, $k_{SO_4{\cdot}^-/MeOH}$ = 9.7 × 10^8 M^{-1} s^{-1}) with these species. TBA exhibits a stronger affinity for reacting with ·OH

radicals, as evidenced by a higher reaction constant ($k_{\cdot OH/TBA}$ = 3.8–7.6 × 10^8 M^{-1} s^{-1}) compared to $k_{SO_4\cdot^-/TBA}$ = 4–9.1 × 10^5 M^{-1} s^{-1}. When TBA and MeOH were added as scavengers to the Fe-P/POP/PMS system to quench ·OH and $SO_4\cdot^-$, respectively, the contribution of ·OH and $SO_4\cdot^-$ to TC degradation was found to be negligible (**Fig. 4-11**).

PBQ was utilized as a quencher for $O_2\cdot^-$, and the rate constant (k) decreased to 0.0663 min^{-1} upon the addition of PBQ, suggesting the production of $O_2\cdot^-$. However, the contribution of $O_2\cdot^-$ to TC degradation was minimal, indicating that it was not the primary active species. In addition to the radical pathways, non-radical pathways may also play a role in the TC removal process in the system. To explore this, L-His was used as a scavenger to detect the presence of $^1O_2$.

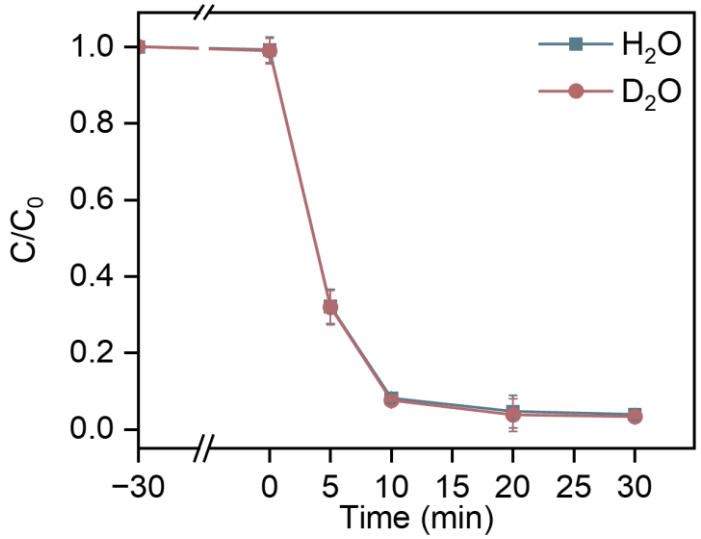

Fig. 4-12. The degradation of TC by the Fe-P/POP/PMS systems in H_2O and D_2O solvent.

The effect of L-His on TC degradation was minimal, indicating that $^1O_2$ might not play a significant role in the process. To further confirm the involvement of $^1O_2$, a solvent exchange experiment was conducted, switching from H_2O to D_2O. The lifetime of $^1O_2$ in D_2O is considerably longer than in H_2O, and thus, if $^1O_2$ were involved in attacking the pollutant, the degradation efficiency should have been enhanced. However, no enhancement in TC degradation was observed in the D_2O system (**Fig. 4-12**), suggesting that $^1O_2$ was not a major contributor to TC degradation.

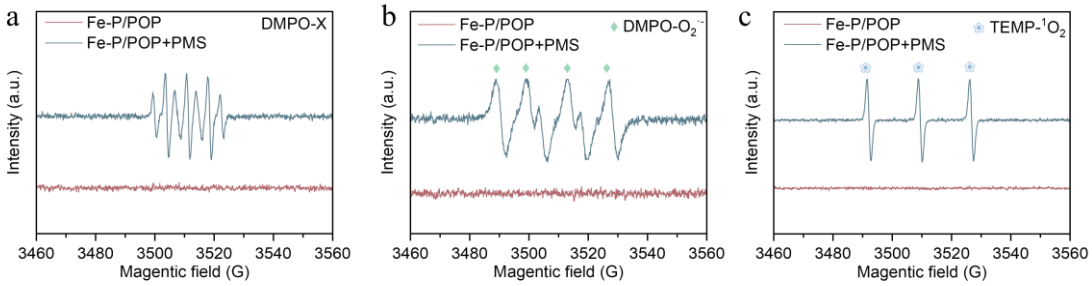

Fig. 4-13. EPR spectra of (a) DMPO-$SO_4^{\cdot-}$ and DMPO-·OH, (b) DMPO-$O_2^{\cdot-}$, and (c) TEMP-$^1O_2$ in Fe-P/POP/PMS systems.

EPR spectroscopy was performed to further identify the presence of reactive oxygen species (ROS) in the Fe-P/POP/PMS system. The results confirmed that the addition of PMS indeed generated $O_2\cdot^-$ and $^1O_2$ (**Fig.4-13b and c**). However, the signals for DMPO-$O_2\cdot^-$ and TEMP-$^1O_2$ were weak, suggesting a limited presence of these species. When DMPO was used as a trapping agent to detect ·OH and $SO_4\cdot^-$, the typical 1:2:2:1 quartet for DMPO-·OH and the 1:1:1:1:1:1 sextet for DMPO-$SO_4\cdot^-$ were absent (**Fig. 4-13a**). Instead, an intense DMPO-X signal was recorded, which could be attributed to the rapid and efficient activation of PMS, producing large amounts of ·OH and $SO_4\cdot^-$, or possibly to surface oxidation reactions, such as the formation of high-valent iron-oxo species. Given the results from the quenching experiments, the latter explanation is more plausible. Therefore, it can be concluded that other reactive species, rather than ·OH, $SO_4\cdot^-$, $O_2\cdot^-$, or $^1O_2$, are primarily responsible for the degradation of TC during Fe-P/POP/PMS oxidation.

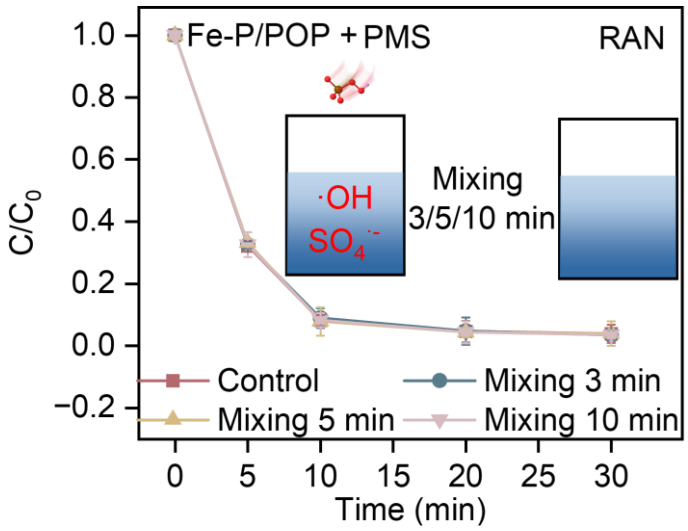

Fig. 4-14. TC oxidation via a premixture of Fe-P/POP and PMS at estimated time intervals.

The contribution of radicals to the oxidation of TC in the Fe-P/POP/PMS system was further examined through a premixing experiment, in which Fe-P/POP and PMS were premixed for various time intervals before the addition of TC. By premixing PMS and the catalyst, radicals were generated instantaneously in the system, resulting in significant consumption of PMS. Therefore, the degradation of pollutants would be affected upon the subsequent addition of TC. This method allowed for a more accurate assessment of the role of free radicals in the system. If the oxidation mechanism were predominantly radical-driven, the premixing of Fe-P/POP and PMS would only have a minor impact on TC oxidation. However, the results revealed that premixing Fe-P/POP and PMS for 3, 5, and 10 minutes resulted in only a weak inhibition of TC oxidation **(Fig. 4-14)**. This suggests that non-radical species (excluding $^1O_2$) played a dominant role in the oxidation of TC, overpowering the effect of radicals. Despite the substantial generation of radicals in the Fe-P/POP/PMS system, non-radical species still made a significant contribution to the degradation of TC.

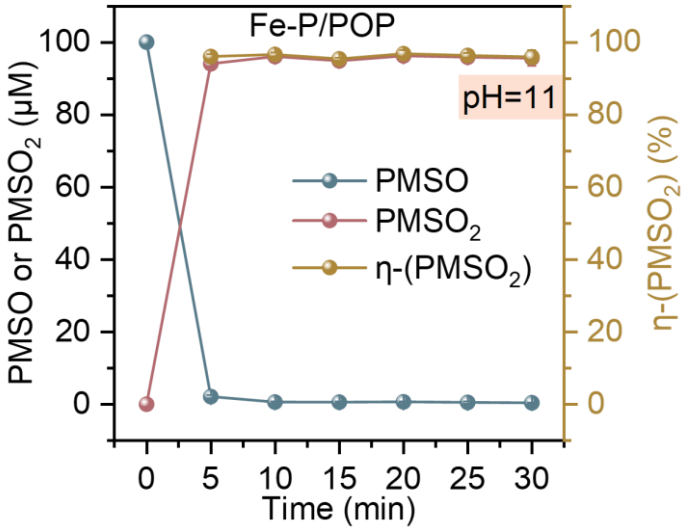

Fig. 4-15. PMSO consumption, $PMSO_2$ production, and η-($PMSO_2$) in the Fe-P/POP/PMS system at pH=11.

This was further corroborated by the detection of methyl phenyl sulfone ($PMSO_2$) during the oxidation of methyl phenyl sulfoxide (PMSO) (**Fig. 4-15**). PMSO can be converted to $PMSO_2$ by Fe(IV)=O through a unique oxygen transfer step, while hydroxylated and/or polymeric products are generated from PMSO oxidation by free radicals ($k_{\cdot OH/PMSO}$ = 3.61 × 10^9 M^{-1} S^{-1} and $k_{SO_4^{\cdot-}/PMSO}$ = 3.17 × 10^8 M^{-1} S^{-1}).[41, 46-48]

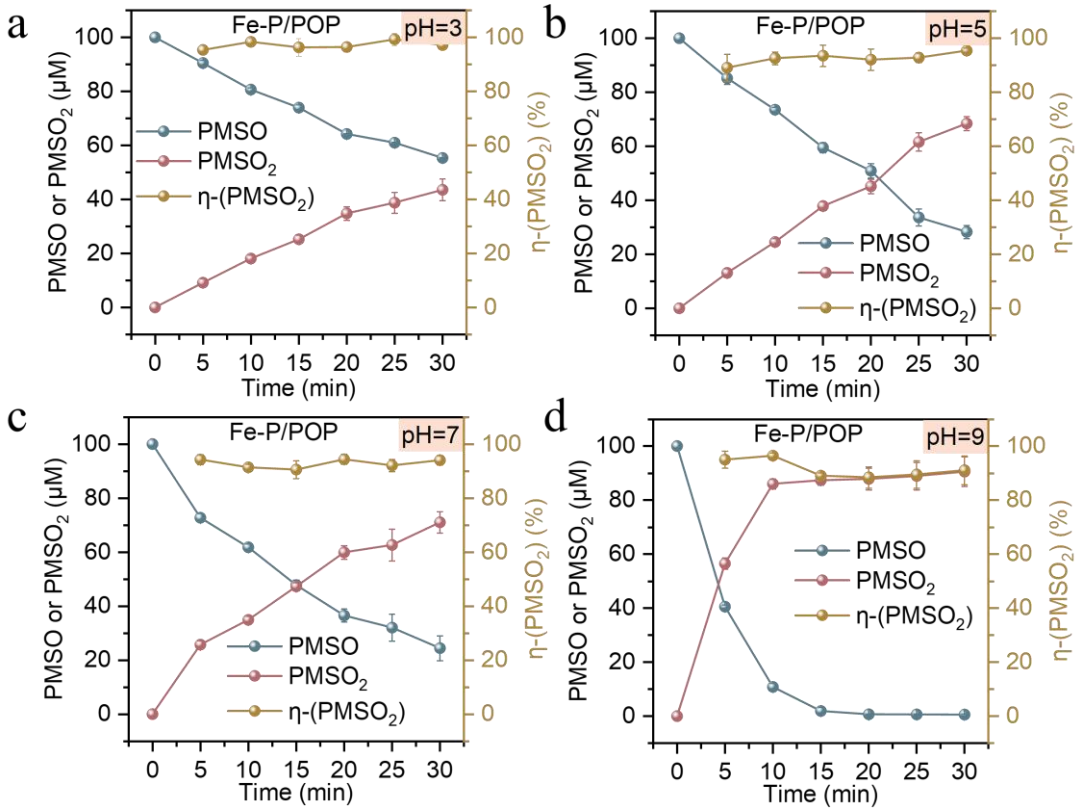

Fig. 4-16. (a)-(d) PMSO consumption, $PMSO_2$ production, and η-($PMSO_2$) in the Fe-P/POP/PMS system at different pH.

Fig. 4-16(a-d) illustrates that Fe(IV)=O can effectively oxidize PMSO within the pH range of 3.0–11.0, with the highest PMSO removal occurring at pH 11.0. Moreover, across the pH range of 3.0–11.0, the consumption of PMSO is directly proportional to the production of $PMSO_2$ (μ-$PMSO_2$ around 100%), indicating the involvement of Fe(IV)=O species in the system rather than free radicals. If free radicals had played a role, achieving an efficiency near 100% for $PMSO_2$ would not have been possible.

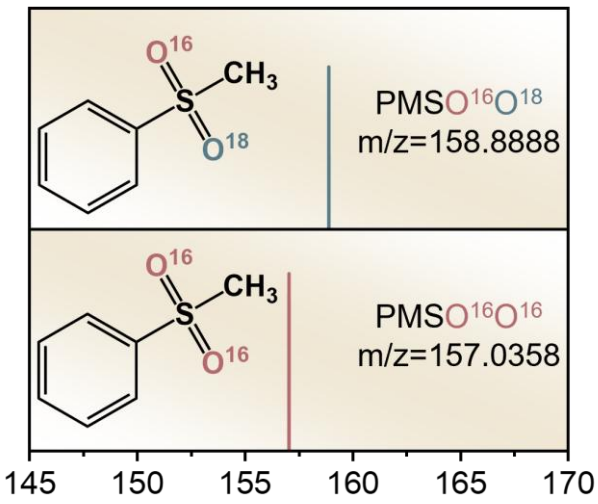

Fig. 4-17. high-resolution mass spectrometry analyses of O^{18}-labeled $PMSO_2$ generated in H_2O^{18} matrix.

Spontaneous exchange of oxygen atoms between the intermetallic Fe–O bond and the solvent water provides additional evidence for the formation and oxidation capacity of Fe(IV)=O. By using O18-isotope-labeled H_2O_{18} as the solvent, Fe(IV)=O would form Fe(IV)=O_{18} through spontaneous O-atom exchange, which would then oxidize PMSO to produce $PMSO_{16}O_{18}$. This oxidation product was detected as expected. When the reaction system was carried out in the H_2O_{18} matrix, the oxidation product $PMSO_{16}O_{18}$ was observed, as evidenced by the two peaks in the extracted ion chromatogram at m/z = 157.0358 ($PMSO_{16}O_{16}$) and 158.8888 ($PMSO_{16}O_{18}$) (**Fig. 4-17**). These results further corroborate the role of Fe(IV)=O as an intermediate in the oxidation process within the Fe-P/POP/PMS system.

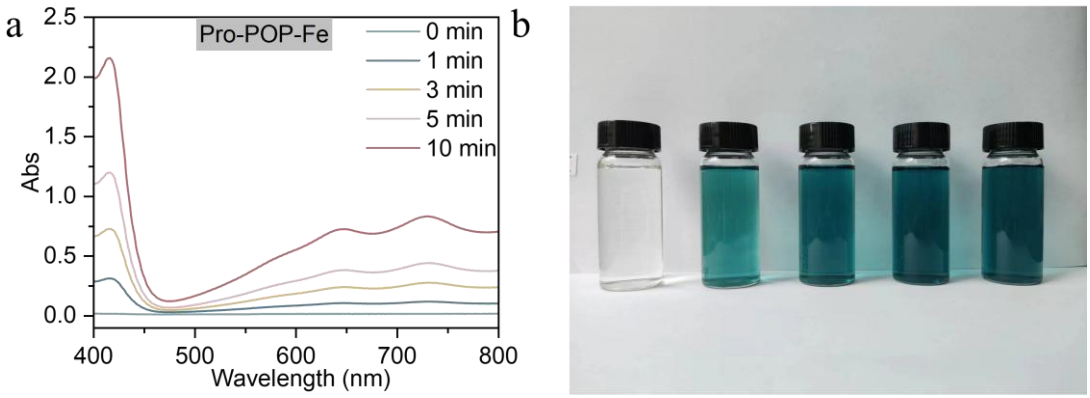

Fig. 4-18. (a) and (b) The UV–Visible absorption spectra of the Fe-P/POP/PMS system were

quenched by ABTS.

Additionally, 2,2'-azinodi(3-ethylbenzothiazoline-6-sulfonic) acid (ABTS) can undergo one-electron oxidation by high-valent metal oxides, resulting in the formation of ABTS·+, which is accompanied by a color change to blue. The generation of ABTS·+ can be detected in the UV-visible spectrum, with prominent absorption peaks around 415 nm and 660 nm. Observations of the spectral changes in ABTS during the Fe-P/POP/PMS catalytic oxidation process further support the generation of Fe(IV)=O species in the reaction (**Fig. 4-18**) (Eqs. (4-1)).

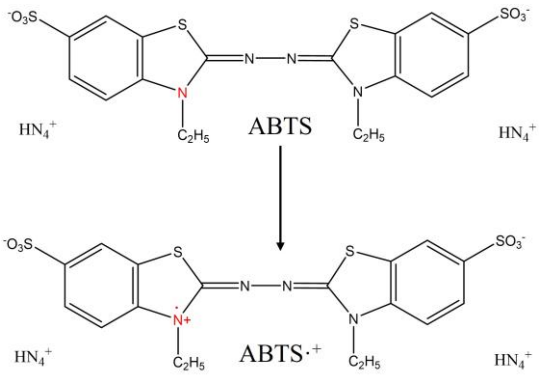

(4-1)

4.3.4 Potential superiority in environmental applications

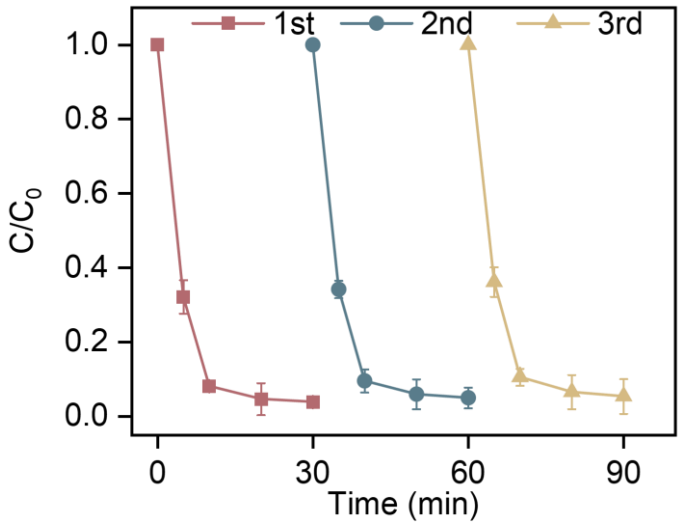

Fig. 4-19. Cycling test of Fe-P/POP for the TC degradation in Fe-P/POP/PMS.

Fig. 4-19 shows that the removal efficiency remains at 94.62% after five

successive degradation cycles, demonstrating that Fe-P/POP exhibits excellent reusability and stability.

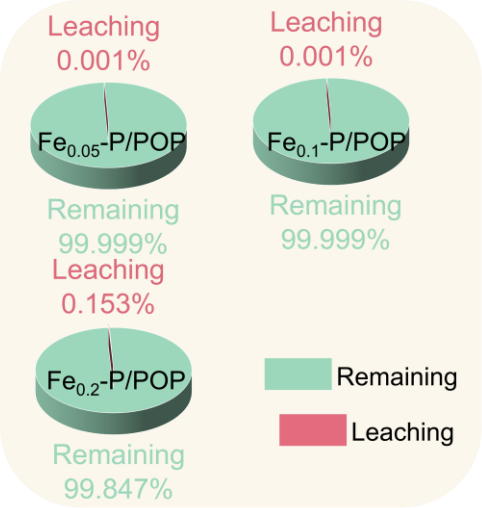

Fig. 4-20. The percentage of leached Fe in $Fe_{0.05}$-P/POP, Fe-P/$POP_{0.1}$ and Fe-P/$POP_{0.2}$ determined by ICP after reaction in 30 min.

Furthermore, ICP analysis was conducted to assess whether the catalyst induces significant metal leaching during use. As shown in **Fig. 4-20**, the leaching concentration of Fe from Fe-P/POP was 0.0028 mg/L. These results suggest that Fe-P/POP is both stable and environmentally friendly, making it well-suited for practical applications.

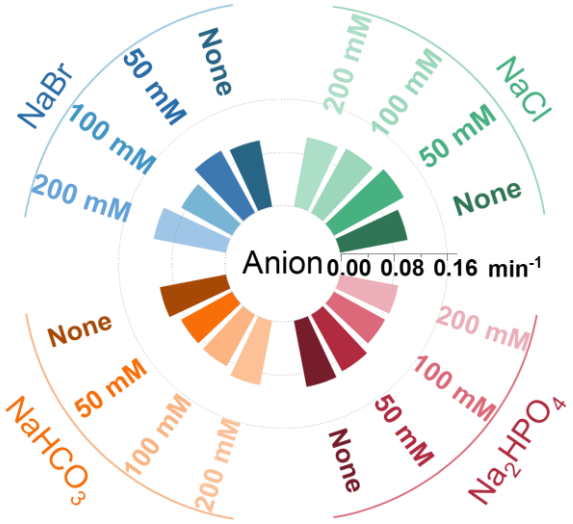

Fig. 4-21. Influences of the degradation of coexisting inorganic ions in Fe-P/POP/PMS system.

Various ions were involved in the actual aqueous matrices. As depicted in **Fig. 4-21**, Cl^-, Br^-, HCO_3^-, and HPO_4^{2-} exhibited little effects on the TC removal, indicating that Fe-P/POP could greatly resist the disturbance of nontarget background substances.

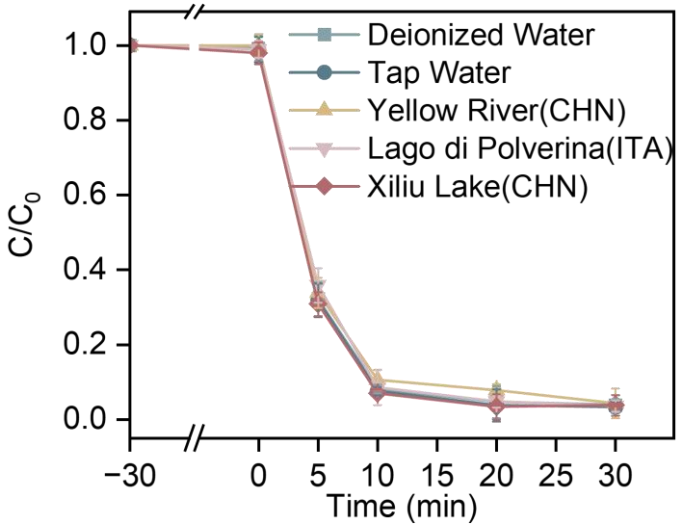

Fig. 4-22. Different water sources in Fe-P/POP/PMS system.

Moreover, as shown in **Fig. 4-22**, nearly 100% of TC was removed within 30 minutes across various water samples, including deionized water, tap water, water from the Yellow River (China), a natural lake (Italy), and Xiliu Lake (Henan). This highlights the system's promising applicability in real-world water environments.

This demonstrates that the Fe-P/POP catalyst enables the efficient utilization of Fe atoms. As outlined in Text, we conducted an economic analysis to assess the feasibility of the Fe-P/POP/PMS system for practical applications in terms of electrical energy per order (EE/O) scenarios.

EE/O is a commonly used metric to evaluate the energy consumption and cost-effectiveness of reaction systems. It is defined as the amount of electrical energy required to reduce the concentration of a specific pollutant by one order of magnitude. This method typically considers the electrical energy and chemical consumption, with the catalyst assumed to be reusable and not treated as a consumable in the system.

In this study, the economic evaluation of the optimal Fe-P/POP/PMS system was based on EE/Ototal, calculated using the following Equations (4-2), (4-3), and (4-4).

Given that the Fe-P/POP/PMS system did not require external energy input such as light or ultrasound, the external energy input was considered zero. As a result, the EE/Ototal value was derived from the PMS/O ratio. According to literature, the non-household electrical energy cost and the cost of PMS were estimated to be 0.1319 $/kWh and 1.30 $/kg, respectively. Consequently, the electrical energy cost of PMS was calculated as 9.85 kWh/kg.

Based on the results shown in **Fig. 4-9**, 99% of TC was removed, and 70% of PMS was consumed within 30 minutes. The calculated EE/Ototal value for the Fe-P/POP/PMS system was 0.001 kWh/m³, corresponding to a cost of 0.0001 $/m³. This cost is significantly lower than that of advanced oxidation processes (AOPs) reported in previous studies. Thus, based on this analysis, the Fe-P/POP/PMS system demonstrates substantial potential for practical applications, offering a more cost-effective alternative in pollutant degradation.

$$EE/O_{Total} = EE/O_{Energy} + EE/O_{Chemicals} = EE/O_{Chemicals} \quad (4\text{-}2)$$

$$EE/O_{Chemicals} = PMS/O = \frac{[PMS]_0 - [PMS]_f}{log\left(\frac{C_i}{C_f}\right)} (mg/L) \quad (4\text{-}3)$$

$$In\left(\frac{C_i}{C_f}\right) = k \times t \quad (4\text{-}4)$$

Where $[PMS]_0$ and [PMS]f represent the concentration of PMS (mg/L) at the initial reaction time (0 min) and after time t (min), respectively. t denotes the reaction time (min), Ci is the initial concentration of TC, and Cf is the concentration of TC after the reaction time of t minutes, both measured in mg/L.

According to our calculations, the Fe-P/POP/PMS system exhibited an EE/O_{total} value of 0.001 kWh/m³, with a corresponding cost of $0.0001/m³. This cost is lower than that of advanced oxidation processes (AOPs) reported in other studies. Taken together, these findings provide valuable insights for the development of highly

efficient and cost-effective Fenton-like systems by fine-tuning FeN4 coordination.

4.4 Conclusion

In this study, an iron-porphyrin-based porous organic polymer (Fe-P/POP) was successfully synthesized and utilized as an efficient catalyst for PMS activation to degrade tetracycline (TC). The well-defined Fe-N_4 coordination structure facilitated effective electron transfer and promoted the formation of high-valent Fe(IV)=O species, which were identified as the dominant reactive species responsible for TC degradation via a non-radical oxidation pathway. Quenching experiments and EPR spectroscopy confirmed the negligible contributions of conventional radicals (•OH, SO_4•$^-$, and O_2•$^-$), further validating the selective oxidation mechanism of Fe(IV)=O. Additionally, Fe-P/POP demonstrated superior performance across a broad pH range, high recyclability, negligible Fe leaching, and strong resistance to environmental interferences, making it a promising candidate for practical wastewater treatment applications. The findings of this study provide valuable insights into the rational design of Fe-based catalysts for PMS activation and highlight Fe-P/POP as an efficient and sustainable solution for the degradation of antibiotic contaminants in aquatic environments.

5. The Preparation of Copper Porphyrin-Based Porous Organic Polymers and Their Application in Persulfate Activation for SMX Degradation

Abstract:

Sulfamethoxazole (SMX), a widely used sulfonamide antibiotic, poses a significant environmental threat due to its persistence in water bodies and resistance to conventional wastewater treatment methods. In this study, a copper porphyrin-based porous organic polymer (Cu-P/POP) was synthesized and employed as an efficient catalyst for peroxymonosulfate (PMS) activation to degrade SMX. The Cu-P/POP system exhibited excellent catalytic performance, achieving nearly 100% SMX removal within 30 minutes. Structural characterization confirmed the successful coordination of Cu within the porphyrin framework, providing abundant active Cu-N_4 sites for PMS activation. Mechanistic studies, including radical quenching experiments, electron paramagnetic resonance (EPR) spectroscopy, and isotope labeling tests, demonstrated that high-valent Cu(III)=O species were the dominant reactive species responsible for SMX degradation, following a non-radical oxidation pathway. Furthermore, Cu-P/POP maintained high catalytic efficiency across a wide pH range, exhibited strong resistance to interference from coexisting ions, and demonstrated excellent recyclability with minimal Cu leaching. The economic evaluation indicated that the Cu-P/POP/PMS system operated at a significantly lower cost compared to conventional advanced oxidation processes (AOPs). This study provides fundamental insights into PMS activation mechanisms and highlights Cu-P/POP as a cost-effective and sustainable solution for antibiotic removal in wastewater treatment.

Keywords: Cu-P/POP; PMS; HVMO; SMX.

5.1 Introduction

Sulfamethoxazole (SMX) is a widely used sulfonamide antibiotic that plays a crucial role in treating bacterial infections.[108-110] However, its extensive application has led to significant environmental concerns, as SMX, along with other pharmaceuticals, is frequently detected in water bodies, posing potential risks to aquatic ecosystems and human health.[111-114] Despite conventional wastewater treatment methods, SMX remains resistant to degradation, resulting in its persistence in the environment.[115-117] Consequently, developing efficient and sustainable methods to remove or degrade SMX from contaminated water has become a critical challenge.[112, 118-120]

Among the various advanced oxidation processes (AOPs) employed to degrade organic pollutants, persulfate (PMS)-based systems have attracted considerable attention due to their ability to generate highly reactive sulfate radicals ($SO_4^{\cdot -}$) and hydroxyl radicals (·OH). These radicals are capable of efficiently breaking down a wide range of organic contaminants, including antibiotics like SMX. However, the activation of PMS often requires the use of highly effective catalysts that can facilitate the generation of these reactive species under mild conditions.

High-valent metal species, such as copper (Cu(Ⅲ)), have been identified as crucial active species in PMS activation. These metals can directly participate in oxidation reactions, significantly enhancing the degradation process. Compared to free radicals like $SO_4^{\cdot -}$ and ·OH, high-valent metals offer several advantages. They exhibit greater stability and selectivity, which can help minimize undesired side reactions and by-product formation. Additionally, high-valent metal species, especially when integrated into porous organic frameworks, provide an optimal environment for catalytic activation, ensuring efficient pollutant degradation.

Copper porphyrin-based porous organic polymers (Cu-P/POP) have recently emerged as promising candidates for catalytic applications due to their unique structure, high surface area, and excellent stability. The copper porphyrin units within these

frameworks serve as active sites for the efficient activation of PMS, facilitating the generation of reactive radicals that can degrade persistent contaminants like SMX. The ability of Cu-P/POP to activate PMS under mild conditions, coupled with its high reactivity and stability, makes it an attractive solution for tackling environmental pollution.

This study aims to synthesize copper porphyrin-based porous organic polymers and investigate their catalytic performance in the activation of PMS for the degradation of SMX. The results are expected to provide valuable insights into the development of effective and sustainable systems for addressing the environmental challenges posed by pharmaceutical pollutants.

5.2 Experiments and Methods

5.2.1 Catalyst Preparation

Synthesis of Porphyrin-Porous Organic Polymer (P/POP)

Tetraphenylporphyrin (0.96 g, 0.2 mmol) and aluminum chloride (4 g, 3.2 mmol) were added to a two-necked flask at room temperature. Under a nitrogen atmosphere, trichloromethane (8 mL) was introduced into the flask. The mixture was refluxed and stirred at 30°C for 8 h, at 40°C for 12 h, and at 58°C for 28 h. After the reaction, the dark precipitate was washed with hydrochloric acid-water (v/v=2:1, 40 mL), distilled water, and ethanol. The solid was then purified by Soxhlet extraction with methanol for 24 h. Finally, it was dried in a vacuum oven at 60°C for 24 h to yield a black polymer powder designated as P/POP.

Synthesis of Porphyrin-Porous Organic Polymer-Cu (Cu-P\POP)

Por-POP (1 g) and copper (II) acetate tetrahydrate ($C_4H_6CuO_4 \cdot 4H_2O$, 0.1 g) were added to an acetonitrile solution (30 mL). The mixture was stirred at 82°C for 24 h. After the reaction, the solid was obtained by centrifugation and washed three times with

methanol, followed by Soxhlet extraction with methanol for 24 h. Finally, the product was dried in a vacuum oven at 60°C for 24 h to yield a black solid powder designated as Cu-P\POP.

5.2.2 Characterization of Cu-P\POP

5.2.2.1 High-Resolution Field Emission Scanning Electron Microscopy (SEM)

The SEM analysis method for Cu-P\POP is detailed in Chapter 2 – 2.2.2.1.

5.2.2.2 X-ray Photoelectron Spectroscopy (XPS)

The XPS analysis method for Cu-P\POP is detailed in Chapter 2 – 2.2.2.2.

5.2.2.3 X-ray Diffraction (XRD)

The XRD analysis method for Cu-P\POP is detailed in Chapter 2 – 2.2.2.3.

5.2.2.4 Fourier Transform Infrared Spectroscopy (FT-IR)

The FT-IR analysis method for Cu-P\POP is detailed in Chapter 2 – 2.2.2.4.

5.2.3 Performance Analysis of Cu-P\POP

5.2.3.1 SMX Degradation Experiments and Analysis Methods

The methods for SMX degradation experiments and detection are detailed in Chapter 2 – 2.2.3.1.

5.2.3.2 Effects of Water Quality on P Cu-P\POP Performance

The experimental method for studying the effects of water quality on Cu-P\POP performance is detailed in Chapter 2 – 2.2.3.2.

5.2.3.3 Recycling Experiments

The experimental method for SMX recycling experiments is detailed in Chapter

2 – 2.2.3.3.

5.2.3.4 Determination of Metal copper Concentrations in the Reaction System

The method for detecting metal copper concentrations in the reaction system is detailed in Chapter 2 – 2.2.3.4.

5.2.4 Mechanistic Analysis of SMX Degradation by Cu-P\POP

5.2.4.1 Radical Quenching Experiments

The method for radical quenching experiments is detailed in Chapter 2 – 2.2.4.1.

5.2.4.2 Detection of Degradation Reaction Intermediates

The method for detecting intermediate products formed during SMX degradation is detailed in Chapter 2 – 2.2.4.4.

5.3 Results and Discussion

5.3.1 Characterization Analysis of Cu-P\POP

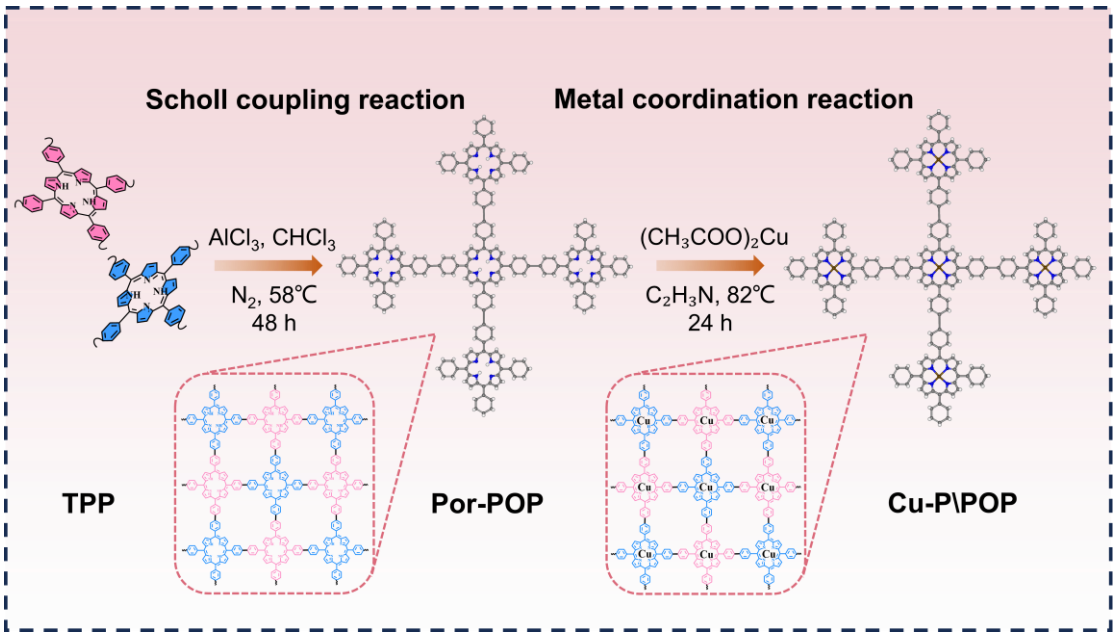

Fig. 5-1. Schematic illustration of the preparation procedures of the Cu-P\PPC samples.

Fig. 5-1 illustrates the preparation process of Cu-Porphyrin-Porous Organic Polymer (Cu-P/POP). Tetraphenylporphyrin was employed as the precursor to construct a porous polymer (POP) featuring an extensively conjugated microporous network through a Friedel-Crafts alkylation coupling reaction catalyzed by $AlCl_3$ under nitrogen atmosphere. During this process, the hydrogen atoms on the aromatic rings of the porphyrin were substituted with alkyl groups, while the pyrrolic nitrogen (N) atoms in the porphyrin structure remained unreacted and did not partake in the coupling reaction. Consequently, these pyrrolic nitrogen atoms were preserved in the framework, providing suitable coordination sites for metal incorporation. Since Cu(II) is a highly effective metal in activating persulfate (PMS), the porous polymer (P/POP) can be metallized with Cu(II) in acetonitrile, resulting in the formation of Cu-P/POP.

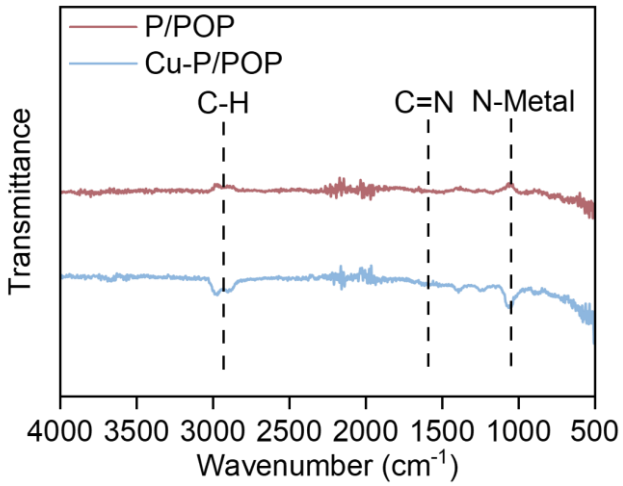

Fig. 5-2. FT-IR spectra of P\PPC and Cu-P\PPC.

Fig. 5-2 displays the FT-IR spectra of P/POP and Cu-P/POP. The distinctive absorption peaks in the range of 1655 to 1570 cm^{-1} for both P/POP and Cu-P/POP are attributed to the C=N and C=C stretching vibrations of the porphyrin macrocycle and the benzene ring. Additionally, the C-H stretching vibration bands of methylene groups

are clearly observed in the 2900-3080 cm^{-1} region, which confirm the presence of methylene linkers in both P/POP and Cu-P/POP, thereby validating the successful incorporation of porphyrin units into the polymer framework. The N-H stretching vibration at 3308 cm^{-1} in the pyrrole ring is absent, while a characteristic N-Cu in-plane bending vibration at 1007 cm^{-1} appears in the FT-IR spectrum of Cu-P/POP, providing further evidence of copper ion coordination within the polymeric structure.

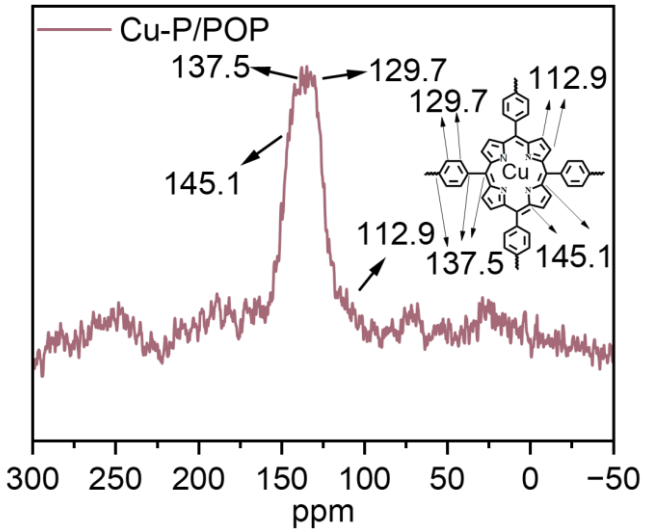

Fig. 5-3. Solid-state ^{13}C NMR spectrum of Cu-P\PPC.

The structural details of Cu-P/POP were examined using solid-state ^{13}C NMR spectroscopy. As shown in **Fig. 5-3**, resonance peaks at approximately 129.7 and 137.5 ppm are attributed to the phenylene linkages, while peaks at around 112.9 and 145.1 ppm are associated with the porphyrin macrocycles. These results provide preliminary evidence that the porphyrin units have been successfully integrated into the polymeric networks.

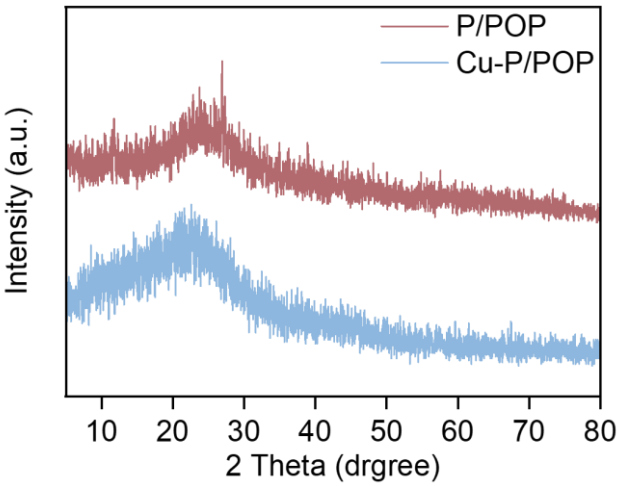

Fig. 5-4. XRD profiles of catalysts.

The XRD patterns of P/POP and Cu-P/POP are presented in **Fig. 5-4**. No distinct characteristic peaks were observed, suggesting a low degree of crystallinity due to the disordered stacking of the polymeric structure. The broadening of the peak at 22.1° is likely due to disruptions between the P/POP and Cu-P/POP polymers, or structural defects within the system, leading to some level of disorder in the pore distribution and reflecting its amorphous nature. Additionally, the absence of diffraction peaks corresponding to metallic Cu nanoparticles or Cu oxides further confirms that such impurities were not formed or present in Cu-P/POP.

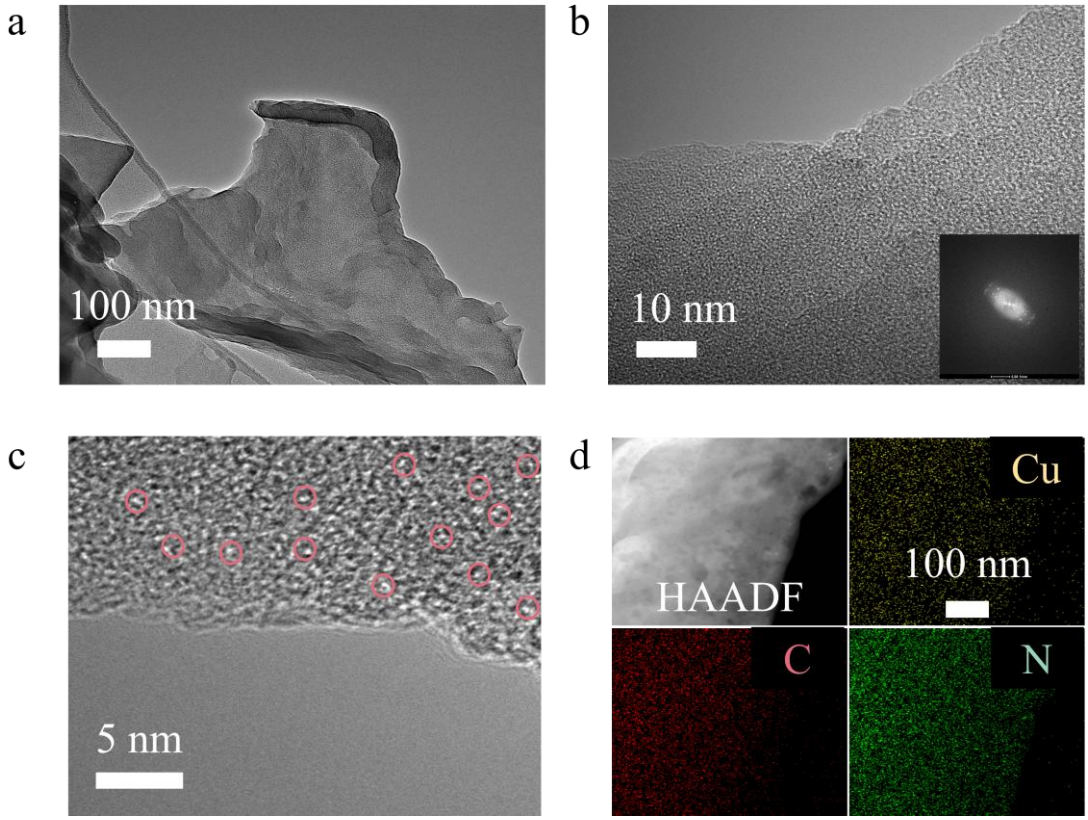

Fig. 5-5. (a) and (b) TEM image of Cu-P/PPC (inset: SAED pattern). (c) AC HAADF-STEM image of Cu-P/PPC, the isolated bright dots marked with red circles are cobalt atoms. (d) HAADF-STEM image with the corresponding EDS elemental mapping.

In **Fig. 5-5 (a** and **b)**, the TEM images reveal that the as-prepared Cu-P/POP possesses a homogeneous two-dimensional lamellar structure, devoid of nanoparticles. The SAED pattern further corroborates the amorphous nature of Cu-P/POP, consistent with the XRD findings. The aberration-corrected HAADF-STEM image (**Fig. 5-5c**) displays numerous isolated bright spots, indicative of the uniformly dispersed individual Cu atoms, with no visible Cu particles present on Cu-P/POP. Moreover, the EDS mapping images (**Fig. 5-5d**) confirm the presence and uniform distribution of Cu, N, and C elements. Collectively, these results strongly suggest the atomic dispersion of Cu within the Cu-P/POP framework.

5.3.2 Catalytic performance

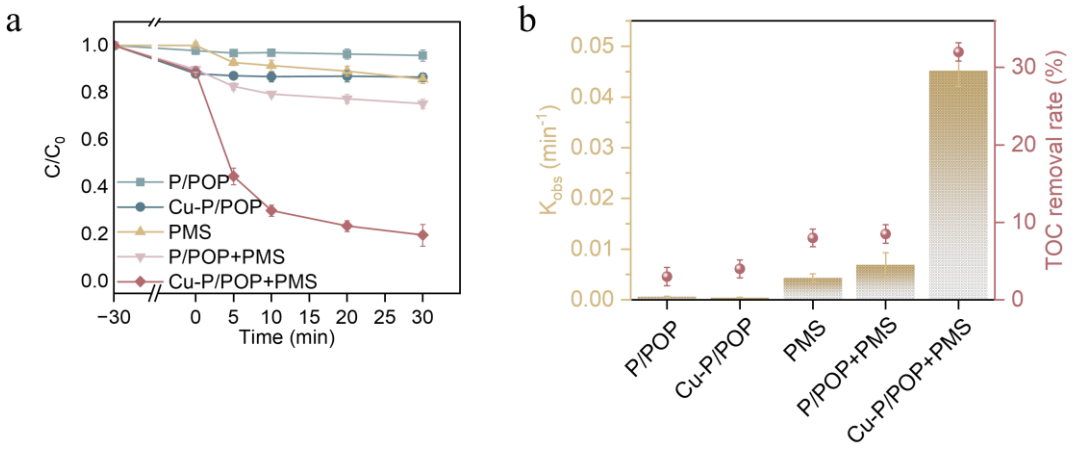

Fig. 5-6. (a) The corresponding pseudo-first-order kinetic constants and TOC removal efficiency of SMX in several systems. (b) SMX removal efficiency and reaction kinetics in different catalyst/PMS systems.

The degradation of SMX was employed as a key indicator to assess the catalytic performance of Cu-P/POP. The catalytic efficiencies of Cu-P/POP and control samples in the SMX degradation process were compared (**Fig. 5-6 a and b)**. Remarkably, the Cu-P/POP/PMS system achieved complete degradation (100%) of SMX, along with a mineralization rate of 32.33% within 30 minutes. In contrast, the P/POP/PMS system demonstrated a significantly lower SMX degradation efficiency of 24.69% and a mineralization rate of only 8.52% under the same conditions. The substantial improvement in degradation rate with Cu-P/POP, as compared to P/POP, underscores the role of atomic Cu in providing additional active sites, thereby greatly enhancing the catalytic performance.

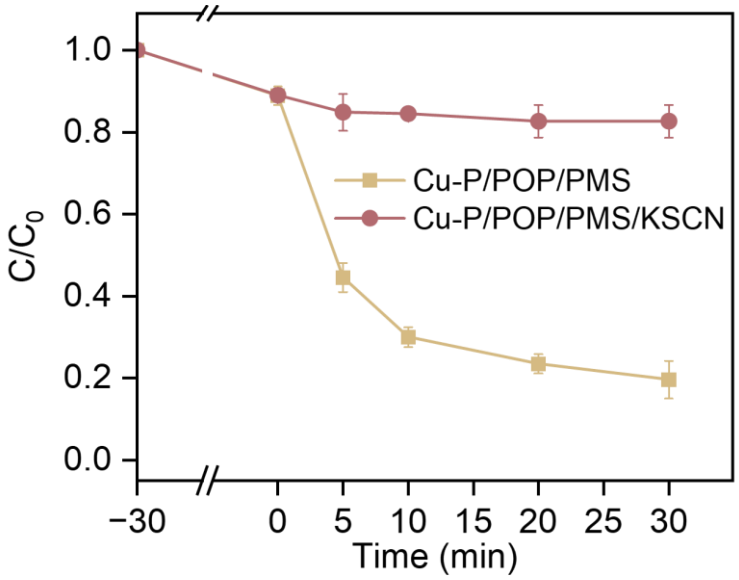

Fig. 5-7. Performance of Cu-P/POP /PMS to degrade SMX with or without KSCN.

When the reaction system was introduced with 10 mM KSCN, the degradation of SMX was almost entirely blocked (**Fig. 5-7**). This suggests that the active site responsible for catalyzing SMX degradation in Cu-P/POP is located at the Fe atom center. The SCN^- ions likely coordinate with the Cu in the $Cu-N_4$ structure, leading to poisoning of the catalytic site. The results of the KSCN poisoning experiment further highlight the crucial role of atomic Cu in activating PMS within the Cu-P/POP system.

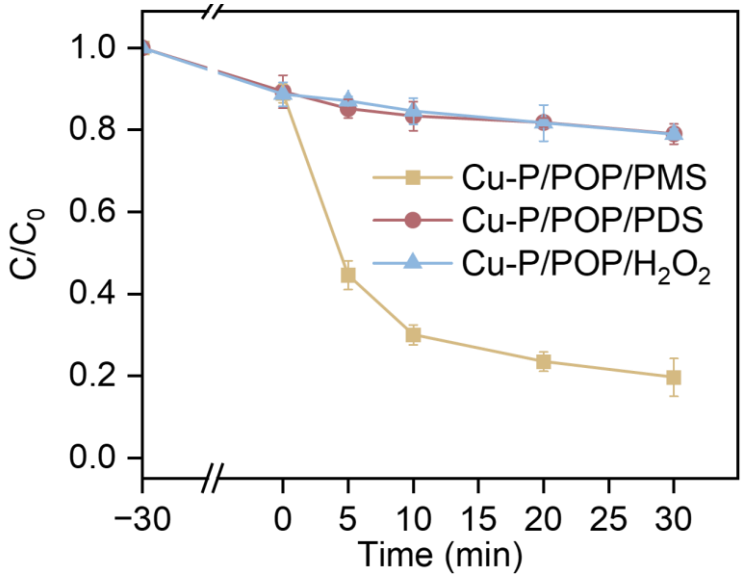

Fig. 5-8. The comparison of SMX degradation efficiency by different oxidants in Cu-P/POP /PMS system.

To further evaluate the activation efficiency of Cu-P/POP with different oxidants, $Na_2S_2O_8$ (PDS) and H_2O_2 were added to the SMX solution for comparison. As shown in **Fig. 5-8**, in the presence of PMS, the SMX degradation rate reached 100% within 30 min, which was significantly higher than those achieved with PDS (26%) and H_2O_2 (11%). The symmetric structure of PDS contributes to its greater stability and steric hindrance compared to PMS, while the high bond energy of the O-O bond in H_2O_2 hinders its cleavage.[79] These factors likely limit the catalytic activation of PDS and H_2O_2. Consequently, PMS was selected as the oxidant for this experiment. Moreover, the influence of cobalt load, PMS dosage, SMX concentration, and catalyst dosage on SMX degradation in Cu-P/POP/PMS system was investigated, because the active species production and SMX degradation are of high dependent on the above factors.

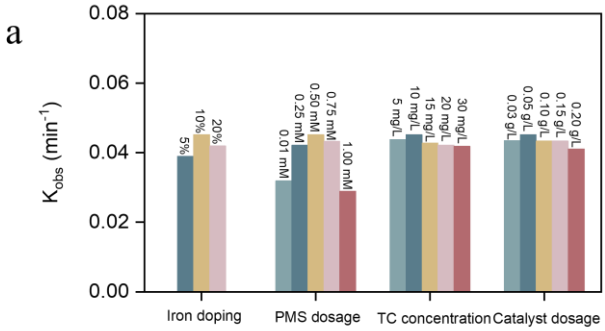
a
0.08
0.06
0.04
0.02
0.00
K_{obs} (min^{-1})
5%
10%
20%
0.01 mM
0.25 mM
0.50 mM
0.75 mM
1.00 mM
5 mg/L
10 mg/L
15 mg/L
20 mg/L
30 mg/L
0.03 g/L
0.05 g/L
0.10 g/L
0.15 g/L
0.20 g/L
Iron doping
PMS dosage
TC concentration
Catalyst dosage

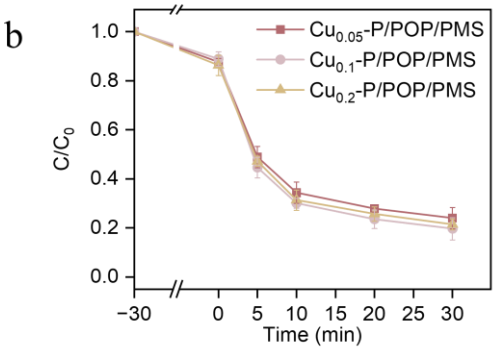
b
$Cu_{0.05}$-P/POP/PMS
$Cu_{0.1}$-P/POP/PMS
$Cu_{0.2}$-P/POP/PMS
C/C$_0$
1.0
0.8
0.6
0.4
0.2
0.0
−30
0
5
10
15
20
25
30
Time (min)

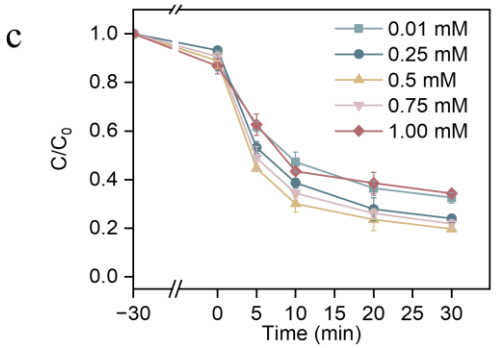
c
0.01 mM
0.25 mM
0.5 mM
0.75 mM
1.00 mM
C/C$_0$
1.0
0.8
0.6
0.4
0.2
0.0
−30
0
5
10
15
20
25
30
Time (min)

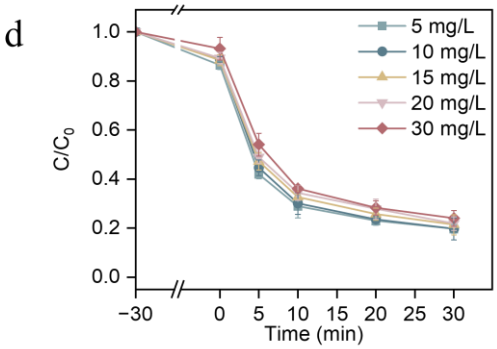
d
5 mg/L
10 mg/L
15 mg/L
20 mg/L
30 mg/L
C/C$_0$
1.0
0.8
0.6
0.4
0.2
0.0
−30
0
5
10
15
20
25
30
Time (min)

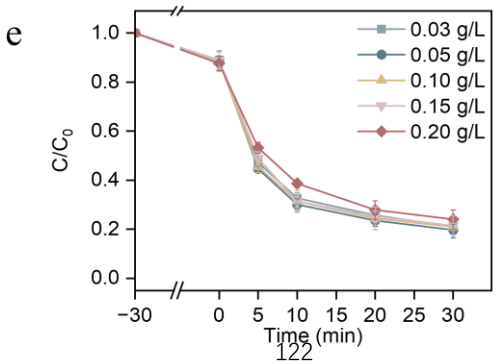
e
0.03 g/L
0.05 g/L
0.10 g/L
0.15 g/L
0.20 g/L
C/C$_0$
1.0
0.8
0.6
0.4
0.2
0.0
−30
0
5
10
15
20
25
30
Time (min)

Fig. 5-9. (a) The corresponding rate constants *k* under various conditions. (b) Effects of cupper load, (c) Effects of PMS concentration, (d) Effects of SMX concentration, (e) Effects of catalyst content on the SMX degradation in Cu-P/POP /PMS system.

Moreover, the influence of iron doping, PMS dosage, SMX concentration, catalyst dosage, and initial pH on SMX degradation in the Cu-P/POP/PMS system was investigated, as the production of active species and SMX degradation are highly dependent on these factors. For better comparison, the apparent rate constant (k) for catalytic degradation was analyzed using the first-order kinetic model [$\ln(C/C_0) = -kt$]. As shown in **Fig. 5-9a and b**, optimization experiments on Cu doping amounts revealed that increasing the Cu content improved the catalytic oxidation of SMX. The catalyst with 10 wt% Cu exhibited the best performance for SMX removal, while excessive Cu doping resulted in clustering and a reduction in catalytic efficiency.

The concentration of the oxidant is a key factor in generating both radical and non-radical oxidizing species. In this experiment, PMS dosages ranged from 0.01 mM to 1 mM. **Fig. 5-9c** demonstrates the effect of different PMS dosages (0.01, 0.25, 0.5, 0.75, and 1 mM) on SMX degradation in the Cu-P/POP/PMS system. At a low PMS concentration (0.01 mM), the system failed to generate sufficient Cu(III)=O, resulting in incomplete SMX degradation. However, increasing the PMS concentration from 0.25 to 0.5 mM significantly accelerated the degradation process, highlighting the importance of adequate PMS levels in enhancing the reaction efficiency.Increasing the PMS concentration from 0.25 to 0.5 mM significantly accelerated the SMX degradation process, with the apparent rate constant (k) increasing from 0.0319 min^{-1} to 0.0451 min^{-1}. Additionally, a low PMS dosage was found to be less conducive to the regeneration of Cu. However, no further enhancement in SMX degradation was observed when the PMS concentration was increased to 0.75 and 1 mM. This is likely because excessive PMS could alter the pH of the solution, thereby reducing the catalytic efficiency.

As shown in **Fig. 5-9d**, increasing the SMX concentration from 5 mg/L to 30 mg/L

resulted in a decreasing trend in degradation rates. This decline may be related to the competition for free radicals generated by the Cu-P/POP/PMS system. As the SMX concentration increased, a higher number of by-products were likely produced. These by-products could compete with the parent contaminant for both free radicals and non-radical species, leading to a reduction in catalytic oxidation efficiency.

Fig. 5-9e illustrates how the degradation efficiency of SMX and the rate constant (k) varied with increasing Cu-P/POP dosage under a constant PMS concentration (0.5 mM) and SMX concentration (10 mg/L). The SMX removal rate increased significantly as the Cu-P/POP dosage was increased from 0.03 to 0.05 g/L. However, further increasing the dosage from 0.05 to 0.20 g/L resulted in a decline in SMX degradation efficiency, with the apparent rate constant (k) decreasing from 0.0452 to 0.0411 min^{-1}. The initial rise in k can be attributed to the increase in surface active sites on Cu-P/POP, which facilitated greater generation of Cu(III)=O during PMS activation. However, at higher catalyst concentrations, the reaction was hindered by slower mass transfer and reduced availability of active sites, leading to a reduction in catalytic efficiency.

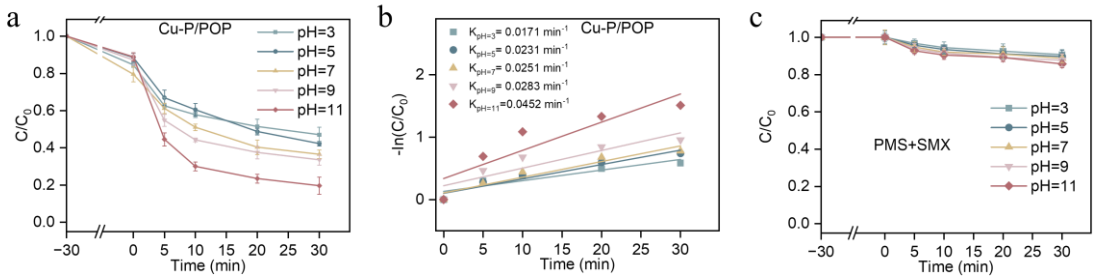

Fig. 5-10. (a) and (b) Effects of initial pH on the SMX degradation in Cu-P/POP /PMS systems. (c) The comparison of SMX degradation efficiency by different pH in PMS system.

The pH value is a critical parameter influencing the efficiency and effectiveness of catalyst-activated persulfate (PMS) degradation of antibiotics. Variations in pH levels can alter the type and quantity of radicals generated, the stability and reactivity of the antibiotic, and the performance of the catalyst. In this study, the effect of different initial pH values on the degradation of SMX in the Cu-P/POP/PMS system was systematically evaluated. As shown in **Fig. 5-10a and b**, the Cu-P/POP/PMS system

demonstrated remarkable versatility and achieved efficient SMX degradation over a broad pH range (3.0–11.0). Interestingly, in contrast to most previous studies on PMS-based degradation of organic pollutants, the Cu-P/POP/PMS system did not show a preference for acidic environments and exhibited superior performance under alkaline conditions. This discrepancy may be attributed to the specific radicals and non-radicals generated during PMS activation, as well as the base-facilitated activation of PMS, both of which likely contribute to the observed results. **Fig. 5-10c** further illustrates the degradation efficiency of SMX by PMS alone across different pH levels. Under alkaline conditions, no significant acceleration in SMX degradation was observed, effectively ruling out the possibility that PMS activation in alkaline environments contributes to the degradation of SMX. Thus, the observed enhanced degradation is likely due to the radicals and non-radical species generated upon PMS activation by Cu-P/POP, which accelerate the degradation of SMX under alkaline conditions.

To validate the aforementioned hypothesis, we further identified the active species involved in the Cu-P/POP/PMS system under varying pH conditions. Tert-butyl alcohol (TBA), methanol (MeOH), p-benzoquinone (PBQ), L-histidine (L-His), and dimethyl sulfoxide (DMSO) were utilized as scavengers to target hydroxyl radicals (·OH), sulfate radicals ($SO_4^{\cdot -}$), superoxide radicals ($O_2^{\cdot -}$), singlet oxygen ($^1O_2$), and highly reactive volatile organic species (HVMO), respectively. The radical pathways in the Cu-P/POP/PMS system under alkaline conditions were initially explored in detail to pinpoint the active species responsible for the efficient degradation of SMX.

3.3.3 Mechanism of PPC Degradation of RAN

3.3.3.1 Identification of Dominant Active Species

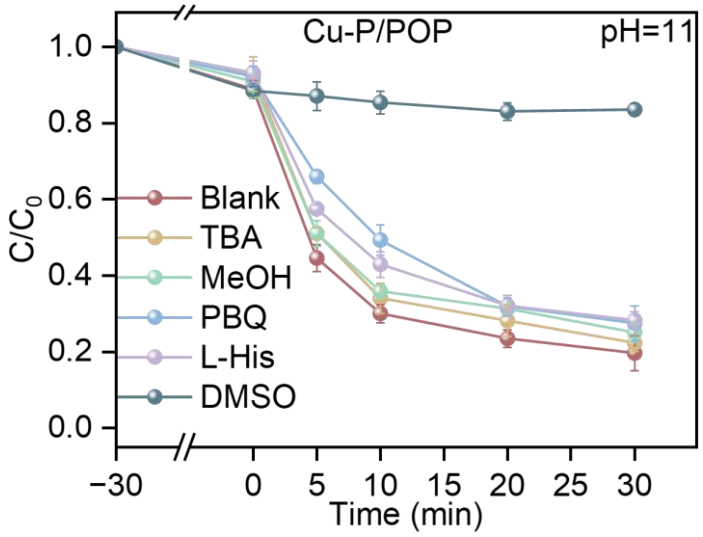

Fig. 5-11 Effect of scavengers on SMX degradation in Cu-P/POP/PMS.

Methanol (MeOH) is commonly used as a quencher for both hydroxyl radicals (•OH) and sulfate radicals ($SO_4^{\bullet-}$) due to its comparable reaction rates with these species ($\mathbf{k}_{\bullet OH/MeOH}$ = 1.6–7.7 × 10^7 M^{-1} s^{-1}, $\mathbf{k}_{SO_4^{\bullet-}/MeOH}$ = 9.7 × 10^8 M^{-1} s^{-1}). Tert-butanol (TBA) exhibits a stronger selectivity for reacting with •OH radicals, as indicated by its higher reaction rate constant ($\mathbf{k}_{\bullet OH/TBA}$ = 3.8–7.6 × 10^8 M^{-1} s^{-1}) compared to $\mathbf{k}_{SO_4^{\bullet-}/TBA}$ = 4–9.1 × 10^5 M^{-1} s^{-1}. When TBA and MeOH were introduced as scavengers in the Cu-P/POP/PMS system to quench •OH and $SO_4^{\bullet-}$, respectively, their contribution to SMX degradation was found to be negligible (**Fig. 5-11**). To further investigate the role of superoxide radicals ($O_2^{\bullet-}$), p-benzoquinone (PBQ) was employed as a quencher. Upon the addition of PBQ, the reaction rate constant (**k**) decreased to 0.0363 min^{-1}, suggesting the presence of $O_2^{\bullet-}$. However, the minimal impact on SMX degradation indicated that $O_2^{\bullet-}$ was not the primary reactive spe. Beyond radical-based pathways, non-radical pathways may also contribute to the smx removal process in the system. To assess this possibility, L-histidine (L-His) was used as a scavenger to detect the presence of singlet oxygen ($^1O_2$).

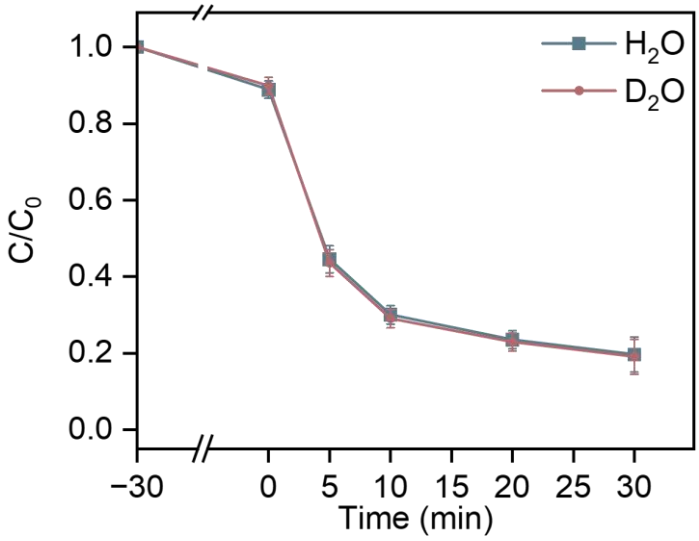

Fig. 5-12. The degradation of SMX by the Cu-P/POP/PMS systems in H_2O and D_2O solvent.

The degradation of SMX showed only a minor effect with the addition of L-histidine (L-His), indicating that singlet oxygen ($^1O_2$) may not play a significant role in the process. To further confirm the involvement of $^1O_2$, a solvent exchange experiment was conducted, switching from H_2O to D_2O. The lifetime of $^1O_2$ in D_2O is significantly longer than in H_2O, and if $^1O_2$ were actively involved in the degradation of SMX, the degradation efficiency would be expected to improve in the D_2O system.

However, as shown in **Fig. 5-12**, SMX degradation was not enhanced in the D_2O system, which suggests that $^1O_2$ does not play a significant role in the degradation of SMX in the Cu-P/POP/PMS system. This finding further supports the conclusion that radical pathways, particularly the generation of sulfate radicals ($SO_4^{\cdot -}$), are the dominant mechanisms for the efficient degradation of SMX in this system.

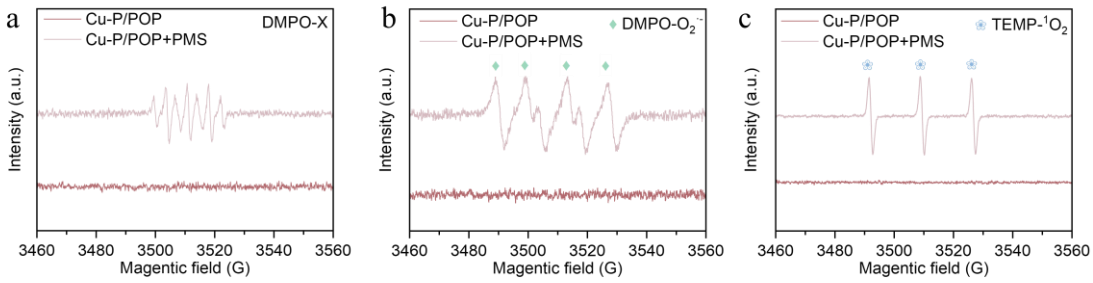

Fig. 5-13. EPR spectra of (a) DMPO-$SO_4^{\cdot -}$ and DMPO-·OH, (b) DMPO-$O_2^{\cdot -}$, and (c) TEMP-$^1O_2$ in Cu-P/POP/PMS systems.

To further confirm the presence of reactive oxygen species (ROS) in the Cu-P/POP/PMS system, electron paramagnetic resonance (EPR) spectroscopy was conducted. The results revealed that the addition of PMS generated both superoxide radicals ($O_2\cdot^-$) and singlet oxygen ($^1O_2$) (**Fig.5-13b and c**), although the detected signals for DMPO-$O_2\cdot^-$ and TEMP-$^1O_2$ were relatively weak. This indicates the generation of these species, but their contributions to the overall degradation process might be limited.

DMPO was used as a trapping agent for hydroxyl radicals (·OH) and sulfate radicals ($SO_4\cdot^-$). However, the expected EPR signals for DMPO-·OH (a typical 1:2:2:1 quartet) and DMPO-$SO_4\cdot^-$ (a 1:1:1:1:1:1 sextet) did not appear (**Fig. 5-13a**). Instead, a strong DMPO-X signal was observed, which suggests that other species, such as high-valent copper-oxo species, may be playing a dominant role in the oxidation process. This is consistent with the quenching experiments, which indicated that ·OH, $SO_4\cdot^-$, $O_2\cdot^-$, and $^1O_2$ are not the primary active species in the system.

These findings imply that, in addition to the commonly known ROS, other reactive species—likely related to copper-based species, such as copper-oxo complexes—are responsible for the efficient degradation of SMX in the Cu-P/POP/PMS system. These species, formed via PMS activation, may be the key contributors to SMX oxidation.

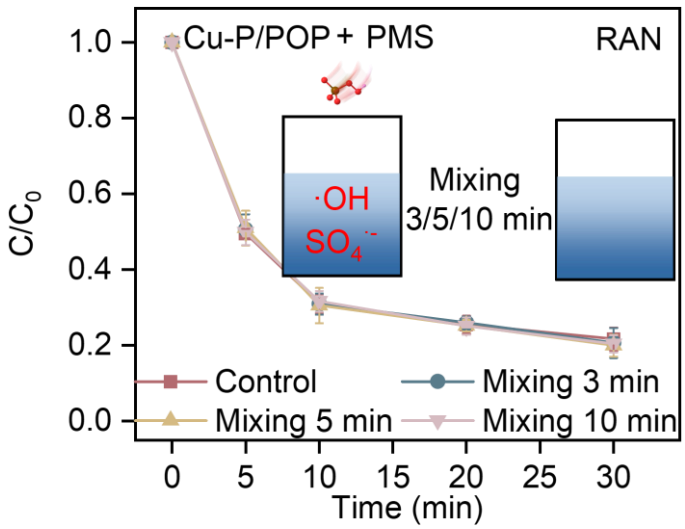

Fig. 5-14. TC oxidation via a premixture of Cu-P/POP and PMS at estimated time intervals.

To further investigate the role of radicals in the oxidation of SMX within the Cu-P/POP/PMS system, a premixing experiment was conducted. In this experiment, Cu-P/POP and PMS were premixed for varying time intervals before adding SMX. This approach allows for the immediate generation of radicals in the system, leading to the consumption of PMS. Therefore, the degradation of pollutants is expected to be influenced by the availability of radicals at the time the pollutants are introduced into the system. This setup enables a more accurate assessment of the role of free radicals in the catalytic process.

If the oxidation mechanism were dominated by radicals, the premixing of Cu-P/POP and PMS would likely result in significant inhibition of SMX oxidation, due to the consumption of PMS before SMX could be introduced. However, the results showed that premixing Cu-P/POP and PMS for 3, 5, and 10 minutes only led to a slight inhibition of SMX oxidation (**Fig. 5-14**). This indicates that while radicals were generated in substantial quantities and contributed to SMX degradation, non-radical species, which are not $^1O_2$, appear to play a dominant role in the oxidation of SMX. Therefore, the overall oxidation mechanism involves a combination of both radical and non-radical pathways, with non-radical species significantly influencing the efficiency of SMX degradation in the Cu-P/POP/PMS system.

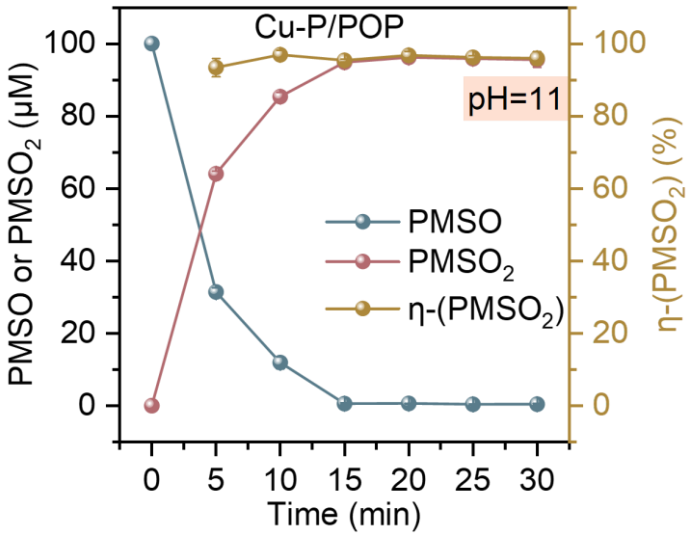

Fig. 5-15. PMSO consumption, $PMSO_2$ production, and η-($PMSO_2$) in the Cu-P/POP/PMS system at pH=11.

This hypothesis was further supported by the detection of methyl phenyl sulfone ($PMSO_2$) during the oxidation of methyl phenyl sulfoxide (PMSO) by the Cu-P/POP/PMS system (**Fig. 5-15**). In this process, PMSO can be converted to $PMSO_2$ via an oxygen transfer step mediated by Cu(III)=O, a high-valent copper-oxo species, highlighting the non-radical pathway involved in the degradation. On the other hand, the oxidation of PMSO by free radicals, such as ·OH and $SO_4{\cdot}^-$, leads to the formation of hydroxylated and/or polymeric products, as indicated by their respective reaction rate constants (k ·OH/PMSO = 3.61×10^9 M^{-1} s^{-1} and k $SO_4{\cdot}^-$/PMSO = 3.17×10^8 M^{-1} s^{-1}) [41, 46-48]. This further validates the dual role of both radical and non-radical species in the oxidation process and underscores the importance of Cu(III)=O species in facilitating non-radical PMS activation for SMX degradation.

In summary, while free radicals contribute to the oxidation process, the Cu(III)=O species and other non-radical species appear to play a dominant role, particularly in cases where PMSO oxidation is involved.

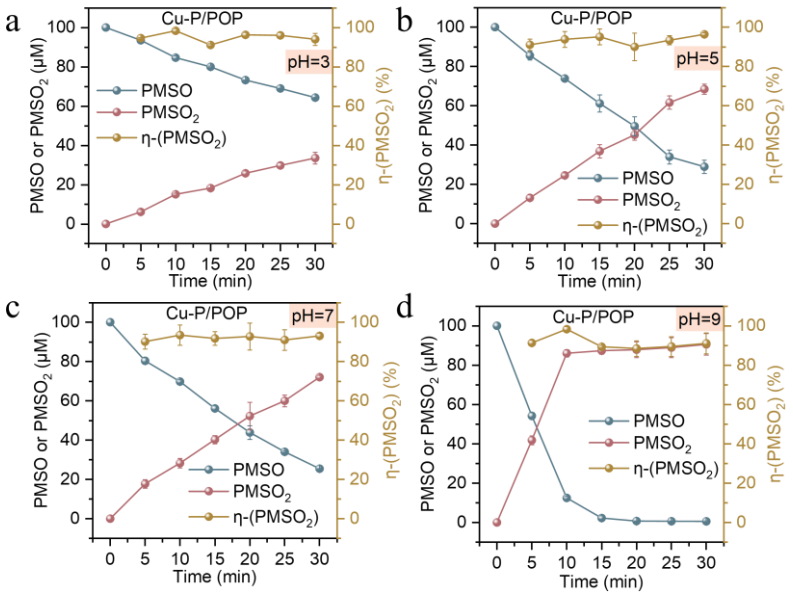

Fig. 5-16. (a)-(d) PMSO consumption, $PMSO_2$ production, and η-($PMSO_2$) in the Cu-P/POP/PMS system at different pH.

As shown in **Fig. 5-16(a-d)**, Cu(III)=O species were found to effectively oxidize PMSO across a wide pH range (pH 3.0–11.0), with the highest PMSO removal observed at pH 11.0. The consumption of PMSO was closely matched by the production of $PMSO_2$ (μ-$PMSO_2$ near 100%) at all pH values studied, further suggesting that the Cu(III)=O species were actively involved in the oxidation process. This observation is significant because if free radicals were the main contributors to the reaction, the efficiency of $PMSO_2$ production would not have been so high. The nearly complete conversion of PMSO to $PMSO_2$ at all tested pH values strongly supports the role of Cu(III)=O in the degradation process, ruling out the possibility of free radicals being the primary oxidants in this system. Thus, these findings emphasize the pivotal role of Cu(III)=O species in driving the non-radical oxidation pathway, particularly in the degradation of PMSO and other pollutants within the Cu-P/POP/PMS system.

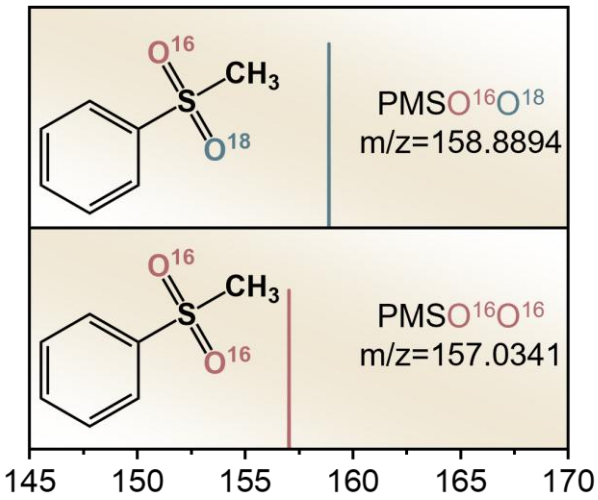

Fig. 5-17. high-resolution mass spectrometry analyses of O^{18}-labeled $PMSO_2$ generated in H_2O^{18} matrix.

The spontaneous exchange of oxygen atoms between the intermetallic Cu–O bond and solvent water provides additional evidence for the formation of Cu(III)=O and its involvement in oxidation reactions. To further investigate this, the reaction was conducted using O_{18}-isotope-labeled H_2O_{18} as the solvent. Under these conditions, Cu(III)=O would undergo a spontaneous O-atom exchange with H_2O_{18}, forming

Cu(III)=O_{18}. This species would then proceed to oxidize PMSO, resulting in the formation of $PMSO_{16}O_{18}$. As expected, the oxidation product $PMSO_{16}O_{18}$ was detected in this study.

The presence of $PMSO_{16}O_{18}$ was confirmed through mass spectrometry, specifically by observing the two peaks in the extracted ion chromatogram at m/z = 157.0341 ($PMSO_{16}O_{16}$) and m/z = 158.8894 ($PMSO_{16}O_{18}$) (**Fig. 5-17**). These findings provide direct evidence that Cu(III)=O plays an intermediate role in the oxidation process within the Cu-P/POP/PMS system, further corroborating its critical function in facilitating non-radical oxidation pathways. This result supports the hypothesis that Cu(III)=O is the primary oxidant involved in the degradation process, rather than free radicals or other reactive species.

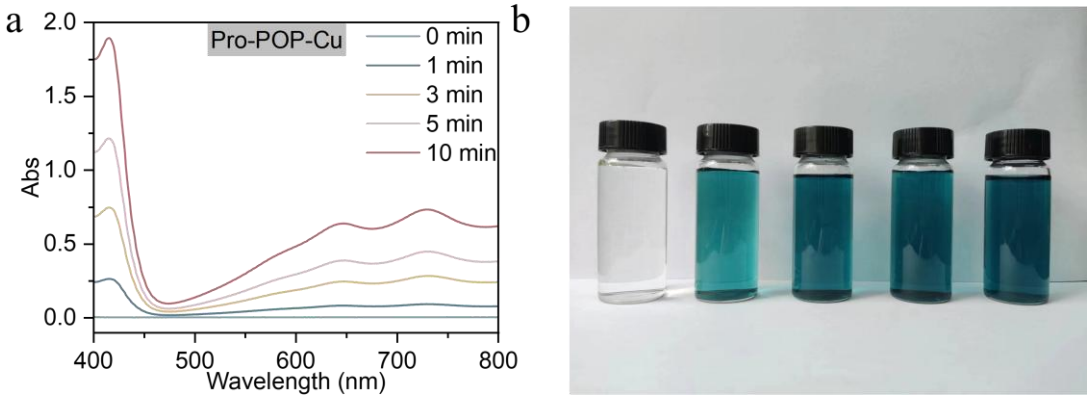

Fig. 5-18. (a) and (b) The UV–Visible absorption spectra of the Cu-P/POP/PMS system were quenched by ABTS.

Additionally, 2,2'-azinodi(3-ethylbenzothiazoline-6-sulfonic) acid (ABTS) is commonly used as a probe to detect high-valent metal oxides through one-electron oxidation. When oxidized, ABTS is converted into its radical cation form ($ABTS^{\cdot+}$), causing a noticeable color change to blue. The formation of $ABTS^{\cdot+}$ can be monitored by UV-visible spectroscopy, with characteristic absorption peaks observed around 415 nm and 660 nm.

In this study, changes in the UV-visible spectrum of ABTS during the Cu-

P/POP/PMS catalytic oxidation process provided further evidence for the generation of Cu(III)=O species. The spectral shifts associated with the oxidation of ABTS indicate the involvement of Cu(III)=O in the reaction (**Fig. 4-18**). This observation supports the hypothesis that Cu(III)=O is an active species in the Cu-P/POP/PMS system, playing a central role in the oxidation of pollutants through non-radical mechanisms (Eq. (5-1)).

This ABTS assay complements the previous findings, offering additional validation for the involvement of Cu(III)=O in the catalytic oxidation process, further confirming its role as a key oxidative species in the system.

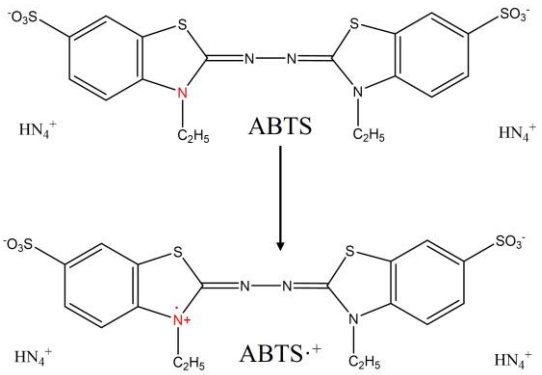

(5-1)

5.3.4 Potential superiority in environmental applications

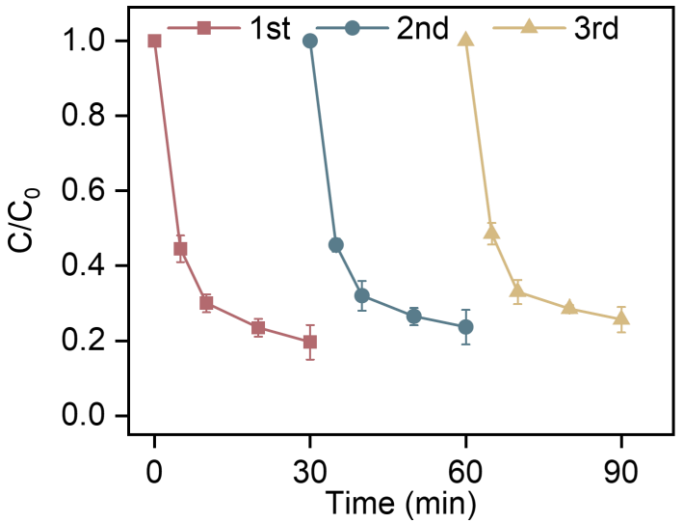

Fig. 5-19. Cycling test of Cu-P/POP for the SMX degradation in Cu-P/POP/PMS.

Fig. 4-19 illustrates that the removal efficiency of SMX remains at 74.37% after

five successive degradation cycles, demonstrating that Cu-P/POP exhibits excellent reusability and stability. This result indicates that the catalyst maintains its catalytic activity over multiple cycles, highlighting its potential for practical applications in pollutant degradation. The good reusability of Cu-P/POP suggests minimal deactivation or loss of active sites, which is crucial for its long-term use in environmental remediation processes.

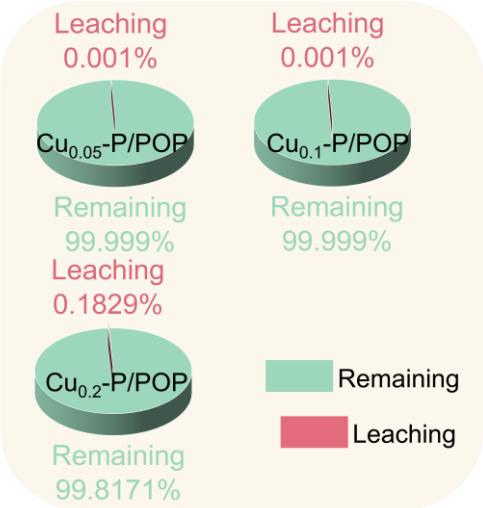

Fig. 5-20. The percentage of leached Cu in $Cu_{0.05}$-P/POP, Cu -P/$POP_{0.1}$ and $Cu_{0.2}$-P/POP determined by ICP after reaction in 30 min.

Furthermore, ICP analysis was conducted to assess whether the catalyst would cause significant metal pollution during its use. As shown in **Fig. 5-20**, the leaching concentration of Cu from Cu-P/POP was found to be 0.0036 mg/L. This result suggests that Cu-P/POP exhibits excellent stability and minimal metal leaching, which makes it more environmentally friendly. The low level of Cu leaching indicates that the catalyst is unlikely to contribute to environmental contamination, ensuring its suitability for practical applications where sustainability and safety are important considerations.

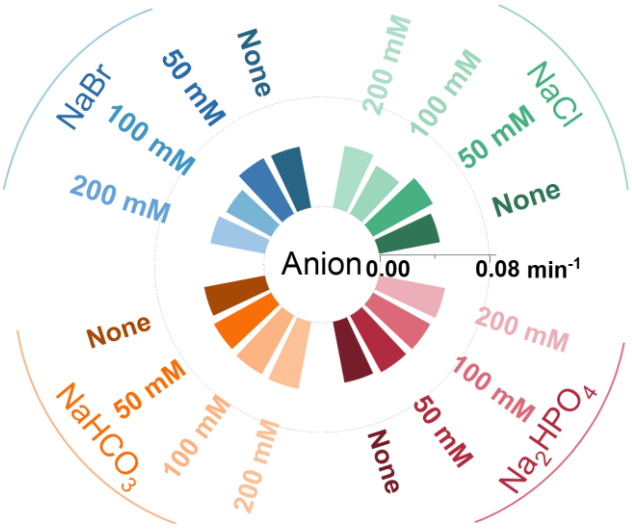

Fig. 5-21. Influences of the degradation of coexisting inorganic ions in Cu-P/POP/PMS system.

Various ions were involved in the actual aqueous matrices to evaluate their influence on SMX removal. As shown in **Fig. 5-21**, ions such as Cl^-, Br^-, HCO_3^-, and HPO_4^{2-} exhibited minimal effects on the degradation of SMX. This suggests that Cu-P/POP is highly resistant to interference from non-target background substances, maintaining its catalytic efficiency even in complex aqueous environments. This resistance to common ions further highlights the robustness and practicality of Cu-P/POP for real-world applications, where diverse ionic species are often present.

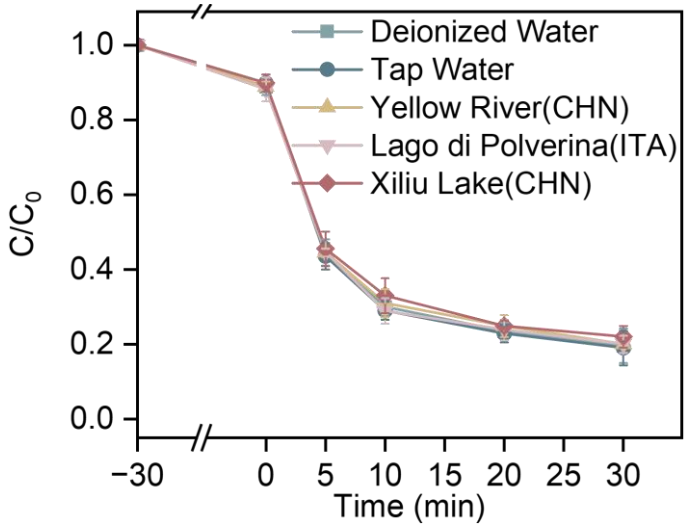

Fig. 5-22. Different water sources in Cu-P/POP/PMS system.

Moreover, as shown in **Fig. 5-22**, nearly 80% of SMX was removed within 30 minutes across various water samples, including deionized water, tap water, water from the Yellow River (China), a natural lake (Italy), and Xiliu Lake (Henan). This demonstrates the broad applicability of the Cu-P/POP/PMS system in real-world water environments, highlighting its potential for efficient SMX degradation in diverse and complex water matrices. The system's effectiveness across different water sources further underscores its practical viability for environmental remediation applications.

This thus demonstrates that the Cu-P/POP catalyst could enable the efficient utilization of Cu atoms. We conducted an economic analysis to determine the feasibility of the Cu-P/POP /PMS system for actual use in electrical energy per order (EE/O) scenarios.

The electrical energy per order (EE/O) has been used as a popular approach for evaluating the energy and cost of reaction system. It is defined as electrical required to reduce the content of a specific pollutant by one order of magnitude. This method often involves consumed electrical energy and chemicals, where the catalyst is usually assumed to be reusable so it is not considered a consumable in the system. Herein, the economic evaluation of the optimal Cu-P/POP /PMS system was performed based on the EE/O_{total} using the following Equations **(5-2), (5-3)**, and **(5-4)**. Due to the lack of input of external energy such as light and ultrasonic energy in the Cu-P/POP /PMS system, the external energy input was zero. Therefore, the value of EE/O_{total} would be converted from PMS/O. According to the literature, the non-house electrical energy cost and PMS were estimated to be 0.1319 \$/kWh and 1.30 \$/kg. Thus, the electrical energy cost of PMS was calculated as 9.85 kWh/kg. Then, based on the results of the **Fig. 5-9a**, 99% of SMX was removed and 70% of PMS was consumed within 30 min. The calculated EE/O_{total} value of the Cu-P/POP /PMS system was 0.001 kWh/m3, and the corresponding cost was 0.0001 $\$/m^3$. The cost was almost lower than that of advanced oxidation processes (AOPs) in previously reported literature. Based on the analysis, our Cu-P/POP /PMS system presented a much more promising application

potential in terms of cost and environmental friendliness.

$$EE/O_{Total} = EE/O_{Energy} + EE/O_{Chemicals} = EE/O_{Chemicals} \quad (5\text{-}2)$$

$$EE/O_{Chemicals} = PMS/O = \frac{[PMS]_0 - [PMS]_f}{log\left(\frac{C_i}{C_f}\right)}(mg/L) \quad (5\text{-}3)$$

$$In\left(\frac{C_i}{C_f}\right) = k \times t \quad (5\text{-}4)$$

Where $[PMS]_0$ and $[PMS]_f$ are the concentration (mg/L) of PMS at the reaction time of 0 and t (min), respectively. t is reaction time (min), C_i is the initial concentration of SMX and C_f is the concentration of SMX after reaction time of t mins with the unit of mg/L, respectively.

According to our calculations, the Cu-P/POP /PMS system had an EE/O_{total} value of 0.001 kWh/m^3, with a corresponding cost of \$0.0001/m^3. This cost is lower than that of AOPs reported in other studies. Taken together, our findings can be used as a reference for establishing highly efficient and economical Fenton-like systems by regulating CuN4 coordination.

5.4 Conclusion

In this study, a copper porphyrin-based porous organic polymer (Cu-P/POP) was successfully synthesized and employed as an efficient PMS activator for the degradation of sulfamethoxazole (SMX). The well-defined Cu-N_4 coordination structure facilitated effective electron transfer and promoted the formation of high-valent Cu(III)=O species, which were identified as the primary reactive species responsible for SMX degradation through a non-radical oxidation pathway. Quenching experiments and EPR spectroscopy confirmed the negligible contributions of conventional radicals (•OH, SO_4•$^-$, and O_2•$^-$), further validating the selective oxidation mechanism of Cu(III)=O. Additionally, the Cu-P/POP catalyst demonstrated high

stability, excellent recyclability, and minimal Cu leaching, making it an environmentally friendly and cost-effective alternative for wastewater treatment. The system maintained its efficiency across various water matrices and showed strong resistance to interference from background ions. An economic analysis further highlighted the low operational cost and high feasibility of the Cu-P/POP/PMS system for real-world applications. This study not only advances the understanding of PMS activation mechanisms but also provides a promising strategy for designing high-performance catalysts for the removal of emerging organic contaminants in aqueous environments.

6. Study on the Degradation Performance of Organic Pollutants by Metal-Porphyrin Porous Organic Polymers

Abstract:

Organic pollutants, particularly persistent organic pollutants (POPs), pose severe environmental and health risks due to their resistance to degradation, bioaccumulation, and toxicity. Advanced oxidation processes (AOPs), especially peroxymonosulfate (PMS)-based systems, have emerged as promising solutions for their removal. In this study, metal-porphyrin porous organic polymers (M-P/POP, where M = Fe, Co, or Cu) were synthesized and employed as catalysts for PMS activation to degrade organic pollutants.[121-124] The well-defined M-N_4 coordination structure facilitated efficient PMS activation, leading to the selective generation of high-valence metal oxo species (HVMOs: Fe(IV)=O, Co(IV)=O, and Cu(III)=O) as the primary oxidative agents.[51, 52, 125-128] Compared to radical-based degradation pathways, the M-P/POP/PMS system exhibited enhanced stability, high selectivity, and superior catalytic efficiency through a non-radical electron transfer mechanism. Experimental results demonstrated that Fe-P/POP and Co-P/POP outperformed Cu-P/POP, achieving nearly 100% pollutant degradation efficiency across a wide range of organic contaminants, including pharmaceuticals and industrial chemicals. Theoretical calculations, including density functional theory (DFT) and molecular orbital (MO) analysis, revealed a strong correlation between pollutant ionization potential (IP) and degradation rate, confirming that electron transfer from pollutant HOMO to catalyst LUMO was the dominant degradation pathway. Additionally, the system exhibited excellent recyclability, negligible metal leaching, and high resistance to background ions, making it a cost-effective and sustainable approach for wastewater treatment. This study provides critical insights into PMS activation mechanisms and highlights M-P/POP as a promising catalyst for environmental remediation.

Keywords: M-P/POP; IP; HOMO-LOMO; HVMO.

6.1 Introduction

Organic pollutants, a broad class of chemical compounds, are characterized by the presence of carbon atoms bonded to hydrogen, oxygen, nitrogen, or other elements. These pollutants often originate from industrial, agricultural, and domestic activities and include a wide range of substances such as pesticides, pharmaceuticals, personal care products, petrochemicals, and industrial solvents. Among these, persistent organic pollutants (POPs) are of particular concern due to their resistance to environmental degradation, bioaccumulation, and potential toxicity to both aquatic ecosystems and human health.

Water bodies are essential components of the global ecosystem, providing habitats for a vast array of aquatic species and serving as critical resources for human consumption, agriculture, and industry. However, the release of organic pollutants into aquatic environments has become a significant environmental issue. These pollutants often enter water bodies through various pathways, including direct discharge from industrial effluents, runoff from agricultural fields, and leakage from waste disposal sites. Their presence in water systems is a major concern due to their detrimental effects on water quality, aquatic life, and public health.

The impact of organic pollutants on water bodies is profound and multifaceted. First, many organic pollutants exhibit high toxicity to aquatic organisms, disrupting cellular processes and causing acute or chronic health effects. Fish, amphibians, and other aquatic life forms can suffer from altered behavior, impaired reproduction, and even mortality when exposed to high concentrations of these chemicals. Second, the presence of organic pollutants in water bodies can lead to long-term ecological imbalances. Pollutants may accumulate in the food chain, causing bioaccumulation and biomagnification, which ultimately affect higher trophic levels, including humans who consume contaminated water or aquatic organisms.

Furthermore, organic pollutants can significantly affect the physicochemical properties of water. Many organic compounds reduce the oxygen content in water by promoting microbial decomposition, leading to hypoxic or anoxic conditions that hinder the survival of oxygen-dependent aquatic organisms. Additionally, some organic pollutants are phototoxic and may degrade when exposed to sunlight, releasing harmful by-products that further degrade water quality.

The persistence of organic pollutants in aquatic environments poses additional challenges. These compounds often resist natural degradation processes due to their stable molecular structure, which prevents their breakdown by microorganisms or photochemical reactions. Consequently, the removal of organic pollutants from water sources requires advanced treatment methods, such as physical, chemical, and biological processes, to mitigate their harmful effects.

In conclusion, organic pollutants are a significant threat to aquatic ecosystems and water quality. The complexity of their sources, toxicity, persistence, and long-term environmental impact necessitates the development of effective strategies for pollution control and water treatment. Understanding the behavior of organic pollutants in aquatic environments, as well as the ecological and human health risks associated with their presence, is crucial for the development of sustainable water management practices and pollution remediation technologies.

Advanced Oxidation Processes (AOPs) are a set of powerful water treatment techniques that utilize highly reactive species, such as hydroxyl radicals (·OH), sulfate radicals ($SO_4^{\cdot -}$), and other non-radical species, to degrade organic pollutants in water. These processes are especially effective for treating persistent organic contaminants that are difficult to degrade by conventional methods, including industrial waste, pharmaceuticals, personal care products, pesticides, and other emerging pollutants. AOPs are recognized for their efficiency in breaking down complex, non-biodegradable compounds into simpler, non-toxic substances, ideally resulting in complete mineralization (conversion to CO_2 and H_2O). This makes AOPs an essential tool for environmental remediation, particularly in the context of wastewater treatment and

groundwater decontamination.

The degradation mechanism of AOPs primarily hinges on the generation of reactive oxygen species (ROS). These ROS, including the hydroxyl radical (·OH), are highly reactive and can rapidly attack a wide range of organic pollutants. Hydroxyl radicals, with a standard reduction potential of 2.8 V, are one of the most powerful oxidative agents, capable of breaking the carbon-carbon bonds in organic molecules, thus leading to their degradation. In AOPs, these radicals are typically generated by the activation of oxidants such as hydrogen peroxide (H_2O_2), ozone (O_3), or persulfate (PS), often in combination with catalysts that promote the production of ROS. In addition to radicals, non-radical species like high-valent metal oxides, also known as metal-oxo species, have garnered increasing interest due to their promising role in catalytic oxidation.

High-valent metal oxides, including high-valent cobalt (Co(IV)=O), iron (Fe(IV)=O), and copper (Cu(III)=O), represent an emerging class of non-radical oxidants in AOPs. Unlike traditional radical-based processes, these metal-oxo species facilitate oxidation reactions through a non-radical pathway, offering several advantages for water treatment applications.

1. Strong Oxidizing Power: High-valent metal-oxo species, such as Co(IV)=O, Fe(IV)=O, and Cu(III)=O, possess strong oxidizing power. Their oxidation potentials (Co(IV)=O: 2.3 V, Fe(IV)=O: 2.2 V, Cu(III)=O: 2.5 V) enable them to efficiently degrade a wide range of organic contaminants, often outperforming hydroxyl radicals in certain scenarios. These metal-oxo species can oxidize pollutants by abstracting electrons from organic molecules, leading to the formation of less complex and more biodegradable intermediates.

2. High Selectivity and Stability: One of the main advantages of metal-oxo species is their ability to selectively oxidize pollutants without generating excessive amounts of free radicals, which can lead to over-oxidation or the formation of harmful by-products. Additionally, these species are often more stable than free radicals, allowing for more controlled and sustained oxidation reactions. For example, Fe(IV)=O

is particularly effective in the activation of persulfates (PS) and peroxymonosulfate (PMS), providing a more stable and efficient oxidizing agent than hydroxyl radicals alone.[129-132]

3. Catalytic Efficiency: High-valent metal oxides can act as catalysts in AOP systems, promoting the activation of oxidants like PMS or H_2O_2 without being consumed in the reaction. This catalytic cycle enables these species to be regenerated and reused multiple times, making them highly efficient for continuous treatment processes. This catalytic efficiency reduces the need for high concentrations of oxidants and minimizes waste production, thus improving the sustainability of the treatment process.

4. Non-Radical Pathways: High-valent metal oxides operate through non-radical oxidation mechanisms, which can overcome some limitations of radical-based AOPs. For instance, the generation of non-radical species can help circumvent issues related to the recombination of radicals or the rapid decay of radicals in aqueous solutions. This makes high-valent metal-oxo species a promising alternative when radical-based oxidation processes are less efficient or when more controlled, selective oxidation is required.

5. Broad pH Range: Unlike hydroxyl radicals, whose generation and efficiency are often limited by pH conditions, high-valent metal oxides such as Co(IV)=O, Fe(IV)=O, and Cu(III)=O can operate effectively across a broad pH range (from acidic to slightly alkaline conditions). This feature enhances their versatility and makes them suitable for a wide variety of environmental conditions, especially in cases where pH variability is a concern.

In conclusion, the use of high-valent metal oxides in AOPs offers significant advantages in terms of oxidizing power, stability, selectivity, and catalytic efficiency. By enabling non-radical oxidation pathways, these species provide a valuable alternative to traditional radical-based processes, making them particularly effective for the degradation of persistent organic pollutants in diverse environmental matrices. The ability of these metal-oxo species to operate over a broad pH range and their high

catalytic efficiency further enhance their applicability in practical water treatment and environmental remediation.

Porous organic polymers (POPs) have garnered significant attention in recent years due to their unique properties, including high surface area, tunable pore structures, and exceptional chemical stability. These features make them ideal candidates for a wide range of applications, including gas storage, catalysis, and environmental remediation. POPs are typically synthesized through the polymerization of organic monomers that can self-assemble into highly porous structures, creating materials with significant potential for various catalytic processes.

One promising approach is the incorporation of metal centers into these organic frameworks, particularly through the use of porphyrin-based monomers. Porphyrins are organic macrocycles with highly conjugated structures that can readily coordinate with metal ions, making them excellent building blocks for creating metal-loaded POPs (M-POPs). The integration of metal ions into the porphyrin structure not only stabilizes the material but also imparts unique catalytic properties, particularly in advanced oxidation processes (AOPs).

In AOPs, reactive oxygen species (ROS) such as hydroxyl radicals (·OH), sulfate radicals ($SO_4^{\cdot -}$), and singlet oxygen ($^1O_2$) are crucial for the degradation of organic pollutants. Porphyrin-based POPs, especially when loaded with transition metals such as Co, Fe, or Cu, can activate persulfate (PMS) to produce high-valent metal-oxo species, such as Co(IV)=O, Fe(IV)=O, and Cu(III)=O. These high-valent metal species exhibit strong oxidative power, which enhances their ability to break down recalcitrant organic pollutants. The high stability and well-defined structure of M-POPs make them particularly effective in PMS activation, facilitating the generation of ROS without significant degradation of the catalyst over time.The unique advantage of M-POPs in AOPs lies in their ability to generate high-valent metal species under mild conditions, which are essential for efficient oxidation. These metal species can effectively attack organic contaminants, leading to their degradation into smaller, non-toxic molecules. Additionally, M-POPs exhibit enhanced stability and reusability, making them ideal for

practical applications in wastewater treatment and environmental cleanup.

Inspired by the biomimetic heme-porphyrin system, this study reports the synthesis of metal-porphyrin-based porous organic polymers (M-P/POP, where M = Fe, Co, or Cu). These materials were fabricated through a polymerization–metal encapsulation strategy, enabling the repeated assembly of M-N_4-C units into a fully conjugated organic framework.[56, 59, 133-135] The resulting M-P/POP structures feature well-defined and stable M-N_4-C active centers, characterized by an abundance of single-atom metal sites. The π-conjugated structure facilitates efficient electron transfer, making M-P/POP an effective activator in peroxymonosulfate (PMS)-based advanced oxidation processes (AOPs).Compared to conventional M-N_4 sites, the precisely defined M-N_4 environment establishes a uniformly charged microenvironment, leading to a symmetric charge distribution. This fine-tuning of the electronic structure modifies the antibonding orbitals of the active metal centers, which in turn influences their catalytic behavior in PMS activation. Experimental results indicate that, in contrast to the radical-based M-N_4-C/PMS system, the fully conjugated M-N_4-C structure in the M-P/POP/PMS system—achieved via polymerization–metal encapsulation—enables nearly 100% generation of high-valence metal oxo species (HVMO = Fe(IV)=O, Co(IV)=O, and Cu(III)=O). Furthermore, selective formation of distinct HVMOs can be controlled by encapsulating different transition metals, thereby allowing tailored degradation of organic pollutants in aqueous systems.In this study, 12 commonly studied organic pollutants were selected from the literature, and their key parameters—including ionization potential (IP), highest occupied molecular orbital (HOMO), and lowest unoccupied molecular orbital (LUMO)—were evaluated. The relationship between these parameters and the oxidative degradation performance of pollutants in the fully conjugated M-N_4-C M-P/POP/PMS system was further elucidated.

6.2. Catalyst Preparation

The preparation method can be found in Chapter 3.2.1, Chapter 4.2.1 and Chapter

6.3 Results and Discussion

6.3.1 Characterization Analysis of M-P/POP

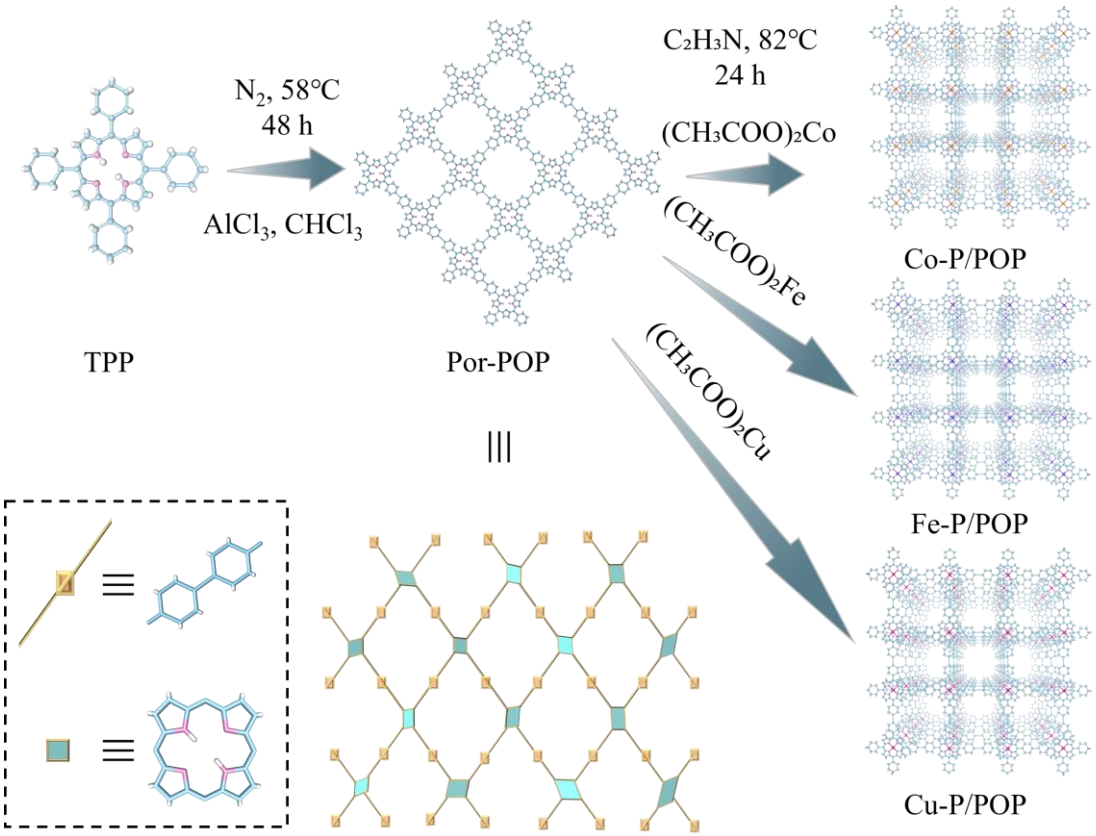

Fig. 6-1. Schematic illustration of the preparation procedures of the M (Co, Fe, and Cu)-P/POP samples.

Fig. 6-1. illustrates the preparation process of Metal-Porphyrin-Porous Organic Polymers (M-P/POP, where M = Co, Fe, or Cu). Tetraphenylporphyrin served as the structural unit for constructing a porous organic polymer (POP) with an extensively conjugated microporous network through a Friedel–Crafts alkylation coupling reaction, catalyzed by $AlCl_3$ under an inert nitrogen atmosphere. During the reaction, hydrogen atoms on the porphyrin's aromatic rings were substituted with alkyl groups, whereas

the pyrrolic nitrogen atoms within the porphyrin framework remained unreacted. Consequently, these pyrrolic nitrogen atoms were retained, providing coordination sites for subsequent metal incorporation.

To synthesize M-P/POP, the obtained porous polymer (P/POP) was metallized with Fe(II), Co(II), or Cu(II) in acetonitrile, yielding Fe-P/POP, Co-P/POP, and Cu-P/POP, respectively. These metals were selected due to their strong capability in activating peroxymonosulfate (PMS) and generating reactive species, thereby enhancing the catalytic performance of the resulting materials in advanced oxidation processes.

6.3.2 Catalytic performance

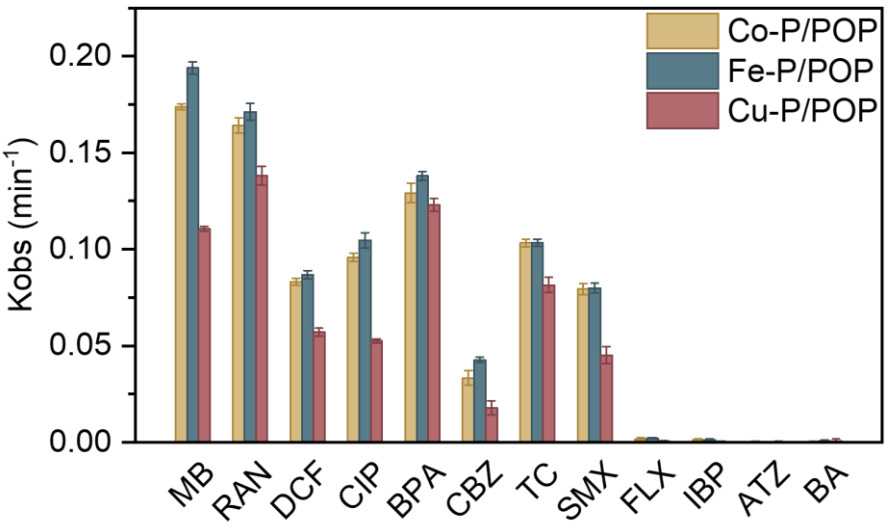

Fig. 6-2. The degradation rate constants (K) of 12 organic pollutants in the M (Co, Fe, and Cu)-P/POP/PMS systems at pH = 11.

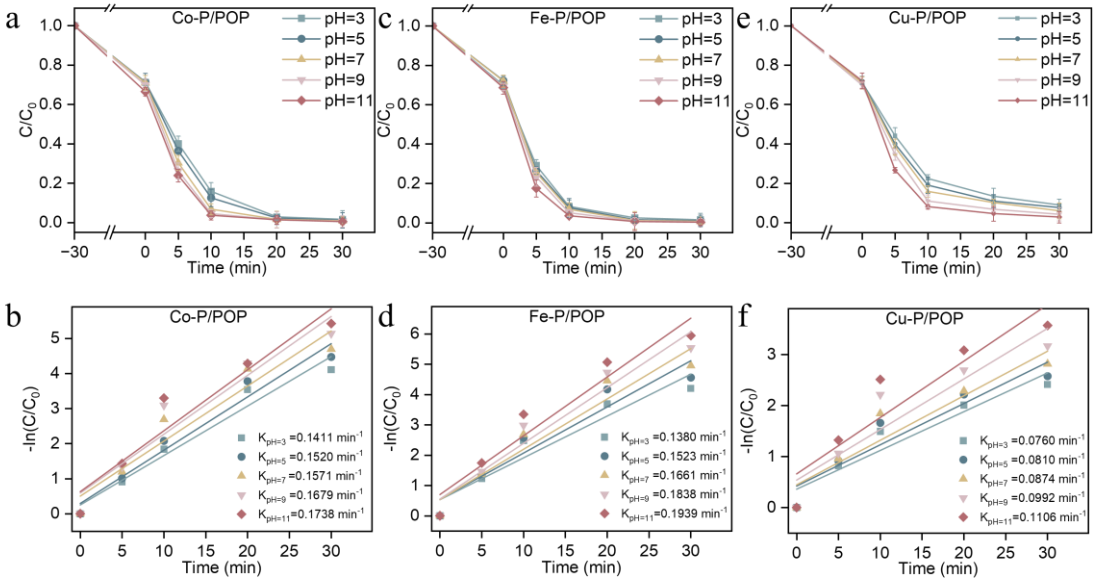

Fig. 6-3. The degradation rate constants (K) of MB in the M (Co, Fe, and Cu)-P/POP/PMS systems at different pH conditions.

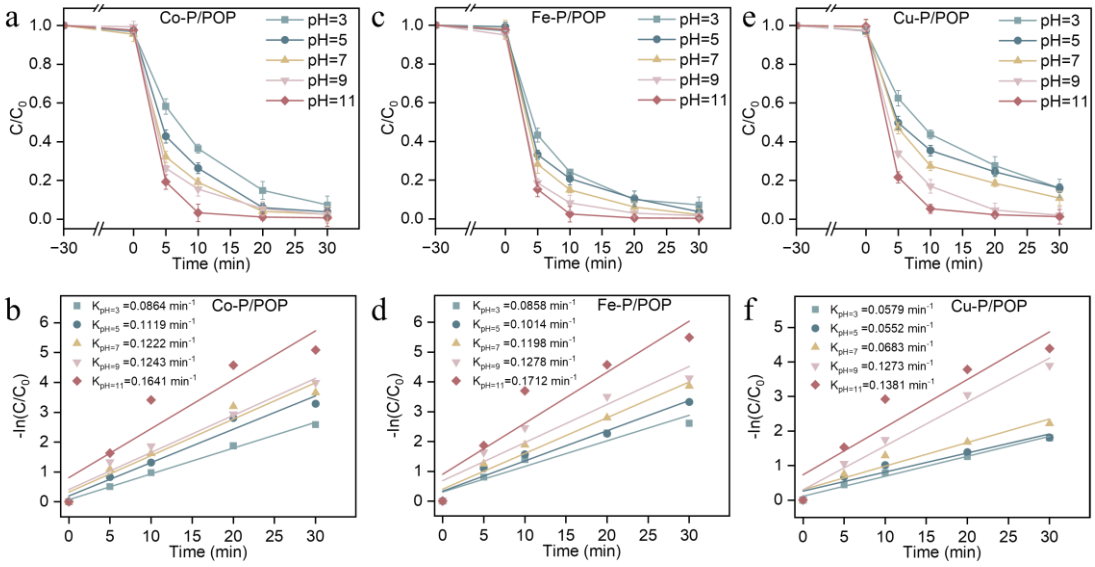

Fig. 6-4. The degradation rate constants (K) of RNA in the M (Co, Fe, and Cu)-P/POP/PMS systems at different pH conditions.

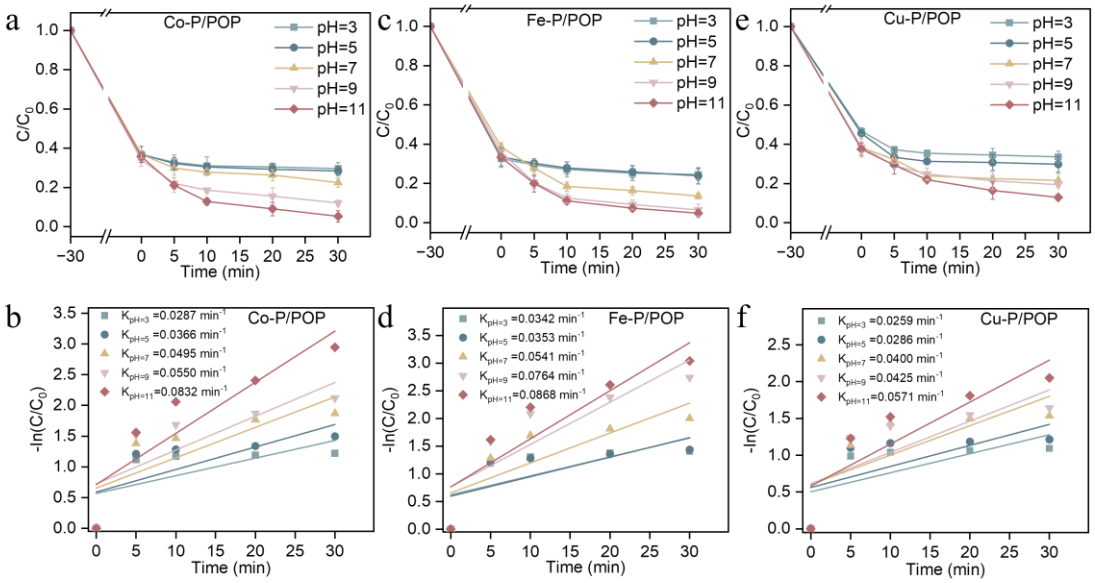

Fig. 6-5. The degradation rate constants (K) of DCF in the M (Co, Fe, and Cu)-P/POP/PMS systems at different pH conditions.

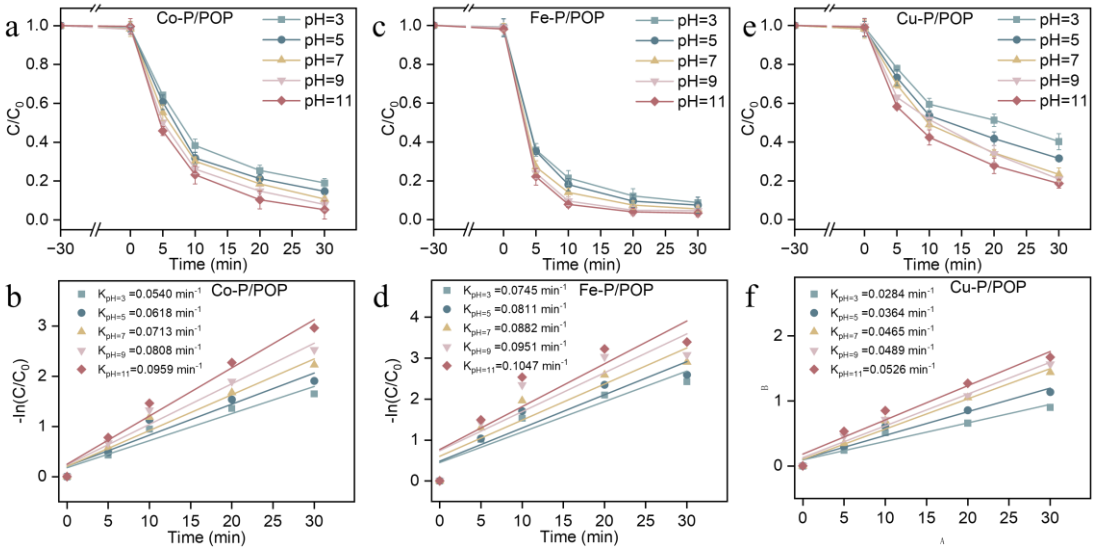

Fig. 6-6. The degradation rate constants (K) of CIP in the M (Co, Fe, and Cu)-P/POP/PMS systems at different pH conditions.

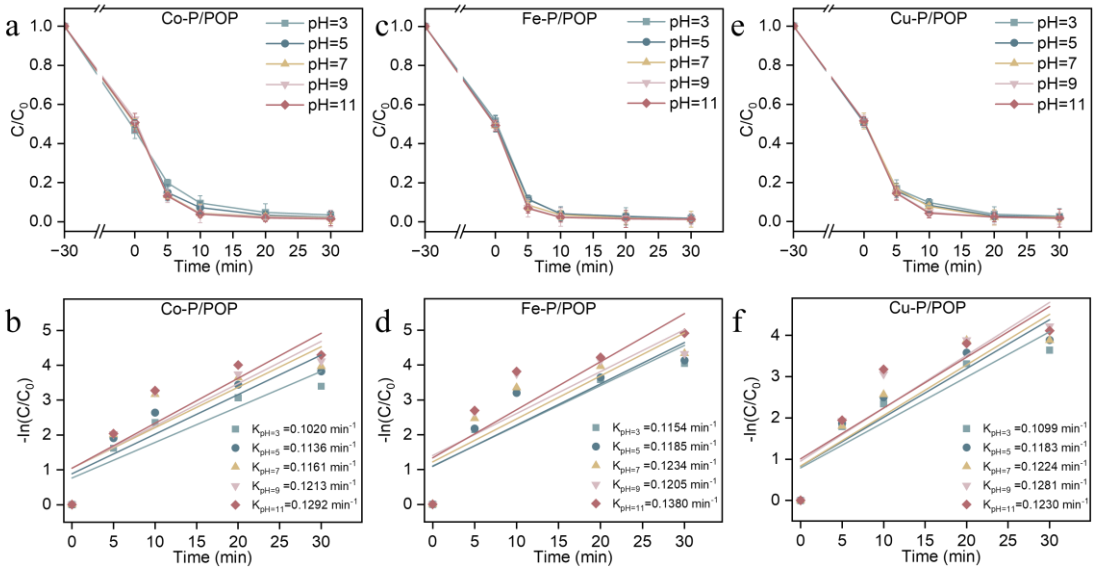

Fig. 6-7. The degradation rate constants (K) of BPA in the M (Co, Fe, and Cu)-P/POP/PMS systems at different pH conditions.

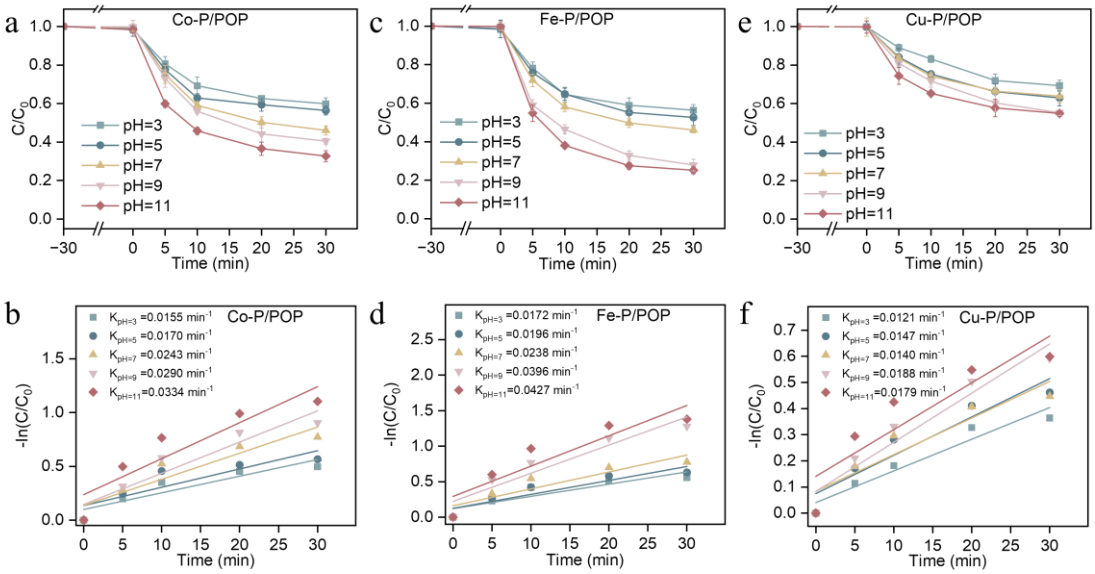

Fig. 6-8. The degradation rate constants (K) of CBZ in the M (Co, Fe, and Cu)-P/POP/PMS systems at different pH conditions.

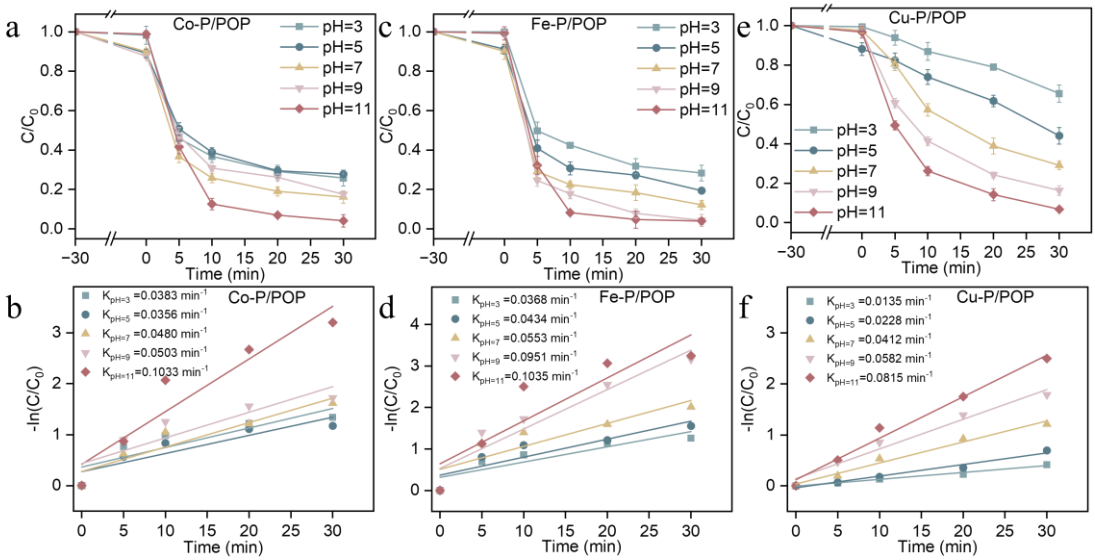

Fig. 6-9. The degradation rate constants (K) of TC in the M (Co, Fe, and Cu)-P/POP/PMS systems at different pH conditions.

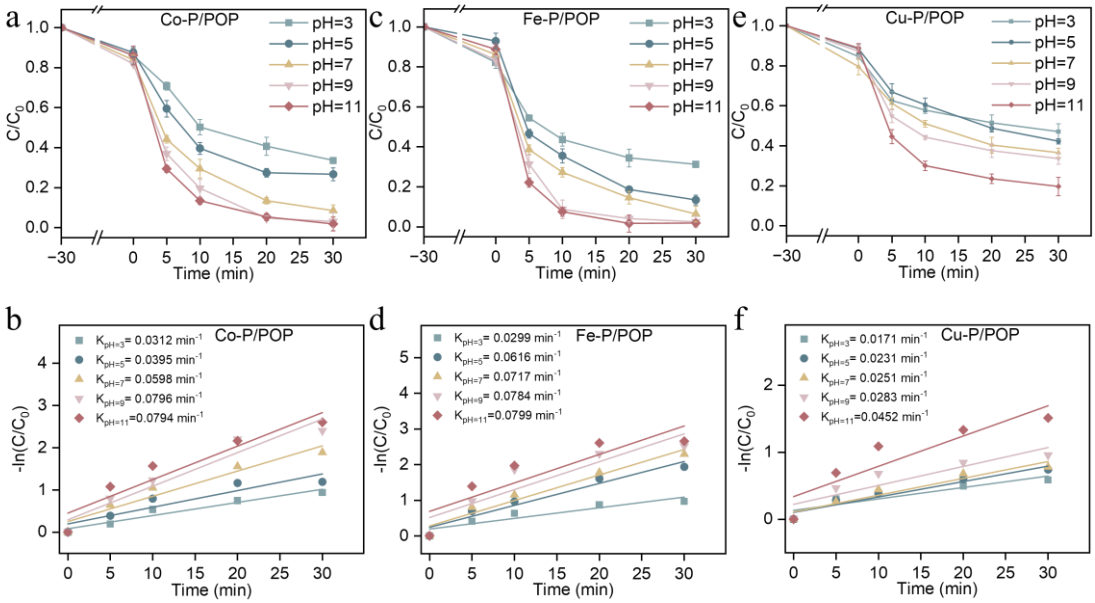

Fig. 6-10. The degradation rate constants (K) of SMX in the M (Co, Fe, and Cu)-P/POP/PMS systems at different pH conditions.

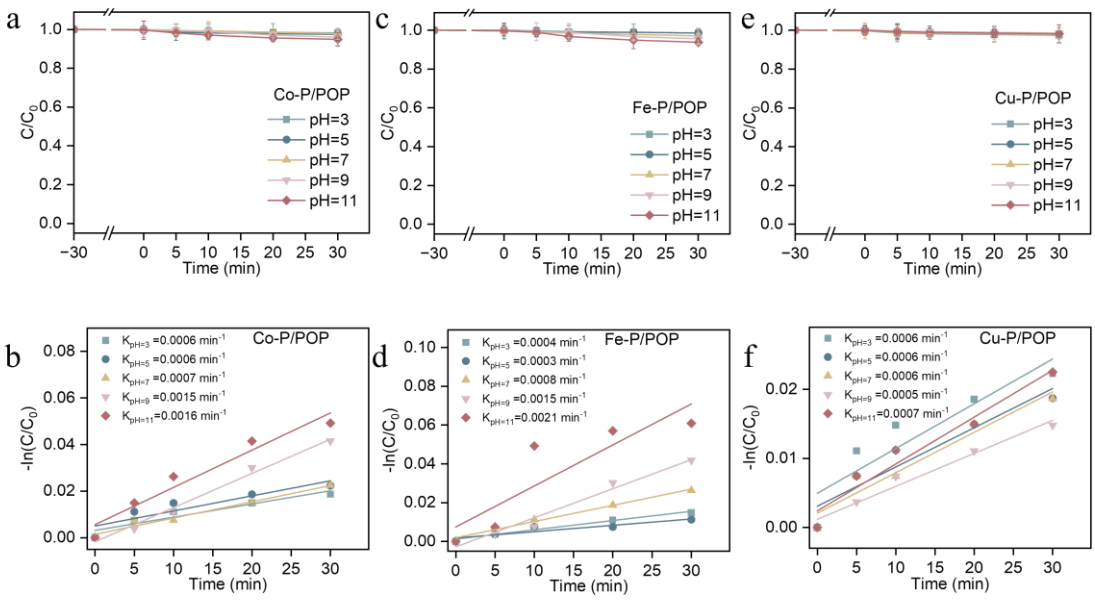

Fig. 6-11. The degradation rate constants (K) of FLX in the M (Co, Fe, and Cu)-P/POP/PMS systems at different pH conditions.

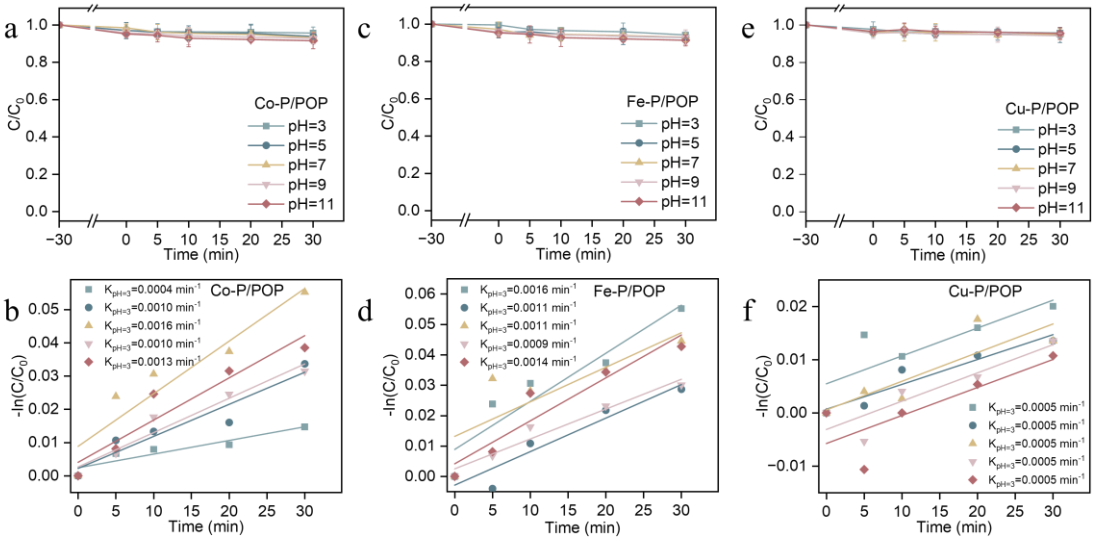

Fig. 6-12. The degradation rate constants (K) of IBP in the M (Co, Fe, and Cu)-P/POP/PMS systems at different pH conditions.

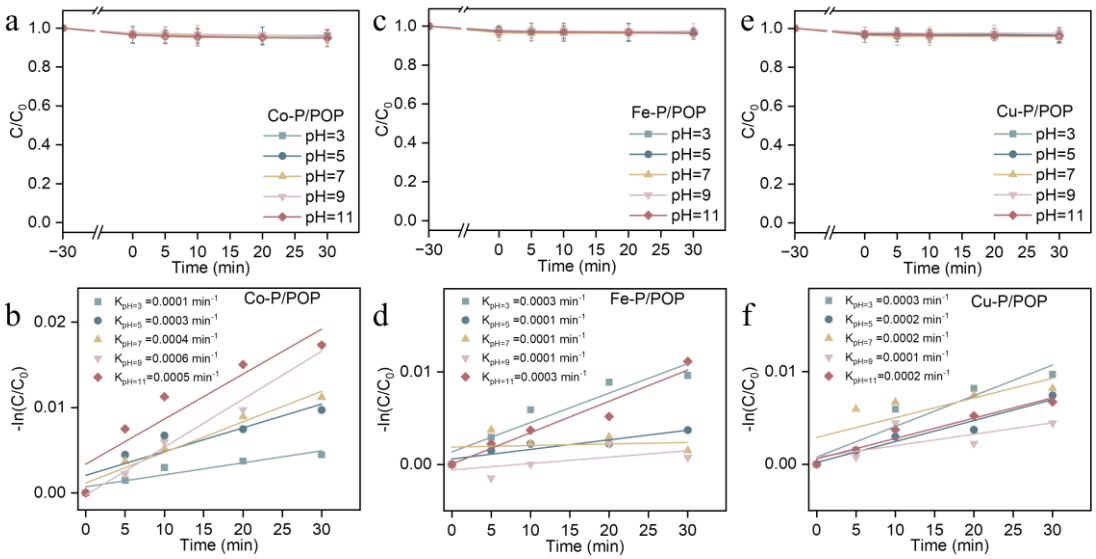

Fig. 6-13. The degradation rate constants (K) of ATZ in the M (Co, Fe, and Cu)-P/POP/PMS systems at different pH conditions.

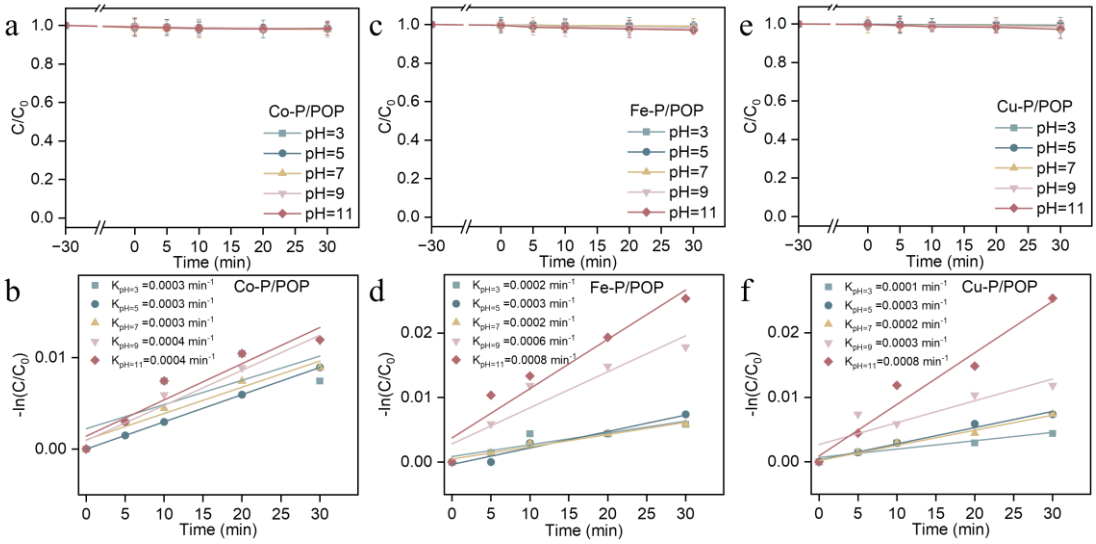

Fig. 6-14. The degradation rate constants (K) of BA in the M (Co, Fe, and Cu)-P/POP/PMS systems at different pH conditions.

The degradation performance of 12 organic pollutants in different M-P/POP/PMS systems (Fe-P/POP/PMS, Co-P/POP/PMS, and Cu-P/POP/PMS) is illustrated in **Fig. 6-2** and (**Fig. 6-3 – Fig. 6-14**). The selected pollutants include methylene blue (MB), ranitidine (RAN), diclofenac (DCF), ciprofloxacin (CIP), bisphenol A (BPA), carbamazepine (CBZ), tetracycline hydrochloride (TC), sulfamethoxazole (SMX),

fluoxetine (FLX), ibuprofen (IBP), atrazine (ATZ), and benzoic acid (BA).Experimental results indicate that pollutants containing electron-donating groups (MB, RAN, DCF, CIP, BPA, CBZ, TC, and SMX) were more susceptible to degradation in the Fe-P/POP/PMS system. In contrast, pollutants with electron-withdrawing groups (FLX, IBP, ATZ, and BA) exhibited greater stability in this system and were less prone to degradation. The Co-P/POP/PMS system displayed a similar degradation pattern but demonstrated superior degradation efficiency for electron-withdrawing group-containing pollutants. The Cu-P/POP/PMS system followed the same degradation trend but exhibited lower catalytic activity overall. In summary, Fe-P/POP and Co-P/POP demonstrated outstanding catalytic performance in PMS activation, making them highly effective for pollutant degradation.

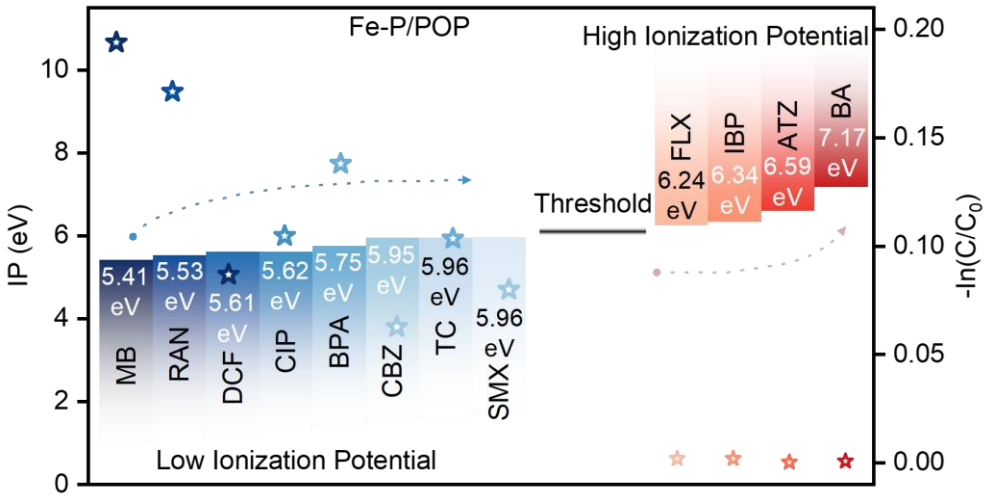

Fig. 6-15. The ionization potential (IP) values of 12 organic pollutants and their degradation rate constants (K) in the Fe-P/POP/PMS system.

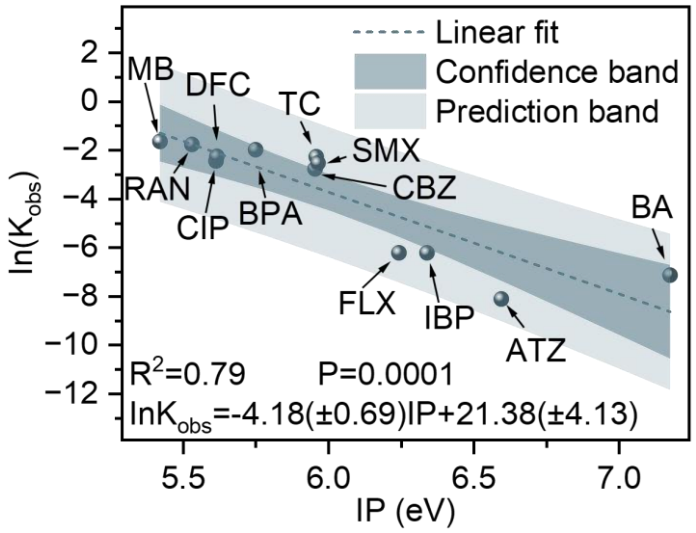

Fig. 6-16. Linearity between the IP values of different pollutants and their ln k_{obs} values in Fe-P/POP/PMS systems.

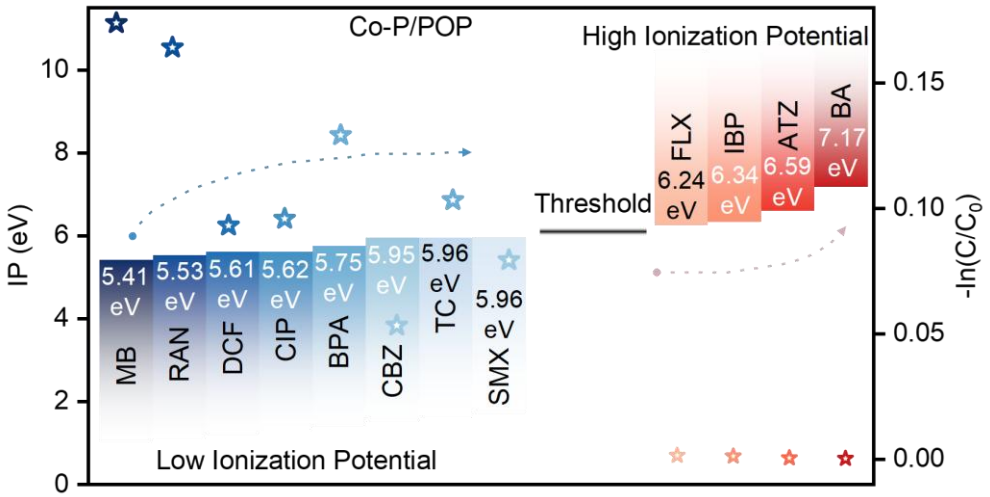

Fig. 6-17. The ionization potential (IP) values of 12 organic pollutants and their degradation rate constants (K) in the Co-P/POP/PMS system.

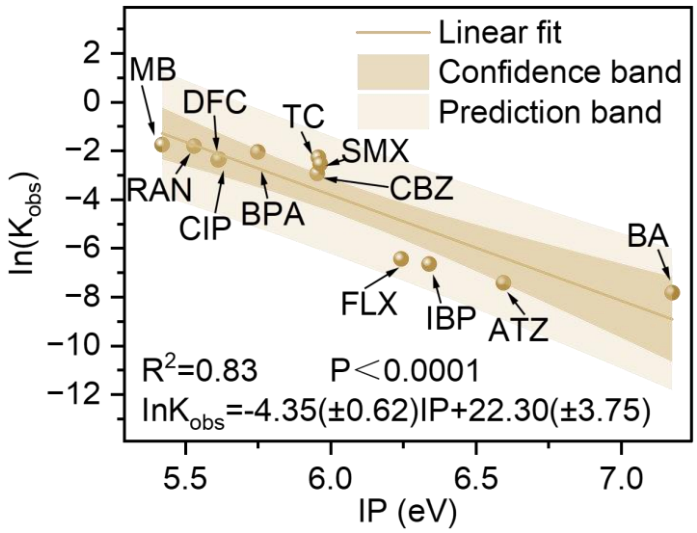

Fig. 6-18. Linearity between the IP values of different pollutants and their ln k_{obs} values in Co-P/POP/PMS systems.

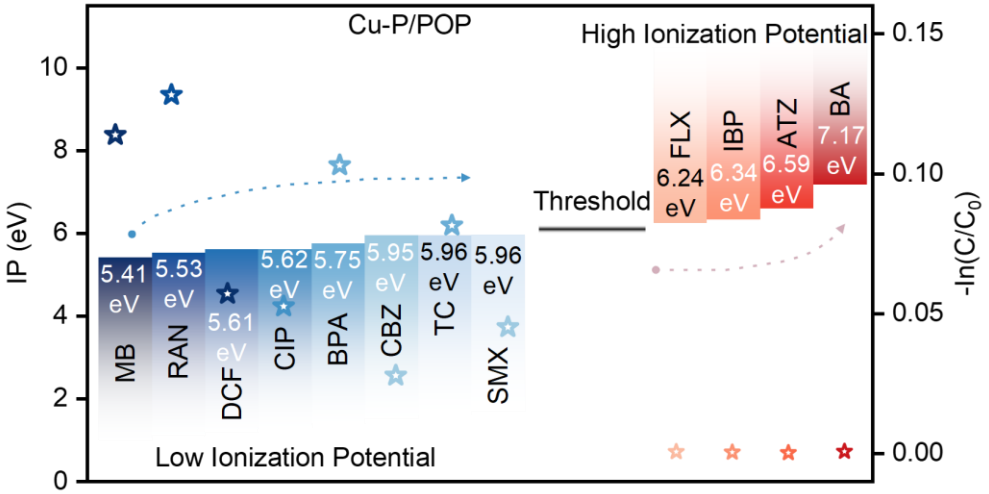

Fig. 6-19. The ionization potential (IP) values of 12 organic pollutants and their degradation rate constants (K) in the Cu-P/POP/PMS system.

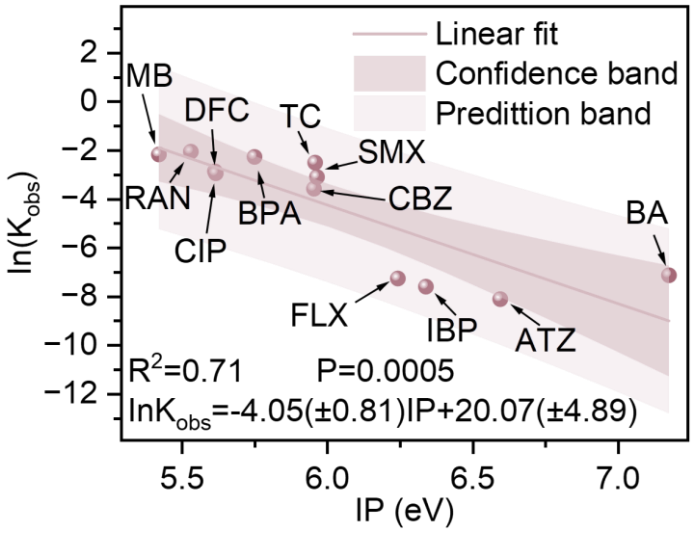

Fig. 6-20. Linearity between the IP values of different pollutants and their ln k_{obs} values in Co-P/POP/PMS systems.

The M-P/POP/PMS system exhibited varying degradation rates for different pollutants, which we hypothesize may be attributed to the physicochemical properties of the pollutants themselves. To elucidate this relationship, density functional theory (DFT) calculations were conducted to investigate the correlation between the physicochemical properties of organic pollutants and their reaction rates. Ionization potential (IP) is one of the key molecular descriptors influencing the reactivity of organic pollutants, as it typically reflects their electrophilicity and nucleophilicity. Previous studies have shown that IP is closely related to selective oxidation in catalytic processes, where lower IP values generally correspond to higher reaction rates. Specifically, organic compounds containing electron-donating groups (e.g., –OH and –NH_2) tend to exhibit lower IP values, making them more susceptible to degradation, whereas those with electron-withdrawing groups (e.g., –NO_2 and –COOH) typically possess higher IP values and are less reactive in the degradation process.

As shown in **Fig. 6-15**, a potential threshold appears to exist around an IP value of 6.0 eV in the Fe-P/POP/PMS system, which correlates with the degradation rate of organic pollutants. Pollutants with IP values exceeding this threshold, such as FLX, IBP, ATZ, and BA, were barely oxidized in the Fe-P/POP/PMS system. In contrast,

pollutants with lower IP values were more readily degraded. Furthermore, an inverse linear relationship was observed between IP and the apparent rate constant (K_{obs}), indicating that the electron-donating ability of organic compounds significantly influences the degradation rate in the Fe-P/POP/PMS system (**Fig. 6-16**). A similar trend was observed in the Co-P/POP/PMS and Cu-P/POP/PMS systems, as illustrated in **Fig. 6-17** - **Fig. 6-20**. Previous studies have reported that this phenomenon commonly occurs when high-valence metal oxides serve as the reactive species in pollutant degradation. To further elucidate the underlying mechanism, the reactive species in the M-P/POP/PMS system were analyzed

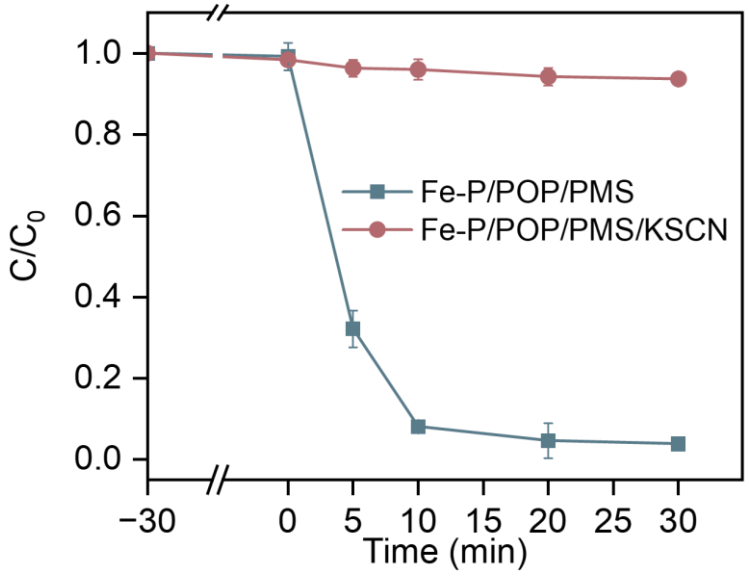

Fig. 6-21. Performance of Fe-P/POP /PMS to organic pollutants with or without KSCN.

To elucidate the origin of the catalytic activity, quenching experiments were conducted to investigate the PMS activation pathway in the Fe-P/POP/PMS system. Potassium thiocyanate (KSCN), a typical probe used to block Fe atoms, was introduced, resulting in the deactivation of the Fe-P/POP/PMS system (**Fig. 6-21**). This observation further confirmed that Fe atoms, rather than C or N sites, serve as the active centers.

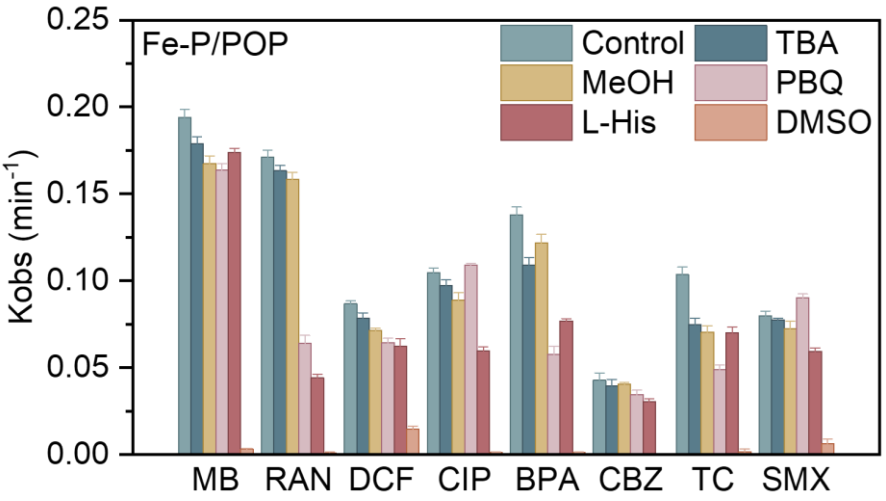

Fig. 6-22 The effect of scavengers on the degradation of 12 organic pollutants in the Fe-P/POP/PMS system

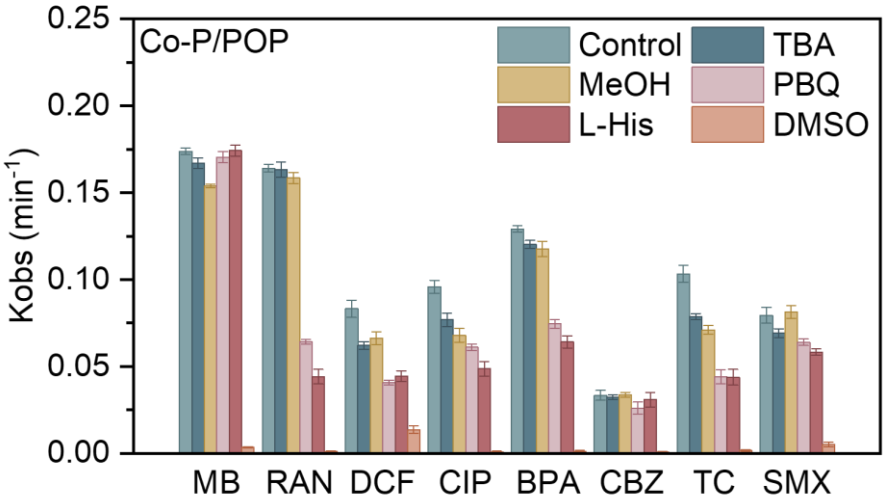

Fig. 6-23 The effect of scavengers on the degradation of 12 organic pollutants in the Co-P/POP/PMS system

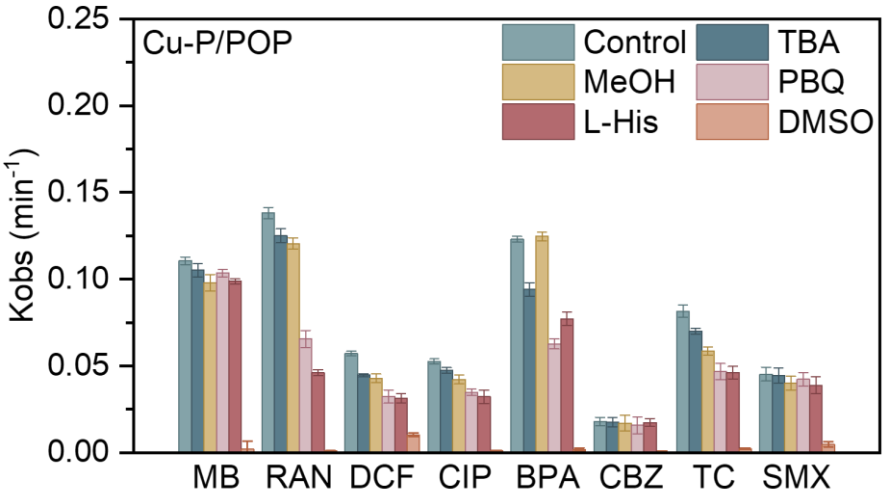

Fig. 6-24 The effect of scavengers on the degradation of 12 organic pollutants in the Cu-P/POP/PMS system

The reactive species in the Fe-P/POP/PMS system were further identified using various scavengers: tert-butanol (TBA), methanol (MeOH), p-benzoquinone (PBQ), L-histidine (L-His), and dimethyl sulfoxide (DMSO), which are selective quenchers for •OH, SO_4•$^-$, superoxide radicals (O_2•$^-$), singlet oxygen ($^1O_2$), and high-valence metal oxides (HVMOs), respectively. As shown in **Fig. 6-22 (Fig. 6-23** and **Fig. 6-24)**, the addition of TBA, MeOH, and PBQ had negligible effects on pollutant degradation, indicating that the contributions of •OH, SO_4•$^-$, O_2•$^-$ and $^1O_2$ could be disregarded. Therefore, the quenching results confirm the selective generation of HVMOs in the M-P/POP/PMS system, which serve as the primary reactive species for organic pollutant degradation.

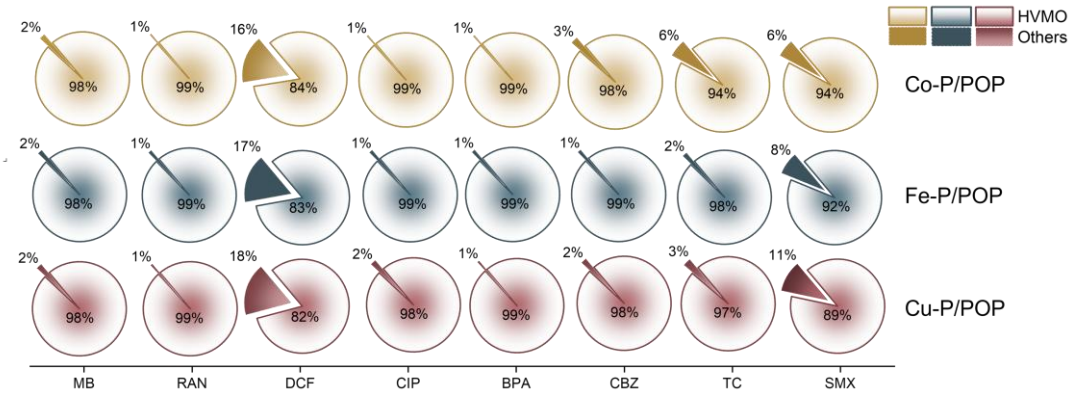

Fig. 6-25 Contribution of reactive species in the M-P/POP/PMS system.

Various radical and non-radical scavengers were used to determine the contribution of reactive species to organic pollutant degradation. The results showed (**Fig. 6-25**) that the contribution of high-valence metal oxides (HVMOs) in the M-P/POP/PMS system was nearly 100% in most cases, indicating the selective generation of HVMOs in the M-P/POP/PMS system.

Consistent with the experimental results presented in Chapters 3, 4, and 5, high-valence metal oxides (HVMOs) were identified as the primary oxidative species in the M-P/POP/PMS system.

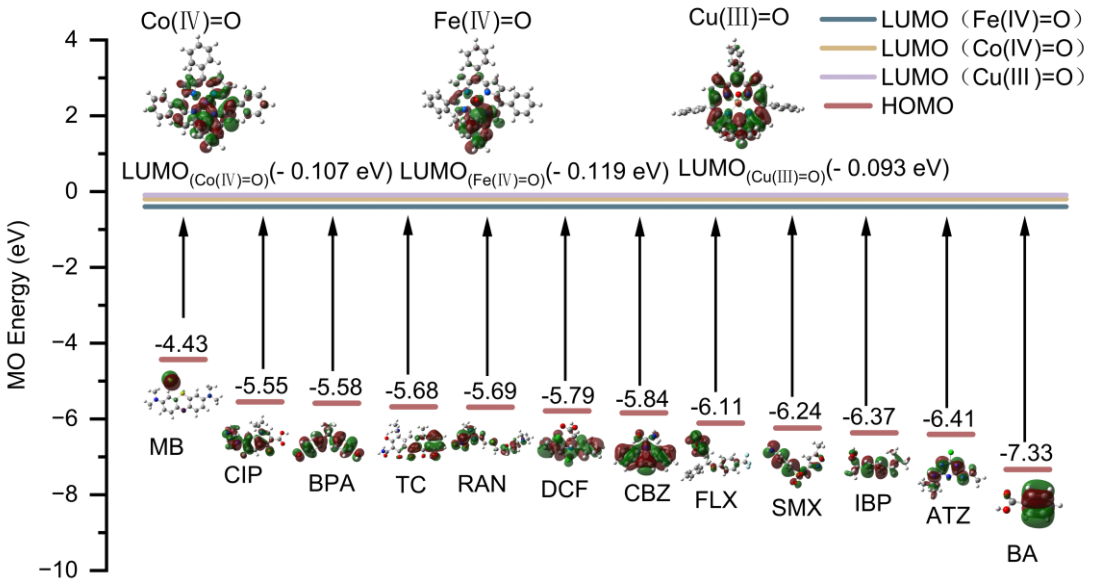

Fig. 6-26 Different energy gaps between different LUMO (M-P/POP/PMS complexes) and HOMO (pollutants).

To further elucidate the selectivity mechanism of HVMO oxidation in the M-P/POP/PMS system, molecular orbital (MO) analysis of HVMO-P/POP and 12 organic pollutants was performed in conjunction with density functional theory (DFT) calculations. The oxidation process in the M-P/POP/PMS system is fundamentally governed by electron transfer from the highest occupied molecular orbital (HOMO) of the pollutant to the lowest unoccupied molecular orbital (LUMO) of the HVMO-P/POP

complex.[136-138]

As shown in **Fig. 6-26**, the LUMO energies of Fe(IV)=O-P/POP (-0.119 eV) and Co(IV)=O-P/POP (-0.107 eV) are more negative compared to that of Cu(III)=O-P/POP (-0.093 eV). This implies that the energy barrier for electron transfer from pollutants to Fe(IV)=O-P/POP and Co(IV)=O-P/POP is lower, facilitating a more efficient electron transfer process and accelerating the HVMO-driven oxidation of organic pollutants.[139, 140] In contrast, Cu(III)=O-P/POP requires a higher energy input for electron donation, hindering pollutant electron transfer and leading to relatively slower HVMO oxidation. These findings also explain why HVMO oxidation in the Cu-P/POP/PMS system is comparatively less efficient. Moreover, the LUMO energy of Fe(IV)=O-P/POP (-0.119 eV) is lower than that of Co(IV)=O-P/POP (-0.107 eV), aligning well with the observed degradation performance in the M-P/POP/PMS system. This suggests that the oxidative capability of HVMO-P/POP complexes correlates with the ionization potential (IP) values of the target pollutants.

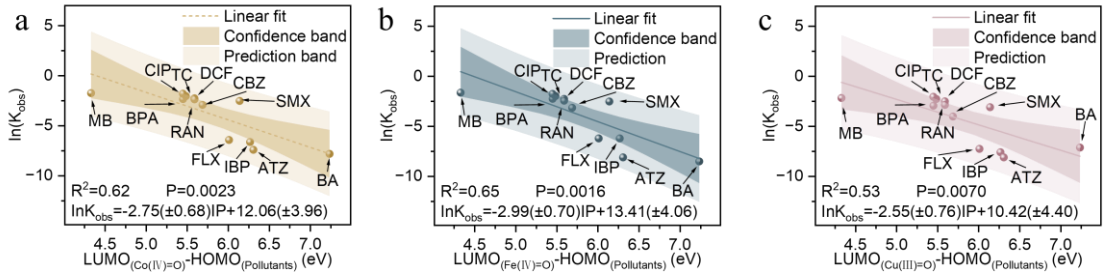

Fig. 6-27 (a–c) Correction between the calculated gaps and lnk_{obs} of pollutants obtained in the (a) Co-P/POP/PMS system, (b) Fe-P/POP/PMS system, and (c) Cu-P/POP/PMS system.

Additionally, the energy gaps between the LUMO of HVMO-P/POP complexes and the HOMO of different organic pollutants were calculated. The computed energy gaps across various M-P/POP/PMS systems exhibited a strong correlation with the observed degradation rate constants (K_{obs}) (**Fig. 6-27**). Specifically, in the M-P/POP/PMS system, HVMO oxidation was more pronounced for pollutants with high HOMO values, as they exhibited stronger electron-donating abilities. Conversely, organic pollutants with lower HOMO values exhibited weaker electron-donating

abilities, thereby reducing the effectiveness of HVMO oxidation. This relationship clearly explains why the Fe-P/POP/PMS system demonstrates superior degradation performance compared to the Cu-P/POP/PMS system.

6.4 Conclusion

In this study, metal-porphyrin porous organic polymers (M-P/POP, where M = Fe, Co, or Cu) were synthesized and successfully applied as catalysts for PMS activation to degrade organic pollutants. The catalytic activity was attributed to the selective generation of high-valence metal oxo species (HVMOs: Fe(IV)=O, Co(IV)=O, and Cu(III)=O), which served as the primary reactive species in a non-radical electron transfer pathway. Mechanistic investigations, including quenching experiments, electron paramagnetic resonance (EPR) spectroscopy, and isotope labeling, confirmed that conventional radicals (•OH, $SO_4^{\bullet-}$, and $O_2^{\bullet-}$) contributed negligibly to pollutant degradation, further validating the predominance of the HVMO oxidation mechanism.

The Fe-P/POP and Co-P/POP catalysts demonstrated superior catalytic performance compared to Cu-P/POP, achieving higher degradation efficiencies across a range of organic pollutants. Theoretical calculations revealed a strong correlation between pollutant ionization potential (IP) and degradation rate constants (K_obs), supporting the hypothesis that oxidation proceeded via electron transfer from the pollutant's HOMO to the catalyst's LUMO. Additionally, the M-P/POP/PMS system exhibited excellent stability, recyclability, and negligible metal leaching, confirming its feasibility for long-term applications.

Overall, this study advances the understanding of PMS activation mechanisms and highlights the potential of M-P/POP catalysts for practical wastewater treatment. The combination of high efficiency, selective degradation pathways, and environmental sustainability makes M-P/POP a promising candidate for the removal of persistent organic pollutants in contaminated water sources.

References

[1] S.R. Carpenter, E.H. Stanley, M.J. Vander Zanden, State of the World's Freshwater Ecosystems: Physical, Chemical, and Biological Changes, 36(Volume 36, 2011) (2011) 75-99.

[2] P.R. Rout, T.C. Zhang, P. Bhunia, R.Y. Surampalli, Treatment technologies for emerging contaminants in wastewater treatment plants: A review, Science of The Total Environment 753 (2021) 141990.

[3] J.O. Back, B. Hupfauf, A. Rößler, S. Penner, M. Rupprich, Adsorptive removal of micropollutants from wastewater with floating-fixed-bed gasification char, Journal of Environmental Chemical Engineering 8(3) (2020) 103757.

[4] E.Y. Klein, T.P. Van Boeckel, E.M. Martinez, S. Pant, S. Gandra, S.A. Levin, H. Goossens, R. Laxminarayan, Global increase and geographic convergence in antibiotic consumption between 2000 and 2015, Proceedings of the National Academy of Sciences 115(15) (2018) E3463-E3470.

[5] J. Subirats, A. Di Cesare, S. Varela della Giustina, A. Fiorentino, E.M. Eckert, S. Rodriguez-Mozaz, C.M. Borrego, G. Corno, High-quality treated wastewater causes remarkable changes in natural microbial communities and intI1 gene abundance, Water Research 167 (2019) 114895.

[6] Y. Tang, Q. Chen, W. Li, X. Xie, W. Zhang, X. Zhang, H. Chai, Y. Huang, Engineering magnetic N-doped porous carbon with super-high ciprofloxacin adsorption capacity and wide pH adaptability, Journal of Hazardous Materials 388 (2020) 122059.

[7] S. Banerjee, A. Jana, D. Mukherjee, S. Ghosh, S. Chakrabarti, S. Majumdar, Synthesis of Hydrophobic Ceramic Ultrafiltration Membrane and Performance Evaluation for Removal of Ciprofloxacin in Water, in: S.K. Ghosh (Ed.) Waste Water Recycling and Management, Springer Singapore, Singapore, 2019, pp. 65-73.

[8] E.C. Doğan, Investigation of ciprofloxacin removal from aqueous solution by nanofiltration process, Global Nest Journal 18(2) 291–308.

[9] Y. Zhao, X. Yuan, X. Li, L. Jiang, H. Wang, Burgeoning prospects of biochar and its composite in persulfate-advanced oxidation process, Journal of Hazardous Materials 409 (2021) 124893.

[10] S. Garcia-Segura, J.D. Ocon, M.N. Chong, Electrochemical oxidation remediation of real wastewater effluents — A review, Process Safety and Environmental Protection 113 (2018) 48-67.

[11] M. Cheng, W. Ma, C. Chen, J. Yao, J. Zhao, Photocatalytic degradation of organic pollutants catalyzed by layered iron(II) bipyridine complex–clay hybrid under visible irradiation, Applied Catalysis B: Environmental 65(3) (2006) 217-226.

[12] A. Zhang, Z. Gu, W. Chen, Q. Li, G. Jiang, Removal of refractory organic pollutants in reverse-osmosis concentrated leachate by Microwave–Fenton process, Environmental Science and Pollution Research 25(29) (2018) 28907-28916.

[13] W.-D. Oh, T.-T. Lim, Design and application of heterogeneous catalysts as peroxydisulfate activator for organics removal: An overview, Chemical Engineering Journal 358 (2019) 110-133.
[14] J. Lee, U. von Gunten, J.-H. Kim, Persulfate-Based Advanced Oxidation: Critical Assessment of Opportunities and Roadblocks, Environmental Science & Technology 54(6) (2020) 3064-3081.
[15] J. Wang, S. Wang, Activation of persulfate (PS) and peroxymonosulfate (PMS) and application for the degradation of emerging contaminants, Chemical Engineering Journal 334 (2018) 1502-1517.
[16] P. Neta, V. Madhavan, H. Zemel, R.W.J.J.o.t.A.C.S. Fessenden, Rate constants and mechanism of reaction of sulfate radical anion with aromatic compounds, 99(1) (1977) 163-164.
[17] W.R. Haag, C.D.J.E.s. Yao, technology, Rate constants for reaction of hydroxyl radicals with several drinking water contaminants, 26(5) (1992) 1005-1013.
[18] R. Norman, P. Storey, P.J.J.o.t.C.S.B.P.O. West, Electron spin resonance studies. Part XXV. Reactions of the sulphate radical anion with organic compounds, (1970) 1087-1095.
[19] C. Walling, D.M. Camaioni, S.S.J.J.o.t.A.C.S. Kim, Aromatic hydroxylation by peroxydisulfate, 100(15) (1978) 4814-4818.
[20] W.-D. Oh, Z. Dong, T.-T.J.A.C.B.E. Lim, Generation of sulfate radical through heterogeneous catalysis for organic contaminants removal: current development, challenges and prospects, 194 (2016) 169-201.
[21] J. Wang, S.J.C.E.J. Wang, Reactive species in advanced oxidation processes: Formation, identification and reaction mechanism, 401 (2020) 126158.
[22] S. Mostafa, F.L.J.E.s. Rosario-Ortiz, technology, Singlet oxygen formation from wastewater organic matter, 47(15) (2013) 8179-8186.
[23] F.E. Scully Jr, J.J.C. Hoigné, Rate constants for reactions of singlet oxygen with phenols and other compounds in water, 16(4) (1987) 681-694.
[24] T.J.T. Matsuura, Bio-mimetic oxygenation, 33(22) (1977) 2869-2905.
[25] H.H. Wasserman, J.L.J.T. Ives, Singlet oxygen in organic synthesis, 37(10) (1981) 1825-1852.
[26] X. Lu, W. Qiu, J. Ma, H. Xu, D. Wang, H. Cheng, W. Zhang, X. He, The overestimated role of singlet oxygen for pollutants degradation in some non-photochemical systems, Chemical Engineering Journal 401 (2020) 126128.
[27] E. Saputra, S. Muhammad, H. Sun, H.M. Ang, M. Tade, S.J.E.s. Wang, technology, Different crystallographic one-dimensional MnO2 nanomaterials and their superior performance in catalytic phenol degradation, 47(11) (2013) 5882-5887.
[28] D. Li, X. Duan, H. Sun, J. Kang, H. Zhang, M.O. Tade, S. Wang, Facile synthesis of nitrogen-doped graphene via low-temperature pyrolysis: The effects of precursors and annealing ambience on metal-free catalytic oxidation, Carbon 115 (2017) 649-658.
[29] F. Wilkinson, W.P. Helman, A.B.J.J.o.P. Ross, C.R. Data, Rate constants for the decay and reactions of the lowest electronically excited singlet state of molecular oxygen in solution. An expanded and revised compilation, 24(2) (1995) 663-677.

[30] X. Li, M. Zhou, Y.J.J.o.h.m. Pan, Enhanced degradation of 2, 4-dichlorophenoxyacetic acid by pre-magnetization Fe-C activated persulfate: Influential factors, mechanism and degradation pathway, 353 (2018) 454-465.
[31] G. Subramanian, P. Parakh, H.J.P. Prakash, P. Sciences, Photodegradation of methyl orange and photoinactivation of bacteria by visible light activation of persulphate using a tris (2, 2′-bipyridyl) ruthenium (II) complex, 12 (2013) 456-466.
[32] T. Chalati, P. Horcajada, R. Gref, P. Couvreur, C.J.J.o.M.C. Serre, Optimisation of the synthesis of MOF nanoparticles made of flexible porous iron fumarate MIL-88A, 21(7) (2011) 2220-2227.
[33] M. Pu, Y. Ma, J. Wan, Y. Wang, J. Wang, M.L.J.C.s. Brusseau, technology, Activation performance and mechanism of a novel heterogeneous persulfate catalyst: metal–organic framework MIL-53 (Fe) with Fe II/Fe III mixed-valence coordinatively unsaturated iron center, 7(5) (2017) 1129-1140.
[34] Q. Liu, Q. Sun, J. Shen, Y. Zhang, H. Li, Y. Zhang, Q. Li, G. Lu, S. Yu, X.J.A.S.S. Li, Construction of DA type porphyrin-phthalocyanine-based polymer hollow tubes for efficient photodegradation and photoelectrochemical sensing of bisphenol A, 638 (2023) 158129.
[35] D. Cui, W. Xie, S. Zhang, Z. Liu, C. Liu, Y.J.M.L. Xu, Copper porphyrin-based conjugated microporous polymers as photosensitizers for singlet oxygen generation, 232 (2018) 18-21.
[36] Y. Ma, X. Yi, S. Wang, T. Li, B. Tan, C. Chen, T. Majima, E.R. Waclawik, H. Zhu, J.J.N.C. Wang, Selective photocatalytic CO2 reduction in aerobic environment by microporous Pd-porphyrin-based polymers coated hollow TiO2, 13(1) (2022) 1400.
[37] Z. Zhong, X. Xia, X. Yang, N. Li, J. He, D. Chen, P. Gu, Q. Xu, J.J.S. Lu, P. Technology, Metal-free modification of porphyrin-based porous organic polymers for effective photocatalytic degradation of bisphenol A in water, 301 (2022) 121981.
[38] S. Zhou, X. Luo, Y. Zhang, Y. Liu, X. Wang, X. Hao, Y. Zhang, D. Wang, P. Gu, G.J.C.C. Liu, Post-cationic modification of a porphyrin-based conjugated microporous polymer for enhanced removal performance of bisphenol A, 59(97) (2023) 14399-14402.
[39] W. Gao, J. Tian, Y. Fang, T. Liu, X. Zhang, X. Xu, X.J.C. Zhang, Visible-light-driven photo-Fenton degradation of organic pollutants by a novel porphyrin-based porous organic polymer at neutral pH, 243 (2020) 125334.
[40] C. Chen, C. Tang, W. Xu, Y. Li, L.J.P.C.C.P. Xu, Design of iron atom modified thiophene-linked metalloporphyrin 2D conjugated microporous polymer as CO 2 reduction photocatalyst, 20(14) (2018) 9536-9542.
[41] X. Zhang, J. Wang, Y. Bian, H. Lv, B. Qiu, Y. Zhang, R. Qin, D. Zhu, S. Zhang, D.J.J.o.C.U. Li, A novel conjugated microporous polymer microspheres comprising cobalt porphyrins for efficient catalytic CO2 cycloaddition under ambient conditions, 58 (2022) 101924.
[42] B.C. Hodges, E.L. Cates, J.-H.J.N.n. Kim, Challenges and prospects of advanced

oxidation water treatment processes using catalytic nanomaterials, 13(8) (2018) 642-650.
[43] S. Zhang, H. Zheng, P.G.J.N.W. Tratnyek, Advanced redox processes for sustainable water treatment, 1(8) (2023) 666-681.
[44] S. Wacławek, H.V. Lutze, K. Grübel, V.V.T. Padil, M. Černík, D.D. Dionysiou, Chemistry of persulfates in water and wastewater treatment: A review, Chem. Eng. J. 330 (2017) 44-62.
[45] J. Lee, U. Von Gunten, J.-H.J.E.s. Kim, technology, Persulfate-based advanced oxidation: critical assessment of opportunities and roadblocks, 54(6) (2020) 3064-3081.
[46] X. Li, X. Wen, J. Lang, Y. Wei, J. Miao, X. Zhang, B. Zhou, M. Long, P.J.J. Alvarez, L. Zhang, CoN1O2 Single-Atom Catalyst for Efficient Peroxymonosulfate Activation and Selective Cobalt(IV)=O Generation, Angew. Chem. 135(27) (2023) e202303267.
[47] B. Liu, W. Guo, W. Jia, H. Wang, S. Zheng, Q. Si, Q. Zhao, H. Luo, J. Jiang, N. Ren, Insights into the oxidation of organic contaminants by Co(II) activated peracetic acid: The overlooked role of high-valent cobalt-oxo species, Water Res. 201 (2021) 117313.
[48] N. Li, W. Lu, K. Pei, Y. Yao, W. Chen, Formation of high-valent cobalt-oxo phthalocyanine species in a cellulose matrix for eliminating organic pollutants, Appl. Catal., B 163 (2015) 105-112.
[49] X. Zheng, X. Niu, D. Zhang, M. Lv, X. Ye, J. Ma, Z. Lin, M. Fu, Metal-based catalysts for persulfate and peroxymonosulfate activation in heterogeneous ways: A review, Chem. Eng. J. 429 (2022) 132323.
[50] B. Liu, W. Guo, H. Wang, S. Zheng, Q. Si, Q. Zhao, H. Luo, N. Ren, Peroxymonosulfate activation by cobalt(II) for degradation of organic contaminants via high-valent cobalt-oxo and radical species, J. Hazard. Mater. 416 (2021) 125679.
[51] W. Ma, X. Ren, J. Li, S. Wang, X. Wei, N. Wang, Y.J.S. Du, Advances in Atomically Dispersed Metal and Nitrogen Co-Doped Carbon Catalysts for Advanced Oxidation Technologies and Water Remediation: From Microenvironment Modulation to Non-Radical Mechanisms, 20(22) (2024) 2308957.
[52] Y. Xiong, H. Li, C. Liu, L. Zheng, C. Liu, J.O. Wang, S. Liu, Y. Han, L. Gu, J.J.A.M. Qian, Single-atom Fe catalysts for Fenton-like reactions: roles of different N species, 34(17) (2022) 2110653.
[53] X. Dong, Z. Chen, A. Tang, D.D. Dionysiou, H.J.A.F.M. Yang, Mineral modulated single atom catalyst for effective water treatment, 32(16) (2022) 2111565.
[54] Z. Wang, E. Almatrafi, H. Wang, H. Qin, W. Wang, L. Du, S. Chen, G. Zeng, P.J.A.C. Xu, Cobalt single atoms anchored on oxygen-doped tubular carbon nitride for efficient peroxymonosulfate activation: simultaneous coordination structure and morphology modulation, 134(29) (2022) e202202338.
[55] X. Zhou, M.-K. Ke, G.-X. Huang, C. Chen, W. Chen, K. Liang, Y. Qu, J. Yang, Y. Wang, F.J.P.o.t.N.A.o.S. Li, Identification of Fenton-like active Cu sites by

heteroatom modulation of electronic density, 119(8) (2022) e2119492119.
[56] X. Li, X. Huang, S. Xi, S. Miao, J. Ding, W. Cai, S. Liu, X. Yang, H. Yang, J.J.J.o.t.A.C.S. Gao, Single cobalt atoms anchored on porous N-doped graphene with dual reaction sites for efficient Fenton-like catalysis, 140(39) (2018) 12469-12475.
[57] B. Liu, W. Guo, W. Jia, H. Wang, S. Zheng, Q. Si, Q. Zhao, H. Luo, J. Jiang, N.J.W.R. Ren, Insights into the oxidation of organic contaminants by Co (II) activated peracetic acid: The overlooked role of high-valent cobalt-oxo species, 201 (2021) 117313.
[58] Y. Wang, H. Shen, Z. Shi, Q. Xing, Y.J.C.E.J. Pi, Activation of peroxymonosulfate by sulfonated cobalt (II) phthalocyanine for the degradation of organic pollutants: The role of high-valent cobalt-oxo species, 455 (2023) 140671.
[59] C. Wang, X. Wang, H. Wang, L. Zhang, Y. Wang, C.-L. Dong, Y.-C. Huang, P. Guo, R. Cai, S.J.J.J.o.H.M. Haigh, Low-coordinated Co-N3 sites induce peroxymonosulfate activation for norfloxacin degradation via high-valent cobalt-oxo species and electron transfer, 455 (2023) 131622.
[60] H. Li, F. Pan, C. Qin, T. Wang, K.J.J.A.E.M. Chen, Porous Organic Polymers-Based Single-Atom Catalysts for Sustainable Energy-Related Electrocatalysis, 13(28) (2023) 2301378.
[61] Y. Li, L. Wu, K. Wang, B. Zhou, Q. Li, Z. Li, B. Yan, C. Gong, Q. Wang, J.J.A.A.M. Jia, Interfaces, Nitrogen-Rich Conjugated Microporous Polymers with Improved Cobalt (II) Density for Highly Efficient Electrocatalytic Oxygen Evolution, 16(7) (2024) 8903-8912.
[62] A.F. Saber, A.M. Elewa, H.-H. Chou, A.F.J.A.C.B.E. EL-Mahdy, Donor-acceptor carbazole-based conjugated microporous polymers as photocatalysts for visible-light-driven H2 and O2 evolution from water splitting, 316 (2022) 121624.
[63] L. Chen, C. Gong, X. Wang, F. Dai, M. Huang, X. Wu, C.-Z. Lu, Y.J.J.o.t.A.C.S. Peng, Substoichiometric 3D covalent organic frameworks based on hexagonal linkers, 143(27) (2021) 10243-10249.
[64] L. Wang, J. Wang, Y. Wang, F. Zhou, J.J.J.o.H.M. Huang, Thioether-functionalized porphyrin-based polymers for Hg2+ efficient removal in aqueous solution, 429 (2022) 128303.
[65] A. Chen, Y. Zhang, J. Chen, L. Chen, Y.J.J.o.M.C.A. Yu, Metalloporphyrin-based organic polymers for carbon dioxide fixation to cyclic carbonate, 3(18) (2015) 9807-9816.
[66] A. Wang, L. Cheng, W. Zhao, X. Shen, W.J.J.o.c. Zhu, i. science, Electrochemical hydrogen and oxygen evolution reactions from a cobalt-porphyrin-based covalent organic polymer, 579 (2020) 598-606.
[67] L. Chen, Y. Yang, D.J.J.o.t.A.C.S. Jiang, CMPs as scaffolds for constructing porous catalytic frameworks: a built-in heterogeneous catalyst with high activity and selectivity based on nanoporous metalloporphyrin polymers, 132(26) (2010) 9138-9143.
[68] A. Wang, L. Cheng, X. Shen, W. Zhu, L.J.D. Li, Pigments, Mechanistic insight on porphyrin based porous titanium coordination polymer as efficient bifunctional

electrocatalyst for hydrogen and oxygen evolution reactions, 181 (2020) 108568.
[69] Y.-F. Yao, W.-Y. Xie, S.-J. Huang, J.-S. Ye, H.-Y. Liu, X.-Y.J.J.o.E.C. Xiao, Pyrolysis-free cobalt porphyrin coordination polymer as electrocatalyst for Zn-air batteries and water splitting, 952 (2024) 117987.
[70] N. Rai, C. Singh, L. Ranjta, M.J.J.o.E.M. Yahya, XRD, DSC, and Dielectric studies of MWNT-doped polymer electrolytes for supercapacitor application, 52(7) (2023) 4269-4278.
[71] C. Yang, Z.-D. Yang, H. Dong, N. Sun, Y. Lu, F.-M. Zhang, G.J.A.E.L. Zhang, Theory-driven design and targeting synthesis of a highly-conjugated basal-plane 2D covalent organic framework for metal-free electrocatalytic OER, 4(9) (2019) 2251-2258.
[72] C. Yang, S. Shang, Y. Fan, K. Shih, X.-y. Li, L.J.A.C.B.E. Lin, Incorporation of atomically dispersed cobalt in the 2D metal–organic framework of a lamellar membrane for highly efficient peroxymonosulfate activation, 325 (2023) 122344.
[73] A. Wang, L. Cheng, W. Zhao, X. Shen, W. Zhu, Electrochemical hydrogen and oxygen evolution reactions from a cobalt-porphyrin-based covalent organic polymer, J. Colloid Interface Sci. 579 (2020) 598-606.
[74] X. Zhang, J. Wang, Y. Bian, H. Lv, B. Qiu, Y. Zhang, R. Qin, D. Zhu, S. Zhang, D. Li, S. Wang, W. Mai, Y. Li, T. Li, A novel conjugated microporous polymer microspheres comprising cobalt porphyrins for efficient catalytic CO2 cycloaddition under ambient conditions, J. CO2 Util. 58 (2022) 101924.
[75] C. Yang, S. Shang, Y. Fan, K. Shih, X.-y. Li, L. Lin, Incorporation of atomically dispersed cobalt in the 2D metal–organic framework of a lamellar membrane for highly efficient peroxymonosulfate activation, Appl. Catal., B 325 (2023) 122344.
[76] X.-Y. Dong, F.-Q. Yan, Q.-Y. Wang, P.-F. Feng, R.-Y. Zou, S. Wang, S.-Q.J.J.o.M.C.A. Zang, A benzimidazole-linked bimetallic phthalocyanine–porphyrin covalent organic framework synergistically promotes CO 2 electroreduction, 11(29) (2023) 15732-15738.
[77] J. Zhen, J. Sun, X. Xu, Z. Wu, W. Song, Y. Ying, S. Liang, L. Miao, J. Cao, W. Lv, C. Song, Y. Yao, M. Xing, M−N3 Configuration on Boron Nitride Boosts Singlet Oxygen Generation via Peroxymonosulfate Activation for Selective Oxidation, Angew. Chem. Int. Ed. 63(26) (2024) e202402669.
[78] X. Zhao, X. Jia, H. Li, H. Zhang, X. Zhou, Y. Zhou, H. Wang, L. Yin, T. Wågberg, G.J.C.E.J. Hu, Efficient degradation of Health-threatening organic pollutants in water by atomically dispersed Cobalt-Activated peroxymonosulfate, 450 (2022) 138098.
[79] M. Fan, C. Wang, X. Yu, J. Ding, L. Yan, G. Qin, Y. Li, L. Wang, Coordination environment engineering of MoS2-based nanocomposite by Ni atom incorporation for enhanced peroxymonosulfate activation, Chem. Eng. J. 487 (2024) 150751.
[80] X. Song, S. Diao, W. He, J. Yang, L. Wang, G. Qin, Y. Li, Q. Chen, Design of active dual atom Ni-Co-2H-MoS2 catalyst: Synergistic effect of Ni-adsorption and co-catalysis for activating peroxymonosulfate, Sep. Purif. Technol. 333 (2024) 125927.
[81] Z. Wan, S. Lin, X. Yang, G. Xiu, L. Zhou, Potential application of SDSO-layered

double hydroxide in wastewater treatment: Synergy between hydrophobicity and activation activity, Sep. Purif. Technol. 355 (2025) 129662.
[82] H.-Z. Liu, X.-X. Shu, M. Huang, B.-B. Wu, J.-J. Chen, X.-S. Wang, H.-L. Li, H.-Q. Yu, Tailoring d-band center of high-valent metal-oxo species for pollutant removal via complete polymerization, Nat. Commun. 15(1) (2024) 2327.
[83] P. He, C. Gu, B. Tang, Y. Zhou, M. Gan, J. Zhu, Expeditious degradation of SMX by high-valent cobalt-oxo species derived from cobalt-doped C3N5-activated peroxymonosulfate with the assistance of visible light, Sep. Purif. Technol. 301 (2022) 122009.
[84] J. Mao, K. Yin, Y. Zhang, Y. Shang, Q. Li, Y. Li, B. Gao, X. Xu, Ultrafast oxidation of refractory organics via PMS activation by Si-O doped biomimetic montmorillonite: Simultaneous enhanced radical/electron transfer pathways and efficient catalytic membrane system, Appl. Catal., B 342 (2024) 123428.
[85] F. Wang, Y. Gao, H. Fu, S.-S. Liu, Y. Wei, P. Wang, C. Zhao, J.-F. Wang, C.-C. Wang, Almost 100 % electron transfer regime over Fe−Co dual-atom catalyst toward pollutants removal: Regulation of peroxymonosulfate adsorption mode, Appl. Catal., B 339 (2023) 123178.
[86] M. Yang, Z. Hou, X. Zhang, B. Gao, Y. Li, Y. Shang, Q. Yue, X. Duan, X. Xu, Unveiling the Origins of Selective Oxidation in Single-Atom Catalysis via Co–N4–C Intensified Radical and Nonradical Pathways, Environ. Sci. Technol. 56(16) (2022) 11635-11645.
[87] Z. Wang, W. Qiu, S. Pang, J. Jiang, Effect of chelators on the production and nature of the reactive intermediates formed in Fe(II) activated peroxydisulfate and hydrogen peroxide processes, Water Res. 164 (2019) 114957.
[88] Z. Wang, J. Jiang, S. Pang, Y. Zhou, C. Guan, Y. Gao, J. Li, Y. Yang, W. Qiu, C. Jiang, Is Sulfate Radical Really Generated from Peroxydisulfate Activated by Iron(II) for Environmental Decontamination?, Environ. Sci. Technol. 52(19) (2018) 11276-11284.
[89] Y. Zong, H. Zhang, X. Zhang, W. Liu, L. Xu, D. Wu, High-valent cobalt-oxo species triggers hydroxyl radical for collaborative environmental decontamination, Appl. Catal., B 300 (2022) 120722.
[90] M. Luo, H. Zhang, J. Zhao, Z. Xie, Y. Ren, P. Zhou, Z. Xiong, Y. Liu, G. Yao, B. Lai, Understanding Two Variation Patterns of Organic Contaminant Degradation with pH in the FeVI System under Acidic Conditions, ACS ES&T Eng. 3(1) (2023) 64-72.
[91] A. Ding, M. Li, C. Liu, T.-S. Chee, Q. Yan, L. Lei, C. Xiao, Recovering palladium and gold by peroxydisulfate-based advanced oxidation process, Sci. Adv. 10(21) eadm9311.
[92] W. Fan, J. Qiao, X. Guan, Multi-wavelength spectrophotometric determination of Cr(VI) in water with ABTS, Chemosphere 171 (2017) 460-467.
[93] Z. Wu, Z. Xiong, B. Huang, G. Yao, S. Zhan, B. Lai, Long-range interactions driving neighboring Fe–N4 sites in Fenton-like reactions for sustainable water decontamination, Nat. Commun. 15(1) (2024) 7775.
[94] S.-F. Hung, A. Xu, X. Wang, F. Li, S.-H. Hsu, Y. Li, J. Wicks, E.G. Cervantes, A.S.

Rasouli, Y.C. Li, M. Luo, D.-H. Nam, N. Wang, T. Peng, Y. Yan, G. Lee, E.H. Sargent, A metal-supported single-atom catalytic site enables carbon dioxide hydrogenation, Nat. Commun. 13(1) (2022) 819.
[95] Y. Ma, H. Wang, X. Lv, D. Xiong, H. Xie, Z. Zhang, Three-dimensional ordered mesoporous Co3O4/peroxymonosulfate triggered nanoconfined heterogeneous catalysis for rapid removal of ranitidine in aqueous solution, Chem. Eng. J. 443 (2022) 136495.
[96] T. Sui, J. Mu, W. Zhen, Z. Zhang, A. Liu, Y. Wang, H. Che, G. Wang, Z. Guo, The property and mechanism of peroxymonosulfate activation boosted carbon cage encapsulated Mo2C/Bi2O2CO3 Z-scheme heterojunction for enhanced catalytic degradation and antibacterial activity, Sep. Purif. Technol. 353 (2025) 128186.
[97] L. Zhang, J. Qi, Z. Fang, L. Xing, Q. Li, X. Li, S. Liu, X. Wang, L. Wang, Interlayer-confined strategy to modulate alkaline reaction microenvironment for in-situ degradation of ofloxacin, Applied Catalysis B: Environment and Energy 357 (2024) 124339.
[98] J. Cao, Z. Yang, W. Xiong, Y. Zhou, Y. Wu, M. Jia, S. Sun, C. Zhou, Y. Zhang, R.J.S. Zhong, P. Technology, Peroxymonosulfate activation of magnetic Co nanoparticles relative to an N-doped porous carbon under confinement: Boosting stability and performance, 250 (2020) 117237.
[99] J. Xie, X. Luo, L. Chen, X. Gong, L. Zhang, J.J.C.E.J. Tian, ZIF-8 derived boron, nitrogen co-doped porous carbon as metal-free peroxymonosulfate activator for tetracycline hydrochloride degradation: Performance, mechanism and biotoxicity, 440 (2022) 135760.
[100] S. Han, P.J.S. Xiao, P. Technology, Catalytic degradation of tetracycline using peroxymonosulfate activated by cobalt and iron co-loaded pomelo peel biochar nanocomposite: Characterization, performance and reaction mechanism, 287 (2022) 120533.
[101] X. Zhang, B. Xu, S. Wang, X. Li, C. Wang, B. Liu, F. Han, Y. Xu, P. Yu, Y.J.C.E.J. Sun, Tetracycline degradation by peroxymonosulfate activated with CoNx active sites: Performance and activation mechanism, 431 (2022) 133477.
[102] B. Hua, L. Zheng, A. Adeboye, F.J.C.E.J. Li, Defect-and nitrogen-rich porous carbon embedded with Co NPs derived from self-assembled Co-ZIF-8@ anionic polyacrylamide network as PMS activator for highly efficient removal of tetracycline hydrochloride from water, 443 (2022) 136439.
[103] D. Xu, T. Yang, Y. Dong, Q. Wang, J. Zhu, G. Zhang, L. Lv, Y. Xia, Z. Ren, P.J.C.I. Wang, Activation of peroxymonosulfate by CoP@ Co2P heterostructures via radical and non-radical pathways for antibiotics degradation, 49(11) (2023) 16999-17007.
[104] H. Luo, Y. Xie, J. Niu, Y. Xiao, Y. Li, Y. Wang, Y. Zhang, T.J.J.o.C.T. Xie, Biotechnology, Cobalt-doped biogenic manganese oxides for enhanced tetracycline degradation by activation of peroxymonosulfate, 94(3) (2019) 752-760.
[105] X. Li, W. Zhang, Z. Liu, S. Wang, X. Zhang, B. Xu, P. Yu, Y. Xu, Y.J.S. Sun, P. Technology, Effective removal of tetracycline from water by catalytic

peroxymonosulfate oxidation over Co@ MoS2: catalytic performance and degradation mechanism, 294 (2022) 121139.
[106] K. Wang, P. Xiang, R. Zhou, M. Huang, P.J.J.o.W.P.E. Lin, Performance and mechanism of antibiotic removal by MOF-on-MOF-derived cobalt and nitrogen-doped magnetic porous carbon activated PMS, 54 (2023) 104043.
[107] H. Zhu, A. Guo, S. Wang, Y. Long, G. Fan, X.J.C.E.J. Yu, Efficient tetracycline degradation via peroxymonosulfate activation by magnetic Co/N co-doped biochar: emphasizing the important role of biochar graphitization, 450 (2022) 138428.
[108] Y. Wang, Q. Chen, Y. Su, Y. He, J. Qian, K.J.J.o.C.T. Xu, Biotechnology, Rapid activation of PMS driven by bimetallic redox on transition metal selenides for sulfamethoxazole degradation: mechanism, degradation pathway and intermediates toxicity, 99(12) (2024) 2665-2676.
[109] W. Tang, Y. Liu, Q. You, X. Yang, G. Liao, D. Wang, Y. Yan, Q.J.J.o.E.C.E. Shang, Constructing a 3D ordered macroporous cobalt monoatomic catalyst for efficient SMX degradation via PMS activation, 12(6) (2024) 114427.
[110] J. Zheng, H. Sun, K. Li, Z.J.S. Wu, P. Technology, Catalytic micro-structured ceramic beads and efficacy evaluation through SMX degradation in PMS-activated systems, 354 (2025) 129060.
[111] H. Wang, Q. Zhang, H. Ji, Y. Zhang, B. Fu, Y. Wu, Y.J.J.o.C.P. Ding, Boron and nitrogen hydrothermal co-doped sludge biochar towards efficiently activate peroxymonosulfate for sulfamethoxazole degradation, (2024) 142843.
[112] X. Wang, T. Li, Z. Fan, P. Duan, L. Wang, J. Pan, B.J.J.o.H.M. Gao, Redox potentials of sulfonamide antibiotics mediating the electron transfer process in single-atom Cu catalyst/peroxymonosulfate system: Selective removal mechanisms for sulfonamides, 485 (2025) 136880.
[113] R. Wang, H. You, Z. Li, J. Zhao, M. Li, J. Zhu, G. Zhang, X. Wang, H. Leng, S.J.C.E.J. Qi, Non-radical mediated reduced graphene oxide/polypyrrole catalytic ceramic membrane-PDS system for source control of SMX, 479 (2024) 147769.
[114] Y. Wang, S. Wang, Y. Liu, J.J.S. Wang, P. Technology, Visible light-enhanced interface interaction for PMS activation towards the removal of emerging organic pollutants: performance, mechanism and toxicity, 354 (2025) 128741.
[115] Y. Zeng, J. Deng, N. Zhou, W. Xia, Z. Wang, B. Song, Z. Wang, Y. Yang, X. Xu, G.J.S. Zeng, Mediated Peroxymonosulfate Activation at the Single Atom Fe-N3O1 Sites: Synergistic Degradation of Antibiotics by Two Non-Radical Pathways, (2024) 2311552.
[116] S. Li, J. Zou, J. Wu, J. Lin, Z. Wu, C. Tang, L. He, X. Liao, J.J.C.E.J. Ma, Overlooked role of protocatechuic acid in enhancing the selective elimination of sulfonamide antibiotics in Fe (III)/peroxymonosulfate process under actually neutral pH conditions, 497 (2024) 154581.
[117] T. Wu, W. Wang, J. Huang, X. Ren, X. Zhao, T.J.J.o.S.C.S. Zhou, Fabricating 3D hierarchical hollow CoAl-LDHs@ CoSx-rGO ball-flower for degrading sulfamethoxazole via visible-light coupling PMS activation: Performance and mechanism insight, 28(6) (2024) 101940.

[118] Y. Qiu, Y. Huang, Y. Wang, X. Liu, D.J.I.J.o.M. Huang, Metallurgy, Materials, Facile synthesis of Cu-doped manganese oxide octahedral molecular sieve for the efficient degradation of sulfamethoxazole via peroxymonosulfate activation, 31(12) (2024) 2770-2780.
[119] N. Li, H. Dai, M. He, J. Wang, Z. Cheng, B. Yan, W. Peng, G.J.E. Chen, Cu Distribution Pattern Controlled Active Species Generation and Sulfamethoxazole Degradation Routes in a Peroxymonosulfate System, 35 (2024) 168-179.
[120] X. Lv, A. Cai, H. Zhang, T. Wang, J. Xiao, M. Zhao, X.J.S. Huang, P. Technology, Hydroquinone enhanced Cu (II)/peroxymonosulfate for the degradation of sulfonamide antibiotics under acidic pH conditions, 360 (2025) 131056.
[121] Z. Chen, F. An, Y. Zhang, Z. Liang, W. Liu, M.J.P.o.t.N.A.o.S. Xing, Single-atom Mo–Co catalyst with low biotoxicity for sustainable degradation of high-ionization-potential organic pollutants, 120(29) (2023) e2305933120.
[122] K. Yin, L. Peng, D. Chen, S. Liu, Y. Zhang, B. Gao, K. Fu, Y. Shang, X.J.A.C.B.E. Xu, High-loading of well dispersed single-atom catalysts derived from Fe-rich marine algae for boosting Fenton-like reaction: Role identification of iron center and catalytic mechanisms, 336 (2023) 122951.
[123] Y. Qi, J. Li, Y. Zhang, Q. Cao, Y. Si, Z. Wu, M. Akram, X.J.A.C.B.E. Xu, Novel lignin-based single atom catalysts as peroxymonosulfate activator for pollutants degradation: Role of single cobalt and electron transfer pathway, 286 (2021) 119910.
[124] F. Mo, C. Song, Q. Zhou, W. Xue, S. Ouyang, Q. Wang, Z. Hou, S. Wang, J.J.P.o.t.N.A.o.S. Wang, The optimized Fenton-like activity of Fe single-atom sites by Fe atomic clusters–mediated electronic configuration modulation, 120(15) (2023) e2300281120.
[125] P. Li, Y. Lin, Q. Huang, W. Li, S. Zhao, Y. Fu, F. Chu, S.J.A.C.B.E. Tian, Coordination environment and architecture engineering over Co4N-based nanocomposite for accelerating advanced oxidation processes, 302 (2022) 120850.
[126] Y. Gao, Y. Zhu, Z. Chen, C.J.A.E. Hu, T. Engineering, Nitrogen-coordinated cobalt embedded in a hollow carbon polyhedron for superior catalytic oxidation of organic contaminants with peroxymonosulfate, 1(1) (2020) 76-85.
[127] X. Mi, P. Wang, S. Xu, L. Su, H. Zhong, H. Wang, Y. Li, S.J.A.C. Zhan, Almost 100% peroxymonosulfate conversion to singlet oxygen on single-atom CoN2+ 2 sites, 133(9) (2021) 4638-4643.
[128] X. Liang, D. Wang, Z. Zhao, T. Li, Y. Gao, C.J.A.F.M. Hu, Coordination number dependent catalytic activity of single-atom cobalt catalysts for Fenton-like reaction, 32(38) (2022) 2203001.
[129] S. Li, Y. Yang, J. Niu, H. Zheng, W. Zhang, Y.K. Leong, J.-S. Chang, B.J.E.S. Lai, Technology, Activation of PAA at the Fe–N x Sites by Boron Nitride Quantum Dots Enhanced Charge Transfer Generates High-Valent Metal-Oxo Species for Antibiotics Degradation, 58(49) (2024) 21871-21881.
[130] Z. Wang, Y. Yu, Q. Guo, C. Guan, J.J.W.R. Jiang, Nano-and micro-scale zerovalent iron-activated peroxydisulfate for methyl phenyl sulfoxide probe transformation in aerobic water: Quantifying the relative roles of SO4·−, Fe (IV),

and· OH, 223 (2022) 119014.
[131] C. Cheng, W. Ren, F. Miao, X. Chen, X. Chen, H.J.A.C.I.E. Zhang, Generation of FeIV= O and its Contribution to Fenton-Like Reactions on a Single-Atom Iron− N− C Catalyst, 62(10) (2023) e202218510.
[132] Y. Lin, Y. Wang, Z. Weng, Y. Zhou, S. Liu, X. Ou, X. Xu, Y. Cai, J. Jiang, B.J.N.C. Han, Coordination engineering of heterogeneous high-valent Fe (IV)-oxo for safe removal of pollutants via powerful Fenton-like reactions, 15(1) (2024) 10032.
[133] J. Jiang, Z. Zhao, J. Gao, T. Li, M. Li, D. Zhou, S.J.E.S. Dong, Technology, Nitrogen vacancy-modulated peroxymonosulfate nonradical activation for organic contaminant removal via high-valent cobalt-oxo species, 56(9) (2022) 5611-5619.
[134] S. Wang, J.J.A.C.B.E. Wang, Single atom cobalt catalyst derived from co-pyrolysis of vitamin B12 and graphitic carbon nitride for PMS activation to degrade emerging pollutants, 321 (2023) 122051.
[135] X. Liang, D. Wang, Z. Zhao, T. Li, Z. Chen, Y. Gao, C.J.A.C.B.E. Hu, Engineering the low-coordinated single cobalt atom to boost persulfate activation for enhanced organic pollutant oxidation, 303 (2022) 120877.
[136] W. Ren, L. Xiong, G. Nie, H. Zhang, X. Duan, S.J.E.S. Wang, Technology, Insights into the electron-transfer regime of peroxydisulfate activation on carbon nanotubes: the role of oxygen functional groups, 54(2) (2019) 1267-1275.
[137] W. Ren, L. Xiong, X. Yuan, Z. Yu, H. Zhang, X. Duan, S.J.E.S. Wang, Technology, Activation of peroxydisulfate on carbon nanotubes: electron-transfer mechanism, 53(24) (2019) 14595-14603.
[138] M. Yang, Z. Hou, X. Zhang, B. Gao, Y. Li, Y. Shang, Q. Yue, X. Duan, X.J.E.S. Xu, Technology, Unveiling the origins of selective oxidation in single-atom catalysis via Co–N4–C intensified radical and nonradical pathways, 56(16) (2022) 11635-11645.
[139] Y. Chai, H. Dai, X. Duan, Z. Sun, F. Hu, J. Qian, X.J.A.C.B.E. Peng, Elucidation of the mechanistic origin of spin-state-dependent P-doped Fe single-atom catalysts for the oxidation of organic pollutants through peroxymonosulfate activation, 341 (2024) 123289.
[140] F. Chen, L.L. Liu, J.H. Wu, X.H. Rui, J.J. Chen, Y.J.A.M. Yu, Single-atom iron anchored tubular g-C3N4 catalysts for ultrafast fenton-like reaction: roles of high-valency iron-oxo species and organic radicals, 34(31) (2022) 2202891.

List of publications and communications

Scientific publications

1. Zr-MOF/MXene composite for enhanced photothermal catalytic CO2 reduction in atmospheric and industrial flue gas streams. Yang Meng, Feng Yue, Shuo Zhang, **Cong Li**, Mengke Shi, Yongpeng Ma, **Mario Berrettoni**, Xiaojing Zhang, Hongzhong Zhang. *Carbon Capture Science and Technology. 2024*
2. Electro-assisted photocatalytic reduction of CO2 in ambient air using Ag/TNTAs at the gas-solid interface. Feng Yue, Zhaoya Fan, **Cong Li**, Yang Meng, Shuo Zhang, Mengke Shi, Minghua Wang, **Mario Berrettoni**, Jun Li, Hongzhong Zhang. *Materials Reports: Energy*. 2024
3. Preparation of Bi2WO6/MXene(Ti3C2Tx) Composite Material and Its Photothermal Catalytic Reduction of CO2 in Air. Lingji Zhang, Mengke Shi,Shuo Zhang, Feng Yue, Cairong Yang, Yang Meng, Wen Li, **Cong Li**, **Mario Berrettoni**, **Silvia Zamponi**, Yongpeng Ma, Hongzhong Zhang. *Catalysts. 2024*
4. Bimetallic NiCo2S4 Nanorod Cocatalyst Modified the Flower-Like Zn3In2S6 Microsphere for Visible-Light-Driven High-Efficiency Photocatalytic Hydrogen Production. Lan Wang, Shuo Zhang, Feng Yue, **Cong Li**, Bang Tan, Chenhao Luo, **Silvia Zamponi**, Hongzhong Zhang. *Energy Technology*. 2024

Contributions to conferences

1. Chemical Energy Conference, Energy Chemistry Division of the Chinese Chemical Society, Sichuan university, China, 28/10/2023-29/10/2023. Reporter

Acknowledgements

Time flies, and before I knew it, I had already spent three years on my PhD journey. Looking back on this challenging yet rewarding path, my heart is filled with immense gratitude. Although the moment of parting is approaching, and I cannot help but feel reluctant, what prevails is my deep appreciation for the experiences I have gained, the knowledge I have acquired, and most importantly, the invaluable support, warmth, and genuine friendships from my mentors and peers.

Having never left my hometown to study, I embarked on the journey of studying abroad with courage. The future was full of uncertainties—I had no idea where the road ahead would lead, nor where the destination lay. Faced with an unfamiliar language and a brand-new environment, I was filled with worries, fearing that I knew nothing and that even the most basic communication would be a challenge. However, standing here today, I have come to realize that the destination does not matter; what truly matters are the sights along the way and the people who have offered me help, encouragement, and companionship, making this journey rich and warm. On this occasion, I would like to extend my sincerest gratitude to all the teachers, friends, and family who have supported, guided, and encouraged me throughout these three years.

First and foremost, I would like to express my heartfelt gratitude to my PhD advisor Prof. Mario Berrettoni. From the application process to the successful completion of my PhD, your dedicated guidance has been invaluable to me. Throughout my doctoral journey, you have consistently led my research direction and provided unwavering academic support. Beyond research, you have cared for and helped me like a mentor and a guardian. You are not only the guide on my academic path but also a role model in life, teaching me invaluable lessons on integrity and conduct. As I complete this dissertation, I extend my deepest appreciation and sincerest best wishes to Prof. Mario Berrettoni.

At the same time, I would like to express my heartfelt gratitude to my co-supervisor Prof. Silvia Zamponi. Your wisdom and dedication to research are perfectly

complemented by your elegance and warmth. Whether in rigorous academic discussions or in casual conversations, your kindness and charisma have always made me feel respected and cared for. Thank you for being a role model in both research and life—your guidance will continue to inspire and influence my future academic and personal journey.

Furthermore, I would like to express my gratitude to Prof. Paolo Conti for your patient guidance and unwavering support throughout my PhD journey. Your help has given me greater confidence in my research endeavors. I am also deeply thankful to my dear friends, Martina Fattobene, Raffaele Emanuele Russo, Elisa Santoni, Muhammad Awais, Paolo Cognigni, Giacomo Seccacini, and Fuyong Liu. Whenever I encountered difficulties, you were always the first to lend a helping hand and offer me your sincere support. Your warm introduction to Italian culture and way of life helped me integrate more quickly into this unfamiliar country. Thank you for your kindness, encouragement, and understanding—your support has given me the strength to keep moving forward, especially during my most challenging moments.

At the same time, I would like to express my gratitude to my advisor in China, Prof. Hongzhong Zhang. From my graduate studies to my PhD, you have consistently guided and supported me. It has been my honor to learn under your dedicated mentorship. I will always be grateful for your wisdom, kindness, and the encouragement and inspiration you have given me.

A special thank you to Prof. Shuaixia Liu. Whenever I felt lost and uncertain, you always illuminated the path ahead for me. In my heart, you are not only an exceptional mentor but also like a caring elder. Whenever I faced challenges, I would seek your guidance like a child, and you would always patiently teach and support me, step by step, leading me toward a brighter future. Your warmth and kindness have brought me great comfort during my time studying abroad. Likewise, I would like to express my gratitude to Prof. Yue Li. Your keen intellect, profound knowledge, and unwavering dedication to research have deeply inspired me. Through your guidance and personal example, you have set a high standard for academic excellence that I aspire to follow. I

sincerely admire and appreciate your mentorship.

Furthermore, I would like to extend my deepest gratitude to my family. No matter how far apart we are, your unwavering love and support have always been my greatest source of strength. Your encouragement has ensured that I never felt alone on this journey of studying abroad and has given me the courage to face every challenge along the way. A special thank you to my girlfriend, Xiaoya Guo. You have always supported my choices and stood firmly by my side, offering me unwavering encouragement no matter the circumstances. Your companionship has brought warmth and strength to my most challenging years as a PhD student. I am deeply grateful for your understanding and patience. The journey we have shared together is one of the most precious treasures of my life.

Finally, I would like to express my gratitude to everyone who has helped me along this journey. Whether it was a kind word, a helping hand, or silent companionship when I needed it most, your presence has brought me warmth and strength. As I write these words late at night, I reflect on the love, support, and encouragement I have received, marking my growth and gratitude along the way. May we all carry this precious bond with us as we continue forward on our respective paths.